Measurement and Manipulation of Quantum States of Travelling Light Fields

Merlin F. W. Cooper
Corpus Christi College
University of Oxford

A thesis submitted for the degree of
Doctor of Philosophy

Trinity term 2014

Measurement and Manipulation of Quantum States of Travelling Light Fields

Merlin F. W. Cooper
Corpus Christi College, Oxford

Submitted for the degree of *Doctor of Philosophy*
Trinity term 2014

Abstract

This thesis is concerned with the generation of non-classical quantum states of light, the photon-level manipulation of quantum states and the accurate tomography of both quantum states and quantum processes. In optics, quantum information can be encoded and processed in both discrete and continuous variables. Hybrid approaches combining for example homodyne detection with conditional state preparation and manipulation are gaining increasing prominence.

The development and characterization of a time-domain balanced homodyne detector (BHD) is presented. The detector has a bandwidth of 80 MHz, a signal-to-noise ratio of 14.5 dB and an efficiency of 86% making it well-suited to pulse-to-pulse measurement of quantum optical states. The BHD is employed to perform quantum state tomography (QST) of non-classical multi-photon Fock states generated by spontaneous parametric down-conversion. A detailed investigation of the mode-matching between the local oscillator used for homodyne detection and the generated Fock states is presented. The one-, two- and three-photon Fock states are reconstructed with a combined preparation and detection efficiency exceeding 50%.

Fock states have a number of applications in quantum state engineering, where non-classical ancilla states and conditional measurements enable photon-level manipulation of quantum states. Fock state filtration (FSF) is investigated – an example of a post-selected beam splitter which is a basic building block for many quantum state engineering protocols. A model is developed incorporating the effect of experimental imperfections. An experimental implementation of a Fock state filter is fully characterized by means of coherent-state quantum process tomography (QPT). The reconstructed process is found to be consistent with the model. The filter preferentially removes the single-photon component from an arbitrary input quantum state.

Calibration of optical detectors in the quantum regime is discussed. Quantum detector tomography (QDT) is reviewed and contrasted with a new technique for performing QST with a calibrated detector known as the fitting of data patterns (FDP). The first experimental characterization of a BHD is performed by probing the detector with phase-averaged coherent states. The FDP method is shown to be applicable to the estimation of quantum processes, where a detector response is not assumed – thus demonstrating the versatility of the FDP approach as a new method in the quantum tomography toolbox.

This thesis is dedicated to my Mother and Father
who provided me with an education and upbringing
for which I am eternally grateful.

Thank you.

Author's Publications

Journal publications

1. M. Cooper, M. Karpiński, and B. J. Smith. "**Local mapping of detector response for realiable quantum state estimation.**" *Nature Communications* **5**, 4332 (2014).
2. M. Cooper, L. J. Wright, C. Söller, and B. J. Smith. "**Experimental generation of multi-photon Fock states.**" *Optics Express*, **21**(5), 5309-5317 (2013).
3. M. Cooper, C. Söller, and B. J. Smith. "**High-stability time-domain balanced homodyne detector for ultrafast optical pulse applications.**" *Journal of Modern Optics*, **60**(8), 611-616 (2013).

Conferences

1. M. Cooper, M. Karpiński, and B. J. Smith. "**Experimental demonstration of optical homodyne tomography by fitting of data patterns.**" *Quantum Optics VIII, Warsaw*, May 2013.
2. M. Cooper, C. Söller, and B. J. Smith. "**High-stability time-domain balanced homodyne detector for ultrafast optical pulse applications.**" *Conference on Lasers & Electro-Optics/Quantum Electronics & Laser Science Conference*, May 2012.

Contents

1 Introduction **1**

1.1 Thesis outline 5

2 Key Concepts **7**

2.1 Stages of a quantum experiment 7

2.1.1 Quantum state 8

2.1.2 Evolution of the quantum state 10

2.1.3 Measurement of the quantum state 11

2.2 Quantization of the electromagnetic field 13

2.2.1 Quantum optical states 18

2.3 Wigner function 21

2.4 Quantum tomography 23

3 Detection of Quantum Light **26**

3.1 Intensity detection 27

3.1.1 Avalanche photodiode 27

3.1.2 Superconducting detectors 29

3.1.3 Multiplexed detection . . . 29

3.2 Balanced homodyne detection . . . 30

3.2.1 Simplified treatment of balanced homodyne detection . . . 31

3.2.2 Spatial-temporal modes . . . 33

3.3 Optical homodyne tomography . . . 40

3.3.1 Maximum-likelihood estimation . . . 42

3.4 Development of a pulsed balanced homodyne detector . . . 44

3.4.1 Electro-optical setup . . . 44

3.4.2 Detector operation and performance . . . 49

3.4.3 Tomography of weak coherent state . . . 67

3.4.4 Comparison with reported BHDs . . . 67

3.5 Summary . . . 71

4 Generation of Multi-Photon Fock States 72

4.1 Parametric down-conversion . . . 74

4.1.1 Derivation of PDC unitary transformation . . . 75

4.1.2 Quantifying the multimode nature of PDC . . . 79

4.2 PDC in bulk KDP . . . 83

4.2.1 Experimental arrangement . . . 85

4.2.2 Difference frequency generation . . . 88

4.3 Homodyne tomography of multi-photon Fock states . . . 95

4.3.1 Mode matching of LO and heralded Fock states . . . 98

4.3.2 Fock state purity . . . 102

4.3.3 Optimization of LO and Fock state mode overlap . . . 104

4.3.4 Heralding of multi-photon Fock states . . . 108

4.3.5 State reconstruction results . . . 109

4.3.6 Summary of properties of reconstructed states 119

4.4 Summary 120

5 Photon-Level Quantum Operations **122**

5.1 Fock state filtration 124

5.1.1 Ideal operation 126

5.1.2 Non-ideal operation 130

5.2 Quantum progress tomography 139

5.2.1 Maximum-likelihood reconstruction 139

5.2.2 Probabilistic processes 142

5.2.3 Coherent state QPT 142

5.3 Complete characterization of realistic Fock state filter 143

5.3.1 Experimental setup: FSF 144

5.3.2 Experimental test: attenuation 150

5.3.3 Experimental reconstruction of FSF process 153

5.4 Summary 163

6 Calibration of Quantum Detectors **165**

6.1 Quantum detector tomography 166

6.2 Fitting of data patterns 172

6.2.1 Outline of FDP procedure 172

6.2.2 Probe state requirements 175

6.2.3 Simulation: optical homodyne tomography 177

6.3 Experimental demonstration of the FDP method 180

6.3.1 Probe state preparation 181

6.3.2 Determination of data pattern set 187

6.3.3 Tomography of non-classical quantum states . . . 189
6.4 Comparison between QDT+QST and FDP . . . 195
6.5 FDP process tomography . . . 196
6.5.1 Description of procedure . . . 196
6.5.2 Trace-preserving processes . . . 199
6.5.3 Probabilistic processes . . . 205
6.6 Summary . . . 208

7 Conclusion **209**
7.1 Future directions . . . 210
7.1.1 FPGA-based signal processing and heralding logic . . . 210
7.1.2 Improved squeezed and Fock state sources . . . 211
7.1.3 On-chip homodyne detection . . . 213
7.1.4 Full characterization of BHD . . . 213
7.1.5 QPT of down-conversion . . . 214

A Source alignment procedure using DFG **215**

B Oscilloscope configuration **217**

C BHD Printed Circuit Board Layout **219**

D Laboratory setup **221**

Bibliography **223**

1 Introduction

Optics is the field of physics concerned both with the fundamental nature of light and the development of instruments to manipulate and detect it. The first known examples of optical instruments are obsidian mirrors dating from 6000 BC [1] and the ancient Egyptian *Nimrud* lens [2], which dates from 700 BC. Theories of light were developed by the ancient Greeks and Indian philosophers [3]. For centuries it was debated whether light should be interpreted as a wave or a particle – with Newton as an authoritative proponent of the particle or corpuscular description [4] and Huygens in favour of the wave description [5]. The debate appeared to have been settled in the 19th century with the famous double-slit experiment by Young in 1803 [6] followed by the derivation of the electromagnetic wave equation by Maxwell in 1873 [7]. However, with the onset of the 20th century came a turn of events which would cast doubt on the by-then widely accepted belief that light should be described with a wave theory. First Planck solved the mystery of the ultraviolet catastrophe by positing that black-body radiation is emitted in discrete packets of energy [8] – a concept which was harnessed by Einstein in 1905 to explain the photoelectric effect [9]. However, although evidence was mounting that light consisted of discrete particles or quanta a formal theory of the quantization of light was lacking. In what was probably the first tabletop experiment to probe the quantum nature of light, in 1909 Taylor [10] observed interference fringes in a double-slit experiment despite attenuation of the light source to the equivalent intensity of “a standard candle burning at a distance slightly exceeding a mile” [10]. The advent of quantum mechanics in the first half of the 20th century provided the conceptual underpinnings for the quantization of light and hence electromagnetic radiation – with the term “photon”, now used in reference to a single quantum of light, coined by Lewis in 1926 [11] and the groundwork for the quantum theory of radiation laid by Dirac in 1927 [12]. Quantum mechanics combines the wave and particle descriptions of light and provides an explanation for the observation of single-photon interference effects [13–15] such as Hong-Ou-Mandel interference [16].

Early research in quantum optics focussed on observing optical phenomena not compatible with classical theory [17] – such as photon anti-bunching which provided direct experimental proof for the quantized nature of the electromagnetic field [18]. Arguably the first quantum optics experiment which had wider consequences for understanding quantum theory was performed by Aspect *et al.* [19] who demonstrated a violation of the CHSH form of Bell’s inequality [20] in an experiment employing entangled photon pairs – thus providing experimental evidence in support of quantum nonlocality. Since this work, quantum optics has been the platform of choice for further tests of quantum theory [21, 22] including indistinguishably of quantum particles [16], verification of commutation relations [23], investigation of local hidden-variable models [24] and demonstrations of micro-macro entanglement [25, 26]. Going beyond tests of quantum mechanics, the quantum phenomenon of squeezing [27] has been employed in the search for gravitational waves based on interferometry with squeezed light [28] and a quantum optical experiment has been proposed to determine whether space-time is quantized [29]. Thus quantum optics plays a key role in improving our understanding of nature, perhaps because many such landmark experiments can fit onto a laboratory tabletop and be performed by a small group of researchers.

In parallel to fundamental experimentation in physics, the burgeoning field of quantum information has spawned various 'quantum-enhanced' applications [21, 30] well-suited to implementation in optical systems [31] including quantum computation and simulation [32–36], quantum communication [37, 38], quantum-enhanced sensing [39, 40] and random number generation [41]. The fundamental driving principle is to harness quantum effects – such as entanglement and the Heisenberg uncertainty principle [42] – to improve the efficiency of encoding and manipulating information. Optics serves as an ideal platform since it naturally lends itself to transmission through fiber-networks or free-space channels, thus enabling large-scale quantum networks to be realized [43, 44]. Furthermore, at ambient temperature there is effectively no thermal noise at optical-frequencies and photons do not interact strongly with the environment, which enables preservation of the quantum coherence that enables such applications [35, 31]

Having identified optics as a strong candidate platform upon which to build the quantum information processors of tomorrow, there is still a great deal of choice in deciding which degrees of freedom of the light should be used to encode information. In optics, information could be encoded in discrete-variables (DV) such as two orthogonal polarization states of a single photon or two spatial modes within a waveguide [35]. Alternatively, continuous-variable (CV) approaches exploit continuous degrees of freedom such as the amplitude and phase of a single electromagnetic field mode [45, 46]. In reality such distinctions are not always rigid – indeed hybrid approaches may ultimately prove the best route for encoding and processing quantum information in optics [47, 48].

A key requirement for the successful realization of quantum-optical technologies is that each part of the quantum optical system be well-characterized. Such characterization is usually performed by means of quantum tomography [49, 50] which is a broad field of research concerned with the development of theoretical and experimental techniques for characterizing the state of quantum systems [51], processes and channels [52] and even measurements [53]. For quantum optical systems, the technique of optical homodyne tomography is well-established [54] and was employed in the first experimental quantum tomography [55]. Just as electronic circuits can be probed with network analysers, so can quantum circuits be probed using tomography techniques to ensure correct operation of quantum devices. Only recently were techniques developed to perform tomography of CV quantum processes [56], such as those which might be encountered in CV quantum computing [57, 58].

The broad aim of this thesis is to build on the state of the art in the field of creating, manipulating and measuring the quantum state of a single electromagnetic field mode, namely that of a travelling wave. This thesis deals with the practical aspects of optical field detection of quantum light, the generation of non-classical multi-photon Fock states and photon-level manipulations to engineer quantum states of a single electromagnetic field mode. Tomography techniques are exploited throughout to verify the quality of the states produced and the fidelity of implemented quantum manipulations with respect to realistic models, which are developed as part of this work. As well as harnessing existing tomography techniques to probe new states and processes, a comparatively new technique known as the *fitting of data patterns* is demonstrated to perform the first independent calibration of a balanced homodyne detector and subsequent tomography of non-classical states. Finally the technique is extended to enable the tomography of quantum processes with calibrated detectors – thus contributing a new technique to the quantum tomography toolbox.

1.1 Thesis outline

The fundamental concepts underpinning the work presented in this thesis are reviewed in chapter 2 – starting with the generic description of a quantum experiment in terms of three key elements – quantum state preparation, evolution of the quantum state and subsequent measurement of the output quantum state. Quantization of the electromagnetic field gives rise to the concept of the photon and the description of a single mode of the electromagnetic field in terms of dimensionless quadrature operators. From these operators the Wigner quasi-probability distribution emerges which naturally leads into a discussion of quantum tomography – a toolbox of techniques to enable characterization of each of the three stages of a quantum experiment.

Having set the theoretical backdrop for the thesis – namely tomography of quantum optical systems – techniques for detecting quantum light are explored in chapter 3, with an emphasis placed on optical field detection via the technique of balanced homodyne detection. The development and characterization of a balanced homodyne detector (BHD) is detailed which enables a broad range of quantum optical experiments in the CV regime.

In chapter 4 the BHD is employed to characterize multi-photon Fock states generated by pulsed parametric down-conversion. Quantum state tomography (QST) of the one-, two-, and three-photon Fock states is demonstrated and applications of photonic Fock states are explored. This leads naturally into the topic of photon-level quantum operations which forms the basis of chapter 5. The manipulation of a single electromagnetic field mode through quantum operations such as photon addition and subtraction is reviewed with specific attention paid to Fock state filtration (FSF) a measurement-induced non-linearity enabling particular Fock layers of a quantum state to be removed. A realistic model of FSF is developed from which the full process tensor is derived, taking into account experimental imperfections. FSF is implemented experimentally and the developed model is corroborated by performing quantum process tomography of the filter.

Finally – continuing the theme of quantum tomography – in chapter 6 attention is turned to the topic of how to calibrate quantum detectors. The method of quantum detector tomography (QDT) is briefly reviewed and contrasted with a new technique for performing QST with a calibrated detector known as the fitting of data patterns (FDP). The FDP technique is employed to independently characterize the BHD and enable QST of non-classical Fock states without assuming a model of the detector. Finally the FDP method is shown to also be applicable to tomography of quantum processes – thus demonstrating the versatility of this comparatively new technique as a valuable part of the quantum tomography toolbox. Chapter 7 summarises the key results of this thesis and offers a perspective on future research directions.

2

Key Concepts

This thesis is concerned with the preparation, manipulation and detection of quantum states of light. In this chapter the key concepts underpinning the work presented in this thesis are outlined – starting with the archetypal description of a quantum experiment where a state is prepared, evolved and ultimately measured. Since this work is concerned with the quantum state of light, a brief outline of the quantization of the electromagnetic field is presented – through which the concept of the photon emerges. Finally quantum tomography is introduced – a broad field of research in itself concerned with methods to determine the mathematical description of a particular stage of a quantum experiment.

2.1 Stages of a quantum experiment

In quantum physics an experiment can be described in terms of the preparation of a quantum system in a particular state, the evolution of the quantum state and the subsequent measurement of that state. This somewhat general framework allows the experiment to be broken into three distinct stages, each of which is completely described by a mathematical object. Most generally, the state is described by a density matrix $\hat{\rho}$, the evolution is described by a completely-positive trace non-increasing map $\mathcal{E}$ and the measurement apparatus is described by a set of operators known as the positive operator-valued measure (POVM) set denoted $\{\hat{\Pi}_i\}$. A brief summary of these is presented in the following sections, whilst a more thorough description is offered in standard texts such as that of Nielsen and Chuang [35].

2.1.1 Quantum state

The quantum state of a system describes the configuration of the system and thus precise knowledge of the quantum state allows the evolution of the state and the probability of measurement outcomes to be predicted. Mathematically a *pure* quantum state is represented as a unit state vector within a Hilbert space $\mathcal{H}$, typically denoted in Dirac notation as $|\psi\rangle$. It is convenient to work with a fixed orthonormal basis spanning the state space $\{|\phi_i\rangle\},\ \ i = 1...N$, where N is the dimension of the Hilbert space. Thus an arbitrary pure state may be expanded in this fixed basis as

$$|\psi\rangle = \sum_i a_i|\phi_i\rangle, \tag{2.1}$$

where the expansion coefficients are given by $a_i = \langle\phi_i|\psi\rangle$ and the state is normalized such that $\sum_i |a_i|^2 = 1$. The probability to find the system in basis state $|\phi_i\rangle$ is given by $\Pr(|\phi_i\rangle) = |\langle\phi_i|\psi\rangle|^2$. The dimensionality of the Hilbert space depends on the physical system being described. Typically, the number of dimensions is limited by a physical consideration. One such example is describing the polarization state of a mode of light. Here the state space is two-dimensional and thus only two basis vectors are required to describe any possible polarization state.

The formulation of the quantum state as a state vector is limiting since it does not enable the inclusion of classical uncertainty about the state of the quantum system. Suppose the state of the system is one of a number of different pure states $|\psi_i\rangle$ with probabilities

p_i. Mathematically this situation is described by the density matrix $\hat{\rho}$ given by

$$\hat{\rho} = \sum_i p_i |\psi_i\rangle\langle\psi_i|, \tag{2.2}$$

where $\sum_i p_i = 1$. The probability to find the system in the basis state $|\phi_j\rangle$ is now given by $\Pr(|\phi_j\rangle) = \sum_i p_i |\langle\phi_j|\psi_i\rangle|^2$, which incorporates both the quantum and classical uncertainty. The density matrix is a normalized, positive operator such that $\mathrm{Tr}[\hat{\rho}] = 1$ and

$$\langle\phi_j|\hat{\rho}|\phi_j\rangle = \sum_i p_i \langle\phi_j|\psi_i\rangle\langle\psi_i|\phi_j\rangle = \sum_i p_i |\langle\phi_j|\psi_i\rangle|^2 \geq 0. \tag{2.3}$$

Of course, the density matrix formalism can perfectly well be used to describe a pure state $|\psi\rangle$ such that $\hat{\rho} = |\psi\rangle\langle\psi|$. Finally, the density matrix can be written in the orthonormal basis $\{|\phi_i\rangle\}$ such that

$$\hat{\rho} = \sum_{i,j} \rho_{ij} |\phi_i\rangle\langle\phi_j|, \tag{2.4}$$

where the expansion coefficients ρ_{ij} are matrix elements of the density matrix given by $\rho_{ij} = \langle\phi_i|\hat{\rho}|\phi_j\rangle$.

In quantum optics, commonly encountered basis vectors are the horizontal and vertical polarization states of light $\{|H\rangle, |V\rangle\}$, the spin up and spin down states of a spin 1/2 particle $\{|\uparrow\rangle, |\downarrow\rangle\}$, and the Fock basis $\{|n\rangle\}$, where $|n\rangle$ is an energy eigenstate of a harmonic oscillator, e.g. vibrational excitations or photons.

2.1.2 Evolution of the quantum state

A quantum system initially described by density matrix $\hat{\rho}$ evolves due to a channel or process into a final density matrix $\hat{\rho}'$. In the most general sense this may be written as

$$\hat{\rho}' = \mathcal{E}(\hat{\rho}), \tag{2.5}$$

where the map $\mathcal{E}$ completely describes the process. The most simple example of evolution in quantum mechanics is unitary evolution described by $|\psi'\rangle = \hat{U}|\psi\rangle$, where $\hat{U}$ is a unitary operator such that $\hat{U}^\dagger\hat{U} = \hat{I}$, in which $\hat{I}$ is the identity operator such that $\hat{I}|\psi\rangle = |\psi\rangle$. Thus for unitary evolution the density matrix transforms as

$$\hat{\rho}' = \hat{U}\hat{\rho}\hat{U}. \tag{2.6}$$

Closed quantum systems evolve according to unitary evolution. However, more general evolution can result from interaction of the system with the environment, which may result in non-unitary evolution of the quantum state and cannot be described as above since non-unitary evolution can result in a pure state becoming mixed.

In the most general form, such evolution can be expressed as the linear map from the input Hilbert space $\mathcal{H}$ to the output Hilbert space $\mathcal{K}$ such that

$$\hat{\rho}' = \mathcal{E}(\hat{\rho}) = \sum_i \hat{E}_i\hat{\rho}\hat{E}_i^\dagger, \tag{2.7}$$

where $\{\hat{E}_i\}$ are a set of operators which map from $\mathcal{H}$ to $\mathcal{K}$ [59]. This representation of the process is known as the Kraus decomposition [59] or operator-sum representation [35]. In general there is some freedom as to the exact form of the operators $\{\hat{E}_i\}$ for a given process. However, for a Hilbert space of dimension d on which the process $\mathcal{E}$ acts, there are at most d^2 operators required to represent any possible operation that Hilbert space.

The probability that the process $\mathcal{E}$ occurs is given by the trace of the output state and must satisfy

$$0 \leq \mathrm{Tr}[\mathcal{E}(\hat{\rho})] \leq 1, \tag{2.8}$$

which imposes a condition on the operators $\{\hat{E}_i\}$ such that $\sum_i \hat{E}_i^\dagger \hat{E}_i \leq \hat{I}$. Furthermore, the process as specified is a completely-positive (CP) map such that the output density matrix is positive semi-definite.*

Finally, for a particular choice of basis, the process $\mathcal{E}$ can be represented as a tensor. For example, if the process is represented in the Fock basis then it must map input density matrices in the Fock basis to output density matrices in the Fock basis. Thus the process $\mathcal{E}$ is a rank-4 tensor [60, 61]. This formalism is used in chapter 5.

2.1.3 Measurement of the quantum state

Measurement in quantum mechanics is described by a set of operators $\{\hat{M}_i\}$, where $i = 1...N$ labels the different measurement outcomes which may occur [35]. The probability that measurement outcome i occurs if the system is in the pure state $|\psi\rangle$ is given by

$$\mathrm{Pr}(i) = \langle\psi|\hat{M}_i^\dagger \hat{M}_i|\psi\rangle. \tag{2.9}$$

*But not necessarily normalized as the output density matrix $\hat{\rho}'$ carries information about the success probability, equation 2.8.

Furthermore, after the measurement has been made the state of the system is altered such that

$$|\psi'\rangle = \frac{\hat{M}_i|\psi\rangle}{\sqrt{\langle\psi|\hat{M}_i^\dagger\hat{M}_i|\psi\rangle}}, \tag{2.10}$$

where the denominator ensures that the post-measurement state is correctly normalized. If the initial state is described by a density matrix $\hat{\rho}$, the density matrix after the measurement $\hat{\rho}'$ is given by

$$\hat{\rho}' = \frac{\hat{M}_i\hat{\rho}\hat{M}_i^\dagger}{\mathrm{Tr}\left[\hat{M}_i^\dagger\hat{M}_i\hat{\rho}\right]}. \tag{2.11}$$

Since the probability of all possible measurement outcomes must sum to one, the measurement operators satisfy the completeness relation

$$\sum_i \hat{M}_i^\dagger\hat{M}_i = \hat{I}, \tag{2.12}$$

which expresses the fact that a single measurement made on the system must yield some outcome.

Often the post-measurement state of the system is of no interest since the very act of measurement may effectively destroy the system. One such example is photodetection – a process whereby light is converted to an electrical signal. The process is irreversible and thus the post-measurement state is not defined *per se*. Often one is only interested in predicting the relative frequency of different measurement outcomes, rather than the continued evolution of the system post-measurement. For such purposes, the positive operator-valued measure (POVM) formalism of measurement is more appropriate. POVM elements $\hat{\Pi}_i$ are related to the measurement operators $\hat{M}_i$ according to

$$\hat{\Pi}_i = \hat{M}_i^{\dagger}\hat{M}_i, \tag{2.13}$$

and thus the probability of obtaining measurement outcome i for a pure state $|\psi\rangle$ is given by $\Pr(i) = \langle\psi|\hat{\Pi}_i|\psi\rangle$. If the system is in a mixed state described by density matrix $\hat{\rho}$, the measurement outcome probabilities are expressed as

$$\Pr(i) = \mathrm{Tr}\left[\hat{\Pi}_i\hat{\rho}\right]. \tag{2.14}$$

POVM elements are positive operators and the POVM set is complete such that

$$\hat{\Pi}_i \geq 0, \quad \forall\ i, \qquad\qquad \sum_i \hat{\Pi}_i = \hat{I}. \tag{2.15}$$

This thesis will employ the POVM description of quantum measurements where appropriate.

2.2 Quantization of the electromagnetic field

Quantization of the electromagnetic field is brought about by the association of a quantum-mechanical harmonic oscillator with each field mode [14, 62]. In a cavity a mode is defined by a particular polarization and wave vector allowed according to cavity boundary conditions.

In the Coulomb gauge ($\nabla \cdot \mathbf{A} = 0$), the electric field and magnetic field density may be written solely in terms of the vector potential $\mathbf{A}$ [14, 62]

$$\mathbf{E}(\mathbf{r},t) = -\frac{\partial \mathbf{A}(\mathbf{r},t)}{\partial t}, \tag{2.16}$$

$$\mathbf{B}(\mathbf{r},t) = \nabla \times \mathbf{A}(\mathbf{r},t). \tag{2.17}$$

For a single mode of the cavity, the vector potential may be written as

$$\mathbf{A}_{\mathbf{k}\lambda}(\mathbf{r},t) = \mathbf{e}_{\mathbf{k}\lambda}\left(A(t)_{\mathbf{k}\lambda}e^{i\mathbf{k}\cdot\mathbf{r}} + A^*_{\mathbf{k}\lambda}(t)e^{-i\mathbf{k}\cdot\mathbf{r}}\right), \tag{2.18}$$

where $\mathbf{k}$ is the wave-vector, $A(t)_{\mathbf{k}\lambda} = A_{\mathbf{k}\lambda}e^{-i\omega_k t}$, $\omega_k = c|\mathbf{k}|$, and $\mathbf{e}_{\mathbf{k}\lambda}$ is the unit polarization vector obeying $\mathbf{k}\cdot\mathbf{e}_{\mathbf{k}\lambda} = 0$ and $\mathbf{e}_{\mathbf{k}\lambda}\cdot\mathbf{e}_{\mathbf{k}\lambda'} = \delta_{\lambda\lambda'}$. The subscript $\mathbf{k}\lambda$ is the mode label for the wave-vector ($\mathbf{k}$) and polarization state ($\lambda = 1, 2$). Using equation 2.16 and equation 2.17 in conjunction with equation 2.18, the electric field and magnetic field density take the form

$$\mathbf{E}_{\mathbf{k}\lambda}(\mathbf{r},t) = i\omega_k\mathbf{e}_{\mathbf{k}\lambda}\left(A_{\mathbf{k}\lambda}e^{i(\mathbf{k}\cdot\mathbf{r}-\omega_k t)} - A^*_{\mathbf{k}\lambda}e^{-i(\mathbf{k}\cdot\mathbf{r}-\omega_k t)}\right), \tag{2.19}$$

$$\mathbf{B}_{\mathbf{k}\lambda}(\mathbf{r},t) = i(\mathbf{k}\times\mathbf{e}_{\mathbf{k}\lambda})\left(A_{\mathbf{k}\lambda}e^{i(\mathbf{k}\cdot\mathbf{r}-\omega_k t)} - A^*_{\mathbf{k}\lambda}e^{-i(\mathbf{k}\cdot\mathbf{r}-\omega_k t)}\right), \tag{2.20}$$

Classically the energy stored in an electromagnetic field occupying a cavity volume $\mathcal{V}$ is given by the integral

$$H = \frac{1}{2}\int_{\mathcal{V}} d^3r \left(\epsilon_0\mathbf{E}^2 + \frac{1}{\mu_0}\mathbf{B}^2\right). \tag{2.21}$$

Substituting the forms for the electric field and magnetic field density (equations 2.19 and 2.20) into equation 2.21 yields the Hamiltonian for a single confined mode of the electromagnetic field [62]

$$H_{\mathbf{k}\lambda} = 2\epsilon_0 V \omega_k^2 A_{\mathbf{k}\lambda} A_{\mathbf{k}\lambda}^*. \tag{2.22}$$

By introducing the canonically-conjugate variables $p_{\mathbf{k}\lambda}$ and $x_{\mathbf{k}\lambda}$ defined according to the relation

$$A_{\mathbf{k}\lambda} = \frac{1}{2\omega_k\sqrt{\epsilon_0 V}}(\omega_k x_{\mathbf{k}\lambda} + ip_{\mathbf{k}\lambda}), \tag{2.23}$$

equation 2.22 may be written in the more familiar form of a simple harmonic oscillator of unit mass

$$H_{\mathbf{k}\lambda} = \frac{1}{2}\left(p_{\mathbf{k}\lambda}^2 + \omega_k^2 x_{\mathbf{k}\lambda}^2\right). \tag{2.24}$$

where $x_{\mathbf{k}\lambda}$ is the position and $p_{\mathbf{k}\lambda}$ is the momentum. Upon replacement of the position and momentum variables in equation 2.24 by the Hermitian operators for position and momentum $\hat{x}_{\mathbf{k}\lambda}$ and $\hat{p}_{\mathbf{k}\lambda}$ which satisfy the commutation relation $[\hat{x}_{\mathbf{k}\lambda}, \hat{p}_{\mathbf{k}'\lambda'}] = i\hbar\delta_{\mathbf{k}\mathbf{k}'}\delta_{\lambda\lambda'}$, the Hamiltonian operator $\hat{H}_{\mathbf{k}\lambda}$ is formed

$$\hat{H}_{\mathbf{k}\lambda} = \frac{1}{2}\left(\hat{p}_{\mathbf{k}\lambda}^2 + \omega_k^2 \hat{x}_{\mathbf{k}\lambda}^2\right). \tag{2.25}$$

The common approach for finding the energy spectrum for such a system is to define two non-Hermitian operators from linear combinations of $\hat{p}_{\mathbf{k}\lambda}$ and $\hat{x}_{\mathbf{k}\lambda}$ – the so called creation and annihilation operators [62]

$$\hat{a}^{\dagger}_{\mathbf{k}\lambda} = \frac{1}{\sqrt{2\hbar\omega_k}} \left(\omega_k \hat{x}_{\mathbf{k}\lambda} - i\hat{p}_{\mathbf{k}\lambda}\right), \tag{2.26}$$

$$\hat{a}_{\mathbf{k}\lambda} = \frac{1}{\sqrt{2\hbar\omega_k}} \left(\omega_k \hat{x}_{\mathbf{k}\lambda} + i\hat{p}_{\mathbf{k}\lambda}\right). \tag{2.27}$$

The action of $\hat{a}^{\dagger}_{\mathbf{k}\lambda}$ ($\hat{a}_{\mathbf{k}\lambda}$) is to create (annihilate) one quantum of energy $\hbar\omega_k$ in the field mode $\mathbf{k}\lambda$. For electromagnetic radiation this quantum is known as a photon [11]. The Hamiltonian for the electromagnetic field can be cast in terms of $\hat{a}^{\dagger}_{\mathbf{k}\lambda}$ and $\hat{a}_{\mathbf{k}\lambda}$ such that

$$\hat{H}_{\mathbf{k}\lambda} = \hbar\omega_k \left(\hat{a}^{\dagger}_{\mathbf{k}\lambda}\hat{a}_{\mathbf{k}\lambda} + \frac{1}{2}\right). \tag{2.28}$$

The vacuum state is the state of the electromagnetic field with no excitations, i.e. containing no photons. Consider a state where n photons have been raised from the vacuum into a given mode. Such states with well-defined photon number are known as Fock states and are represented as $|n\rangle_{\mathbf{k}\lambda}$. The energy eigenvalue equation for $|n\rangle_{\mathbf{k}\lambda}$ using equation 2.28 is

$$\hat{H}_{\mathbf{k}\lambda}|n\rangle_{\mathbf{k}\lambda} = \hbar\omega_k \left(\hat{a}^{\dagger}_{\mathbf{k}\lambda}\hat{a}_{\mathbf{k}\lambda} + \frac{1}{2}\right)|n\rangle_{\mathbf{k}\lambda} = E_n|n\rangle_{\mathbf{k}\lambda}. \tag{2.29}$$

Using the commutation relation $[\hat{a}_{\mathbf{k}\lambda}, \hat{a}^{\dagger}_{\mathbf{k}'\lambda'}] = \delta_{\mathbf{k}\mathbf{k}'}\delta_{\lambda\lambda'}$ it can be verified that the state $\hat{a}^{\dagger}_{\mathbf{k}\lambda}|n\rangle_{\mathbf{k}\lambda}$ is an eigenstate of the Hamiltonian with energy $E_n + \hbar\omega_k$. Therefore, the action of the creation operator $\hat{a}^{\dagger}_{\mathbf{k}\lambda}$ is to create one quantum of energy in a particular mode, i.e. a photon. Conversely, the annihilation operator $\hat{a}_{\mathbf{k}\lambda}$ has the effect of removing one quantum of energy $\hbar\omega_k$ from the mode. The action of $\hat{a}_{\mathbf{k}\lambda}$ and $\hat{a}^{\dagger}_{\mathbf{k}\lambda}$ on the Fock state $|n\rangle_{\mathbf{k}\lambda}$ is given by

$$\hat{a}_{\mathbf{k}\lambda}|n\rangle_{\mathbf{k}\lambda} = \sqrt{n}|n-1\rangle_{\mathbf{k}\lambda}, \tag{2.30}$$

$$\hat{a}^{\dagger}_{\mathbf{k}\lambda}|n\rangle_{\mathbf{k}\lambda} = \sqrt{n+1}|n+1\rangle_{\mathbf{k}\lambda}. \tag{2.31}$$

The classical electric and magnetic fields become Hermitian operators in quantum optics. The electric field operator for mode $\mathbf{k}\lambda$ is given by equation 2.19, using the creation and annihilation operators such that

$$\hat{\mathbf{E}}(\mathbf{r},t) = i\sum_{\mathbf{k},\lambda}\sqrt{\frac{\hbar\omega_k}{2\epsilon_0 V}}\mathbf{e}_{\mathbf{k}\lambda}\left(\hat{a}_{\mathbf{k}\lambda}\exp(i\mathbf{k}\cdot\mathbf{r})\exp(-i\omega_k t) - \hat{a}^{\dagger}_{\mathbf{k}\lambda}\exp(-i\mathbf{k}\cdot\mathbf{r})\exp(i\omega_k t)\right). \tag{2.32}$$

Two dimensionless Hermitian operators, known as the field quadrature operators, can be cast in terms of $\hat{a}_{\mathbf{k}\lambda}$ and $\hat{a}^{\dagger}_{\mathbf{k}\lambda}$ according to the definition [14, 62, 54]

$$\hat{X}_{\mathbf{k}\lambda} = \frac{1}{\sqrt{2}}(\hat{a}^{\dagger}_{\mathbf{k}\lambda} + \hat{a}_{\mathbf{k}\lambda}), \tag{2.33}$$

$$\hat{P}_{\mathbf{k}\lambda} = \frac{1}{\sqrt{2}i}(\hat{a}_{\mathbf{k}\lambda} - \hat{a}^{\dagger}_{\mathbf{k}\lambda}). \tag{2.34}$$

where $\hat{X}_{\mathbf{k}\lambda}$ and $\hat{P}_{\mathbf{k}\lambda}$ satisfy the commutation relation $[\hat{X}_{\mathbf{k}\lambda}, \hat{P}_{\mathbf{k}'\lambda'}] = \delta_{\mathbf{k}\mathbf{k}'}\delta_{\lambda\lambda'}$. At first sight these operators look awfully similar to the position and momentum of the harmonic oscillator which satisfy $[\hat{x}_{\mathbf{k}\lambda}, \hat{p}_{\mathbf{k}'\lambda'}] = i\hbar\delta_{\mathbf{k}\mathbf{k}'}\delta_{\lambda\lambda'}$. However, they are actually the in-phase and out-of-phase amplitudes of the electric field, which becomes apparent by re-writing equation 2.32 in terms of $\hat{X}_{\mathbf{k}\lambda}$ and $\hat{P}_{\mathbf{k}\lambda}$ such that

$$\hat{\mathbf{E}}(\mathbf{r},t) = \sum_{\mathbf{k},\lambda}\sqrt{\frac{\hbar\omega_k}{\epsilon_0 V}}\mathbf{e}_{\mathbf{k}\lambda}\left(\hat{X}_{\mathbf{k}\lambda}\cos\left[\omega_k t - \mathbf{k}\cdot\mathbf{r} - \frac{\pi}{2}\right] + \hat{P}_{\mathbf{k}\lambda}\sin\left[\omega_k t - \mathbf{k}\cdot\mathbf{r} - \frac{\pi}{2}\right]\right). \tag{2.35}$$

In chapter 3 it will be shown how balanced homodyne detection measures the dimensionless field quadratures of the electric field $\hat{X}$ and $\hat{P}$. Throughout this thesis the amplitude and phase of a *single* field mode will be manipulated and detected and therefore the mode labels are usually suppressed.

2.2.1 Quantum optical states

A variety of different quantum optical states exist, many of which can be generated in the laboratory. Some of the key states are introduced here, for a full account see e.g. reference [14].

Fock state

The Fock state was already introduced in section 2.2. The n-photon Fock state is obtained through repeated action of the creation operator on a state initially prepared in the vacuum $|0\rangle$ according to

$$|n\rangle = \frac{1}{\sqrt{n!}}(\hat{a}^{\dagger})^{n}|0\rangle. \tag{2.36}$$

Fock states are states of definite energy and therefore have a completely undefined phase. Furthermore, they are also eigenstates of the photon-number operator $\hat{n} = \hat{a}^{\dagger}\hat{a}$ such that

$$\hat{n}|n\rangle = n|n\rangle. \tag{2.37}$$

Various methods have been exploited to generate Fock states of light in the laboratory, a subject which is discussed in detail in chapter 4.

Coherent state

Coherent states – produced by ideal lasers, neglecting technical noise – are eigenstates of the annihilation operator such that

$$\hat{a}|\alpha\rangle = \alpha|\alpha\rangle, \tag{2.38}$$

where α is the complex amplitude of the coherent state. Coherent states are generated by acting on the vacuum state with the displacement operator

$$\hat{D}(\alpha)|\mathrm{vac}\rangle = \exp(\alpha\hat{a}^\dagger - \alpha^*\hat{a})|0\rangle. \tag{2.39}$$

The coherent state can be represented in the Fock basis such that

$$|\alpha\rangle = \exp(-|\alpha|^2/2)\sum_{n=0}^{\infty}\frac{\alpha^n}{\sqrt{n!}}|n\rangle. \tag{2.40}$$

Squeezed state

The single-mode squeezing operator is defined as

$$\hat{S}(\zeta) = \exp\left(\frac{\zeta}{2}\hat{a}^{\dagger 2} + \frac{\zeta^*}{2}\hat{a}^2\right), \tag{2.41}$$

where $\zeta = r\exp(i\phi)$ is the squeezing parameter which defines the amount and direction of squeezing in phase space. The single-mode squeezed vacuum state is given by

$$\begin{aligned} |\zeta\rangle &= \hat{S}(\zeta)|0\rangle, \\ &= \sqrt{\mathrm{sech}(r)}\sum_{n=0}^{\infty}\frac{\sqrt{[(2n)!]}}{n!}\left[-\frac{1}{2}\exp(i\phi)\tanh(r)\right]^n|2n\rangle. \end{aligned} \tag{2.42}$$

The two-mode squeezing operator for two modes A and B with annihilation operators $\hat{a}$ and $\hat{b}$ is given by

$$\hat{S}_{AB}(\zeta) = \exp\left(-\zeta \hat{a}^\dagger \hat{b}^\dagger + \zeta^* \hat{b}\hat{a}\right), \tag{2.43}$$

where the squeezing parameter ζ is defined as before. The action of $\hat{S}_{AB}$ on the two-mode vacuum state $|0_A; 0_B\rangle$ is to generate the two-mode squeezed vacuum (TMSV) state

$$\begin{aligned} |\zeta_{AB}\rangle &= \hat{S}_{AB}|0_A; 0_B\rangle \\ &= \operatorname{sech}(r) \sum_{n=0}^{\infty} [-\exp(i\phi)\tanh(r)]^n \, |n_A; n_B\rangle, \end{aligned} \tag{2.44}$$

where $|n_A; n_B\rangle$ is the state with n photons in mode A and mode B. The TMSV state exhibits photon number correlations between modes A and B. This property enables the TMSV state to be used in conjunction with photon-number resolving detection to prepare single-mode Fock states $|n\rangle$ of the electromagnetic field. This is the arrangement employed in this work to generate multi-photon Fock states, explored in chapter 4.

Quadrature state

Finally, quadrature states are eigenstates of the quadrature operator, defined in equations 2.33 and 2.34 such that

$$\hat{X}|X\rangle = X|X\rangle, \qquad \hat{P}|P\rangle = P|P\rangle. \tag{2.45}$$

The quadrature states are delta-orthogonal, i.e. $\langle X|X'\rangle = \delta(X - X')$ and $\langle P|P'\rangle = \delta(P - P')$ and form a complete basis such that

$$\int_{-\infty}^{\infty} dX|X\rangle\langle X| = \hat{I}, \quad \int_{-\infty}^{\infty} dP|P\rangle\langle P| = \hat{I}. \tag{2.46}$$

Although quadrature states are a useful tool for certain calculations, quadrature eigenstates cannot be prepared in the laboratory since they are effectively infinitely squeezed vacuum states.

2.3 Wigner function

The quadrature operators $\hat{X}$ and $\hat{P}$ defined in section 2.2 define a phase-space within which any single-mode quantum-optical state can be represented [54]. Thus one can imagine defining a phase-space probability distribution $W(X, P)$ which gives the probability to observe quadrature values X and P in their simultaneous measurement. For a classical harmonic oscillator such a proposition is sensible since one is not prohibited from measuring the position and momentum simultaneously and precisely. However, for quantum optical field modes, which behave like harmonic oscillators but with dimensionless quadrature operators in place of position and momentum, the Heisenberg uncertainty principle dictates that such a simultaneous measurement with arbitrary precision is not possible [42]. Therefore the distribution $W(X, P)$, known as the Wigner function, is referred to a quasi-probability distribution since it may assume negative values.

Continuing with the analogue of the joint phase-space probability distribution, even though the Wigner function cannot be interpreted as such, a valid postulate is that the marginal distributions of the Wigner function should be probability distributions of the phase-space coordinates X and P [63] such that

$$\Pr(X) = \int_{-\infty}^{\infty} W(X,P)dP, \qquad \Pr(P) = \int_{-\infty}^{\infty} W(X,P)dX. \tag{2.47}$$

Furthermore, for an optical field mode prepared in state $\hat{\rho}$, quadrature probability distributions are given by

$$\Pr(X) = \langle X|\hat{\rho}|X\rangle, \qquad \Pr(P) = \langle P|\hat{\rho}|P\rangle, \tag{2.48}$$

where $|X\rangle$ and $|P\rangle$ are the 'position' and 'momentum' quadrature eigenstates. The form of the Wigner function which satisfies the requirements of equations 2.47 and 2.48 is given by [64, 65]

$$W(X,P) = \frac{1}{2\pi}\int_{-\infty}^{\infty} \exp(iPY)\left\langle X - \frac{Y}{2}\middle|\hat{\rho}\middle|X + \frac{Y}{2}\right\rangle dY. \tag{2.49}$$

The Wigner function is a real-valued, normalized quasi-probability distribution such that

$$\int_{-\infty}^{\infty}\int_{-\infty}^{\infty} W(X,P)dXdP = 1. \tag{2.50}$$

Furthermore the trace-overlap between two quantum states can be expressed in terms of the Wigner functions of the states according to [54]

$$\mathrm{Tr}\left[\hat{\rho}_1\hat{\rho}_2\right] = 2\pi\int_{-\infty}^{\infty}\int_{-\infty}^{\infty} W_1(X,P)W_2(X,P)dXdP, \tag{2.51}$$

which is known simply as the overlap formula. This leads to a further constraint on the Wigner function, namely since the purity of a quantum state $\hat{\rho}$, given by $\mathrm{Tr}\left[\hat{\rho}^2\right]$, ranges between zero and one, the integral of the squared Wigner function must be less than or equal to $1/(2\pi)$. Finally, the values the Wigner function may take are bounded such that $|W(X, P)| \leq \frac{1}{\pi}$ [54].

2.4 Quantum tomography

The field of quantum tomography encompasses the experimental and theoretical methods to determine either the quantum state, process or measurements introduced in section 2.1. At least this is the field of quantum tomography as it stands today. Initially quantum tomography was synonymous with determination of the quantum state. Vogel and Riskin pointed out in 1989 [66] that a measurement scheme known as balanced homodyne detection – explored in detail in chapter 3 – could be used to experimentally determine the marginal distributions of the Wigner function defined in equation 2.47, from which the Wigner function could be reconstructed by applying an inversion formula known as the inverse Radon transform [67]. The term tomography is inspired by the fact that marginal distributions are integral projections of the Wigner function in a manner exactly paralleled by CT scans, where one measures the attenuation of X-rays penetrating human tissue at different angles and applies an inverse Radon transform to reconstruct the 2D density profile of the tissue [68].

The method of Vogel and Riskin [66] was demonstrated experimentally in 1993 by Smithey and co-workers [55] whereby the inverse Radom transform was applied to invert experimental marginal distributions of a vacuum state and squeezed vacuum state of light – thereby reconstructing the Wigner function and hence the density matrix of each state. Quantum tomography techniques were also employed to interrogate matter systems. Two notable early experiments were the reconstruction of the motional quantum state of a trapped atom [69] and the reconstruction of the quantum state of a molecular vibrational mode [70]. Since these pioneering works the field of quantum tomography has exploded,

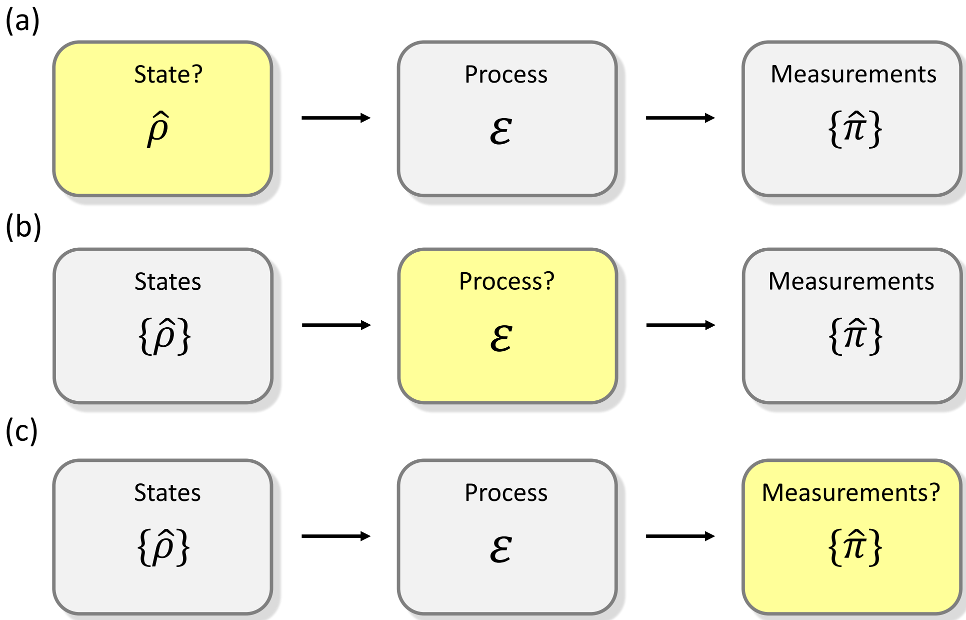

Figure 2.1: Schematic for performing tomography of one part of a quantum experiment. (a) quantum state tomography allows determination of an unknown state described by density matrix $\hat{\rho}$ provided the evolution of the state and measurements are known. (b) Quantum process tomography determines the quantum process $\mathcal{E}$ and requires a set of known input probe states $\{\hat{\rho}\}$ and known measurements. (c) Quantum detector tomography enables determination of the set of measurements described by POVM $\{\hat{\Pi}_i\}$ provided a set of known reference states is available $\{\hat{\rho}\}$ and their evolution prior to detection is known.

with the development of more sophisticated statistical inference techniques [49, 50]. Today the field is far abstracted from the original concept of Wigner function reconstruction from balanced homodyne measurements [66, 55, 54]. The concept of quantum state tomography (QST) was followed by quantum process tomography (QPT) [52] and most recently quantum detector tomography (QDT) [53].

Figure 2.1 outlines the underpinning concept for performing tomography on part of a quantum experiment. Determination of the quantum state $\hat{\rho}$ requires that the evolution of the state prior to measurement is known, figure 2.1(a). Similar arguments hold for performing tomography of the process $\mathcal{E}$ or measurements $\{\hat{\Pi}_i\}$, figure 2.1(b,c). Thus one must in general always have either prior knowledge or make assumptions about part of the experiment in order to determine an unknown element. More recently these previously rigid requirements have been blurred somewhat with the development of alternative tomography techniques which are able to address determination of two unknown elements out of the three [49, 71–73]. QST, QPT, and QDT are discussed in detail in the following chapters – where specifics of some of the numerical inversion techniques are explored.

3 Detection of Quantum Light

Almost every conceivable scenario in which light is generated, manipulated and transmitted to a final destination ultimately concludes with photo-detection. The nature of the photo-detection employed depends on how information is encoded in the light. Practically all detection schemes involve converting the light into an electrical signal of some description [21, 74]. Post-analysis of the electrical signal is then used to infer properties of the incident light, typically with the addition of knowledge about the photo-detector.

Detection of light constitutes detection of an electro-magnetic field, which has both an instantaneous amplitude and phase*. Depending on how information is encoded in the light, either field or intensity detection can be employed. Field detection at optical frequencies is challenging because photo-detectors are not fast enough to respond to the optical field oscillations† [21], and instead average over many cycles of the field. To this end, field detection at optical frequencies is performed indirectly by either heterodyne or homodyne detection – both of which employ intensity detection and an additional reference field to enable phase sensitivity. Thus at optical frequencies, all detection schemes rely first and foremost on registering the intensity of the incident light, and thus to understand

*Relative to some absolute reference or clock

†At radio frequencies field detection can be performed directly, a technique which is becoming increasingly common in mobile communications with the advent of software defined radio.

any such scheme it is first necessary to consider intensity detection on a fundamental level.

3.1 Intensity detection

Most modern photo-detectors rely on the photoelectric effect whereby an incident photon generates an electron-hole pair within the depletion region of a p-n junction, thus generating a photocurrent due to the built-in voltage across the junction [75, 21]. Such devices are commonly referred to as photodiodes, since the p-n junction is nothing but a semiconductor diode. The optical wavelengths which can be efficiently detected by such a photodiode depends on the band-gap of the semiconducting material, with silicon the most common material for visible light.

Photodiode performance is characterized by a number of parameters. The quantum efficiency relates the fraction of incident photons which generate an electon-hole pair and thus lead to a photo-detection event. The quantum efficiency can be improved by increasing the thickness of the semiconductor – thereby increasing the probability of absorption of a photon. However, this often comes at the expense of increasing the capacitance of the junction, which leads to a decrease in photodiode electronic bandwidth. Even when the photodiode is not illuminated it is possible for electron-hole pairs to be generated at random. These are indistinguishable from real photo-detection events and lead to a dark current, which ultimately limits the sensitivity of the photodiode. For this reason, conventional photodiodes cannot be used to directly detect single photons, since the current generated by a single photon is indistinguishable from the background dark current.

3.1.1 Avalanche photodiode

Avalanche photodiodes (APDs) [76] enable intensity detection with single-photon sensitivity through an internal amplification process. Avalanche multiplication occurs when the electron-hole pair initially generated by the photoelectric effect stimulates the generation of further pairs through impact ionization in a region of the semiconducting material where a large reverse bias voltage is applied. This leads to a substantial internal gain within the APD such that a single photon can generate a macroscopic current, significantly above the background dark noise. However, in order to achieve such a high gain the APD is typically biased above the breakdown voltage, a regime of operation known as the Geiger mode. This necessitates the use of a quenching circuit which rapidly removes the reverse bias as soon as an avalanche event starts, thus preventing damage to the junction [77].

APDs are commonly used in quantum optics settings since they enable intensity detection with single-photon sensitivity at room temperature [78]. Furthermore, APDs can exhibit quantum efficiencies in excess of 60% at visible wavelengths, operate with high-repetition ate sources and are available at relatively low cost. The primary limitation to photon-counting with APDs is the binary nature of the detector output – such that illumination with several photons produces an output voltage pulse which is effectively indistinguishable from that when illuminated with only a single photon. Thus the POVM set describing an APD has only two elements, *viz.* the 'click' event and the 'no click' event. Ignoring dark counts and after-pulsing these are given by [75]

$$\hat{\Pi}_{\text{no click}} = \sum_{n=0}^{\infty}(1-\eta)^n|n\rangle\langle n|, \tag{3.1}$$

$$\hat{\Pi}_{\text{click}} = \hat{I} - \sum_{n=0}^{\infty}(1-\eta)^n|n\rangle\langle n|, \tag{3.2}$$

where η is the quantum efficiency of the APD. The factor $(1-\eta)^n$ is the probability that n incident photons will be lost, i.e. not detected. If only one out of n photons survive this will still produce a 'click' – hence the relatively simple form of the POVM.

3.1.2 Superconducting detectors

There are two main classes of superconducting detectors: transition edge sensors (TESs) and superconducting nanowire single-photon detectors (SNSPDs) [79]. TESs rely on the absorption of an incident photon causing a small rise in temperature of a superconducting material held at the transition temperature. Thus a macroscopic change in the material electrical resistance is observed when a photon is absorbed. TESs are intrinsically photon-number resolving since the amount of heating is proportional to the number of incident photons. TESs can exhibit quantum efficiencies in excess of 95% [79]. However, they must be operated at cryogenic temperatures (100 mK) and exhibit a relatively large dead time (of the order 1 μs) and timing jitter (100 ns), owing to the thermal nature of the detection process. Thus TESs are far less-easily accessible in the laboratory compared with APDs. SNSPDs on the other hand are not intrinsically photon-number resolving. However, they exhibit better performance both in terms of dead time and timing jitter and can be operated at higher temperatures than TESs (10 K) [79].

3.1.3 Multiplexed detection

Multiplexed detectors were developed out of the need to gain some degree of photon-number resolution with conventional APDs. The idea is relatively simple: an incoming wave-packet is split into several modes, each of which is detected by an APD [75]. The modes can either be distinct spatial modes – in which case the number of APDs required is equal to the number of modes – or temporal modes, whereby a single APD can be used. In practice both spatial and temporal multiplexing are typically combined [80–82] to maximize both the available resources and photon-number resolution.

Multiplexed direct intensity detection can be used to infer non-classicality of the detected light through reconstruction of the photon-number statistics, which may be sub-

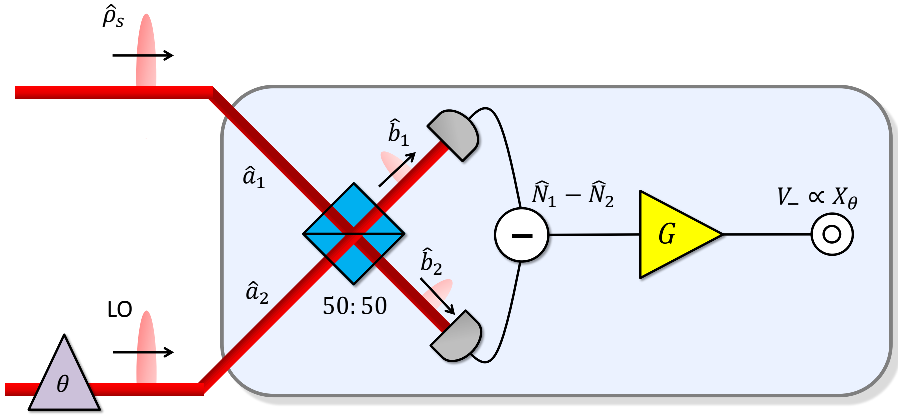

Figure 3.1: Simplified schematic of balanced homodyne detection. Signal field mode $\hat{a}_1$ prepared in state $\hat{\rho}_s$ interferes with the local oscillator mode $\hat{a}_2$, prepared in a bright coherent state, at a 50:50 beam splitter. Output modes $\hat{b}_{1,2}$ are detected with square-law detectors. The difference photon number $\hat{N}_- = \hat{N}_1 - \hat{N}_2$ is obtained through photocurrent subtraction and integration by a charge-sensitive amplifier, gain G. The detector output voltage is proportional to samples of the signal field quadrature $V_- \propto X_\theta$.

Poissonian [83]. However, this information alone is not sufficient to reconstruct the complete quantum state or Wigner function of the detected mode.

3.2 Balanced homodyne detection

In the optical regime, field detection can be performed by combining the interference of the optical mode to be detected with a reference mode and conventional intensity detection using photodiodes [21]. One such scheme, known as balanced homodyne detection [84, 54, 21], is fundamental to many quantum and classical optics applications where complete or partial information about the amplitude and phase of a single optical field mode is required. Such applications include, but are not limited to, quantum state discrimination [85, 86], quantum key distribution [87–89], quantum state and process tomography [55, 50, 56, 90], quantum-enhanced reading of a classical memory [91], ultra-sensitive linear sampling of fiber optical systems [92] and gravitational wave detection [28]. Alternative phase-sensitive detection techniques have recently been developed by combining multiplexed detectors with a weak reference mode [93, 94], enabling point-by-point sampling of the Wigner function [95].

Despite the key role played by balanced homodyne detection across such a diverse range of applications, there exists no off-the-shelf, commercial, 'plug and play' balanced homodyne detector (BHD).* Therefore a prerequisite to realizing an optical system where balanced homodyne measurements are required is to first design, construct and fully characterize the necessary custom electronics and optical setup to perform balanced homodyne detection, tailored to the particular scenario within which it is to be employed.† Within the quantum optics community, significant effort over the past decade has focused on increasing the bandwidth, efficiency and signal-to-noise characteristics of BHDs to enable coherent detection of pulsed optical field modes at the shot-noise limit [55, 96–103]. Increased electronic bandwidth enables experiments to be performed with at a high repetition rate, which enables exploration of low-probability, non-deterministic events. An often overlooked parameter in addition to those mentioned is the long-term stability of the BHD [97, 100, 102], which governs the frequency with which the BHD must be calibrated against a known reference state. In the remainder of this chapter the theoretical and practical aspects of balanced homodyne detection are discussed. A detailed description of the development of a pulsed BHD is described in section 3.4.

3.2.1 Simplified treatment of balanced homodyne detection

In balanced homodyne detection a signal field mode represented by annihilation operator $\hat{a}_1$, which is prepared in some unknown quantum state $\hat{\rho}_s$ to be characterized, is interfered with a reference mode $\hat{a}_2$ known as the local oscillator (LO) on a 50:50 beam splitter (BS) [54, 50], as shown in figure 3.1. The BS transforms the input fields $\hat{a}_{1(2)}$ into output fields

*To the best of the author's knowledge.

†i.e. wavelength, pulse duration, repetition rate.

$\hat{b}_{1(2)}$ according to

$$\hat{b}_1 = \frac{1}{\sqrt{2}} \left(\hat{a}_1 + \hat{a}_2 \right), \tag{3.3}$$

$$\hat{b}_2 = \frac{1}{\sqrt{2}} \left(\hat{a}_1 - \hat{a}_2 \right). \tag{3.4}$$

The output field modes $\hat{b}_{1(2)}$ are detected with square-law intensity detectors. The intensity detected, which is proportional to the number of photons in mode 1 (2) is given by $\hat{N}_{1(2)} = \hat{b}^\dagger_{1(2)}\hat{b}_{1(2)}$ [14]. The two photocurrents are subtracted to yield a quantity proportional to the difference photon number* $\hat{N}_-$ given by

$$\hat{N}_- = \hat{N}_1 - \hat{N}_2 = \hat{b}^\dagger_1\hat{b}_1 - \hat{b}^\dagger_2\hat{b}_2. \tag{3.5}$$

Using the beam splitter transformations of the field operators, equations 3.3 and 3.4, to express equation 3.5 in terms of the input field operators $\hat{a}_1$ and $\hat{a}_2$ gives

$$\begin{aligned}\hat{N}_- &= \frac{1}{2}\left[(\hat{a}^\dagger_1 + \hat{a}^\dagger_2)(\hat{a}_1 + \hat{a}_2) - (\hat{a}^\dagger_1 - \hat{a}^\dagger_2)(\hat{a}_1 - \hat{a}_2)\right], \\ &= \hat{a}^\dagger_2\hat{a}_1 + \hat{a}_2\hat{a}^\dagger_1. \end{aligned} \tag{3.6}$$

The LO mode $\hat{a}_2$ is usually prepared in a strong coherent state $|\alpha_{\mathrm{LO}}\rangle$ [54]. This allows the field operator $\hat{a}_2$ to be replaced by the classical amplitude of the LO coherent state

*The difference number $\hat{N}_-$ is in fact obtained by integration of the difference photocurrent, which is subsequently amplified by a transimpedance amplifier of gain G, figure 3.1. This yields a macroscopic voltage at the output of the BHD which is proportional to samples of the quadrature operator, such that $V_- \propto \sqrt{2}|\alpha_{\mathrm{LO}}|X_\theta$. The subtleties related to the photocurrent integration and amplification are discussed in detail in section 3.4.

$\alpha_{\mathrm{LO}} = |\alpha_{\mathrm{LO}}| \exp(i\theta)$, since $\hat{a}_2|\alpha_{\mathrm{LO}}\rangle_2 = \alpha_{\mathrm{LO}}|\alpha_{\mathrm{LO}}\rangle_2$. Thus equation 3.6 becomes

$$\begin{aligned} \hat{N}_- &= \alpha_{\mathrm{LO}}^* \hat{a}_1 + \alpha_{\mathrm{LO}} \hat{a}_1^\dagger, \\ &= |\alpha_{\mathrm{LO}}| \left(\hat{a}_1 \exp(-i\theta) + \hat{a}_1^\dagger \exp(i\theta) \right), \\ &= \sqrt{2} |\alpha_{\mathrm{LO}}| \hat{X}_\theta, \end{aligned} \tag{3.7}$$

where the generalized quadrature operator $\hat{X}_\theta$ is defined as [54]

$$\hat{X}_\theta = \frac{1}{\sqrt{2}} \left(\hat{a}_1 \exp(-i\theta) + \hat{a}_1^\dagger \exp(i\theta) \right). \tag{3.8}$$

For $\theta = 0$ the BHD measures the real quadrature $\hat{X} = (1/\sqrt{2})(\hat{a}_1 + \hat{a}_1^\dagger)$ whereas for $\theta = \pi/2$ the BHD measures the imaginary quadrature $\hat{P} = (1/i\sqrt{2})(\hat{a}_1 - \hat{a}_1^\dagger)$ [14]. From equation 3.7 it is clear that the role of the LO is to effectively amplify the quadrature fluctuations of the signal and provide a phase ference θ between different Fock layers [54]. The LO shot-noise itself is suppressed in the balanced detection scheme [84, 104, 55].*

3.2.2 Spatial-temporal modes

The treatment of balanced homodyne detection presented above is rather simplistic in that the signal mode is assumed to be perfectly matched to that of the local oscillator. To make a more general treatment of balanced homodyne detection and gain insight into the mode-selective properties it is necessary to introduce the concept of non-monochromatic wave-packet modes [106, 49, 107]. In general the positive-frequency electric field operator

*This is often a misudnerstood concept about balanced homodyne detection. The correct interrpetation for the noise measured in the absence of an input signal is that the BHD measures the vacuum state entering the 'un-excited' input port of the 50:50 beam splitter [84, 104]. If the LO shot-noise were not suppressed it would not be possible to observe quadrature squeezing, e.g. [55, 105].

can be expanded in the set of monochromatic plane-wave modes as follows [14, 107]

$$\hat{\mathbf{E}}^{(+)}(\mathbf{r},t) = i\sum_{\lambda}\int \frac{d^3k}{(2\pi)^3}\sqrt{\frac{\hbar\omega_k}{2\epsilon_0 V}}\hat{a}_{\mathbf{k},\lambda}\mathbf{e}_{\mathbf{k},\lambda}\exp(i\mathbf{k}\cdot\mathbf{r})\exp(-i\omega_k t), \tag{3.9}$$

where the plane-wave modes are normalized in some volume V, $\mathbf{e}_{\mathbf{k},\lambda}$ is the unit polarization vector and the annihilation operators obey the commutation relation $[\hat{a}_{\mathbf{k},\lambda}, \hat{a}^{\dagger}_{\mathbf{k}',\lambda'}] = (2\pi)^3\delta^{(3)}(\mathbf{k}-\mathbf{k}')\delta_{\lambda,\lambda'}$ [107]. Photon-flux amplitude operators $\hat{\mathbf{\Phi}}^{(+)}(\mathbf{r},t)$ may be defined [108, 54, 49] as

$$\hat{\mathbf{\Phi}}^{(+)}(\mathbf{r},t) = i\sqrt{c}\sum_{\lambda}\int \frac{d^3k}{(2\pi)^3}\frac{1}{\sqrt{V}}\hat{a}_{\mathbf{k},\lambda}\mathbf{e}_{\mathbf{k},\lambda}\exp(i\mathbf{k}\cdot\mathbf{r})\exp(-i\omega_k t). \tag{3.10}$$

Here the wave-packet approach is applied not to the electric and magnetic field operators but rather to the photon-flux amplitude operators [109, 49]. There is a subtle distinction when defining wave-packet modes for the photon-flux amplitude which means the modes naturally form an orthonormal set over volume V.* The photon-flux amplitude operator can be expressed in terms of wave packets modes $\mathbf{v}_{j,\lambda}(\mathbf{x},t)$ as [49]

$$\hat{\mathbf{\Phi}}^{(+)}(\mathbf{r},t) = i\sqrt{c}\sum_{j}\sum_{\lambda}\mathbf{v}_{j,\lambda}(\mathbf{r},t)\hat{b}_{j,\lambda}, \tag{3.11}$$

where the wave packet modes $\mathbf{v}_{j,\lambda}(\mathbf{r},t)$ are related to the plane-wave modes as [107]

$$\mathbf{v}_{j,\lambda}(\mathbf{r},t) = \int \frac{d^3k}{(2\pi)^3}\frac{1}{\sqrt{V}}U_j^{\lambda}(\mathbf{k})\mathbf{e}_{\mathbf{k},\lambda}\exp(i\mathbf{k}\cdot\mathbf{r})\exp(-i\omega_k t), \tag{3.12}$$

where $U_j^{\lambda}(\mathbf{k})$ is a unitary transformation 'matrix' of coefficients which dictates the contribution of each plane-wave mode to wave-packet mode $\mathbf{v}_{j,\lambda}(\mathbf{r},t)$ [107]. Similarly, wave-packet annihilation operators $\hat{b}_{j,\lambda}$ are related to the plane-wave annihilation operators

*Note, this is not true of wave-packet modes of the electric and magnetic fields [107].

according to $\hat{b}_{j,\lambda} = \int \frac{d^3k}{(2\pi)^3} U_j^\lambda(\mathbf{k}) \hat{a}_{j,\lambda}$, and obey the commutation relation $[\hat{b}_{j,\lambda}, \hat{b}^\dagger_{j',\lambda'}] = \delta jj' \delta_{\lambda\lambda'}$. The n-photon wave-packet state is created through application of the wave-packet creation operator on the vacuum state, $|n\rangle_{j,\lambda} = (1/\sqrt{n!})(\hat{b}^\dagger_{j,\lambda})^n |\mathrm{vac}\rangle$ [107]. An important property of the wave-packet modes introduced above is that they are orthonormal in the same large volume V as the plane-wave modes [49], such that

$$\int_V d^3r \mathbf{v}^*_{j,\lambda}(\mathbf{r},t) \cdot \mathbf{v}_{m,\lambda'}(\mathbf{r},t) = \delta_{jm}\delta_{\lambda\lambda'}. \tag{3.13}$$

In balanced homodyne detection a signal electric field $\hat{\mathbf{E}}_{\mathrm{S}}^{(+)}$ is combined with the LO electric field $\hat{\mathbf{E}}_{\mathrm{LO}}^{(+)}$ at a 50:50 beam splitter, as depicted in figure 3.1. The output electric fields may be expressed in terms of the input electric fields as [54, 49]

$$\hat{\mathbf{E}}_1^{(+)} = \frac{1}{\sqrt{2}}\left(\hat{\mathbf{E}}_{\mathrm{S}}^{(+)} + \hat{\mathbf{E}}_{\mathrm{LO}}^{(+)}\right), \tag{3.14}$$

$$\hat{\mathbf{E}}_2^{(+)} = \frac{1}{\sqrt{2}}\left(\hat{\mathbf{E}}_{\mathrm{S}}^{(+)} - \hat{\mathbf{E}}_{\mathrm{LO}}^{(+)}\right). \tag{3.15}$$

Assuming the beam splitter reflectivity and transmittance are wavelength independent, the transformation of the signal and LO modes (equations 3.14 and 3.15) can be written in terms of the photon-flux amplitudes [54, 49] (equation 3.10) such that

$$\hat{\mathbf{\Phi}}_1^{(+)} = \frac{1}{\sqrt{2}}\left(\hat{\mathbf{\Phi}}_{\mathrm{S}}^{(+)} + \hat{\mathbf{\Phi}}_{\mathrm{LO}}^{(+)}\right), \tag{3.16}$$

$$\hat{\mathbf{\Phi}}_2^{(+)} = \frac{1}{\sqrt{2}}\left(\hat{\mathbf{\Phi}}_{\mathrm{S}}^{(+)} - \hat{\mathbf{\Phi}}_{\mathrm{LO}}^{(+)}\right). \tag{3.17}$$

The number of photons per second $\hat{i}_j(t)$ incident on detector D_j $(j = 1, 2)$ is given by

$$\hat{i}_j(t) = \int_S d^2x \hat{\mathbf{\Phi}}_j^{(-)}(\mathbf{x}, z=0, t) \cdot \hat{\mathbf{\Phi}}_j^{(+)}(\mathbf{x}, z=0, t), \tag{3.18}$$

where the integration is carried out over the surface of the detector S, which is defined to lie in the $z = 0$ plane, $\mathbf{x}$ denotes only the transverse spatial co-orinates (x, y) and $\hat{\mathbf{\Phi}}_j^{(-)}$ is the Hermitian conjugate of $\hat{\mathbf{\Phi}}_j^{(+)}$ [108, 54]. The number of photons registered by the detector in the time interval $(t, t+\tau)$ is obtained by integration of $\hat{i}_j(t)$ such that

$$\hat{N}_j = \int_t^{t+\tau} dt' \hat{i}_j(t') = \int_t^{t+\tau} dt' \int_S d^2x \hat{\mathbf{\Phi}}_j^{(-)}(\mathbf{x}, 0, t') \cdot \hat{\mathbf{\Phi}}_j^{(+)}(\mathbf{x}, 0, t') \tag{3.19}$$

The photon number difference $\hat{N}_-$, obtained by subtraction of the integrated photon flux from the two BHD photodiodes D_1 and D_2 (assuming identical detector responses), is given by

$$\hat{N}_- = \hat{N}_1 - \hat{N}_2 = \int_t^{t+\tau} dt'(\hat{i}_1(t') - \hat{i}_2(t')). \tag{3.20}$$

Using the transformations defined in equations 3.16 and 3.17 to express $\hat{N}_-$ in terms of the signal and LO photon-flux amplitudes gives

$$\hat{N}_- = \int_t^{t+\tau} dt' \int_S d^2x \left(\hat{\mathbf{\Phi}}_{\mathrm{LO}}^{(-)}(\mathbf{x}, 0, t') \cdot \hat{\mathbf{\Phi}}_{\mathrm{S}}^{(+)}(\mathbf{x}, 0, t') + \hat{\mathbf{\Phi}}_{\mathrm{LO}}^{(+)}(\mathbf{x}, 0, t') \cdot \hat{\mathbf{\Phi}}_{\mathrm{S}}^{(-)}(\mathbf{x}, 0, t') \right). \tag{3.21}$$

Again, the LO typically consists of a strong coherent state of a particular temporal-spatial wave-packet mode.* Therefore the LO photon-flux amplitude operator is expressed in terms of the particular wave-packet mode excited in the strong coherent state, $\mathbf{v}_{L,\lambda}(\mathbf{r}, t)$, and all other wave-packet modes which are in the vacuum state [108, 54] (not excited)

*e.g. a train of optical pulses propagating in a TEM_{00} spatial mode such that

$$\hat{\mathbf{\Phi}}_{\mathrm{LO}}^{(+)}(\mathbf{r},t) = i\sqrt{c}\mathbf{v}_{L,\lambda}(\mathbf{r},t)\hat{b}_{L,\lambda} + \text{vacuum terms}. \tag{3.22}$$

The photon number difference operator now takes the form

$$\begin{aligned}\hat{N}_{-} \approxeq & -i\sqrt{c}\hat{b}^{\dagger}_{L,\lambda}\int_{t}^{t+\tau} dt' \int_{S} d^2x \mathbf{v}^{*}_{L,\lambda}(\mathbf{x},0,t')\cdot\hat{\mathbf{\Phi}}_{\mathrm{S}}^{(+)}(\mathbf{x},0,t') \\ & +i\sqrt{c}\hat{b}_{L,\lambda}\int_{t}^{t+\tau} dt' \int_{S} d^2x \mathbf{v}_{L,\lambda}(\mathbf{x},0,t')\cdot\hat{\mathbf{\Phi}}_{\mathrm{S}}^{(-)}(\mathbf{x},0,t'),\end{aligned} \tag{3.23}$$

where $\approxeq$ indicates that the contribution to the difference photon number of the other vacuum terms has been neglected. Under normal operating conditions the LO mode typically contains $\mathcal{O}(10^9)$ photons whereas the signal is typically at the few-photon intensity level. Thus the LO amplitude excited in mode $\mathbf{v}_{L,\lambda}(\mathbf{r},t)$ dominates $\hat{N}_{-}$ and therefore the approximation made above is so accurate that henceforth it is expressed as an equality *.

In general the signal photon-flux amplitude is distributed across a superposition of wave-packet modes as in equation 3.11 such that

$$\hat{\mathbf{\Phi}}_{\mathrm{S}}^{(+)}(\mathbf{r},t) = i\sqrt{c}\sum_{k}\sum_{\lambda'}\mathbf{v}_{k,\lambda'}(\mathbf{r},t)\hat{c}_{k,\lambda'}, \tag{3.24}$$

where $\hat{c}_{k,\lambda}$ is the annihilation operator for the signal wave-packet mode $\mathbf{v}_{k,\lambda}(\mathbf{r},t)$. Substi-

*This is the so-called strong LO approximation tuting equation 3.24 into equation 3.23 gives

$$
\begin{aligned}
\hat{N}_- = &\sum_k \sum_{\lambda'} \Bigg(\hat{b}^\dagger_{L,\lambda} \hat{c}_{k,\lambda'} \int_t^{t+\tau} cdt' \int_S d^2x \mathbf{v}^*_{L,\lambda}(\mathbf{x},0,t') \cdot \mathbf{v}_{k,\lambda'}(\mathbf{x},0,t') \\
&\qquad + \hat{b}_{L,\lambda} \hat{c}^\dagger_{k,\lambda'} \int_t^{t+\tau} cdt' \int_S d^2x \mathbf{v}_{L,\lambda}(\mathbf{x},0,t') \cdot \mathbf{v}^*_{k,\lambda'}(\mathbf{x},0,t') \Bigg), \\
= &\, \hat{b}^\dagger_{L,\lambda} \hat{c} + \hat{b}_{L,\lambda} \hat{c}^\dagger, \qquad (3.25)
\end{aligned}
$$

where a new annihilation operator for the signal mode $\hat{c}$ is defined as

$$
\hat{c} = \sum_k \sum_{\lambda'} \hat{c}_{k,\lambda'} \int_t^{t+\tau} cdt' \int_S d^2x \mathbf{v}^*_{L,\lambda}(\mathbf{x},0,t') \cdot \mathbf{v}_{k,\lambda'}(\mathbf{x},0,t'). \qquad (3.26)
$$

At this point the resemblance between equations 3.25 and 3.6 is clear. The new expression for the photon number difference operator $\hat{N}_-$ derived using wave-packet modes exactly matches the form derived according to the simplistic treatment in section 3.2, where an effective annihilation operator for the signal mode is introduced, equation 3.26. Provided the photodetector surface S captures the whole transverse profile for the modes of interest and the integration time τ is much larger than the duration of the pulse, the integrals in equation 3.26 act like an integral over the three spatial coordinates [108, 49] *. Thus the orthonormality relation of equation 3.13 can be applied directly† to equation 3.26. Hence $\hat{c} = \hat{c}_{L,\lambda}$, i.e. the detected signal mode has the same spatial-temporal profile and polarization as the LO. Put another way, if the signal is excited in a superposition of wave-packet modes and polarization states, only part of the signal will contribute to the homodyne difference signal $\hat{N}_-$. Thus one often speaks of mode-matching the signal to the LO or vice versa, since it is often desired to detect the signal in its entirety. Should the

* $\int_0^\tau cdt \int_S d^2x$ acts similarly to $\int_0^{c\tau} dz \int_S d^2x$

† Provided the wave packet modes are much shorter in temporal extent than the integration time τ and the spatial modes have small divergence

signal be excited in a statistical mixture of different modes it is impossible to mode-match the single-mode LO perfectly with the signal [110, 111]. This is disucssed in detail in chapter 4.

The degree of mode-matching between signal and LO can be quantified by an effective efficiency parameter $\eta_{\rm mm}$ [108, 54, 49]. Suppose the signal is excited in spatial-temporal mode $\mathbf{w}_{S,\lambda'}(\mathbf{r}, t)$, then the overlap with the LO mode $\mathbf{v}_{L,\lambda}(\mathbf{r}, t)$ results in an effective mode-matching efficiency*

$$\boxed{\sqrt{\eta_{\rm mm}} = \left| \int_t^{t+\tau} cdt' \int_S d^2x \mathbf{v}^*_{L,\lambda}(\mathbf{x}, 0, t') \cdot \mathbf{w}_{S,\lambda'}(\mathbf{x}, 0, t') \right| = \mathcal{V},} \tag{3.27}$$

where $\mathcal{V}$ is equal to the interference visibility between signal and LO assuming equal intensities, observed at one output port of the 50:50 beam splitter defined in the usual manner [112, 21] as

$$\mathcal{V} = \frac{\langle I \rangle_{\rm max} - \langle I \rangle_{\rm min}}{\langle I \rangle_{\rm max} + \langle I \rangle_{\rm min}}, \tag{3.28}$$

where $\langle I \rangle_{\rm max}$ and $\langle I \rangle_{\rm min}$ are the maximum and minimum intensities recorded by a photodetector monitoring one output port of the 50:50 beam splitter as the phase of the LO is varied through at least 2π, and $\langle ... \rangle$ denotes ensemble-averaging due to the limited detector response time.

Equation 3.27 gives the overlap of the signal and LO field modes. The effective mode-matching efficiency $\eta_{\rm mm}$ is thus equal to the square of the field overlap.† A simple beam splitter model for optical loss with transmittance $|t|^2 = \eta_{\rm mm}$ in the signal mode can be used to model the effect of mode-mismatch on the inferred quadrature statistics of the

*Note, the phase of one of the fields can always be chosen such that the overlap is a real, non-negative number [54].

†This is the convention used throughout this thesis.

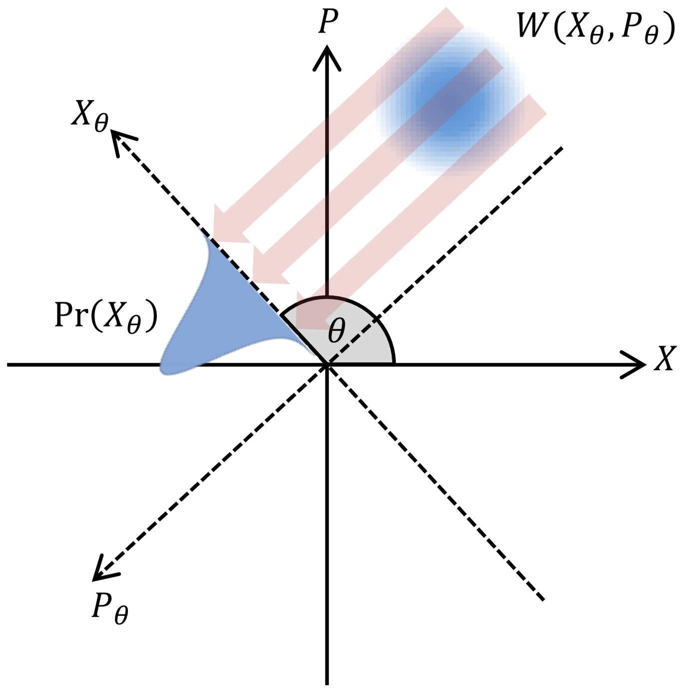

Figure 3.2: In optical homodyne tomography, quadrature probability distributions $\Pr(X_\theta)$ – estimated from repeated measurements of $\hat{X}_\theta$ – are given by the integral projection of the Wigner function $W(X_\theta, P_\theta)$ of the measured state $\hat{\rho}_s$.

signal field mode [54].*

3.3 Optical homodyne tomography

A single measurement outcome of the BHD with unit efficiency yields one value of the quadrature $\hat{X}_\theta$. By making repeated measurements of $\hat{X}_\theta$ on an ensemble of identically prepared quantum states $\hat{\rho}_s$, one can estimate the quadrature probability distribution

$$\Pr(X_\theta) = \langle X_\theta|\hat{\rho}_s|X_\theta\rangle = \int_{-\infty}^{\infty} dP_\theta W(X_\theta, P_\theta), \tag{3.29}$$

*In principle, provided the signal is in a *coherent* superposition of wave-packet modes it can always be perfectly matched with the coherent LO (spatial-temporal shaping of the LO mode and appropriate polarization rotations). Thus any mismatch is either due to mixedness of the signal state or laziness of the experimentalist.

by constructing a histogram of the obtained quadrature values. Here $|X_\theta\rangle$ is the quadrature eigenstate with eigenvalue X_θ, and $W(X_\theta, P_\theta)$ is the Wigner function of state $\hat{\rho}_s$. Estimation of $\Pr(X_\theta)$ for a range of LO phases enables reconstruction of the Wigner function by applying an inverse Radon transform [66, 54] – a procedure known as optical homodyne tomography (OHT). Alternatively if the LO is phase-averaged the photon-number statistics $P(n) = \mathrm{Tr}(\hat{\rho}_s \hat{n})$ may be extracted using pattern functions [113, 114]. For non-unit BHD efficiency the underlying probability distribution is smoothed [49]. The true Wigner function of the signal mode can be obtained through a deconvolution procedure, although this is highly sensitive to statistical noise [49].

The inverse Radon transform enables reconstruction of the Wigner function, which necessarily means that the complete density matrix of the state may also be obtained by integration of the Wigner function weighted with known projection operators [54]. Although the inverse Radon transform has been applied successfully for performing OHT [55] it suffers from a number of drawbacks. The method is highly sensitive to the filtering and phase-space cut-off employed during the inversion and the reconstructed Wigner function need not necessarily correspond to a physical quantum state [54], i.e. the reconstructed density matrix may have negative eigenvalues. One method for dealing with negative eigenvalues is to demonstrate that they arise primarily due to the finite number of quadrature samples obtained and are thus statistically insignificant. Alternatively, an *ad hoc* regularization of the reconstructed density matrix could be performed to artificially remove negative eigenvalues from the density matrix – thus rendering it a physical state. Quantum state sampling using pattern functions to obtain the photon-number statistics suffers also suffers from negative eigenvalues [49, 113, 114] and thus does not directly provide a solution to this problem.

3.3.1 Maximum-likelihood estimation

As a means of overcoming the above-mentioned difficulties, maximum-likelihood estimation (MLE) of the density matrix was proposed [115] and investigated for performing OHT [116–118]. MLE seeks to find the ensemble $\hat{\rho}$ which is most likely to give the observed set of data [115, 118], e.g. the observed quadrature-phase pairs $\{X_i, \theta_i\}$. Broadly speaking, one defines a likelihood functional $\mathcal{L}(\hat{\rho})$ such that

$$\mathcal{L}(\hat{\rho}) = \prod_{i=1}^{N} \mathrm{Tr}(\hat{\rho}\hat{\Pi}_i), \tag{3.30}$$

where N is the total number of measurements* (i.e. the size of the dataset) and $\hat{\Pi}_i$ is the POVM element† corresponding to measurement outcome labelled by i, which for an ideal BHD is given by

$$\hat{\Pi}_i = |X_{\theta,i}\rangle\langle X_{\theta,i}|, \tag{3.31}$$

where $|X_{\theta,i}\rangle$ is the quadrature eigenstate corresponding to the data pair (X_i, θ_i). The goal is maximize equation 3.30 over the set of density matrices $\hat{\rho}$, which can be performed by direct convex optimization [115, 118] or using an iterative algorithm [119, 90]. Besides the obvious advantage that MLE directly obtains a physical estimate for the unknown state $\hat{\rho}_s$, it also enables imperfections such as finite detector efficiency to be incorporated into the reconstruction procedure [90], thus relinquishing the need to perform further post-processing on the reconstructed state.

*Note that the index i runs over each measured data point (X_i, θ_i) in the set $\{X_i, \theta_i\}$. Sometimes the likelihood functional is defined in terms of discrete measurement outcomes (bins). In this case the functional is of the form $\mathcal{L}(\hat{\rho}) = \prod_j \left(\mathrm{Tr}(\hat{\rho}\hat{\Pi}_j)\right)^{f_j}$, where j indexes the discrete bins and f_j is the frequency with which each measurement outcome is observed.

†Assumed to be well-known, i.e. the measurement apparatus is well-calibrated.

Iterative procedure

The likelihood functional of equation 3.30 can be maximised according to an iterative procedure [90]. One starts with an unbiased initial estimate of the density matrix such as the identity matrix such that $\hat{\rho}^{(0)} = \mathcal{N}[\hat{I}]$. The iterative procedure is given as

$$\hat{\rho}^{(k+1)} = \mathcal{N}\left[\hat{R}(\hat{\rho}^{(k)})\hat{\rho}^{(k)}\hat{R}(\hat{\rho}^{(k)})\right], \tag{3.32}$$

where the operator $\hat{R}$ is given by

$$\hat{R}(\hat{\rho}) = \sum_i \frac{f_i}{\mathrm{Tr}(\hat{\rho}\hat{\Pi}_i)}\hat{\Pi}_i, \tag{3.33}$$

and f_i is the observed frequency of outcome i in the recorded dataset. Since $\hat{R}$ is a Hermitian operator the estimated density matrix is guaranteed to be Hermitian [90]. Furthermore, non-unit efficiency of the BHD can be accounted for directly in the iterative procedure through modification of the POVM elements $\hat{\Pi}_i$. The ideal quadrature eigenstate projectors of equation 3.31 are replaced by operators of the form [90]

$$\hat{\Pi}_i(\eta) = \sum_{m,n,k} B_{m+k,m}(\eta)B_{n+k,n}(\eta)\langle n|X_{\theta,i}\rangle\langle X_{\theta,i}|m\rangle|n+k\rangle\langle m+k|, \tag{3.34}$$

where $B_{n+k,n}(\eta) = \sqrt{\binom{n+k}{n}\eta^n(1-\eta)^k}$, and η is the efficiency of the BHD [90]. The iterative maximum-likelihood algorithm for performing optical homodyne tomography thus described is employed in chapter 4 to reconstruct the density matrices of multi-photon Fock states from balanced homodyne measurements.

3.4 Development of a pulsed balanced homodyne detector

In what follows the design, testing and operation of a pulsed BHD is described. Key performance parameters characterizing the detector operation in the pulsed domain are introduced and experimentally measured. Many of the details presented in this section have been published, see [120, 121].

At the outset a key design requirement was that the BHD should be capable of shot-to-shot measurements with an 80 MHz pulsed LO train, to enable conditionally-prepared quantum states and non-deterministic quantum processes to be characterized. This necessitates an electronic bandwidth on the order of the pulse repetition rate. Achieving the required 80 MHz bandwidth and sufficient electronic gain whilst ensuring the detector electronic noise and efficiency are not impacted presents certain design challenges [74, 122, 123]. Excess noise and non-unit efficiency lead to effective smoothing of the measured quadrature probability distributions [54, 49, 124]. In addition, the often overlooked parameter of long-term detector stability is investigated [97, 100]. Detector stability influences the frequency with which the detector must be calibrated and hence impacts the usable data acquisition rate.

3.4.1 Electro-optical setup

An optical schematic of the BHD experimental arrangement is shown in figure 3.3 along with an electronic schematic of the BHD circuit, figure 3.4(a). The LO is derived from a Ti:Sapphire oscillator (80 MHz repetition rate, $\approx$ 100 fs pulse duration at 830 nm) which is spatially filtered with a 15 cm long polarization-maintaining single-mode fiber (PM-SMF) and spectrally filtered with an interference filter (IF) to define the LO spatial-temporal mode. The length of the fiber is kept as short as practicable to minimize both the spectral chirp introduced to the LO pulse and the effect of guided acoustic-wave Brillouin scattering

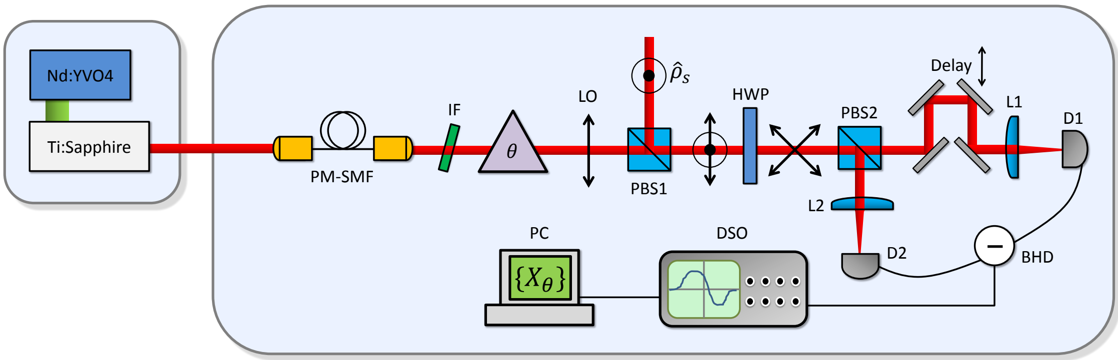

Figure 3.3: Optical schematic of BHD. The output of a Ti:Sapphire oscillator is spatially and spectrally filtered to define the LO spatial-temporal mode. LO is combined with signal in state $\hat{\rho}_s$ on a PBS. A HWP/PBS combination forms an effective 50:50 beam splitter, the output modes of which are focussed by two identical lenses (L1,L2) onto the two p-i-n photodiodes of the BHD (D1,D2). A delay stage enables adjustment of the relative time of arrival of the two optical modes and aids in photocurrent subtraction.

(a) (b)

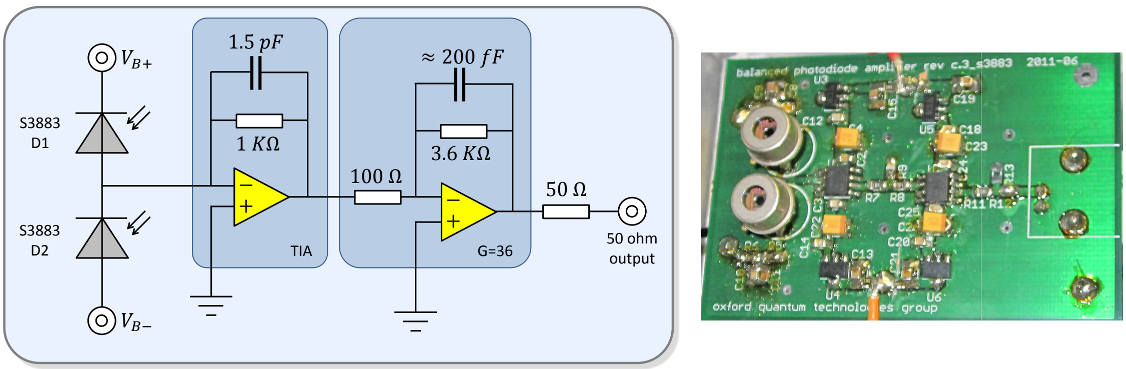

Figure 3.4: (a) Electronic schematic of the BHD developed for this thesis. Photocurrents generated by two Hamamatsu S3883 photodiodes D1(2), reverse biased with voltages $V_{B+(-)}$ are subtracted on a transmission line. The resulting difference photocurrent is converted to a voltage by a transimpedance amplifier (TIA) based on the Texas Instruments OPA847. The TIA output is further amplified by a second OPA847 with gain $G = 36$. The net transimpedance gain of the two stages combined is 36 kVA^{-1}. The amplifier chain is terminated in a 50 Ω resistor to enable the detector output to be coupled to a digitizer using standard coaxial cable. (b) Photograph of BHD printed circuit board with all components soldered in place. The layout from left to right is consistent with the schematic, (a). The reverse side (not shown) has minimal components and comprises mainly a ground plane. The PCB measures 6.5 x 4.5 cm.

(GAWBS) [125, 126]. Concerning the latter phenomenon, the scattering probability is typically of the order 10^{-10} m^{-1} in an optical fiber [125]. Thus for a 15 cm fiber and LO pulses containing on the order of 10^9 photons, the additional phase and amplitude noise added to the LO coherent state due to GAWBS is negligible. The phenomenon can however become a practical limitation if a weak signal pulse co-propagates with the intense LO within the same optical fiber, e.g. in a CV-QKD system [127], or if a significantly longer fiber is used to transmit the LO to a remote location – whereby the LO may no longer be shot-noise limited.

The LO is combined with the signal mode, derived from the same Ti:Sapphire oscillator pulse train, in quantum state $\hat{\rho}_s$ on a PBS. A HWP/PBS combination forms an effective 50:50 beam splitter to mix the signal and LO optical fields [55]. One output mode of the beam splitter contains a delay stage to control the relative time of arrival of the optical pulses at the BHD. The optical modes are focussed onto two p-i-n photodiodes (D1(2), Hamamatsu S3883) by two identical lenses. The size of the optical mode at the focus is sufficiently small that the entire mode is collected by the photodiode whilst ensuring the photodiode does not saturate.

The S3883 photodiodes were chosen due to their high specified quantum efficiency, $\eta_{\mathrm{pd}} = 0.90$ at 830 nm, and sufficient electronic bandwidth of 300 MHz. Furthermore, the S3883 photodiodes have a low noise equivalent power (NEP) [122] of 6.7×10^{-15} $\mathrm{WHz}^{-1/2}$ with a reverse bias voltage of 20 V applied. The photodidoes are operated in photoconductive mode [74, 122, 123] with bias voltages V_{B}^{+} and V_{B}^{-} independently tunable and wired in series such that the photocurrents are directly subtracted on the transmission line to produce the difference photocurrent required for balanced homodyne detection.

The difference photocurrent is converted to a voltage by a transimpedance amplifier (TIA) [74, 122], figure 3.4(a). The output voltage of the TIA is amplified by a second

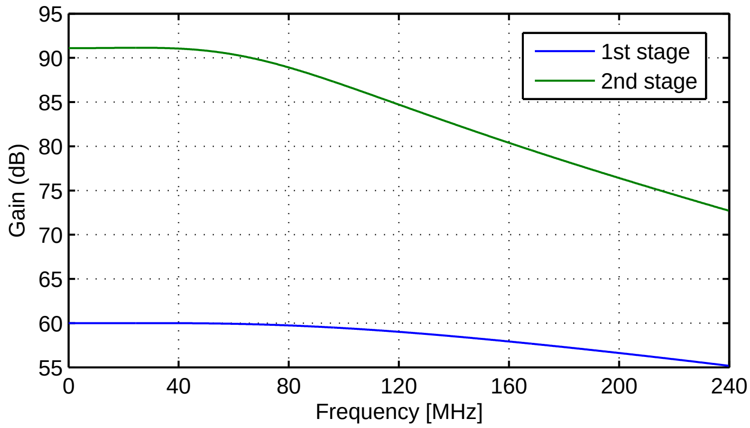

Figure 3.5: SPICE model of BHD gain after the first (blue) and second (green) amplification stage.

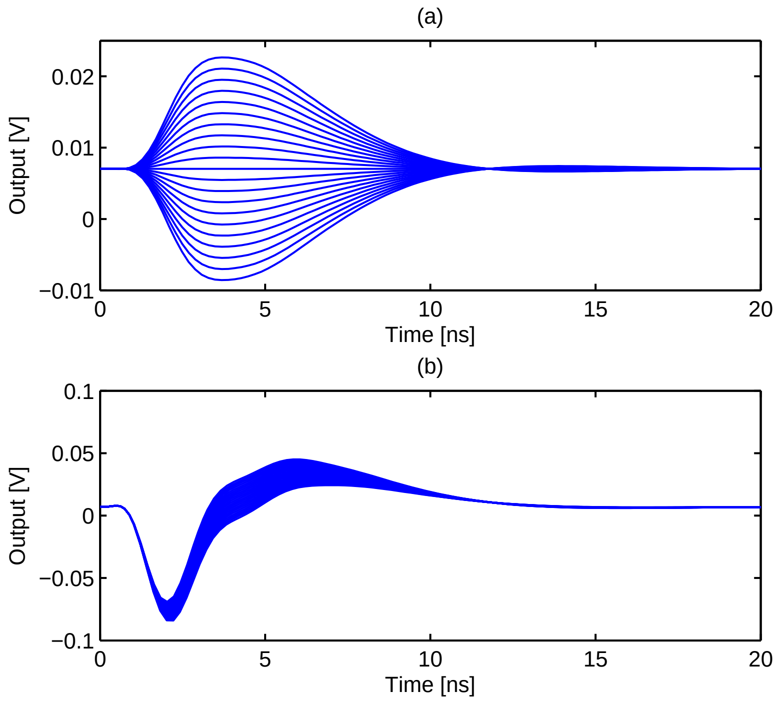

Figure 3.6: SPICE model of the BHD output voltage with a pulsed LO for (a) identical photodiodes, (b) photodiodes with capacitances differing by 100 fF. The latter situation results in a large residual voltage on which the vacuum fluctuations are superimposed.

stage with a voltage gain $G = 36$. This gives a combined transimpedance gain of 36 kVA^{-1}. Both amplifier stages utilize the Texas Instruments OPA847 operational amplifier (op-amp) owing to the excellent gain-bandwidth product*, low noise figure† and low cost‡ of said device. The amplifier chain is terminated in a 50 Ω resistor to allow the detector output to be fed to a digitizer through standard coaxial cable. A Tektronix MSO5104 digital storage oscilloscope (DSO) is used to digitize and capture the BHD output voltage.

Great care was taken when designing both the circuit schematic and the physical layout of the printed circuit board (PCB), photographed in figure 3.4(b). Values for each component were optimized for the target electronic bandwidth using a SPICE model of the circuit shown in figure 3.4(a). The SPICE model was found to be very accurate when compared with the performance of the real circuit. Figure 3.5 shows the SPICE model prediction of the circuit gain as a function of frequency after the first (blue line) and second (green line) amplifier stage. Figure 3.6 is the SPICE simulation of the BHD output voltage when simulating homodyne detection of the vacuum state with a 5 mW LO at 80 MHz (i.e. 2.6×10^8 photons per LO pulse). In (a) the two photodiodes are modelled to have identical capacitance, which leads to uniform voltage fluctuations. In (b) one photodiode has a capacitance 100 fF larger than the other, which results in a large residual voltage on which the same vacuum fluctuations are superimposed.

The PCB layout influences the performance of the circuit due to parasitic capacitance and inductance. Precautions were taken to ensure signal tracks were kept as short as practically possible and generally at right-angles to tracks carrying power supplies to the amplifiers and photodiodes. The PCB features both a top and bottom ground plane to reduce crosstalk between tracks. Surface-mount devices are used throughout the circuit

*The gain-bandwidth product of the OPA847 is 3.9 GHz. Thus with a gain of $G = 36$ in the second amplification stage stage a bandiwdth of approximately 100 MHz should be achievable.

†$0.85\ \mathrm{nVHz}^{-1/2}$.

‡Approximately £5 per device at the time of writing.

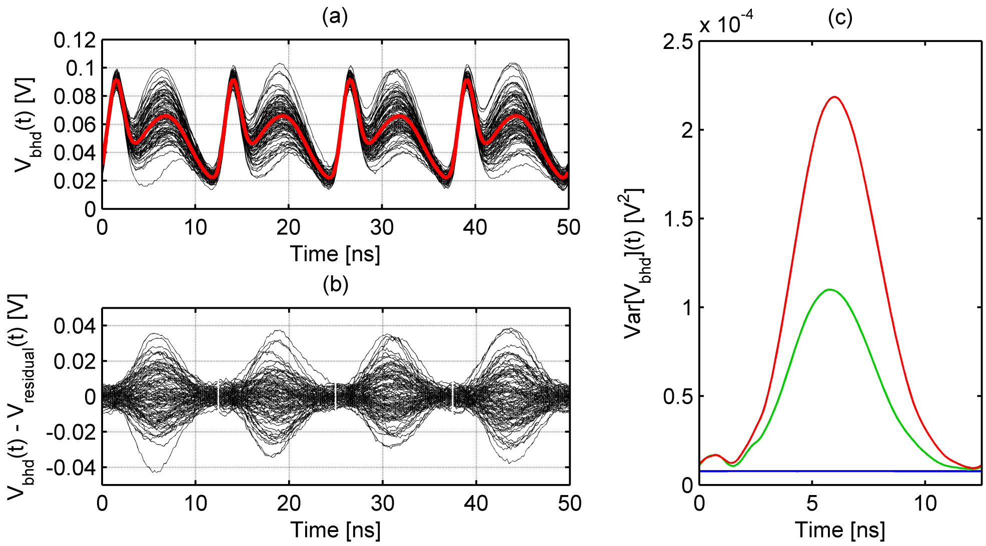

Figure 3.7: (a) 100 overlayed voltage traces $V_{\text{bhd}}(t)$ spanning a time interval of 50 ns obtained from the BHD with vacuum state input and 5 mW LO power, red line: residual voltage $V_{\text{residual}}(t)$. (b) The same traces as in (a) but with the residual voltage defined in equation 3.37 subtracted, i.e. $V_{\text{bhd}}(t) - V_{\text{residual}}(t)$. (c) Variance of BHD voltage $\text{Var}[V_{\text{bhd}}](t)$ during one pulse period (12.5 ns) for three LO power settings: 5 mW (red), 2.4 mW (green) and 0 mW, i.e. electronic noise (blue).

to enable the PCB to be as compact as possible, and reduce stray capacitances and inductances associated with component leads. The two op-amps have completely separate power supplies, which prevents positive feedback and hence reduces the detector electronic noise.

3.4.2 Detector operation and performance

Figure 3.7(a) shows typical voltage traces $V_{\text{bhd}}(t)$ obtained from the BHD with a LO power of 5 mW for vacuum state input, recorded by the DSO. In this figure, 100 traces spanning a time duration of 50 ns are overlayed, which corresponds to 4 pulses of the 80 MHz LO pulse train. By inspection it is evident that the electronic pulses produced by the BHD are well isolated. The full-width half-maximum of a single electrical pulse is 5.5 ns.

The raw output voltage $V_{\text{bhd}}(t)$ must be processed in order to obtain correctly scaled samples of the signal state field quadrature, $\hat{X}_\theta = \hat{X}\cos\theta + \hat{P}\sin\theta$, where θ is the phase of the LO relative to the signal. This involves both a rescaling of $V_{\text{bhd}}(t)$ and removal of any D.C. offset resulting from improper balancing of the detector. A single sample of $\hat{X}_\theta$ is obtained from each optical pulse and hence each electronic pulse at the detector output. Equation 3.25 was derived by considering the optical fields alone – the photodiode and amplifier responses internal to the BHD were not considered. In practice, one obtains a time-domain voltage, to which one can ascribe the operator

$$\begin{aligned}\hat{V}_{\text{bhd}}(t) = ec\sum_k\sum_{\lambda'}\Big(&\hat{b}^\dagger_{L,\lambda}\hat{c}_{k,\lambda'}\int_{-\infty}^{\infty}dt'G(t-t')\int_S d^2x\mathbf{v}^*_{L,\lambda}(\mathbf{x},0,t')\cdot\mathbf{v}_{k,\lambda'}(\mathbf{x},0,t')\\ &+\hat{b}_{L,\lambda}\hat{c}^\dagger_{k,\lambda'}\int_{-\infty}^{\infty}dt'G(t-t')\int_S d^2x\mathbf{v}_{L,\lambda}(\mathbf{x},0,t')\cdot\mathbf{v}^*_{k,\lambda'}(\mathbf{x},0,t')\Big),\end{aligned} \tag{3.35}$$

where e is the electronic charge and $G(t-t')$ is a transfer function which accommodates for the combined time-domain response of the photodiodes and amplifier chain, incorporating multiplicative factors relating to the photodiode quantum efficiency and net transimpedance gain. Here, the two photodiodes are assumed to have equal responses. By comparison with equation 3.25, aside from multiplicative factors, the question arises as to whether the BHD voltage $\hat{V}_{\text{bhd}}(t)$ need be integrated over some time interval τ, as was the case with the photon-number difference in equation 3.25. From equation 3.35, if the detector response time, encapsulated within the transfer function $G(t-t')$ is far greater than the duration of the optical wave-packets then the optical wave-packet is effectively a delta function in the time-domain. Thus the wave-packet modes may be approximated as

$$\begin{aligned}\mathbf{v}_{k,\lambda'}(\mathbf{x},0,t') &= \mathbf{u}_{k,\lambda'}(\mathbf{x},0)\delta(t'-t_k),\\ \mathbf{v}_{L,\lambda'}(\mathbf{x},0,t') &= \mathbf{u}_{L,\lambda'}(\mathbf{x},0)\delta(t'-t_L).\end{aligned}$$

Using these approximate wave-packet modes in equation 3.35 gives

$$\hat{V}_{\mathrm{bhd}}(t) = ec\sum_{k}\sum_{\lambda'} G(t-t_k)\Big(\hat{b}^{\dagger}_{L,\lambda}\hat{c}_{k,\lambda'}\delta(t_k-t_L)\int_S d^2x\mathbf{u}^{*}_{L,\lambda}(\mathbf{x},0)\cdot\mathbf{u}_{k,\lambda'}(\mathbf{x},0)$$
$$+\hat{b}_{L,\lambda}\hat{c}^{\dagger}_{k,\lambda'}\delta(t_k-t_L)\int_S d^2x\mathbf{u}_{L,\lambda}(\mathbf{x},0)\cdot\mathbf{u}^{*}_{k,\lambda'}(\mathbf{x},0)\Big), \quad (3.36)$$

Thus the voltage pulse shape in this regime is simply given by the characteristic detector response $G(t)$. Hence the BHD effectively performs integration of the photocurrent directly and thus the peak value of the voltage pulse is proportional to integral of the pulse. If the optical wave-packet is of similar duration to the detector response time then this is not the case, and the voltage itself must be integrated to ensure a true quadrature sample is obtained. Thus in general, quadrature samples X_θ are related to $V_{\mathrm{bhd}}(t)$ through

$$X_\theta \propto \frac{\int_t^{t+\tau_p} dt' V_{\mathrm{bhd}}(t') - \int_t^{t+\tau_p} dt' V_{\mathrm{residual}}(t')}{\sqrt{2}\eta_{\mathrm{pd}} Ge|\alpha_{\mathrm{LO}}|}, \quad (3.37)$$

where τ_p is the temporal duration of one electronic pulse, η_{pd} is the quantum efficiency of the photodiodes, e is the elementary charge, G is the net transimpedance gain of the amplifier stages and $|\alpha_{\mathrm{LO}}|$ is the coherent state amplitude of the LO. To aid analysis it turns out to be useful to introduce the fictitious time-dependent voltage $V_{\mathrm{residual}}(t)$,* which represents the residual voltage at the detector output due to imperfect photocurrent subtraction and the presence of a D.C. offset.† Later it is shown how $V_{\mathrm{residual}}(t)$ can model instability of the detector. The processed voltage trace given by $V_{\mathrm{bhd}}(t) - V_{\mathrm{residual}}(t)$ is shown in figure 3.7(b).

The denominator of equation 3.37 is a combined scale factor which converts the integrated voltage to units of dimensionless field quadrature. Fortunately, it is not necessary

*Fictitious because the only physical voltage is $V_{\mathrm{bhd}}(t)$, which is what appears at the output of the detector circuit and is subsequently digitized by the DSO.

†This is made clear by rearranging equation 3.37 such that $\int V_{\mathrm{bhd}}(t) = AX_\theta + \int V_{\mathrm{residual}}(t)$.

to determine the value of each contributing factor separately. By blocking the signal input mode of the 50:50 beam splitter, the detected field mode is prepared in the vacuum state.* The operational calibration procedure is to acquire a set of quadrature samples $\{X_\theta\}$ of the vacuum state and determine the scale factor $\sqrt{2}\eta_{\text{pd}}Ge|\alpha_{\text{LO}}|$ and offset $\int_t^{t+\tau_p} dt' V_{\text{residual}}(t')$ such that $\langle X_\theta\rangle = 0$ and $\text{Var}[X_\theta] = \langle X_\theta^2\rangle - \langle X_\theta\rangle^2 = 1/2$, where averaging is performed over the set of acquired samples $\{X_\theta\}$. Once the BHD has been calibrated the signal mode can be unblocked and the determined calibration applied to samples of the unknown state. It is typically necessary to acquire several thousand samples of the vacuum state to ensure sufficiently good statistics for calibration.

Signal-to-noise ratio

In situations where the LO pulse duration is significantly shorter than the response time of the detector, the detector electronics effectively perform integration of the difference photocurrent directly, as explored above. This is the regime in which the BHD is operated throughout this thesis since LO pulses of duration 100-300 fs are used, whereas the detector response time is on the order of several nanoseconds. In this regime the BHD output voltage $V_{\text{bhd}}(t)$ can be sampled at the peak, since the peak voltage is proportional to the area under the pulse.† One may ask what is meant by "the peak". To answer this, figure 3.7(c) shows the variance of the BHD voltage $\text{Var}[V_{\text{bhd}}](t)$ during a 12.5 ns interval calculated from several thousand pulses for an input signal in the vacuum state where

$$\text{Var}[V_{\text{bhd}}](t) = \langle V_{\text{bhd}}^2(t)\rangle - \langle V_{\text{bhd}}(t)\rangle^2, \tag{3.38}$$

*One of the easiest states to prepare for optical fields. This is challenging as one goes to lower frequency fields, where thermal excitations persist.

†Assuming the detector response is linear.

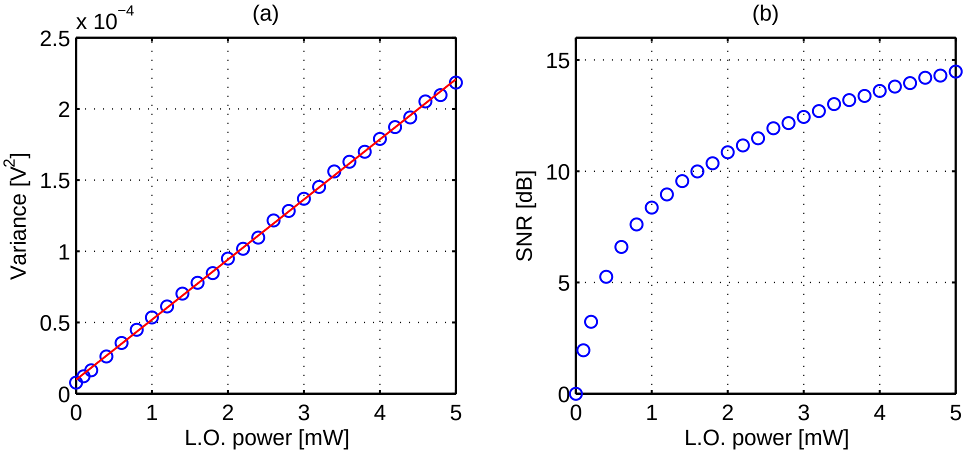

Figure 3.8: (a) Voltage variance of BHD output measuring the vacuum state as a function of LO power. A linear fit confirms the BHD is shot-noise limited (red line). (b) Signal-to-noise ratio as a function of LO power.

and $\langle ... \rangle$ denotes averaging over an ensemble of pulses. For 5 mW LO power ($|\alpha_{\mathrm{LO}}|^2 \propto P_{\mathrm{LO}} = 5$ mW) (red line) the variance exhibits a clear peak around 6 ns. With the LO switched off (blue line), the variance is observed to be constant. This is due to the electronic noise of the detector electronics. The variance for an intermediate power setting $P_{\mathrm{LO}} = 2.4$ mW is also plotted (green line). The signal-to-noise ratio for the BHD at a particular LO power setting P_{LO} is defined as [124]

$$\mathrm{SNR}_{P_{\mathrm{LO}}}(t) = 10 \log_{10} \left(\frac{\mathrm{Var}[V_{\mathrm{bhd}}](t)_{P_{\mathrm{LO}}}}{\mathrm{Var}[V_{\mathrm{bhd}}](t)_{P_{\mathrm{LO}}=0\mathrm{mW}}} \right) = 10 \log_{10} \mathcal{S}_{P_{\mathrm{LO}}}(t). \tag{3.39}$$

From figure 3.7(b) it is evident that the signal-to-noise ratio $\mathrm{SNR}_{P_{\mathrm{LO}}}(t)$ is optimum when sampling the BHD output at time T_0 corresponding to the peak in $\mathrm{Var}[V_{\mathrm{bhd}}](t)^*$. Furthermore, the signal-to-noise ratio depends on the LO power setting, as shown in figure 3.8(b) where $\mathrm{SNR}_{P_{\mathrm{LO}}}(T_0)$ is plotted for different LO power settings. For $P_{\mathrm{LO}} = 5$ mW the signal-to-noise ratio is 14.5 dB. For $P_{\mathrm{LO}} = 0.14$ mW the shot-noise variance is equal

*As mentioned, integration of the voltage pulse according to equation 3.37 is not necessary in the ultra-short optical pulse regime. Were the pulse to be integrated the signal-to-noise ratio would be slightly deteriorated since the envelope of $\mathrm{Var}[V_{\mathrm{bhd}}](t)$ tails off, figure 3.7(b), whereas the electronic noise is constant.

to the electronic-noise variance. Thus at an 80 MHz repetition rate the noise equivalent power (NEP) for the LO is equal to 0.14 mW. This corresponds to 7.2×10^6 photons per LO pulse.

The signal-to-noise ratio quantifies the ability of the BHD to distinguish characteristic fluctuations of the signal field quadrature $\hat{X}_\theta$ prepared in quantum state $\hat{\rho}_s$ from the random electronic noise inherent in the detector electronics, which effects a smoothing of the inferred marginal distributions $\Pr(X_\theta|\hat{\rho}_s) = \langle X_\theta|\hat{\rho}_s|X_\theta\rangle$. The smoothing results from the convolution of the difference photocurrent distribution with the electronic noise distribution in a way which parallels the influence of optical loss on the detected signal [124]. Indeed it has been shown that provided the electronic noise is Gaussian one can define an effective quantum efficiency η_{en} given by [124]

$$\eta_{\mathrm{en}} = \frac{\mathcal{S}_{P_{\mathrm{LO}}}(T_0) - 1}{\mathcal{S}_{P_{\mathrm{LO}}}(T_0)}, \tag{3.40}$$

where $\mathcal{S}_{P_{\mathrm{LO}}}(T_0)$ is the peak ratio of the variances defined in equation 3.39. Evaluating equation 3.40 for the BHD presented here with $P_{\mathrm{LO}} = 5$ mW gives $\eta_{\mathrm{en}} = (28.2-1.0)/28.2 = 0.96$.

Shot-noise-limited detection

The voltage noise variance $\mathrm{Var}[V_{\mathrm{bhd}}](T_0)$ sampled at T_0 (maximum signal-to-noise ratio) with a vacuum state input ($\hat{\rho}_s = |0\rangle\langle 0|$) is expected to scale linearly as a function of P_{LO}, with a constant offset due to the electronic noise contribution. Sources of classical noise, for example fluctuations in the balance of the detector or drifting of components in the detector electronics, will contribute to $\mathrm{Var}[V_{\mathrm{bhd}}](T_0)$ but with a quadratic dependence on P_{LO}.

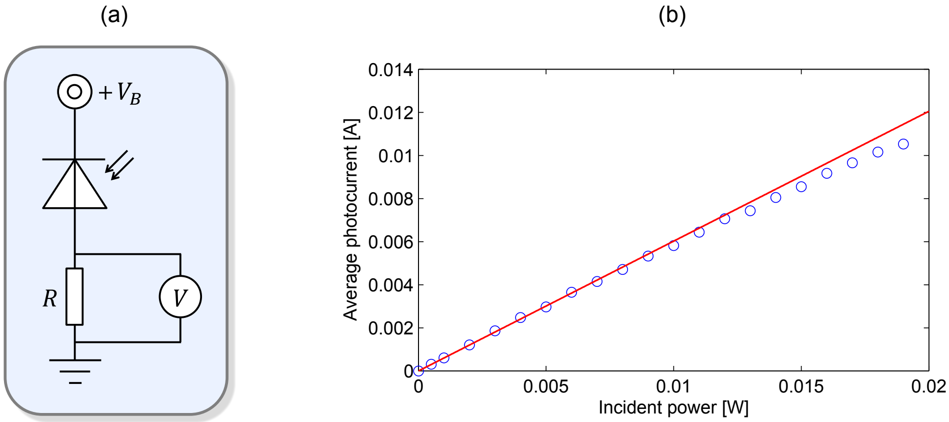

Figure 3.9: (a) Circuit used to characterize photodiode linearity. Photodiode is operated in photoconductive mode with applied bias voltage V_B. The photocurrent generated causes a voltage drop across resistor R which is measured with a simple volt meter. (b) Dependence of average photocurrent $I = V/R$ on average incident optical power. Red line: linear fit to measured data near origin.

To characterize the noise scaling with LO power, $\mathrm{Var}[V_{\mathrm{bhd}}](T_0)$ was determined for a range of LO power settings, figure 3.8(a). Each value was calculated from 40,000 samples of $V_{\mathrm{bhd}}(T_0)$ at the full 80 MHz repetition rate of the Ti:Sapphire oscillator, corresponding to a measurement duration of 500 μs. The data show a clear linear dependence of the voltage noise variance on LO power (red line) with no second-order dependence. This demonstrates the BHD is shot-noise limited* with no significant classical noise contamination for measurement durations of 500 μs. Below it is discussed whether this is true for longer measurement time-scales.

Photodiode linearity

Strictly speaking, for the assessment of the linear dependence of $\mathrm{Var}[V_{\mathrm{bhd}}](T_0)$ on P_{LO} above to be valid it must be ensured that the Hamamatsu S3883 photodiodes employed respond linearly to the incident optical power.† The photocurrent produced by the S3883

*The term "shot-noise limited" is used extensively in the literature. Note that the presence of any amount of electronic noise means this is not strictly true.

†This is especially important since when working with ultra-short optical pulses exhibiting a large peak intensity

photodiode as a function of incident optical power was measured using the simple circuit shown in figure 3.9(a). A linear dependence of the photocurrent on average incident optical power was observed up to 10 mW, figure 3.9(b). Thus at the typical LO power of 5 mW (2.5 mW per diode) the S3883 photodiodes employed in the BHD are operating in the linear regime.

Detector efficiency

The photodiode quantum efficiency $\eta_{\rm pd}$ can be extracted from the linear fit in figure 3.9(b) as

$$\eta_{\rm pd} = \Delta \times \frac{hc}{e\lambda_0}, \tag{3.41}$$

where Δ is the gradient of the linear fit (red line, figure 3.9(b)) and λ_0 is the central wavelength (830 nm) of the incident optical pulses. The photodiode quantum efficiency is determined in this manner to be $\eta_{\rm pd} = 0.90$,* which agrees with the value quoted in the S3883 specification sheet. When combined with the electronic noise effective quantum efficiency $\eta_{\rm en} = 0.96$ this gives an overall detector efficiency $\eta_{\rm bhd} = \eta_{\rm en}\eta_{\rm pd} = 0.86$.†

Correlation coefficient

Frequency spectra of the BHD output figure 3.10(a) were obtained by evaluating the Fourier transform of the BHD voltage $V_{\rm bhd}(t)$ directly on the oscilloscope. Spectra were obtained of the electronic noise power (green line) and the shot noise power with 5 mW LO power (blue line). The -3 dB point in the shot noise power at approximately 80 MHz already gives a good indication that the detector bandwidth should be sufficient to enable

*The photodiode quantum efficiency could be increased to approximately $\eta_{\rm pd} = 0.97$ by removing the input window from each S3883 package.

†This is well above the minimum threshold $\eta_{\rm bhd} = 0.5$ necessary to directly infer non-classical behaviour of the signal state from the measured quadrature statistics [54, 50].

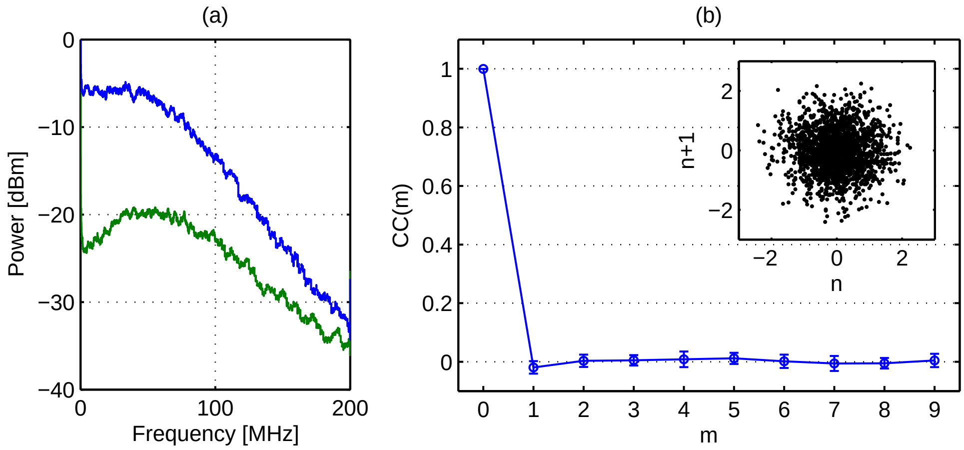

Figure 3.10: (a) Frequency spectrum of shot noise at 5 mW LO power (blue line) and electronic noise (green line). (b) Correlation coefficient CC(m) evaluated from 20 separate datasets at 5 mW LO power. Inset: parametric plot of vacuum state quadrature samples obtained from neighbouring LO pulses.

shot-to-shot quadrature measurements with an 80 MHz LO repetition rate. However, since the BHD will be employed for time-domain measurements as opposed to frequency-domain measurements, a more instructive measure of the detector capability to resolve individual pulses is provided by examining the pulse-to-pulse quadrature statistics directly.

A suitable measure for examining time-domain BHDs is provided by the correlation coefficient CC(m) defined as [101]

$$\mathrm{CC}(m) = \frac{\langle X_n X_{n+m}\rangle - \langle X_n\rangle\langle X_{n+m}\rangle}{\sqrt{\mathrm{Var}[X_n]}\sqrt{\mathrm{Var}[X_{n+m}]}}, \tag{3.42}$$

where $\langle ... \rangle$ denotes averaging over an ensemble of measurements, X_n and X_{n+m} are obtained quadrature samples for pulses separated by m temporal periods of the laser and $\mathrm{Var}[X_n]$ is the variance of the quadrature statistics in the measurement ensemble which provides normalization of CC(m). Ideally the quadrature sample obtained from pulse $n + m$ should not depend on the sample obtained from pulse n for $m \geq 1$. For a vacuum state input there should be no correlation between the statistics obtained from different pulses,* such that $\mathrm{CC}(m) = 0$ for $m \geq 1$ and $\mathrm{CC}(0) = 1$.

$\mathrm{CC}(m)$ was evaluated for $m = 0...9$ with vacuum state input and 5 mW LO power, figure 3.10(b). The uncertainties in each value are given by the standard deviation in $\mathrm{CC}(m)$ from 20 separate measurement runs and give an indication of the contribution caused by random statistical fluctuations. $\mathrm{CC}(1) = -0.019 \pm 0.020$ which is comparable with other reported BHDs [99, 101] and confirms that there is no significant correlation between quadrature samples obtained from neighbouring pulses at the 80 MHz LO repetition rate, which is visually evident from the parametric plot shown in figure 3.10(b).

Common mode rejection ratio

The common mode rejection ratio (CMRR) quantifies the ability of the BHD to perform the necessary subtraction of the photocurrents produced by photodiodes D1 and D2. A sensible definition of the CMRR is

$$\mathrm{CMRR}\ [\mathrm{dB}] = 10 \log_{10} \left(\frac{\int_0^\infty d\nu |\tilde{P}_{\mathrm{unbalanced}}(\nu)| - \int_0^\infty d\nu |\tilde{P}_{\mathrm{en}}(\nu)|}{\int_0^\infty d\nu |\tilde{P}_{\mathrm{balanced}}(\nu)| - \int_0^\infty d\nu |\tilde{P}_{\mathrm{en}}(\nu)|} \right), \tag{3.43}$$

where $|\tilde{P}_{\mathrm{balanced}}(\nu)|$ is the spectral power density of the BHD output with the detector unbalanced (one photodiode blocked), $|\tilde{P}_{\mathrm{unbalanced}}(\nu)|$ is as before but with the detector balanced and $|\tilde{P}_{\mathrm{en}}(\nu)|$ is the spectral power density of the detector electronic noise. For a BHD with vacuum state input and LO in a coherent state with mean photon number N, the CMRR is ultimately limited by the shot noise $\sqrt{N}$, where N is the average number of photons in each LO pulse, i.e. $N = |\alpha_{\mathrm{LO}}|^2$. The target CMRR for this BHD† is $\mathrm{CMRR} = 10 \log_{10} \sqrt{N} \approxeq 42$ dB. However, for BHD operation in the pulsed regime it is

*$\mathrm{CC}(m)$ in equation 3.42 is defined such it is independent of any coherent amplitude of the quantum state generating samples X_n, X_{n+m}. Clearly when measuring a state with a large coherent amplitude, e.g. a coherent state, there will be a strong correlation between quadrature samples. However, this correlation is due to the underlying state, not an artifact of the detector.

†5 mW LO power, 80 MHz repetition rate, central wavelength 830 nm.

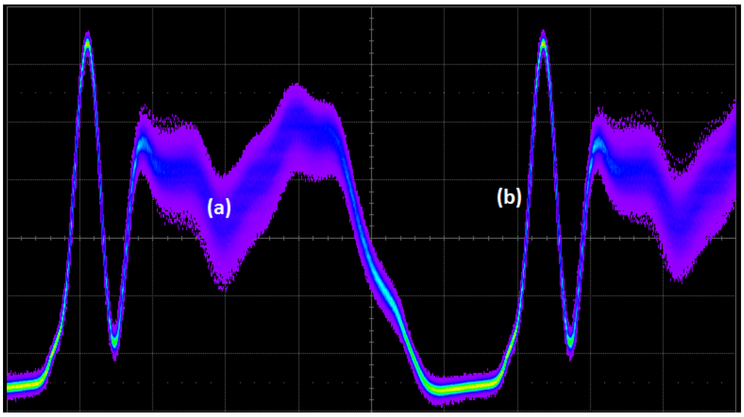

Figure 3.11: Oscilloscope trace of $V_{\mathrm{bhd}}(t)$ for poorly matched photodiode responses. The shot noise fluctuations (a) are superimposed on a periodic residual signal $V_{\mathrm{residual}}(t)$ (b). The horizontal scale is 2 ns/div.

most common to determine the CMRR at the laser repetition rate*, rather than integrating over the whole power spectrum as defined in equation 3.43. At the laser repetition rate, CMRR=63 dB at 5 mW LO power was measured.

In the pulsed LO regime, achieving a good CMRR is complicated by the fact that the temporal profiles of the current pulses produced by the two photodiodes must be nearly identical in both amplitude and response shape. An example of poor photocurrent subtraction is shown in figure 3.11. The key to achieving an excellent CMRR in this BHD is to control the photodiode responses separately. Photodiodes typically have a substantial terminal capacitance C_t which has several contributing factors. The main factor is the capacitance of the p-i-n junction itself C_j, with an additional small contribution from the photodiode package and legs. When combined with a load resistance R_L, an effective RC circuit results, leading to a response time $\tau_D = R_L C_t$. The response time τ_D can be controlled through adjustment of either the circuit load resistance R_L or the photodiode terminal capacitance C_t.

*The voltage produced by the BHD $V_{\mathrm{bhd}}(t)$ in a highly unbalanced configuration can approximately be expanded as a Fourier series, where the fundamental frequency is equal to the laser repetition rate. Since the bandwidth is of the order the repetition rate the fundamental component will have the largest amplitude (neglecting any D.C. offset) and therefore when the BHD is balanced this component should be minimized.

The junction capacitance is dependent on the applied reverse bias voltage V_B according to

$$C_j \propto A\left[(V_B + V_i)\epsilon\right]^{-\frac{1}{2}\text{ to }-\frac{1}{3}}, \tag{3.44}$$

where A is the p-i-n junction area, V_i is the built-in junction voltage and ϵ is the dielectric permittivity [74]. To this end, in this BHD design the photodiode bias voltages V_{B}^{+} and V_{B}^{-} can be independently set. This enables first-order control of the impulse response of each photodiode D1 and D2. The relative time of arrival of the two optical pulses on D1 and D2 is also adjusted. These two adjustments proved to be sufficient to directly achieve excellent photocurrent subtraction (and hence good CMRR) without the need for additional electronic filtering or shaping of the current pulses.

Digitizer considerations

In most scenarios the BHD output $V_{\mathrm{bhd}}(t)$ is digitized such that it can be processed by a digital computer for applications such as quantum state tomography. A Tektronix MSO5104 digital oscilloscope is used to capture and store waveforms from the BHD. This particular model has a sampling rate of 10 GS/s and 8-bits of vertical resolution. The latter can potentially become a limiting factor if the photocurrent subtraction discussed before is not near ideal.

Assuming the signal $V_{\mathrm{bhd}}(t)$ does not saturate the 8-bit digitizer, the full signal is discretized into at most $2^8 = 256$ levels. The underlying signal state quadrature probability distribution $\Pr(X_\theta|\hat{\rho}_s)$ should be sampled adequately.* Now consider that the voltage fluctuations directly corresponding to $\Pr(X_\theta|\hat{\rho}_s)$ are superimposed on the residual waveform $V_{\mathrm{residual}}(t)$ (equation 3.37), due to imperfect photocurrent subtraction, as shown in

*Where samples X_θ are related to the BHD voltage according to equation 3.37.

figure 3.11. Since the signal $V_{\mathrm{bhd}}(t)$ must not in general saturate the digitizer, the input sensitivity of the digitizer front-end must be adjusted to re-accommodate the signal. This results in fewer discrete voltage bins sampling the underlying distribution $\Pr(X_\theta|\hat{\rho}_s)$, and thus degraded sampling resolution. As noted above, electronic filtering of $V_{\mathrm{bhd}}(t)$ has been suggested to improve the CMRR [103], which according to the argument made here should also enable better sampling resolution. There are however fundamental drawbacks to this approach, which are discussed below.

Detector stability

Calibration of the BHD enables transformation of the raw detector voltage $\int_t^{t+\tau_p} dt' V_{\mathrm{bhd}}(t')$ to units of dimensionless quadrature, through determination of the detector baseline $\int_t^{t+\tau_p} dt' V_{\mathrm{residual}}(t')$ and scale factor $\sqrt{2}\eta_{\mathrm{pd}} eG|\alpha_{\mathrm{LO}}|$, equation 3.37. In practice the calibration is not valid indefinitely due to changes in either the scale factor or the detector baseline, as defined above. Changes in the baseline were found to be the dominant source of drift. Ideally, $V_{\mathrm{residual}}(t + n\tau) = V_{\mathrm{residual}}(t)$ for $n = -\infty...\infty$, where τ is the repetition period of the LO. A gradual change in $V_{\mathrm{residual}}(t)$ after calibration is a source of low-frequency classical noise. Without compensation this effectively causes the quadrature origin to drift leading to errors in state tomography and state discrimination applications.

There are potentially many underlying physical causes of such detector instability including fluctuations in the photodiode bias voltages, variation of the 50:50 beam splitter ratio*, scattering of light from dust particles, drifts in the LO central wavelength/bandwidth† and laser pointing instability‡ [128]. The effect of detector instability is shown in figure

*Due to the high CMRR, the BHD is sensitive to changes in this ratio on the order of one part per million.

†Due to the potential of a small dependence of the beam splitter ratio on wavelength.

‡If the quantum efficiency of photodiode i is a function of the transverse spatial co-ordinates such that $\eta_{\mathrm{pd},i} = \eta_{\mathrm{pd},i}(x, y)$ then a small change in beam pointing will potentially cause a small change in photocurrent. Such changes can be uncorrelated since the two photodiodes in the BHD are not identical, and thus they contribute to the difference photocurrent.

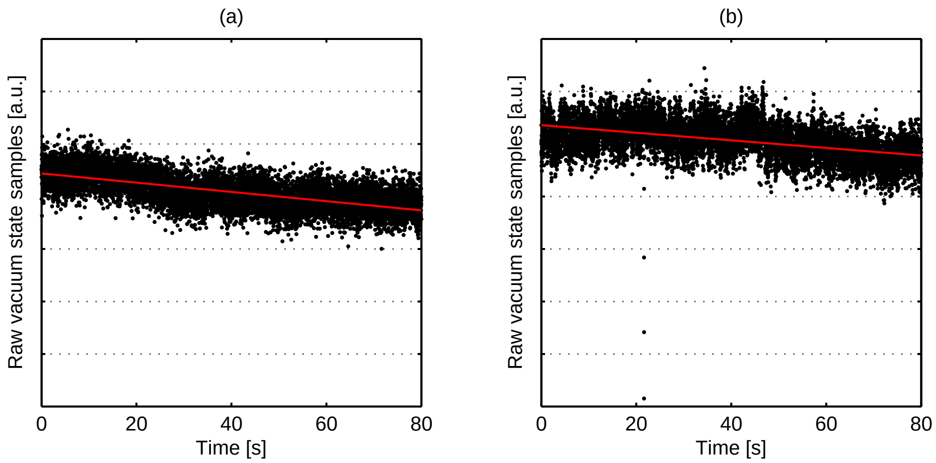

Figure 3.12: Drifting of detector baseline during acquisition of vacuum state quadrature samples. (a) an approximately linear drift is evident. (b) Again, a linear drift is evident in addition to a sudden spike around $t = 20$ s. This is likely due to scattering of light from a dust particle in one of the paths proceeding the 50:50 beam splitter. The vertical scales are the same in both plots and are proportional to the raw detector voltage.

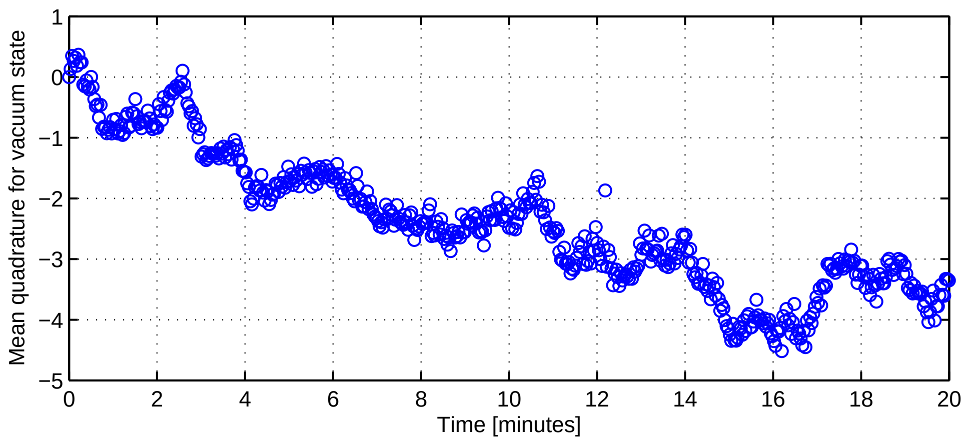

Figure 3.13: Behaviour of the detector baseline over a longer period of time. Each point is calculated from 10,000 samples of the vacuum state. The y-axis is in units of dimensionless quadrature, scaled using a single calibrated set.

3.12, where samples of the vacuum state (black dots) were obtained over a time interval of 80 s with 5 mW LO power. During this time interval the detector baseline (i.e. the rolling average of the quadrature samples) has clearly drifted in an approximately linear manner with time (red line) for the two separate measurements (a) and (b). Furthermore, figure 3.12(b) shows the effect of a dust particle drifting through one of the beams proceeding the 50:50 beam splitter.

To perform a more quantitative analysis of the typical instabilities shown in figure 3.12, the Allan deviation $\sigma_{\text{AD}}(\tau_A)$ of the vacuum state quadrature samples [129] is calculated. The Allan deviation was originally devised to assess to frequency stability of oscillators. More generally, it enables determination of the stability of some parameter on different timescales [129], and has been applied to BHDs [97, 100, 121] and optical tweezers [130]. The Allan deviation is defined as

$$\sigma_{\text{AD}}(\tau_A) = \sqrt{\frac{1}{2}\left\langle \left(\bar{X}_{n+1} - \bar{X}_n\right)^2 \right\rangle}, \tag{3.45}$$

where $\bar{X}_{n+1}$ and $\bar{X}_n$ are averages of the vacuum state quadrature samples over adjacent intervals of duration τ_A and $\langle ... \rangle$ denotes averaging over the whole dataset, i.e. as many adjacent intervals of duration τ_A that fit within the total measurement duration of 80 s.* 10 separate data sets such as those shown in figure 3.12 were collected and the Allan deviation $\sigma_{\text{AD}}(\tau_A)$ for each set was computed. The average of $\sigma_{\text{AD}}(\tau_A)$ for the 10 separate sets was calculated (blue dots, Fig.3.14) along with the standard deviation (blue bands, Fig.3.14).

For Gaussian white noise (i.e. shot noise) the Allan deviation is expected to scale as $\sigma_{\text{AD}}(\tau_A) \propto \tau_A^{-1/2}$ whereas for random walk noise $\sigma_{\text{AD}}(\tau_A) \propto \tau_A^{1/2}$ [129]. Random walk noise is what results from changes in the detector baseline over time. The red line in figure 3.14

*e.g. for $\tau_A = 40$ s there are only two adjacent intervals in the dataset.

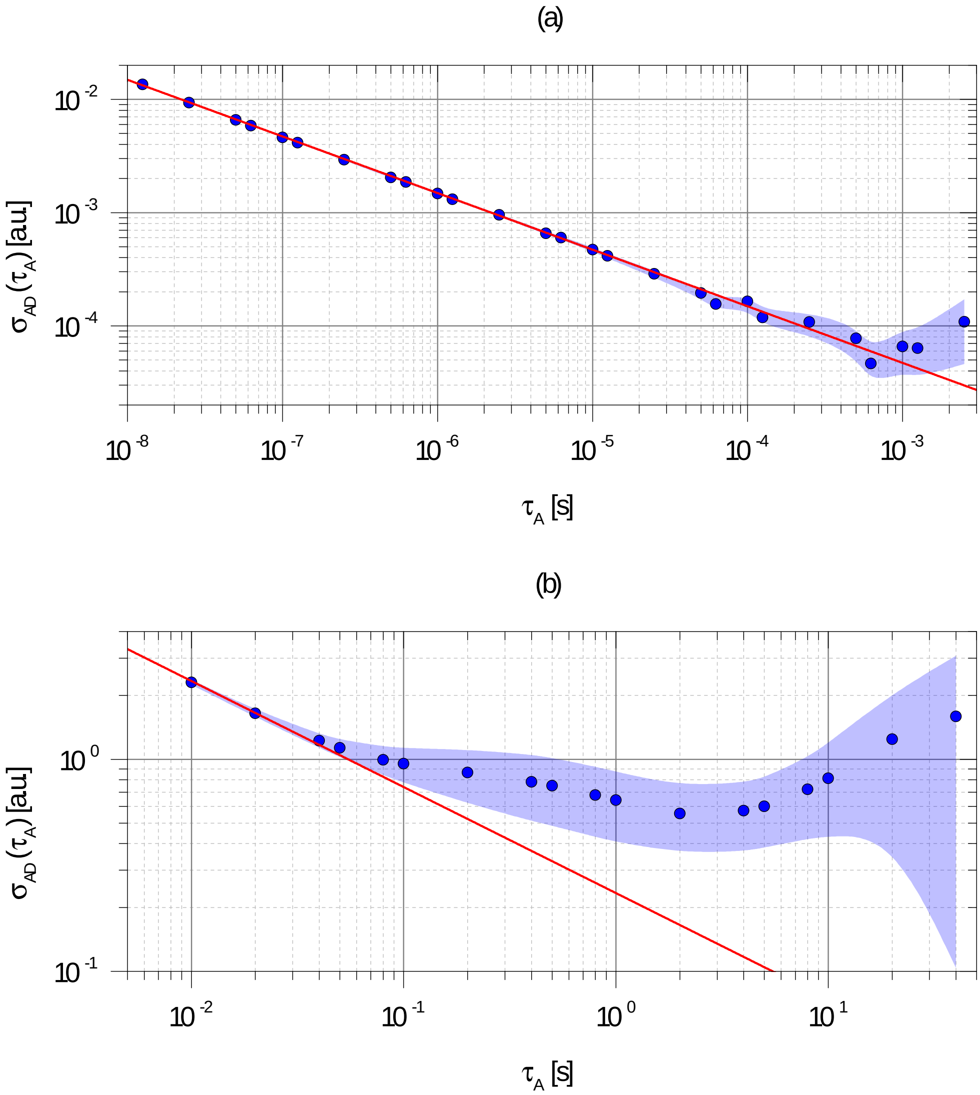

Figure 3.14: Average Allan deviation $\sigma_{\mathrm{AD}}(\tau_A)$ computed from 10 separate data sets (blue dots) and standard deviation (blue band). Fit to Allan deviation with fixed gradient of $\tau_A^{-1/2}$ (red line). The full range τ_A examined is split into two (a) and (b). This is due to data acquisition limitations for the vastly different time scales which also means that the y-axis scaling in the two plots is different. However, the analysis relies only on the scaling of $\sigma_{\mathrm{AD}}(\tau_A)$ with τ_A. Significant departure from $\sigma_{\mathrm{AD}}(\tau_A) \propto \tau_A^{-1/2}$ occurs at ≈ 0.1 s, whilst $\sigma_{\mathrm{AD}}(\tau_A)$ does not start to increase until ≈ 2 s (b).

is a fit to the measured Allan deviation with a fixed gradient of $\tau_A^{-1/2}$. Significant deviation of $\sigma_{\mathrm{AD}}(\tau_A)$ from the fit occurs around $\tau_A \approxeq 0.1$ s. This indicates that for measurement intervals much longer than 0.1 s, the recorded statistics are influenced not only by shot noise (due to the underlying quadrature statistics) but also by random walk noise from the slowly-varying detector baseline. However, figure 3.14(b) shows that for measurements times up to approximately $\tau_A = 2$ s the Allan deviation continues to decrease. This indicates that the random walk noise only starts to dominate the measured statistics for measurement intervals longer than ≈ 2 s, despite the onset occurring around 0.1 s. This inference is intuitively valid from examining the data shown in figure 3.12(a,b) where it is clear that for measurement intervals up to ≈ 2 s the drift is not significant compared to the distribution of quadrature samples for the vacuum state. The measured stability is several orders of magnitude better than other reported figures for BHDs operating at similar repetition rates [97, 100].

Electronic filtering and post-processing

One possibility to improve the detector stability is to employ notch filters centred at the laser repetition rate and harmonics, along with high- and low-pass filters between the BHD output and the digitizer [131]. Such a filtering scheme can enhance the CMRR, thereby suppressing the fluctuating detector baseline $\int_t^{t+\tau_p} dt' V_{\mathrm{residual}}(t')$ and hence potentially improving detector stability [103]. However, in situations where the BHD bandwidth is on the same order as the LO repetition rate such filtering has the effect of discarding all information about the phase-space displacement of the measured quantum state $\hat{\rho}_s$. This was confirmed by applying DSP filters to the raw waveforms $V_{\mathrm{bhd}}(t)$ acquired from the BHD and observing the effective removal of the displacement amplitude from the measured quadrature probability distributions of a weak coherent state, figure 3.15. For

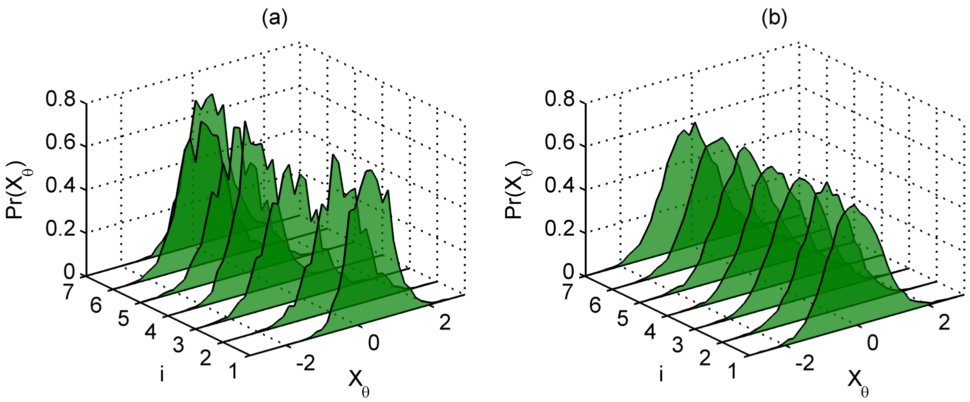

Figure 3.15: Measured quadrature probability distributions $\mathrm{Pr}(X_\theta)$ for a weak coherent state obtained at 7 discrete LO phases $\theta_i, i = 1..7$. (a) Without any filtering of the detector output $V_{\mathrm{bhd}}(t)$, (b) after application of high- and low-pass filters and notch filters centred at 80 MHz and 160 MHz. It is clear that in (b) all inferred probability distributions satisfy $\int dX_\theta X_\theta \mathrm{Pr}(X_\theta) = \langle X_\theta \rangle \approxeq 0$, i.e. information about the coherent displacement of the input state has been removed by the filters, implying one would infer the vacuum state.

measurement of states possessing no coherent displacement* such filtering has no adverse effect.

Alternatively, it was pointed out that since the ideal quadrature probability distributions satisfy the condition

$$\mathrm{Pr}(X_\theta|\hat{\rho}_s) \equiv \mathrm{Pr}(-X_{\theta+\pi}|\hat{\rho}_s), \tag{3.46}$$

any baseline offset δX present in the measured quadrature statistics can be elucidated [132]. However, this technique has limited applicability to the case where the offset δX is constant for the duration of acquisition of the whole set of quadrature samples $\{X_\theta\}$ from which the probability distributions for all LO phases $\{\mathrm{Pr}(X_\theta|\hat{\rho}_s)\}_\theta$ are estimated. Additionally, one must have knowledge of the LO phase θ independently of the homodyne measurement, thus requiring the use of an axillary phase reference. In general it is important that the BHD be as intrinsically stable as possible, as the two workarounds discussed

*e.g. squeezed vacuum states or mixtures of Fock states.

above have limited applicability to measuring particular classes of states.

3.4.3 Tomography of weak coherent state

To demonstrate the BHD performance at the single-photon intensity level, a weak coherent state $|\alpha\rangle$ with amplitude $|\alpha| = 1.00$ was prepared and subsequently measured by the BHD, figure 3.16. A total of 35,000 quadrature samples were acquired at 7 LO phases, figure 3.17(a). A chopper wheel (CW) was employed to enable vacuum state calibration of the BHD before acquisition of each set of 5,000 quadrature samples. The LO phase θ relative to the coherent state was measured independently using a continuous-wave diode laser at 1550 nm*, figure 3.17(b).

An iterative maximum-likelihood algorithm [90] was used to find the quantum state $\hat{\rho}$ consistent with the measured quadrature data $\{X, \theta\}$. The reconstructed state has a fidelity of 0.998 with a pure coherent state of magnitude $|\beta| = 0.86$, which is consistent with the measured losses between state preparation and measurement†. The reconstructed and best-fit photon number statistics $P(n)$ are shown in figure 3.17(c).

3.4.4 Comparison with reported BHDs

In table 3.1 the performance characteristics of other reported BHDs operating with pulsed LO modes are compared. The detector developed as part of this work compares favourably to other reported detectors in many of the metrics, including SNR, CC(1) and bandwidth. The BHD reported in [102] appears to have better stability, with typical measurement

*$\theta = (\lambda_{\text{diode}}/\lambda_{\text{oscillator}})\theta_{\text{diode}}$

†The combined detection efficiency of the coherent state is given by $\eta = \eta_{\text{bhd}}\eta_{\text{mm}}\eta_{\text{loss}}$, where $\eta_{\text{bhd}} = 0.86$, $\eta_{\text{mm}} = \mathcal{V}^2 = 0.96$ (measured interference between coherent state and LO, $\mathcal{V} = 0.98 \pm 0.02$) and $\eta_{\text{loss}} = 0.88$ (independently measured transmission loss due to an uncoated Wollaston prism used for this experiment). Using these values gives an estimated net detection efficiency $\eta = 0.73 \pm 0.03$. The reconstructed coherent state amplitude is predicted as $|\beta| = |\sqrt{\eta}\alpha| = 0.85 \pm 0.02$. The reconstructed coherent state has an amplitude $|\beta| = 0.86$.

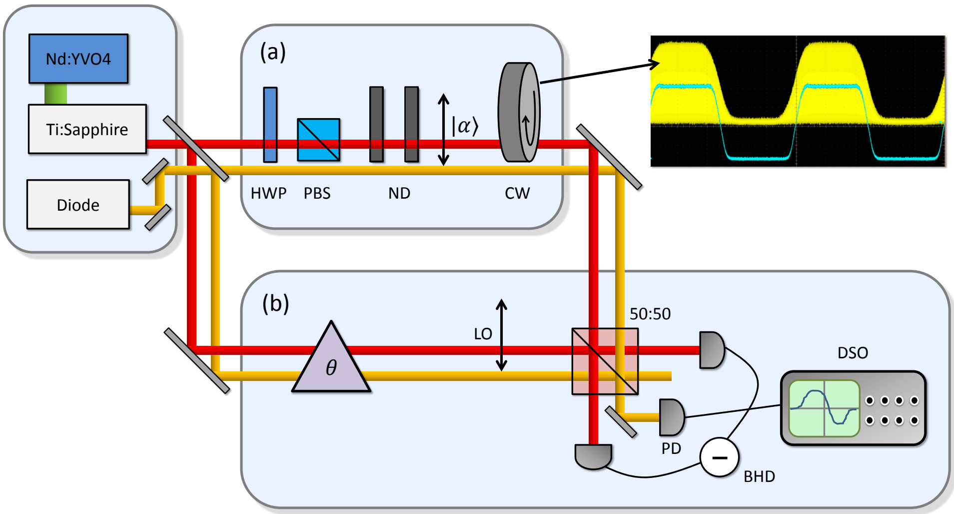

Figure 3.16: Experimental setup for performing homodyne tomography of a weak coherent state. (a) Preparation of coherent state: HWP/PBS and neutral density (ND) filters are used to set amplitude $|\alpha|$. A chopper wheel (CW) periodically blocks the signal mode (inset oscilloscope trace), enabling vacuum calibration of the BHD. (b) Balanced homodyne detection: 50:50 BS is formed of a PBS to combine signal and LO, and a HWP and Wollaston prism combination. An InGaAs photodiode monitors the diode laser interference fringes at 1550 nm, from which the the LO phase θ is extracted.

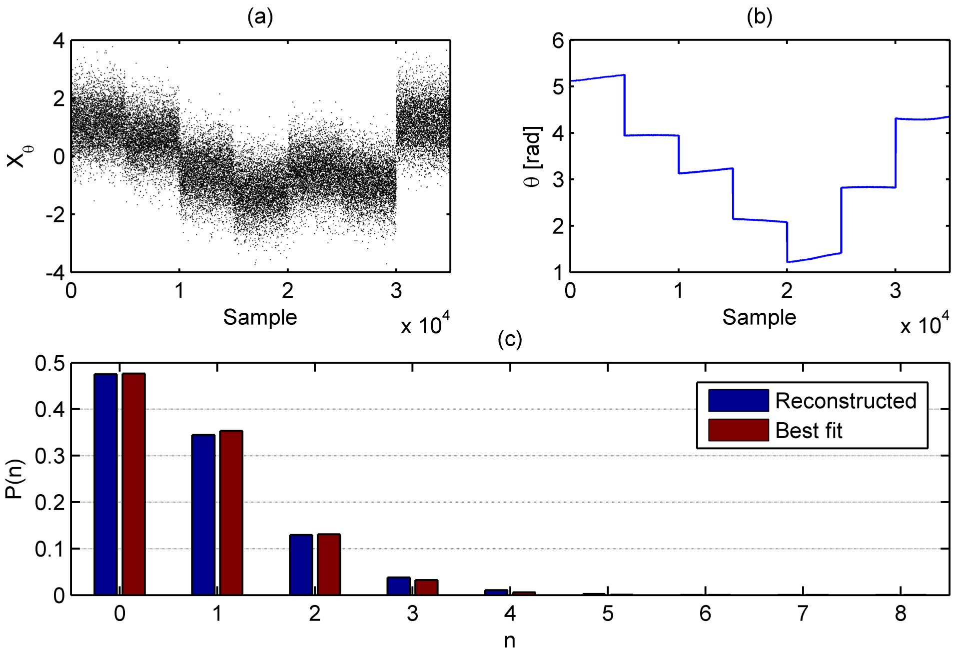

Figure 3.17: (a) Quadrature samples X_θ recorded by the BHD for a weak coherent state input $|\alpha\rangle$, $|\alpha| = 1.00$. (b) LO phase θ relative to the coherent state, measured independently with a diode laser. (c) Reconstructed (blue) and best-fit (red) photon number statistics $P(n)$. Best fit state has an amplitude $|\beta| = 0.86$.

intervals of 100 s possible before re-calibration*. However, this BHD has a bandwidth of only 2 MHz [102]. A time-bandwidth product, defined as TBP $= \Delta\nu\Delta\tau$, where $\Delta\nu$ is the -3 dB bandwidth and $\Delta\tau$ is the stability interval, enables comparison of the theoretical data harvesting capability of a BHD between calibrations. Evaluating the time-bandwidth product for the BHD of [102] gives TBP $= 2 \times 10^8$ whereas for the BHD developed here TBP $= 1.6 \times 10^8$.

*This is likely to be due to the fiber-based design of the detector [102], which eliminates sources of noise such as pointing instability [128].

	This	[103]	[101]	[99]	[100]	[96]	[97]	[98]	[55]	[133, 134]	[102]
Wavelength [nm]	830	791	1550	1064	800	700	786	786	1064	846	
Rep. rate [MHz]	80	76	32	76	53.8	0.80	82	82	4.2×10^{-4}	0.79	2
Pulse duration [fs]	300	1800	5.0×10^{7}		230	1600	3000	3000	4.0×10^{5}	150	1.0×10^{8}
Bandwidth [MHz]	80	80	100	250	40	1	80	80			2
CMRR [dB]	63	52	46	45	56	85	42	34		40	76
SNR [dB]	14.5	13	13	7.5	12	14	4	12	9	11	20
Stability [s]	2				5.0×10^{-5}		1.0×10^{-6}				100
CC(1)	-0.02		0.05	0.04							-0.07
Filters	None	HP, LP, Notch	None	None	HP	HP	None	HP			None

Table 3.1: Comparison of reported time-domain BHDs operating with pulsed LO modes. Some parameters were not reported and thus some table entries are blank. The abbreviations used in the "filters" row are: high-pass filter (HP) (AC-coupled detectors are denoted as HP), low-pass filter (LP), notch filters at repetition rate and/or harmonics (Notch).

3.5 Summary

Detection of light with single-photon sensitivity it crucial for experimentation in quantum optics [21] and emerging quantum technologies based on photonics [31]. Detection of electromagnetic field modes can be broken into two broad camps – field detection and intensity detection. The former cannot be achieved directly with present photo-detection technology due to the inability of photo-detectors to faithfully convert optical-frequency oscillations into electrical signals. Field detection is desirable since it allows access to both the and amplitude and phase information of a particular mode of light. Field detection with photon-level sensitivity can be achieved by the technique of balanced homodyne detection. This scheme has numerous applications such as quantum key distribution [87, 88, 85, 89] and quantum state tomography [55, 50]. In this chapter the development of a balanced homodyne detector was detailed. The detector was characterized by a number of measures to assess the detector performance – indicating that the detector is capable of pulse-by-pulse measurements of an 80 MHz train of ultrafast optical pulses at the shot-noise limit. The detector is employed throughout the remainder of this work to perform quantum state and process tomography of non-classical states and photon-level operations.

4

Generation of Multi-Photon Fock States

Individual photons are the fundamental quantum excitation of the electromagnetic field. Fock, or photon-number states, which are eigenstates of the number operator, are the generalization of single-photon states to higher excitation numbers [14, 62]. The state with n photons in a particular wave-packet mode is defined as

$$|n\rangle_{j,\lambda} = \frac{1}{\sqrt{n!}}(\hat{b}^{\dagger}_{j,\lambda})^n|\mathrm{vac}\rangle, \tag{4.1}$$

where $\hat{b}^{\dagger}_{j,\lambda}$ is the wave packet creation operator defined in section 3.2.2. Single-photon Fock states may be generated using single-emitters such as atoms [135, 136], nitrogen-vacancy centres [137] and quantum dots [138, 139], or alternatively through non-linear optical processes such as spontaneous parametric down-conversion (SPDC) [140] or spontaneous four-wave mixing (SFWM) [141, 142]. Sources based on SPDC and SWFM rely on the pairwise emission of the generated photons to enable the non-deterministic generation of Fock states through a process known as heralding. By conditioning on higher-order photo-detection events it is possible to generate not only single-photon states but also higher-order Fock states using these non-linear processes [143, 144].

Single-photon states hold great promise in a variety of applications [145–147] such as

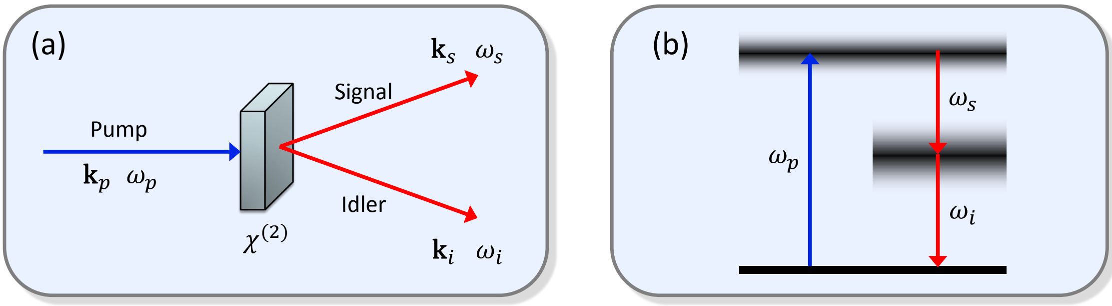

Figure 4.1: (a) Schematic representation of parametric down conversion. A pump photon with wave vector $\mathbf{k}_p$ and frequency ω_p decays probabilistically into signal ($\mathbf{k}_s$, ω_s) and idler ($\mathbf{k}_i$, ω_i) photons in a crystal exhibiting a $\chi^{(2)}$ non-linearity. Emission is symmetrical about the pump wave vector, due to conservation of momentum, equation 4.3. (b) Schematic representation of the energy conservation condition, equation 4.2. The broadened levels are due to the pump bandwidth (top) and phase matching bandwidth (middle).

linear-optical quantum computing (LOQC) [34], quantum metrology [148] and communication [149]. Higher-order Fock states on the other hand have received less attention. The ability to create Fock states of a well-defined single electromagnetic field mode with a prescribed excitation number is not only of foundational interest [143], but also enables synthesis of arbitrary quantum states through beam splitter interactions and conditional measurement [150–157, 144]. A key requirement to realize such quantum state engineering is that the Fock states should be prepared in a single, well-defined optical mode such that they exhibit high-visibility interference with other auxiliary states that occupy the same mode [158].

In this chapter the preparation of Fock states up to $n = 3$ is investigated. The states are generated using SPDC and characterized by means of optical homodyne tomography (OHT) to enable complete determination of the quantum state in a well-defined field mode [159, 111]. Many of the results presented here have also been published [160].

4.1 Parametric down-conversion

Parametric down-conversion (PDC) is a non-linear optical three-wave mixing process in which a pump photon (p) probabilistically splits into a pair of lower frequency photons, historically called signal (s) and idler (i), inside a crystal exhibiting a second-order non-linear optical response $\chi^{(2)}$, figure 4.1. The process should conserve energy and momentum such that

$$\omega_s + \omega_i = \omega_p, \tag{4.2}$$

$$\mathbf{k}_s + \mathbf{k}_i = \mathbf{k}_p. \tag{4.3}$$

The conservation of momentum condition, equation 4.3, is also known as the phase matching condition. Due to the dispersion of the non-linear crystal the two conditions are not independent, which leads to the presence of spatial-temporal correlations in the down-converted fields.

When the signal and idler modes are initially in the vacuum state, spontaneous parametric down-conversion (SPDC) occurs. Single-mode squeezed vacuum (SMSV) states and two-mode squeezed vacuum (TMSV) states [14], are generated through SPDC. It is also possible to seed either the signal or idler mode to stimulate emission in the conjugate mode. This process is known as difference frequency generation (DFG). PDC is usually divided into two classes known as type-I and type-II. In type-I PDC the down-converted modes have the same polarization, orthogonal to that of the pump, whereas in type-II PDC the two down-converted modes are orthogonally polarized. Type-I SPDC can be used to generate SMSV and TMSV states, the latter being possible when the down-converted fields are emitted at distinct angles. Type-II SPDC necessarily generates a TMSV state, since the signal and idler modes are orthogonally polarized.* In this thesis type-II collinear SPDC in bulk potassium di-hydrogen phosphate (KDP) is employed to generate TMSV states. Multi-photon Fock states are heralded by performing photon-counting measurements on one mode of the TMSV state.

4.1.1 Derivation of PDC unitary transformation

For the following analysis it is assumed that down-conversion takes place in a single spatial mode [162–164]. Although this may appear to be a rather drastic simplification, the down-converted modes will ultimately be spatially filtered either by single-mode fibers (SMF) or by the local oscillator (LO) when performing balanced homodyne detection. This means that only the temporal mode-structure of the down-converted fields is of relevance.

The Hamiltonian for the three-wave mixing process of PDC is given by [165–167]

$$\hat{H}_{\text{int}} = \int_V d^3r \chi^{(2)} \hat{E}_p^{(+)}(\mathbf{r},t)\hat{E}_s^{(-)}(\mathbf{r},t)\hat{E}_i^{(-)}(\mathbf{r},t) + \text{h.c.}, \tag{4.4}$$

where V is the interaction volume of the non-linear crystal, $\chi^{(2)}$ is the second-order non-linear susceptibility of the crystal and h.c. denotes the Hermitian conjugate. The negative frequency component of the signal and idler electric field operators $\hat{E}_{s,i}^{(-)}(z,t)$ are expanded in a set of monochromatic plane-wave modes defined as [14]

$$\begin{aligned}\hat{E}_{s,i}^{(-)}(\mathbf{r},t) &= -i\int_0^\infty d\omega_{s,i}\sqrt{\frac{\hbar\omega_{s,i}}{2\epsilon_0 n(\omega_{s,i})V}}\exp\left[-i(\mathbf{k}_{s,i}(\omega_{s,i})\cdot\mathbf{r}-\omega_{s,i}t)\right]\hat{a}_{s,i}^\dagger(\omega_{s,i}) \\ &= A_{s,i}\int_0^\infty d\omega_{s,i}\exp\left[-i(\mathbf{k}_{s,i}(\omega_{s,i})\cdot\mathbf{r}-\omega_{s,i}t)\right]\hat{a}_{s,i}^\dagger(\omega_{s,i}) \end{aligned}\tag{4.5}$$

where the parameter $A_{s,i}$ accumulates all constants and slowly varying field amplitudes,

*Although the two polarization modes can be mixed to generate two separate SMSV states [161], if both polarization modes have the same spatial-temporal mode structure.

$\hat{a}^{\dagger}_{s,i}(\omega_{s,i})$ is the plane-wave creation operator and $\hat{E}^{(-)}_{s,i}(\mathbf{r},t) = \left(\hat{E}^{(+)}_{s,i}(\mathbf{r},t)\right)^{\dagger}$. The pump is assumed to have a large electric field amplitude and can thus be treated classically [166, 167], such that

$$\hat{E}^{(+)}_{p}(\mathbf{r},t) \Rightarrow E_p(\mathbf{r},t) = A_p \int_0^{\infty} d\omega_p \alpha(\omega_p) \exp\left[i(\mathbf{k}_p(\omega_p)\cdot\mathbf{r} - \omega_p t)\right], \tag{4.6}$$

where A_p is the pump electric field amplitude and the normalized function $\alpha(\omega_p)$ defines the pump spectrum. The unitary transformation due to the PDC interaction Hamiltonian $\hat{H}_{\text{int}}$ is given by [168]

$$\hat{U}_{\text{PDC}} = \exp\left[-\frac{i}{\hbar}\int_0^{t_{\text{int}}} dt' \hat{H}_{\text{int}}(t')\right] \equiv \exp\left[-\frac{i}{\hbar}\int_{-\infty}^{\infty} dt' \hat{H}_{\text{int}}(t')\right], \tag{4.7}$$

where the integration limits can be taken to infinity because the interaction time is defined by the short pump pulse and of interest are the scattered fields at a time well after the pulses have exited the crystal. Substituting the definitions for the pump, signal and idler electric fields gives

$$\begin{aligned} \hat{U}_{\text{PDC}} = \exp\Bigg[-\frac{i}{\hbar}\Bigg(& A_p A_s A_i \chi^{(2)} \int_{-\infty}^{\infty} dt' \int_V d^3 r \int_0^{\infty} d\omega_p \int_0^{\infty} d\omega_s \int_0^{\infty} d\omega_i \\ & \times \exp\left[i(\mathbf{k}_p(\omega_p) - \mathbf{k}_s(\omega_s) - \mathbf{k}_i(\omega_i))\cdot\mathbf{r}\right] \\ & \times \exp\left[i(\omega_s + \omega_i - \omega_p)t'\right] \alpha(\omega_p)\hat{a}^{\dagger}_s(\omega_s)\hat{a}^{\dagger}_i(\omega_i) + \text{h.c.}\Bigg)\Bigg] \end{aligned} \tag{4.8}$$

The time integral gives a delta function $\delta(\omega_s + \omega_i - \omega_p)$ which represents the energy conservation condition, equation 4.2. This allows equation 4.8 to be expressed independent of the pump frequency ω_p. Furthermore, assuming all fields propagate in the z direction gives

$$\hat{U}_{\mathrm{PDC}} = \exp\Bigg[-\frac{i}{\hbar}\Bigg(\mathcal{A}' \int_0^L dz \int_0^\infty d\omega_s \int_0^\infty d\omega_i \\ \times \alpha(\omega_s+\omega_i) \exp[i\Delta k_z z] \hat{a}_s^\dagger(\omega_s)\hat{a}_i^\dagger(\omega_i) + \mathrm{h.c.}\Bigg)\Bigg], \quad (4.9)$$

where $\Delta k_z = k_p(\omega_s+\omega_i) - k_s(\omega_s) - k_i(\omega_i)$ is the wave vector mismatch and the new constant $\mathcal{A}'$ incorporates all the constant terms for simplicity. The integral over the crystal length L can be performed to give

$$\hat{U}_{\mathrm{PDC}} = \exp\left[-\frac{i}{\hbar}\left(\mathcal{A}\int_0^\infty d\omega_s \int_0^\infty d\omega_i \alpha(\omega_s+\omega_i)\Phi(\omega_s,\omega_i)\hat{a}_s^\dagger(\omega_s)\hat{a}_i^\dagger(\omega_i) + \mathrm{h.c.}\right)\right], \quad (4.10)$$

where $\Phi(\omega_s,\omega_i) = \exp\left[\frac{i\Delta kL}{2}\right]\mathrm{sinc}\left(\frac{\Delta kL}{2}\right)$ is known as the phase-matching function. The product of the phase-matching function with the pump envelope function defines the joint spectral amplitude (JSA) $f(\omega_s,\omega_i)$ of the generated state

$$f(\omega_s,\omega_i) = \alpha(\omega_s+\omega_i)\Phi(\omega_s,\omega_i). \quad (4.11)$$

The JSA completely characterizes the spectral-temporal correlations which exist between the signal and idler down-converted fields [169, 170, 163, 164]. The final expression for the unitary transformation due to the PDC process is

$$\hat{U}_{\mathrm{PDC}} = \exp\left[-\frac{i}{\hbar}\left(\mathcal{A}\int_0^\infty d\omega_s \int_0^\infty d\omega_i f(\omega_s,\omega_i)\hat{a}_s^\dagger(\omega_s)\hat{a}_i^\dagger(\omega_i) + \mathrm{h.c.}\right)\right], \quad (4.12)$$

In order to make the connection between equation 4.12 and the two-mode squeezing operator of equation 2.43 it is necessary to decompose the two terms in the exponential of equation 4.12 using the Schmidt decomposition [170, 171, 169, 172] such that

$$-\frac{i}{\hbar}\mathcal{A}f(\omega_s,\omega_i) = \sum_k r_k \psi_k^*(\omega_s)\phi_k^*(\omega_i), \tag{4.13}$$

$$-\frac{i}{\hbar}\mathcal{A}^* f^*(\omega_s,\omega_i) = -\sum_k r_k \psi_k(\omega_s)\phi_k(\omega_i), \tag{4.14}$$

where $\{\psi_k(\omega_s)\}$ and $\{\phi_k(\omega_i)\}$ are a complete set of orthonormal basis functions for the signal and idler spectral amplitudes respectively, known as the Schmidt modes [170, 171]. The functions are obtained uniquely from the underlying structure of the JSA $f(\omega_s,\omega_i)$. The amplitudes of the generated modes are given by coefficients r_k appearing in the expansions of equation 4.13 and equation 4.14. New broadband annihilation operators for the signal and idler modes can be defined in terms of the Schmidt modes [170, 171]

$$\begin{aligned} \hat{A}_k &= \int_0^\infty d\omega_s \psi_k(\omega_s)\hat{a}_s(\omega_s), \\ \hat{B}_k &= \int_0^\infty d\omega_i \phi_k(\omega_i)\hat{a}_i(\omega_i). \end{aligned} \tag{4.15}$$

Writing the unitary transformation equation 4.12 in terms of the new basis functions and coefficients from the Schmidt decomposition gives

$$\begin{aligned} \hat{U}_{\mathrm{PDC}} &= \exp\left[\int_0^\infty d\omega_s \int_0^\infty d\omega_i \sum_k r_k \psi_k^*(\omega_s)\phi_k^*(\omega_i)\hat{a}_s^\dagger(\omega_s)\hat{a}_i^\dagger(\omega_i) - \text{h.c.}\right], \\ &= \exp\left[\sum_k r_k \int_0^\infty d\omega_s \psi^*(\omega_s)\hat{a}_s^\dagger(\omega_s) \int_0^\infty d\omega_i \phi^*(\omega_i)\hat{a}_i^\dagger(\omega_i) - \text{h.c.}\right]. \end{aligned} \tag{4.16}$$

Invoking the broadband annihilation operators of equation 4.15 in equation 4.16 gives

$$\hat{U}_{\mathrm{PDC}} = \exp\left[\sum_k r_k \hat{A}_k^\dagger \hat{B}_k^\dagger - \mathrm{h.c.}\right], \tag{4.17}$$

$$= \bigotimes_k \exp\left[r_k \hat{A}_k^\dagger \hat{B}_k^\dagger - \mathrm{h.c.}\right]. \tag{4.18}$$

By inspection the individual terms appearing in the tensor product in equation 4.18 have the same form as the two-mode squeezing operator, equation 2.43 [173]. Thus the unitary transformation describing the PDC process can be written as

$$\hat{U}_{\mathrm{PDC}} = \bigotimes_k \hat{S}_{A_k B_k}(-r_k), \tag{4.19}$$

where $\hat{S}_{A_k B_k}(-r_k)$ is the two-mode squeezing operator for the pair of broadband field modes $\hat{A}_k$ and $\hat{B}_k$ and $-r_k$ is the squeezing parameter [163]. Assuming all modes are initially in the vacuum state, the output state produced by the down-converter is

$$\boxed{|\psi_{\mathrm{PDC}}\rangle = \bigotimes_k |\zeta_k\rangle_{A_k,B_k},} \tag{4.20}$$

where $\zeta_k = -r_k$ and $|\zeta_k\rangle_{A_k,B_k}$ is the TMSV state for the pair of modes $\hat{A}_k$ and $\hat{B}_k$.

This remarkable result shows that in general the output state produced by SPDC is a tensor product of distinct broadband TMSV states [174, 175]. The squeezing of each pair of modes $\hat{A}_k$ and $\hat{B}_k$ is governed by the nature of the JSA $f(\omega_s, \omega_i)$ as well as the overall efficiency of the process, which is encapsulated in the combined factor $\mathcal{A}$ [163].

4.1.2 Quantifying the multimode nature of PDC

In the above treatment the Schmidt decomposition was applied in order to demonstrate how the PDC unitary can be decomposed into a set of two-mode squeezing operators. The effective squeezing amplitudes r_k describe both the overall efficiency of the PDC process, through the combined efficiency term $\mathcal{A}$ in equation 4.12, and also the relative contributions of the Schmidt modes $\psi_k(\omega_s)$ and $\phi_k(\omega_i)$ used in the expansion of equations 4.13 and 4.13 [163, 164].

Since the combined efficiency $\mathcal{A}$ is constant and independent of the Schmidt modes under investigation, the squeezing amplitudes r_k can be normalized to give a distribution κ_k such that $\sum_k \kappa_k^2 = 1$, where the normalization is effected according to

$$\kappa_k = N r_k, \tag{4.21}$$

where N quantifies the total amount of squeezing generated across all Schmidt modes [101, 164]. Coefficients κ_k describe the underlying mode structure of the down-converter and will be employed later in this section.

In the low squeezing regime the PDC unitary, equation 4.17, can be approximated as

$$\hat{U}_{\text{PDC}} = \exp\left[\sum_k r_k \hat{A}_k^\dagger \hat{B}_k^\dagger - \text{h.c.}\right] \approxeq \hat{1} + \left(\sum_k r_k \hat{A}_k^\dagger \hat{B}_k^\dagger - \text{h.c.}\right). \tag{4.22}$$

This limits discussion to the pair production regime. If all input modes to the down-converter are in the vacuum state the PDC output state, obtained by applying equation 4.22 to the vacuum state $|\text{vac}\rangle$, is of the form

$$|\psi_{\text{PDC}}\rangle \approxeq |\text{vac}\rangle + \sum_k r_k |1_{A_k}; 1_{B_k}\rangle, \tag{4.23}$$

where $|\text{vac}\rangle$ represents all modes in the vacuum state and $|1_{A_k}; 1_{B_k}\rangle$ is the state with one photon in each of modes A and B in Schmidt mode labelled k, i.e. $|1_{A_k}\rangle = \hat{A}_k^\dagger |0_A\rangle$, where the broadband annihilation operators $\hat{A}_k$ and $\hat{B}_k$ were defined in equation 4.15. Under this approximation the SPDC output state comprises a large vacuum component and a superposition of photon-pair states excited in the broadband Schmidt modes.*

One of the most common applications of SPDC is to use the generated TMSV states to prepare Fock states by a process known as heralding [140]. Since the TMSV state is correlated in photon number, detection of m photons in one mode should collapse the other mode into the m-photon Fock state, $|m\rangle$. Starting from the approximate form of the SPDC output state of equation 4.23 and concentrating on the preparation of single-photon states, the state prepared in mode A due to conditional detection in mode B is given by

$$\hat{\rho}_A = \mathrm{Tr}_B\left(\hat{\Pi}_B|\psi_{\mathrm{PDC}}\rangle\langle\psi_{\mathrm{PDC}}|\right), \tag{4.24}$$

where $\hat{\Pi}_B$ is the POVM element describing the ensemble of states selected by the detector in mode B, which includes the effect of any temporal filtering performed by the detector or additional optical filters placed before the detector. Assume the detector is a perfect photon-number resolving detector but has no ability to resolve frequency. Furthermore, the preparation of $\hat{\rho}_A$ is conditioned on the detection of one photon in mode B. The POVM element describing this detection is [111]

$$\hat{\Pi}_B = \int d\omega |1_\omega\rangle_B\langle 1_\omega|_B, \tag{4.25}$$

where $|1_\omega\rangle_B$ is a single photon state with frequency ω in mode B. From equation 4.24 the heralded state in mode A is given by

$$\hat{\rho}_A = N^2\sum_k |r_k|^2|1_{A_k}\rangle\langle 1_{A_k}|, \tag{4.26}$$

*Note that equation 4.23 is not normalized.

where N^2 is a normalization factor which takes into account the success probability for heralding a single photon, which depends on the initial squeezing produced. This is nothing but the normalization introduced in equation 4.21.

In general it is desirable that the heralded Fock states be pure in every degree of freedom, i.e. spatial, spectral and polarization. Non-unit purity degrades the interference visibility attainable between two separate Fock states or between a Fock state and a coherent state, which consequently impacts on the efficacy of quantum state engineering protocols. The modal purity of the heralded state is given by

$$P = \mathrm{Tr}_A\left(\hat{\rho}_A^2\right) = N^4 \sum_k |r_k|^4 = \sum_k |\kappa_k|^4, \tag{4.27}$$

where the normalized coefficients κ_k introduced in equation 4.21 are used. The purity of the heralded state* depends on the number and relative amplitudes of the TMSV states produced by SPDC. The effective number of modes can be quantified using the cooperativity parameter K [176, 169], also known as the Schmidt number, where

$$K = \frac{1}{\sum_k |\kappa_k|^4}. \tag{4.28}$$

To herald a pure ($P = 1$) Fock state with a completely frequency-insensitive detector requires that $K = 1$, i.e. the down-converter produces a *single* two-mode squeezed vacuum state [169, 177]. This is in general not the case since it requires that the JSA, equation 4.11, is factorizable such that

$$f(\omega_s, \omega_i) = \psi^*(\omega_s) \times \phi^*(\omega_i), \tag{4.29}$$

*The purity will be the same when heralding higher order Fock states, assuming the heralding detector is perfectly number resolving.

i.e. if the JSA can be written as a product, equation 4.29, the Schmidt decomposition, equation 4.13, will contain only one term and hence $K = 1$.

Alternatively, if the down-converter naturally produces multiple TMSV states ($K > 1$), frequency filtering can be employed such that the heralding detector approximately selects only one of the emitted Schmidt modes. This is achieved by employing narrowband spectral filters in the heralding mode to select only the first Schmidt mode, which for most practical purposes is approximately a Gaussian distribution [111, 110, 50].* The heralding detector POVM is then of the form

$$\hat{\Pi}_B = \int d\omega T(\omega) |1_\omega\rangle_B \langle 1_\omega|_B, \tag{4.30}$$

where $T(\omega)$ describes the ensemble selected by the spectral filter. One disadvantage of employing filtering in the heralding mode is that it necessarily rejects a significant fraction of the down-converted light, thus reducing the heralding rate, and even within the filter passband the transmission can be poor. Furthermore, the achieved purity is typically highly sensitive to the precise alignment of the spectral filter.

4.2 PDC in bulk KDP

For the experiments detailed throughout this thesis, Type-II SPDC was performed in a bulk potassium di-hydrogen phosphate (KDP) crystal [162]. This source is engineered such that the output comprises very nearly a single TMSV state, i.e. the cooperativity parameter, equation 4.28, $K \approxeq 1$ [169, 162], figure 4.2. The single Schmidt mode emission is achieved by choosing the pump wavelength and non-linear crystal such that the pump field, which propagates as an e-ray, is group-velocity matched to the down-converted o-

*A true Schmidt mode filter is difficult to implement.

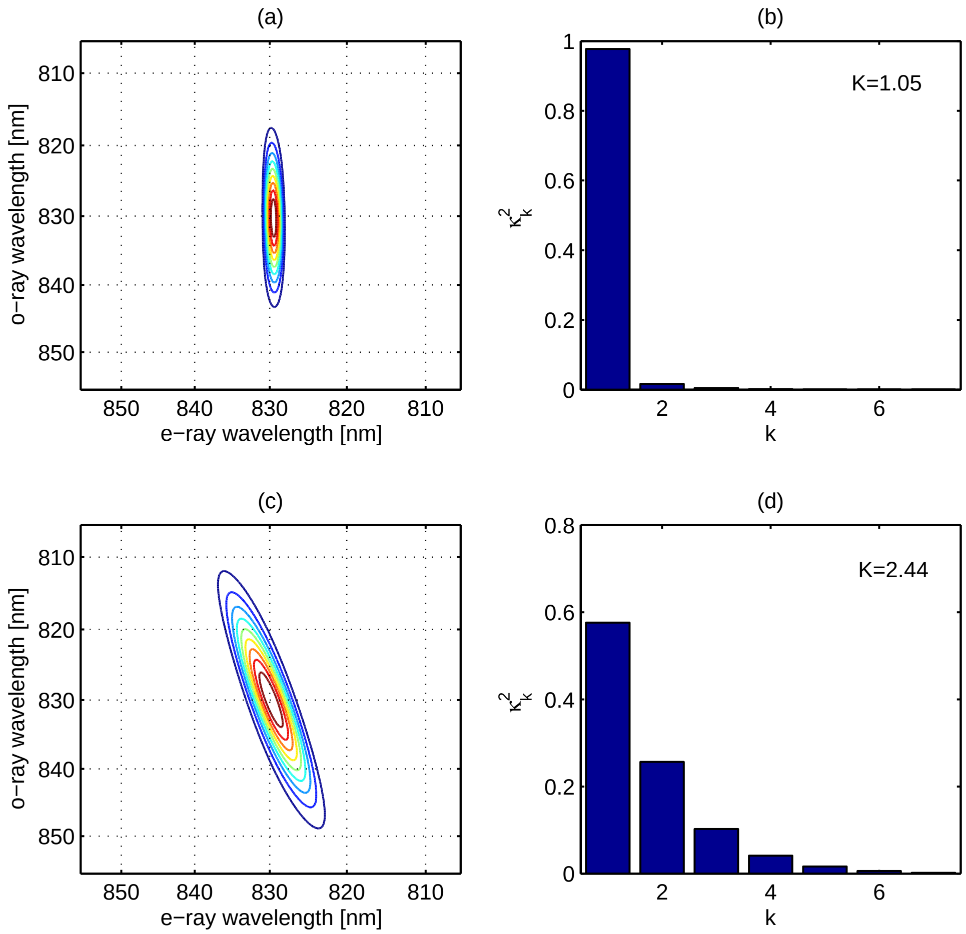

Figure 4.2: (a) Contour plot of joint spectral intensity (JSI) $|f(\omega_o, \omega_w)|^2$ for degenerate PDC in an 8 mm thick KDP crystal with pump FWHM bandwidth of 3.5 nm. (b) Mode distribution κ_k^2 showing one dominant mode, cooperativity parameter $K = 1.05$. (c) Contour plot of JSI for degenerate PDC in a 2 mm thick BBO crystal, same pump bandwidth as in (a). (d) Mode distribution with several dominant modes, $K = 2.44$.

ray field [169, 162]. This ensures that only a single temporal mode is produced* [169]. Since only a single TMSV state is produced by this SPDC source, the state generated is described by

$$\begin{aligned}|\mathrm{TMSV}\rangle &= \sqrt{1-\lambda^2}\sum_{n=0}^{\infty}\lambda^n|n,n\rangle \\ &\approxeq \sqrt{1-\lambda^2}\left(|0,0\rangle+\lambda|1,1\rangle+\lambda^2|2,2\rangle+\lambda^3|3,3\rangle+\mathcal{O}(\lambda^4)\right),\end{aligned} \tag{4.31}$$

where $\lambda = \tanh(\zeta)$ (for the real-valued squeezing parameter ζ) and depends on the pump field amplitude and effective $\chi^{(2)}$ non-linearity of the KDP crystal. $|n,m\rangle$ is the state with $n(m)$ photons in what we now refer to as the signal and trigger modes respectively.† The trigger mode is the o-ray down-converted field and the signal mode is the e-ray down-converted field. Detection of m photons in the trigger mode prepares the signal mode in a pure m photon Fock state $|m\rangle$. In principle, since for this source $K \approxeq 1$ it is not necessary to employ spectral filtering of the trigger mode prior to detection [162].‡ This has the advantage of not rejecting a significant proportion of the down-converted light, thus enabling heralding of higher-order Fock states without the use of an amplified laser system.

4.2.1 Experimental arrangement

The full schematic of the experimental arrangement for generating and performing homodyne tomography of multi-photon Fock states is shown in figure 4.3. An 80 MHz train of ≈100 fs pulses with a central wavelength of 830 nm is produced by a Ti:Sapphire oscillator (Spectra-Physics Tsunami). Most of the laser output is up-converted in a 700 μm thick β-

*Although spatial filtering is still necessary.
†The trigger mode will always be detected to herald Fock states in the signal mode
‡Although spatial filtering is employed.

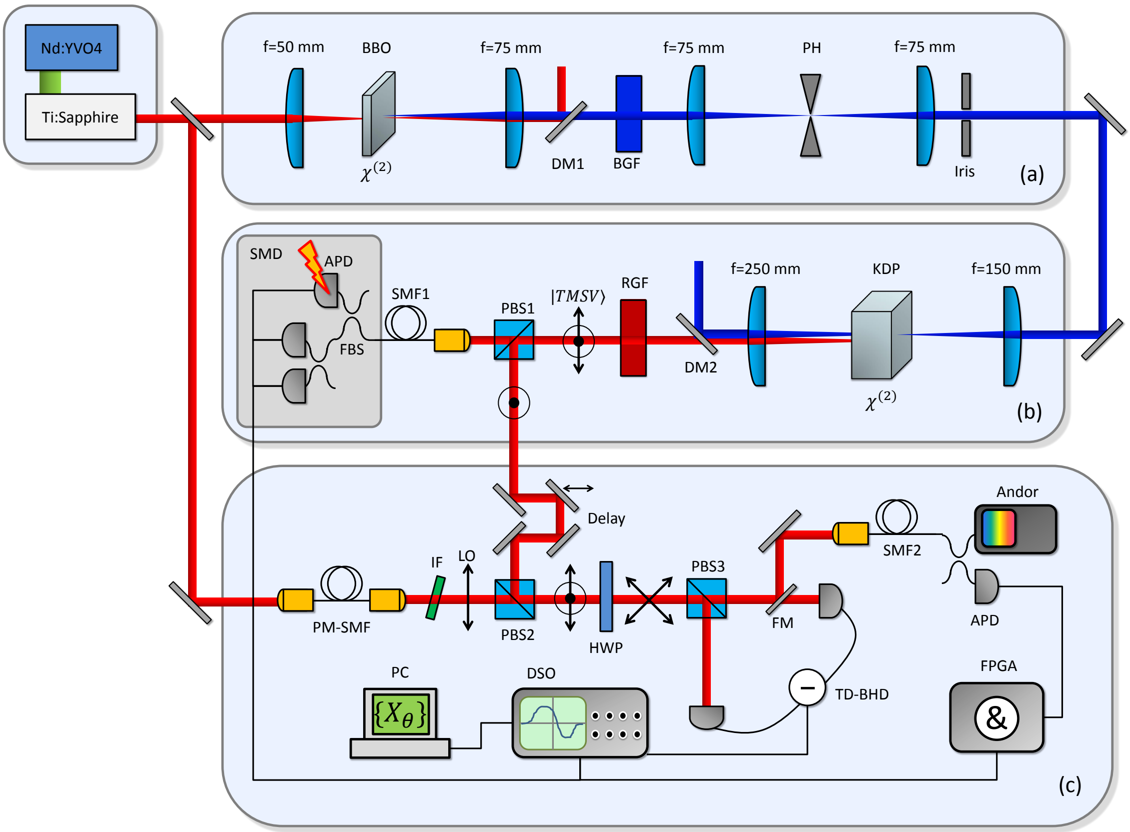

Figure 4.3: Schematic of the experimental setup used to prepare multi-photon Fock states and characterize them by means of homodyne tomography. (a) Second harmonic generation in BBO. (b) SPDC in KDP to generate TMSV state $|\text{TMSV}\rangle$, separated at PBS1 into trigger and signal modes. The trigger mode is coupled to a spatially multiplexed detector (SMD) to enable heralding of multi-photon Fock states. (c) Balanced homodyne detection and source characterization. For full description see main text.

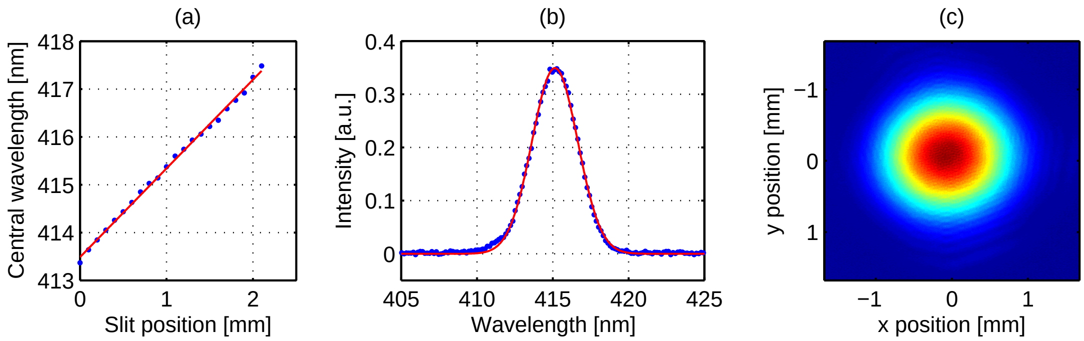

Figure 4.4: Characterization of the PDC pump mode obtained through second harmonic generation. (a) Spatial chirp of 1.85 nm mm^{-1} measured after the spatial filter. The magnitude and orientation of the spatial chirp with respect to the crystal optical axis can impact the modal purity of the heralded state for this KDP source, see [162, 177]. (b) Spectrum of the pump beam and Gaussian fit with full-width half-maximum bandwidth of 3.6 nm. (c) Spatial mode of pump beam measured after spatial filter. Birefringent walk-off in BBO produces an elliptical second-harmonic spatial mode, which is filtered by the pinhole, resulting in the symmetrical pump mode depicted.

barium borate (BBO) crystal, figure 4.3(a), with a conversion efficiency of approximately 30%. The residual fundamental is filtered out with a dichroic mirror (DM1) and Schott glass filter (BGF). The resulting second harmonic is spatially filtered with a 50 μm pinhole (PH). The spatial chirp, spectrum and spatial mode of the resulting second harmonic field after the spatial filter were measured, figure 4.4. The spatial chirp is one of the critical factors in ensuring the cooperativity parameter $K \approxeq 1$ [177]. Up to 500 mW of filtered second harmonic power is typically available to pump the KDP crystal.

The second harmonic pump beam is focussed into an 8 mm thick KDP crystal cut for Type-II collinear frequency-degenerate parametric down-conversion for a pump wavelength of 415 nm, figure 4.3(b) [162]. After the KDP crystal, the blue pump beam is filtered out using a dichroic mirror (DM2) and a Schott glass filter (RGF). The generated TMSV state is separated at a polarizing beam splitter (PBS1) into signal and trigger modes. The trigger mode is horizontally polarized whilst the signal mode is vertically polarized. The trigger mode is coupled into a single-mode fiber (SMF1), which constitutes spatial filtering of the down-converted light. SMF1 is coupled to a spatially multiplexed detector (SMD) comprising a fiber beam-splitter network (FBS) and three avalanche photodiodes (APDs).

The signal mode is combined with the LO used for performing balanced homodyne detection on a polarizing beam splitter (PBS2). A half-wave plate (HWP) and polarizing beam splitter (PBS3) form an effective 50:50 beam splitter. A flip-mirror in one output mode of the 50:50 beam splitter enables re-coupling of both the LO and signal modes for alignment purposes, as detailed later.

4.2.2 Difference frequency generation

All the experiments detailed in this thesis were performed largely in free space using bulk optics. When working with the extremely-low light intensities encountered with SPDC, experimental alignment can be challenging – especially when one cannot rely on fiber networks or waveguides to define spatial modes. For this reason, the PDC source was configured such that one of the two modes (trigger [o-ray] or signal [e-ray]) could be seeded with a bright coherent state from the Ti:Sapphire oscillator. When overlapped with the 415 nm pump beam inside the KDP crystal, a non-linear interaction occurs between the pump and the seed beam in a process known as optical parametric amplification or difference frequency generation (DFG) [178, 179].

DFG serves as a valuable alignment tool because the output generated in the process has a spatial-temporal mode very similar to that of the mode produced when the source is operated in the spontaneous regime [111, 180, 50, 181]. This enables much of the experimental alignment, such as optimizing the mode overlap of the LO with the heralded Fock states, to be performed using a bright beam in place of a few-photon intensity beam. Thus spectral-temporal overlap, spatial overlap and polarization overlap between the signal mode and the LO mode can be verified with standard laboratory instruments

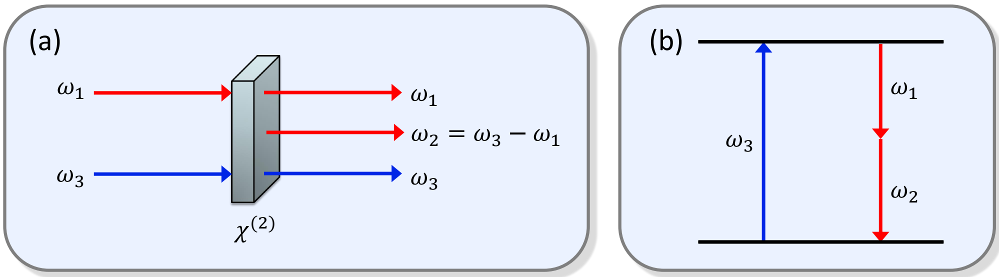

Figure 4.5: Difference frequency generation: (a) Two fields at frequencies ω_1 and ω_3 (where $\omega_3 > \omega_1$) are incident on a medium with a $\chi^{(2)}$ non-linearity. A new field at frequency $\omega_2 = \omega_3 - \omega_1$ is generated. (b) Energy level diagram of the process.

such as power meters and conventional spectrometers. Final optimization of the source alignment is performed with the seed beam blocked, i.e. SPDC generating a TMSV state. In practice the generated DFG emission is not identical to that in the spontaneous regime due to gain-induced diffraction in both the spectral and spatial degrees of freedom [182]. Furthermore, the DFG emission is necessarily coherent and thus modal impurity is not exhibited by the DFG emission. However, since the gain of the process is low in the regime explored by the experiment it is expected that spectral bandwidth narrowing is unlikely to be significant.

As with PDC, the DFG process should satisfy energy and momentum conservation such that $\omega_3 = \omega_1 + \omega_2$ and $\mathbf{k}_3 = \mathbf{k}_1 + \mathbf{k}_2$ [178, 179], as shown in figure 4.5. In this simplified treatment all fields will be treated as scalar quantities and will be modelled as monochromatic plane waves propagating in the z direction. The total electric field inside the crystal is

$$\begin{aligned} E &= E_1 + E_2 + E_3, \\ &= \mathcal{E}_1 e^{-i\omega_1 t} + \mathcal{E}_2 e^{-i\omega_2 t} + \mathcal{E}_2 e^{-i\omega_2 t} + \text{c.c.}, \end{aligned} \tag{4.32}$$

where in the second line the 'fast' time dependence* of the fields has been separated and $\mathcal{E}_j = A_j e^{ik_j z}$ is the spatially dependent part of the electric field with A_j denoting the slowly varying envelope. The electric field in equation 4.32 gives rise to an induced polarization P due to the $\chi^{(2)}$ non-linearity of the medium [179], where

$$\begin{aligned} P =& \chi^{(2)} E^2, \\ =& \chi^{(2)} \left(\mathcal{E}_1^2 e^{-2i\omega_1 t} + \mathcal{E}_2^2 e^{-2i\omega_2 t} \mathcal{E}_3^2 e^{-2i\omega_3 t} + \text{c.c.} \right) \\ &+ 2\chi^{(2)} \left(\mathcal{E}_1 \mathcal{E}_2 e^{-i(\omega_1+\omega_2)t} + \mathcal{E}_3 \mathcal{E}_1^* e^{-i(\omega_3-\omega_1)t} + \mathcal{E}_3 \mathcal{E}_2^* e^{-i(\omega_3-\omega_2)t} + \text{c.c.} \right) \\ &+ 2\chi^{(2)} \left(\mathcal{E}_1 \mathcal{E}_2^* e^{-i(\omega_1-\omega_2)t} + \mathcal{E}_3 \mathcal{E}_1 e^{-i(\omega_1+\omega_3)t} + \mathcal{E}_3 \mathcal{E}_2 e^{-i(\omega_3+\omega_2)t} + \text{c.c.} \right) \\ &+ 2\chi^{(2)} \left(|\mathcal{E}_1|^2 + |\mathcal{E}_2|^2 + |\mathcal{E}_3|^2 \right). \end{aligned} \tag{4.33}$$

Evolution equations for the electric field components oscillating at frequencies ω_j ($j = 1, 2, 3$) can be derived from Maxwell's equations† with the non-linear polarization as a source term [179, 13]

$$\frac{\partial^2 E_j}{\partial z^2} - \frac{n_j^2}{c^2} \frac{\partial^2 E_j}{\partial t^2} = \frac{1}{\epsilon_0 c^2} \frac{\partial^2}{\partial t^2} P(\omega_j), \tag{4.34}$$

where $P(\omega_1) = 2\chi^{(2)}(\mathcal{E}_2^* \mathcal{E}_3^* e^{-i\omega_1 t} + \text{c.c.})$, $P(\omega_2) = 2\chi^{(2)}(\mathcal{E}_1^* \mathcal{E}_3^* e^{-i\omega_2 t} + \text{c.c.})$ and $P(\omega_3) = 2\chi^{(2)}(\mathcal{E}_1 \mathcal{E}_2^* e^{-i\omega_3 t} + \text{c.c.})$ are the sources of electromagnetic field oscillating at frequencies ω_1, ω_2 and ω_3 respectively‡ [179]. These source terms lead to three coupled equations describing the evolution of the three electric field contributions. Using the slowly varying

*The slowly varying envelope A_j also has a time-dependence, but the frequency is far smaller than the optical frequency ω_j [178, 179].

†Equation 4.34 is the scalar version of the non-linear Maxwell equation $\nabla^2 \mathbf{E} - \frac{n^2}{c^2} \frac{\partial^2 \mathbf{E}}{\partial t^2} = \frac{1}{\epsilon_0 c^2} \frac{\partial^2 \mathbf{P}_{\text{NL}}}{\partial t^2}$, where P_{NL} is the non-linear polarization due to the $\chi^{(2)}$ non-linearity.

‡Polarization terms oscillating at higher frequencies are ignored, as are the terms such as $\chi^{(2)} \mathcal{E}_j^2 e^{-2i\omega_j t}$ since these are assumed not to be phase-matched. The zero-frequency terms clearly do not contribute.

envelope approximation* leads to the three equations†

$$\frac{dA_1}{dz} = \frac{i\omega_1\chi^{(2)}}{\epsilon_0 c n_1} A_2^* A_3 e^{iz\Delta k}, \tag{4.35}$$

$$\frac{dA_2}{dz} = \frac{i\omega_2\chi^{(2)}}{\epsilon_0 c n_2} A_1^* A_3 e^{iz\Delta k}, \tag{4.36}$$

$$\frac{dA_3}{dz} = \frac{i\omega_3\chi^{(2)}}{\epsilon_0 c n_3} A_1 A_2 e^{-iz\Delta k}, \tag{4.37}$$

where $\Delta k = k_3 - k_2 - k_1$ is the phase mismatch and n_j is the refractive index at frequency ω_j. For the experimental DFG employed here, both input fields E_1 and E_3 to the non-linear medium are intense and thus depletion of either field is assumed to be negligible‡ such that the slowly varying amplitudes A_1 and A_3 do not decay

$$\frac{dA_1}{dz} = 0, \qquad \frac{dA_2}{dz} = 0. \tag{4.38}$$

Thus only equation 4.36, describing the DFG emission at fequency ω_2 remains. This can be integrated to give the intensity of the DFG emission at the output of the crystal

$$|A_2(L)|^2 = \left(\frac{L\omega_2\chi^{(2)}}{\epsilon_0 c n_2}\right)^2 |A_3|^2 |A_1|^2 \mathrm{sinc}^2\left(\frac{L\Delta k}{2}\right), \tag{4.39}$$

where L is the crystal length. Equation 4.39 shows that the generated DFG intensity at frequency ω_2 is proportional to the product of the pump intensity $|A_3|^2$ at frequency ω_3 and the seed intensity $|A_1|^2$ at frequency ω_1.

*The slowly varying envelope approximation assumes the wavelength of the light is much smaller than the length scale over which the electric field amplitude A_j varies. This means that $\left|k_j \frac{\partial A_j}{\partial z}\right| >> \left|\frac{\partial^2 A_j}{\partial z^2}\right|$ and therefore the terms proportional to $\frac{\partial^2 A_j}{\partial z^2}$ are dropped [179, 13]. Furthermore in deriving equations 4.35–4.37 the slowly-varying amplitudes A_j are assumed to be time-independent – the so-called free running approximation [179].

†The complex conjugate components can be cancelled on both sides of equation 4.34 [178].

‡The overall efficiency of the DFG process is sufficiently low that this approximation is valid. This is partly due to the relatively small value of $\chi^{(2)}$ for KDP.

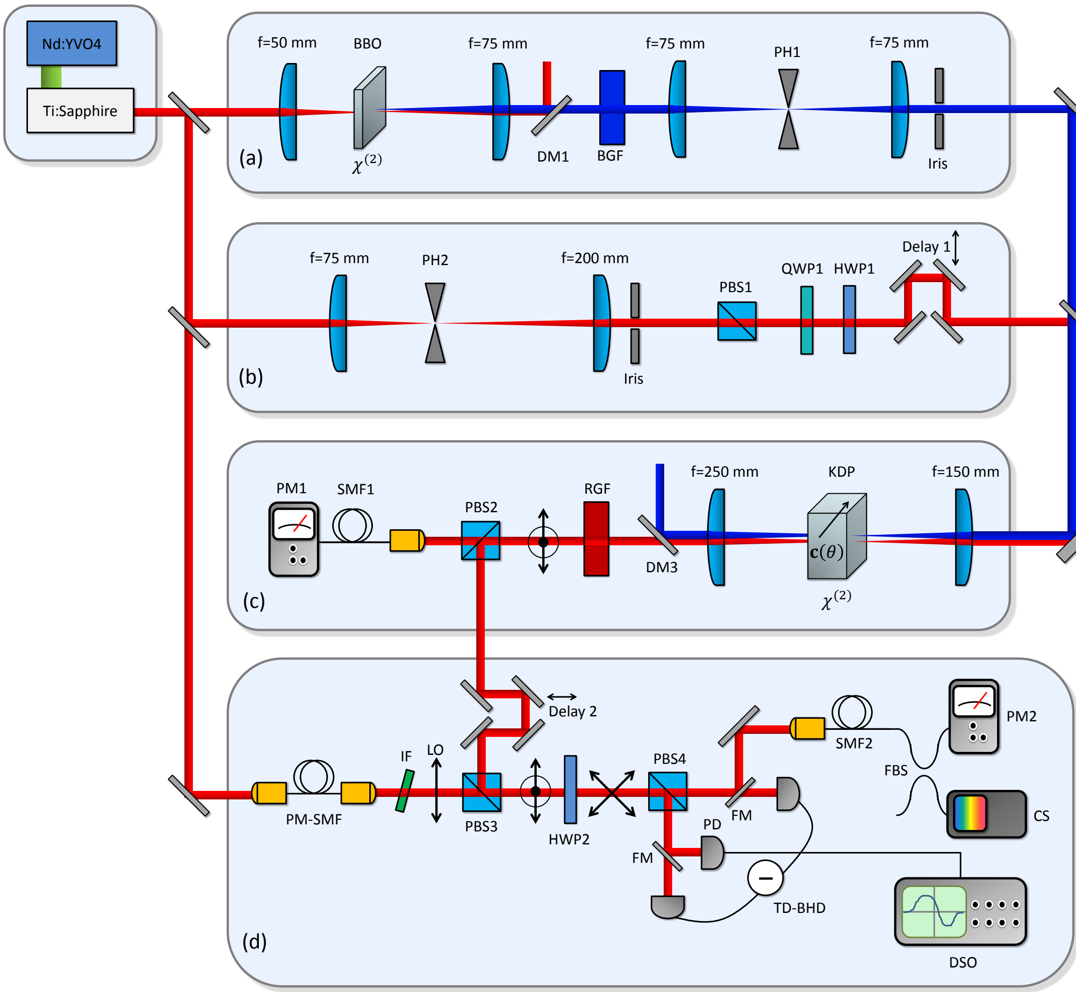

Figure 4.6: Experimental arrangement for performing DFG in KDP (for full details see main text). (a) second harmonic generation. (b) Preparation of seed beam. (c) Seed beam (o-ray) and pump (o-ray) focussed into KDP resutling in DFG. Generated e-ray reflected from PBS2, o-ray coupled into SMF1. (d) LO and e-ray spatial-temporal overlap verification.

The experimental arrangement used for performing DFG is shown in figure 4.6. SHG produces the 415 nm pump beam as before figure 4.6(a). In addition, a portion of the fundamental Ti:Sapphire output is picked off before SHG to act as the seed beam, figure 4.6(b). The seed beam is spatially filtered with a pinhole (PH2) and horizontally polarized by PBS1. A delay line (Delay 1) is used to ensure the seed pulses are temporally overlapped with the pump pulses inside the KDP crystal. The seed and pump beams are combined using a dichroic mirror (DM2) and focussed into the KDP crystal to perform DFG, figure 4.6(c). The seed beam propagates as an o-ray. This generates the e-ray mode which is the signal mode of the down-converter. Precise setting of the seed beam polarization is critical to ensure minimal leakage of the seed beam into the e-ray mode, which could obscure the e-ray emission or lead to interference between the stimulated e-ray and the residual seed beam leaking into this mode.

From equation 4.39 it is expected that for a given pump and seed beam focussing geometry and spatial-temporal overlap, the average generated e-ray optical power $P_{\text{e-ray}}$ is given by

$$P_{\text{e-ray}} \propto P_{\text{pump}} \times P_{\text{seed}}, \tag{4.40}$$

where P_{pump} is the average pump optical power at 415 nm and P_{seed} is the average seed (o-ray) optical power at 830 nm. The generated e-ray optical power was measured for a range of seed and pump optical powers, shown in figure 4.7(a). A fit was performed according to the expected dependence on the seed and pump optical power given by equation 4.40, shown as the surface in figure 4.7(a). The measured data are in excellent agreement with the expected DFG behaviour.

Figure 4.7(b) shows the generated e-ray power as a function of the relative delay

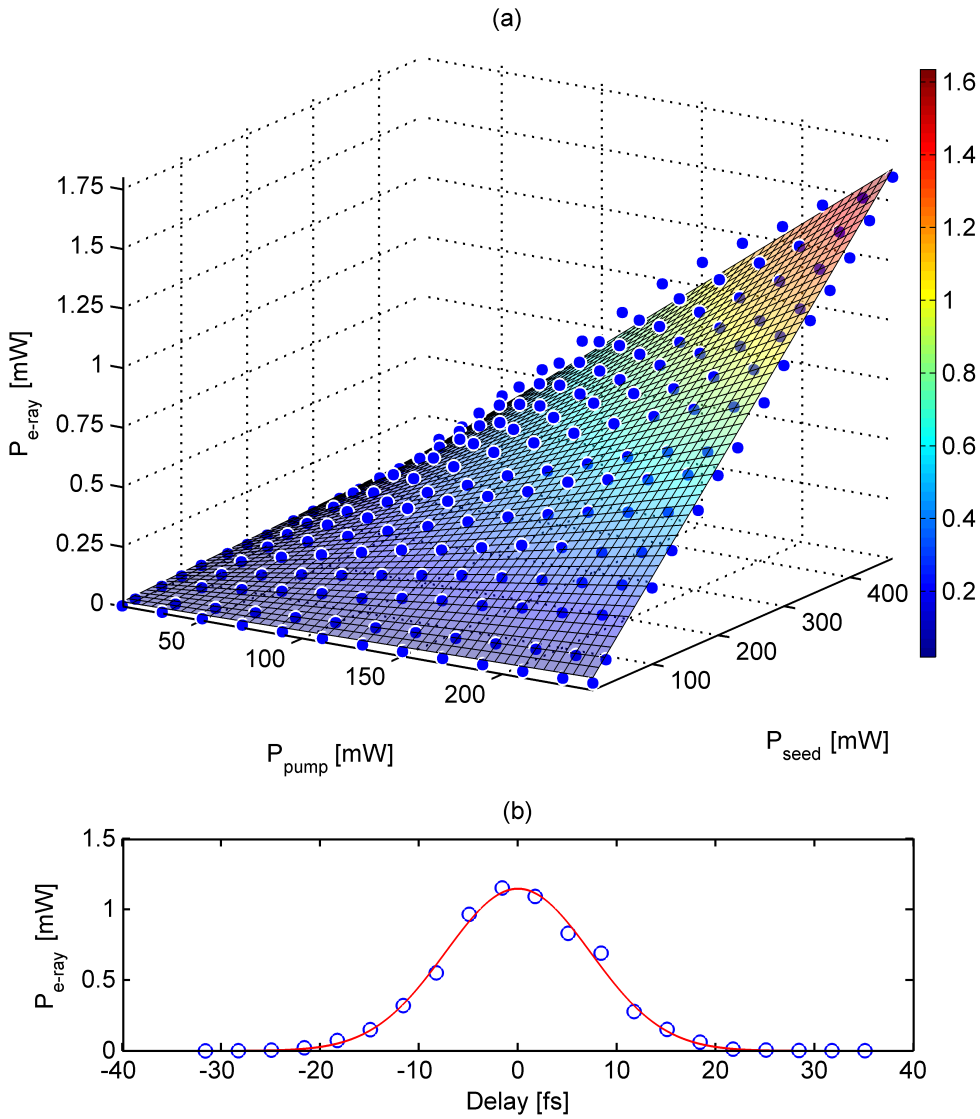

Figure 4.7: (a) Generated e-ray optical power $P_{\text{e-ray}}$ as a function of the pump optical power P_{pump} and seed optical power P_{seed}. The model of DFG predicts that $P_{\text{e-ray}} \propto P_{\text{pump}} \times P_{\text{seed}}$ (equation 4.40). The fitted model is shown as the surface, whilst the measured data are the blue points. Excellent correspondence between the model and data is evident. (b) Dependence of $P_{\text{e-ray}}$ on the relative time delay between the seed and pump pulses in the KDP crystal.

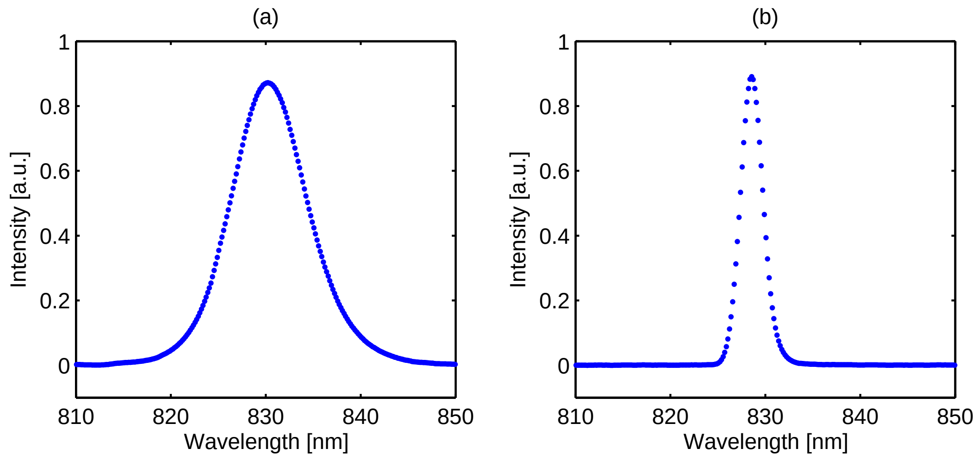

Figure 4.8: Spectra of the o-ray seed beam (a) and the e-ray DFG emission (b). The o-ray FWHM bandwidth is 11.3 nm and the e-ray FWHM bandwidth is 2.8 nm.

between the arrival of pump and seed beam pulses in the KDP crystal. This demonstrates how critical the temporal alignment between seed and pump pulse is to establish DFG with broadband optical pulses. The spectra of the seed and pump modes were measured using a compact spectrometer (CS), figure 4.8. The seed beam (o-ray) spectrum is the spectrum of the Ti:Sapphire oscillator output and has a full-width half-maximum (FWHM) bandwidth of 11.3 nm. The spectrum of the e-ray is significantly more narrowband than the seed beam, FWHM=2.8 nm, as expected for this KDP source [169, 162]. This demonstrates how the properties of the DFG emission closely match the mode-structure of the PDC source when operated in the spontaneous regime. The e-ray was measured after coupling into SMF2, figure 4.6). The source alignment procedure using the DFG emission is detailed in appendix A.

4.3 Homodyne tomography of multi-photon Fock states

Yurke *et al.* first considered homodyne detection of Fock states by gating the BHD based on photo-detection events made on a number-correlated state obtained through PDC [183]. The first optical homodyne tomography (OHT) of a Fock state was demonstrated in 2001 by Lvovsky *et al.*, who performed reconstruction of the single-photon Fock state exhibiting a negative Wigner function [159]. This was made possible by the development of a BHD, compatible with the pulsed optical modes employed in the experiment [96]. This first demonstration was followed by several others [184–186], where increased BHD bandwidth enabled characterization of a single-photon state in near real-time [186]. Ourjoumtsev *et al.* performed the first OHT of the two-photon state [143] in 2006. Furthermore, coherent superpositions of $|0\rangle$ and $|1\rangle$ photons [155], and $|0\rangle$, $|1\rangle$ and $|2\rangle$ photon states [152] have been prepared in the laboratory and characterized by means of OHT – which naturally allows not only the photon-number statistics to be assessed but also the coherences between Fock layers. Contemporaneously with our publication of the first OHT of the three-photon Fock state [160] in 2013, Yukawa *et al.* also demonstrated a similar result in the continuous-wave domain [144]. Furthermore, the latter demonstration extended the scheme of [152] to generate arbitrary superpositions of up to three photons [144].

Recent theoretical analyses [187, 188] and experiments [189, 144, 190] have demonstrated OHT of narrowband Fock states. Efficient detection requires correct filtering of the homodyne photocurrent to select the particular temporal mode corresponding to that generated by the source [189, 191]. One potential disadvantage of such continuous-wave Fock states is that the states are created at random time intervals, whereas for pulsed-pump sources an effective clock is defined by the pump pulse train. This allows multiple sources to be concatenated without the need for a memory or variable delay to synchronise the wave packets [192, 193]. On the other hand, a potential advantage of employing a continuous-wave pumped optical parametric oscillator (OPO) [191, 144] as opposed to a single-pass pulsed optical parametric amplifier (OPA) is that a secondary mode-cleaning cavity can be employed to filter the LO used for homodyne detection [190, 28, 194]. This enables the LO spatial mode to be easily well-matched to that of the generated Fock states or squeezed state.

There are numerous motivations for examining heralded Fock states by OHT as opposed to direct photon counting using using multiplexed detectors [81] or superconducting transition-edge sensors (TES) [79]. BHDs can exhibit a quantum efficiency in excess of 90% and have sufficient electronic bandwidth to operate at a repetition rate of 80 MHz or above. This is in stark contrast to TESs and multiplexed detectors which are limited to kHz [79] and a few-MHz [81] repetition rates respectively. The ability to perform detection with a high repetition rate is desirable since it enables acquisition of sufficient data to characterize the state within shorter period of time – avoiding long-term experimental drifts.

Additionally, the mode-selective nature of balanced homodyne detection ensures that only a single spatial-temporal mode of the generated Fock states is examined. This may at first appear to be disadvantageous since, as shown in section 3.2.2, the single-mode filtering of the LO contributes an effective inefficiency, equation 3.27. However, Fock states are often generated for the purpose of interfering them with auxiliary states (e.g. coherent, squeezed or other Fock states) in order to engineer specific quantum states by conditional detection [150, 152, 159, 153, 157, 144, 151, 158]. Proposals for linear optical quantum computing based on single-photon sources and detection [34, 195] rely on efficient single-photon sources generating states with minimal admixture of vacuum. The minimum value of the product of the single-photon source efficiency with the detector efficiency ranges between 1/2 [196] and 2/3 [197] depending on the particular implementation. Such applications require Fock states which are well mode-matched with the auxiliary states. Hong-Ou-Mandel interference [16] provides one possibility for assessing the degree of mode-overlap between, for example, a single-photon Fock state and a weak coherent state [198]. However, it cannot easily be generalized to scenarios involving higher-order Fock states.

In contrast balanced homodyne detection, through determination of the effective mode-matching efficiency, enables the degree of spatial-temporal overlap of optical modes to be directly probed. Furthermore, state preparation schemes relying on conditional homodyne measurements benefit from reduced noise due to this mode-selective property [199–202].

4.3.1 Mode matching of LO and heralded Fock states

The net detection efficiency $\eta_{\rm net}$ when performing balanced homodyne detection of heralded Fock states is given by

$$\eta_{\rm net} = \eta_{\rm bhd}\eta_{\rm dc}\eta_{\rm mm}, \tag{4.41}$$

where $\eta_{\rm bhd}$ is the efficiency of the BHD, $\eta_{\rm dc}$ is the fraction of heralding events which are actually false (i.e. dark counts) and $\eta_{\rm mm}$ is related to the spatial-temporal overlap of the LO and Fock state modes.

In chapter 3 it was shown how balanced homodyne detection selects a particular field mode, with the mode-matching efficiency defined in equation 3.27. It was assumed that the signal was excited in some particular pure wave-packet mode. Under these circumstances it is always possible to achieve perfect mode overlap with the coherent LO by pulse shaping. When performing OHT, the purity of the heralded states must be taken into account in the mode matching calculation. This will be shown to set an upper bound on the degree of mode matching which can be achieved. Equation 3.27 can be expressed in Dirac notation [110] such that

$$\begin{aligned}\eta_{\rm mm} &= \left| \int_t^{t+\tau} cdt' \int_S d^2x \mathbf{v}^*_{L,\lambda}(\mathbf{x},0,t') \cdot \mathbf{w}_{S,\lambda'}(\mathbf{x},0,t') \right|^2, \\ &= |\langle \mathcal{E}_{\rm L} | \mathcal{E}_{\rm S} \rangle|^2 = \langle \mathcal{E}_{\rm L} | \hat{\rho}_{\rm S} | \mathcal{E}_{\rm L} \rangle, \end{aligned} \tag{4.42}$$

where $|\mathcal{E}_{\mathrm{L}}\rangle$ and $|\mathcal{E}_{\mathrm{S}}\rangle$ are the wave packet modes of the LO and signal respectively and $\hat{\rho}_{\mathrm{S}}$ is the density matrix of the signal. Now suppose that the LO is excited in a single wave packet mode whereas the signal $\hat{\rho}_{\mathrm{S}}$ is excited in an incoherent mixture of different wave packet modes. This differs from the treatment of [110] where only pure states were considered for both signal and LO. Expressing $|\mathcal{E}_{\mathrm{L}}\rangle$ and $\hat{\rho}_{\mathrm{S}}$ in some fixed, orthonormal basis* $\{|\psi_i\rangle\}$ gives

$$|\mathcal{E}_{\mathrm{L}}\rangle = \sum_i a_i|\psi_i\rangle, \tag{4.43}$$

$$\hat{\rho}_{\mathrm{S}} = \sum_n p_n|\psi_n\rangle\langle\psi_n|, \tag{4.44}$$

where the expansion coefficients must satisfy $\sum_i |a_i|^2 = 1$ and $\sum_n p_n = 1$. The mode overlap can now be evaluated according to equation 4.42

$$\begin{aligned}\eta_{\mathrm{mm}} &= \sum_i \langle\psi_i|a_i^* \left(\sum_n p_n|\psi_n\rangle\langle\psi_n|\right)\sum_j a_j|\psi_j\rangle,\\ &= \sum_n a_n^* p_n a_n = \sum_n |a_n|^2 p_n. \end{aligned}\tag{4.45}$$

By inspection of equation 4.45 it is clear that if the signal is excited in only one mode m such that

$$p_n = \begin{cases} 1 & : n = m \\ 0 & : n \neq m \end{cases}$$

it is possible to achieve perfect mode matching, $\eta_{\mathrm{mm}} = 1$, by shaping the LO such that $|\mathcal{E}_{\mathrm{L}}\rangle = |\psi_m\rangle$. In order to derive a bound for the best-possible mode matching for the case

*A natural choice of basis states are the Schmidt modes introduced in section 4.1.1.

where the signal is mixed, both sides of equation 4.45 are squared such that

$$\eta_{\mathrm{mm}}^2 = \left(\sum_n |a_n|^2 p_n\right)^2 \leq \left(\sum_n |a_n|^4\right)\left(\sum_n p_n^2\right), \tag{4.46}$$

where the Cauchy-Schwartz inequality has been used. The upper bound, i.e. optimum mode matching, is attained when $|a_n|^2 \propto p_n$. Because of normalization this means that*

$$|a_n|^2 = p_n, \quad \forall\ n. \tag{4.47}$$

For this choice of LO expansion coefficients, the optimum mode matching is thus

$$\boxed{\eta_{\mathrm{mm,max}} = \sum_n p_n^2 = P = \frac{1}{K},} \tag{4.48}$$

where P is the purity of the signal state, equation 4.27, and K is the co-operativity parameter defined in equation 4.28. Thus the best possible efficiency with which a Fock state of purity P can be detected with balanced homodyne detection is $\eta_{\mathrm{mm,max}} = P$.† In practice it is difficult to achieve the condition of equation 4.47 due to limited capability to arbitrarily shape the LO spatial-temporal mode $|\mathcal{E}_{\mathrm{L}}\rangle$. This can be accounted for by introducing a parameter η_{exp} [111, 184, 159] such that

$$\eta_{\mathrm{mm}} = \eta_{\mathrm{exp}} P, \tag{4.49}$$

where η_{exp}, which accounts for non-perfect overlap of the signal and LO marginal distributions, comprises three contributions due to spatial, spectral and polarization matching

*This corresponds to shaping the LO such that the intensity marginal distribution matches that of the signal.

†This differs from the analysis presented in [110] where the best possible efficiency is calculated to be $\sqrt{P}$.

such that*

$$\eta_{\mathrm{exp}} = \eta_{\mathrm{spatial}}\eta_{\mathrm{spectral}}\eta_{\mathrm{pol}}. \tag{4.50}$$

The polarization matching between the LO and Fock states is optimized using the generated e-ray in DFG . Furthermore, the LO polarization is well-defined at the PBS where the LO and heralded Fock state are combined (PBS2, figure 4.3(c)), thus ensuring near-perfect polarization matching of the two modes.

The spatial overlap is determined by performing coincidence counting between the trigger and signal modes collected by SMFs, figure 4.3. As before, SMF2 effectively defines the LO spatial mode. The modes are detected with APDs and coincidence counting is performed using a coincidence counting programme embedded in a field-programmable gate array (FPGA). Since no spectral filtering is employed and the APDs exhibit a uniform detection efficiency for the bandwidth of the modes detected, the spatial overlap between the LO and Fock state modes is estimated as

$$\eta_{\mathrm{spatial}} = \frac{R_C}{\eta_{\mathrm{apd}} R_t}, \tag{4.51}$$

where R_C is the raw coincidence rate registered by the FPGA, R_t is the raw singles rate in the trigger APD and η_{apd} is the efficiency of the APD. A spatial overlap of $\eta_{\mathrm{spatial}} = 0.68$ was commonly achieved after correcting for $\eta_{\mathrm{apd}} = 0.45$.†

The spectral overlap η_{spectral} is determined by measuring the spectrum of the LO and the marginal spectrum of the signal mode of the down-converter, both coupled into SMF2 (figure 4.3(c)), using an Andor Shamrock 303 spectrograph together with an Andor iDus

*Assuming there is no space-time-polarization coupling such that the separate contributions can be factored out in this manner.

†Value quoted in specifications sheet for Perkin-Elmer SPCM-AQ4C.

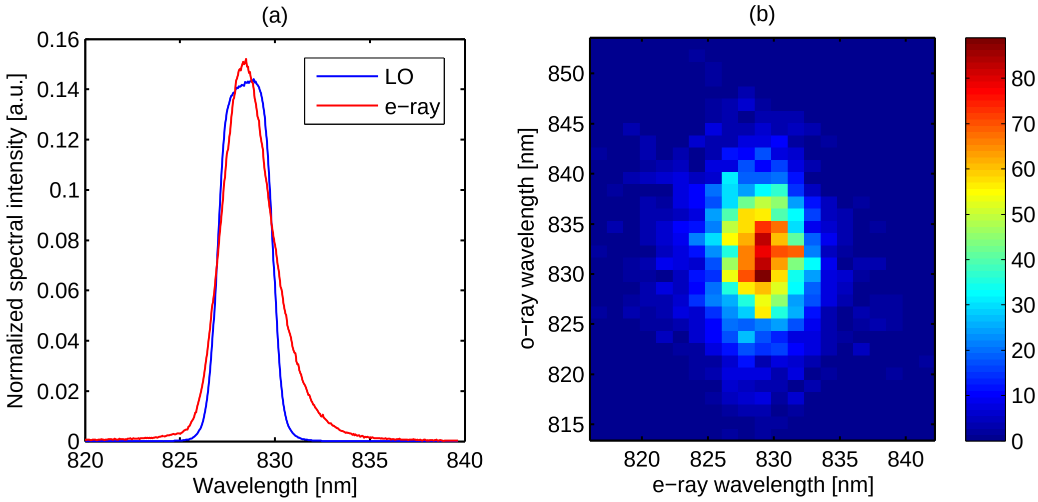

Figure 4.9: (a) LO spectrum (blue line) and e-ray marginal spectrum (red line) for both modes coupled into SMF2, figure 4.3. (b) JSI measurement for collected o- and e-ray modes. Colour scale represents the number of coincidence events recorded in each spectral bin.

401 series charge-coupled device (CCD) camera. The spectra, shown in figure 4.9(a), exhibit an overlap of $\eta_{\text{spectral}} = 0.97$, assuming a constant spectral phase. Thus the combined value of η_{exp} is estimated to be typically $\eta_{\text{exp}} = 0.97 \times 0.68 = 0.66$.*

4.3.2 Fock state purity

Having estimated η_{exp}, in order to complete the estimate for η_{mm} (equation 4.49) the purity P of the heralded Fock states should be estimated. Assuming there are no correlations between the spatial, spectral and polarization degrees of freedom, the purity is a product of the spatial, spectral and polarization purity such that

$$P = P_{\text{spatial}} P_{\text{spectral}} P_{\text{pol}}. \tag{4.52}$$

*An alternative technique to estimate η_{exp} is to use the DFG emission. The interference visibility $\mathcal{V}$ between the LO and DFG emission can be measured and η_{exp} estimated according to equation 3.27 [111, 159, 184, 186]. However, phenomena such as gain-induced diffraction [182] mean that the DFG emission will not perfectly match the mode produced in the spontaneous regime. In spite of this, typical interference visibilities of $\mathcal{V} \approxeq 0.80$ were observed, which is consistent with $\eta_{\text{exp}} = 0.66$, i.e. $\mathcal{V}^2 = \eta \approxeq 0.64$.

Since the polarization is well-defined by the pump beam it is expected that $P_{\text{pol}} = 1$. Furthermore, the trigger mode is filtered using a single-mode fiber prior to detection. This should ensure that $P_{\text{spatial}} \approxeq 1$ [177].

To estimate P_{temporal} a joint spectral intensity (JSI) measurement was performed [203]. The JSI is given by $|f(\omega_o, \omega_e)|^2$, where $f(\omega_o, \omega_e)$ is the JSA* defined in equation 4.11. The JSI does not give access to the spectral phase of the down-converted state. Since phase correlations could in principle be present in the JSA, the JSI measurement only gives an upper-bound to P_{temporal} [162].

To perform the JSI measurement, the trigger and signal modes were first coupled into SMF1 and SMF2 respectively, figure 4.3). The coupled spatial mode for the trigger is the same mode coupled to the SMD for heralding Fock states, whilst the mode coupled to SMF2 is the mode overlapped with the LO used for homodyne detection. The fibers were sent to two separate monochromators [203]. This arrangement enables a spectrally-resolved coincidence measurement of the trigger and signal modes to be performed, i.e. a JSI measurement. The monochromators, which each comprised a spectrograph and scanning multi-mode fiber at the output, were calibrated using the oscillator spectrum. The measured JSI is presented in figure 4.9(b).

By inspection it is apparent that the measured JSI exhibits minimal correlations between the trigger and signal modes, as expected due to the group-velocity matching employed in this PDC source [169]. The cooperativity parameter K (equation 4.28) and hence the state purity can be approximated by evaluating the Schmidt decomposition of the JSI [162], assuming negligible correlations in the spectral phase. For the measured data presented in figure 4.9(b) the estimated upper-bound for the spectral purity is

*The modes are now labelled according to o-ray and e-ray, rather than signal and idler as before.

$P_{\text{temporal}} = 0.95 \pm 0.01$.* The uncertainty was calculated by Monte Carlo simulation.†

Thus the estimated contribution to the mode matching efficiency η_{mm} due to the purity of the heralded Fock state is $P = 0.95 \pm 0.01$. When combined with $\eta_{\text{exp}} = 0.66$ the overall estimated mode matching efficiency achievable between LO and Fock state with this source is $\eta_{\text{mm}} = \eta_{\text{exp}} P = 0.63$‡. Finally, combining η_{mm} with the BHD efficiency $\eta_{\text{bhd}} = 0.86$ gives the estimated raw detection efficiency for the Fock states (equation 4.41) of§

$$\boxed{\eta_{\text{net}} = \eta_{\text{bhd}}\eta_{\text{mm}} = 0.54.} \tag{4.53}$$

This efficiency is greater than the threshold of 0.5 required to directly infer negativity of the single-photon state Wigner function [54].

4.3.3 Optimization of LO and Fock state mode overlap

The signal mode of the down-converter is overlapped with the LO on an effective 50:50 beam splitter for performing OHT of the heralded Fock states, figure 4.3(c). The LO is derived from the Ti:Sapphire oscillator and is spatially filtered using a short (15 cm) polarization-maintaining single-mode fiber (PM-SMF) and spectrally filtered using an interference filter (IF) (Semrock LL01-830-12.5). The fiber length is sufficiently short that it introduces negligible dispersion to the LO pulse, which has a bandwidth of approximately 3 nm.

Fine tuning of the mode overlap between the LO and heralded Fock state is performed

*This figure is slightly lower than the measured value of $P_{\text{temporal}} = 0.98$ originally obtained for a similar KDP source [162]. This is partly due to the limited pump bandwidth which was available for this work.

†Since the measured JSI comprises spectral bins in which a finite number of counts are registered, the uncertainty in the number of counts N_i for each bin i is given by $\sqrt{N_i}$, assuming Poissonian statistics.

‡The uncertainty in P is negligable.

§Dark counts have been neglected (i.e. $\eta_{\text{dc}} \approxeq 1$ in equation 4.41) since they typically occur at a rate of 300 s^{-1} whilst the heralding rate is 1.8×10^5 s^{-1} for the single-photon state. For higher order Fock states, the trigger event is two- or three-fold coincidence and thus the dark count rate is further reduced.

by heralding the single-photon Fock state and monitoring the BHD output. The ensemble registered by the BHD, neglecting higher-order photon-number contributions, is of the form

$$\hat{\rho}_1 = (1 - \eta_{\text{net}})|0\rangle\langle 0| + \eta_{\text{net}}|1\rangle\langle 1|, \tag{4.54}$$

where η_{net} is the net detection efficiency defined above and $|0\rangle$ and $|1\rangle$ are the vacuum and single-photon state respectively. An estimate of η_{net} can be extracted directly from the recorded BHD voltage $V_{\text{bhd}}(t)$ without performing a full state reconstruction. The quadrature variance $\text{Var}[X_\theta]$ of state $\hat{\rho}_1$ is given by

$$\begin{aligned} \text{Var}[\hat{X}_\theta] &= \text{Tr}\left(\hat{X}_\theta^2 \hat{\rho}_1\right) - \text{Tr}\left(\hat{X}_\theta \hat{\rho}_1\right)^2, \\ &= \frac{1}{2}(1 - \eta_{\text{net}}) + \frac{3}{2}\eta_{\text{net}}. \end{aligned} \tag{4.55}$$

Thus by monitoring the pulse variance for the heralded single-photon state the efficiency can be extracted directly as

$$\begin{aligned} \eta_{\text{net}} &= \text{Var}[\hat{X}_\theta] - \frac{1}{2}, \\ &= \frac{R-1}{2}, \end{aligned} \tag{4.56}$$

where R is the ratio between the variance for the heralded state $\hat{\rho}_1$ and that of the vacuum state. Expressing η_{net} in terms of the ratio R means that only a comparison with the voltage variance of the vacuum pulses is necessary. Thus a full detector calibration is not necessary.

This scenario is depicted in figure 4.10 which shows voltage traces (a) and the corresponding voltage variance (b) of the BHD output for four neighbouring LO pulses. The

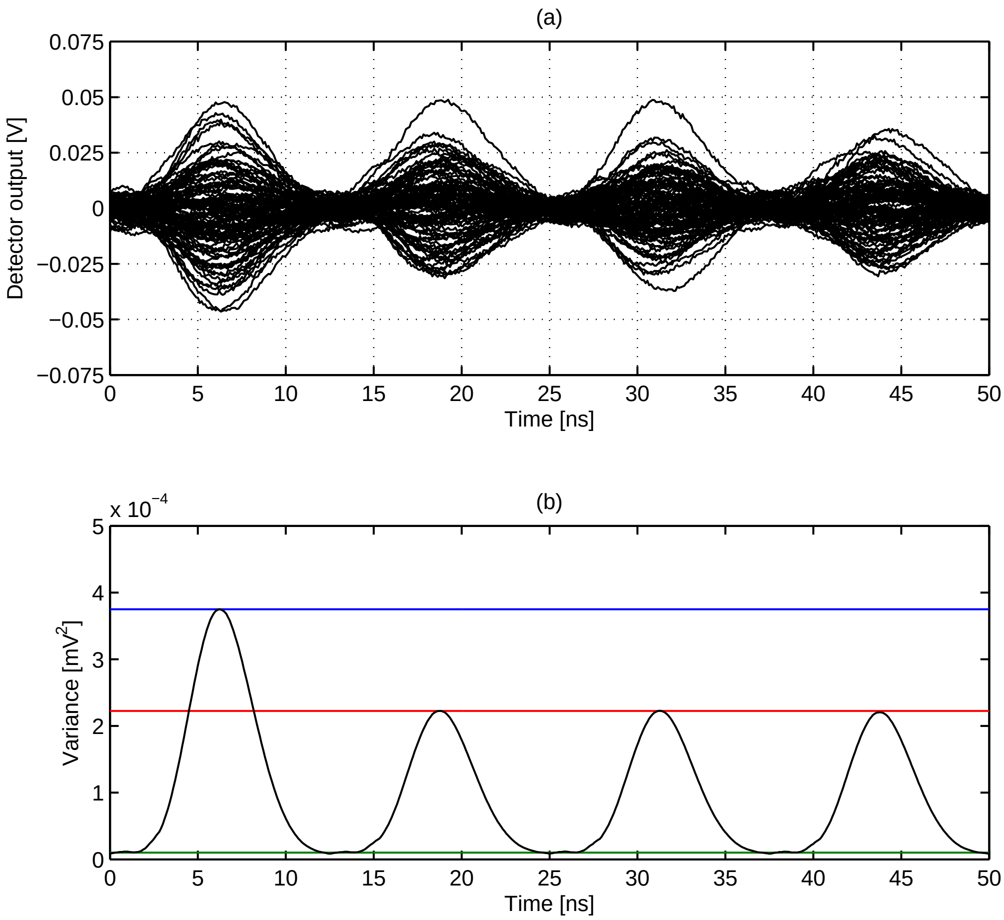

Figure 4.10: (a) Set of voltage traces $V_{\mathrm{bhd}}(t)$ acquired from the BHD for the heralded single-photon state (first pulse) and the vacuum state (subsequent three pulses). (b) Variance calculated from the set of pulses shown in (a) indicating peak voltage variance for the heralded single-photon state (blue line), the vacuum state (red line) and the detector electronic noise (green line).

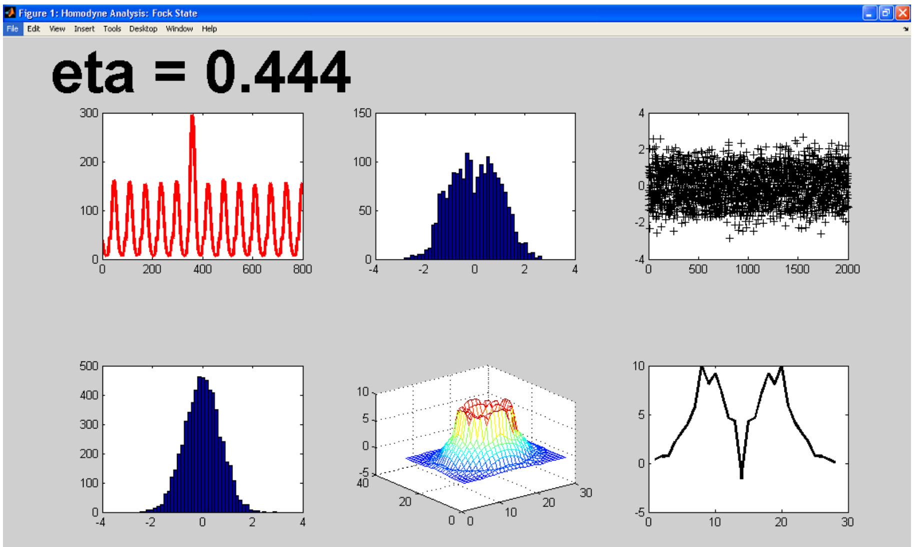

Figure 4.11: Screenshot of MATLAB interface displaying near-realtime characteristics of the heralded single-photon state, used for optimization of the PDC source. From top left to bottom right: reported efficiency η_{bhd} is displayed above the pulse-train variance (the pulse prepared in the single-photon state clearly exhibits a larger variance than the surrounding vacuum state pulses); histogram of single-photon pulse quadrature samples; single-photon pulse quadrature samples (to monitor the presence of any detector drift); histogram of vacuum pulse quadrature samples; Wigner function $W(X, P)$ of single-photon state obtained from fast inverse Radon transform of single-photon state histogram; cross-section of Wigner function in $P = 0$ plane, exhibiting negativity at the origin.

first pulse is prepared in the single-photon state $\hat{\rho}_1$ described by equation 4.54. The subsequent three pulses are prepared in a thermal state which for the PDC source parameters very closely approximates the vacuum state. The peak variance for the single-photon state is represented by the blue line, for the vacuum state by the red line and the detector electronic noise floor is given by the green line (shown for reference). Ratio R defined in equation 4.56 is given by the simple expression

$$R = \frac{V_1}{V_0}, \tag{4.57}$$

where V_1 and V_0 are the peak pulse variances represented by the blue and red lines respectively in figure 4.10(b).

For alignment purposes, the oscilloscope is set to trigger on one-click events from the SMD. A trigger rate of approximately 180,000 s^{-1} was routinely observed. The digitized BHD voltage $V_{\mathrm{bhd}}(t)$ is transmitted to a computer over a TCP/IP connection, where it is processed in MATLAB to extract the variance, as shown in figure 4.10(b), and hence the ratio R and net efficiency η_{net}. An update-rate of approximately 0.5 Hz was achieved when acquiring segments containing 1000 frames each spanning 4 pulses, figure 4.10. This enables the estimate of η_{bhd} to be calculated in near real-time and displayed on a computer screen to aid experimental alignment, figure 4.11. The spatial-temporal overlap between the LO and Fock state can thus be optimized directly by monitoring the reported value η_{net}. This procedure constitutes the fine-alignment of the SPDC source and takes place after the alignment procedure performed with the DFG emission described in section 4.2.2.

4.3.4 Heralding of multi-photon Fock states

One-, two- and three-photon Fock states are heralded in the signal mode by detecting exactly one, two, and three photons respectively in the trigger mode, due to the form of the TMSV state, equation 4.31. Thus in order to herald the various Fock states, a photon-number resolving detector is required.

The trigger mode is coupled into a SMF connected to a spatially multiplexed detector (SMD) comprising two 50:50 polarization non-maintaining fiber beam splitters (FBS) and an array of three APDs (Perkin-Elmer SPCM-AQ4C), figure 4.3(b). An incoming wave packet in the trigger mode is split probabilistically between the three APDs. The Tektronix MSO5104 oscilloscope used to record the BHD voltage is configured to trigger based on detecting one, two, or three clicks simultaneously from the SMD. This is accomplished using the internal pattern state trigger function of the oscilloscope, see appendix B for further details.*

Care must be taken to ensure the TTL pulses produced by the APDs in the SMD are temporally compensated such that they arrive at the oscilloscope with minimal relative delay. The Tektronix MSO5104 used for the experiment does not have internal programmable delays, therefore the compensation must be performed externally. An example of an issue which can arise from incorrect timing of the TTL pulses from the SMD is shown in figure 4.12. Here, the trigger event was for three TTL pulses from the SMD to be positive simultaneously, i.e. to herald a three-photon Fock state. However, incorrect timing of the TTL pulses has lead to the heralding of a two-photon Fock state followed by a single-photon Fock state in the subsequent pulse, as evidenced by the two peaks in the variance, figure 4.12(a). With correct compensation, the same trigger logic leads to heralding the three-photon state, figure 4.12(b). This demonstrates the importance of correctly compensating the delays of the TTL pulses produced by the SMD, as shown in figure 4.13†.

4.3.5 State reconstruction results

From the measured parameters presented in the previous sections the Fock state preparation efficiency is estimated to be $\eta_{\text{net}} = 0.54$. This estimate assumes that $\eta_{\text{dc}} \approxeq 1$, which is justified because the single-photon state is the most sensitive to dark counts and in this case the dark count rate is typically $\approxeq 300\ \text{s}^{-1}$ whilst the heralding rate is $1.8 \times 10^5\ \text{s}^{-1}$‡. Quadrature samples $\{X_\theta\}$ acquired for each Fock state were inverted using the iterative maximum-likelihood algorithm implemented in MATLAB, described in section 3.3. The LO phase was allowed to drift freely during the measurements since the Fock states are

*Hence no FPGA is required for performing the data acquisition.

†The initial attempt at heralding a three-photon Fock state produced the data presented in figure 4.12(a).

‡A coincidence window is defined on the oscilloscope, using the pattern logic trigger functionality.

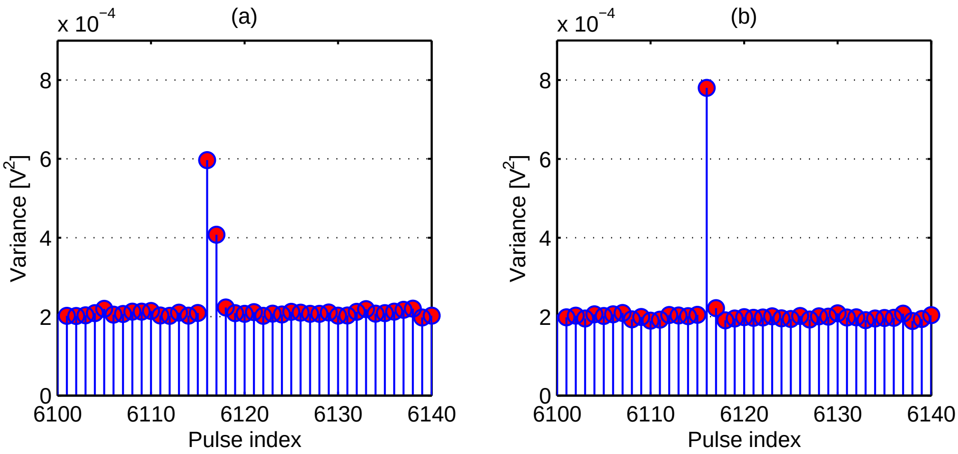

Figure 4.12: Pulse variance of the BHD output. (a) Most pulses are in the vacuum state but two neighbouring pulses are excited in higher-order Fock states, in this case a two-photon state followed by a single-photon state. (b) The same trigger logic on the oscilloscope but with correct temporal compensation of the TTL pulses produced by the SMD enables heralding of a three-photon state, indicated by the larger variance compared with either of the heralded states in (a). All other pulses are in the vacuum state. Both events (a) and (b) have similiar production rates.

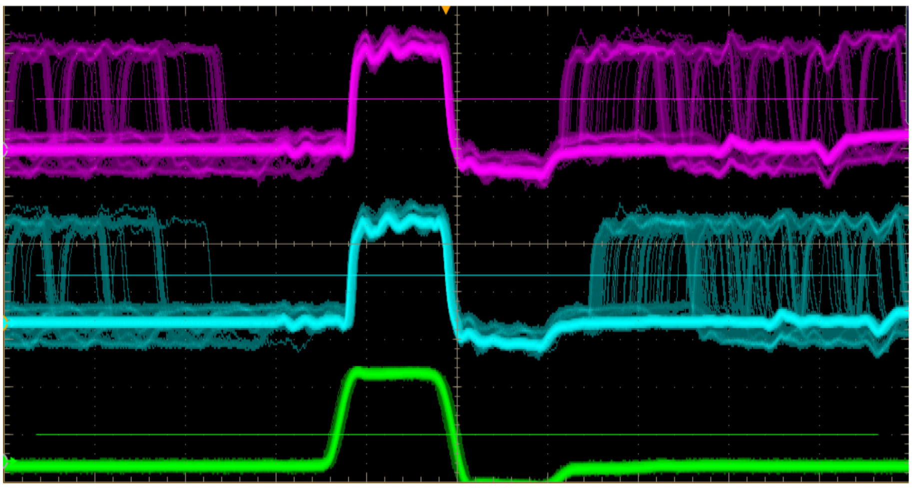

Figure 4.13: Screen capture from Tektronix MSO5104 oscilloscope demonstrating temporal alignment of all 3 TTL pulses generated by the SMD. The horizontal scale is 20 ns/div.

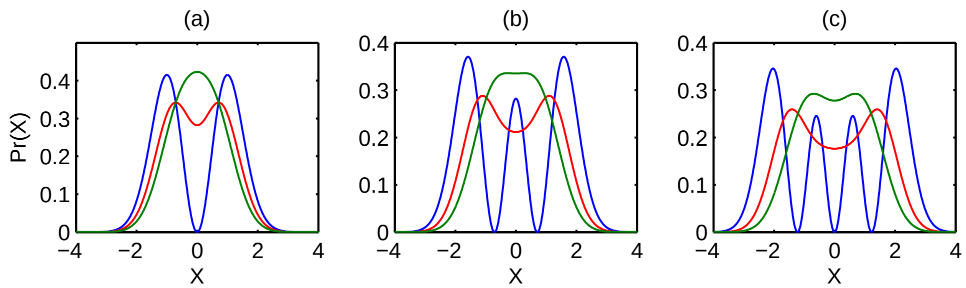

Figure 4.14: Theoretical quadrature probability distributions $\Pr(X)$ for (a) single-photon state; (b) two-photon state; (c) three-photon state. Distributions were calculated for three values of the net detection efficiency: $\eta_{\rm net}$=1.00 (blue); $\eta_{\rm net}$=0.50 (red); $\eta_{\rm net}$=0.25 (green).

assumed to be phase-invariant. Thus the reconstructed density matrices are diagonal in the Fock basis. For each Fock state the reconstruction was performed both with and without correction for the BHD efficiency $\eta_{\rm bhd} = 0.86$. Theoretical quadrature probability distributions $\Pr(X)$ for the three Fock states are shown in figure 4.14 for a range of net detection efficiencies $\eta_{\rm net}$. The oscillatory, non-Gaussian structure is observed to be smoothed out as the detection efficiency is decreased [204]. The net efficiency for these experiments is predicted to be $\eta_{\rm net} = 0.54$, equation 4.41. Thus it is anticipated that the quadrature probability distributions obtained by forming histograms of the experimentally obtained quadrature samples $\{X_\theta\}$ will be similar to the red curves in figure 4.14.

Single-photon state

Results for single-photon state reconstruction are presented in figure 4.15. A total of 8×10^5 quadrature samples were acquired at a trigger rate of 1.8×10^5 s^{-1} and subsequently sorted into 100 bins spanning an interval $X \in [-4 : 4]$, figure 4.15(a). Calibration of the BHD was performed using quadrature samples from surrounding pulses, approximately in the vacuum state, e.g. figure 4.10. The oscilloscope was operated in "fast frame" mode such that batches of 10,000 frames each spanning 8 pulses (i.e. 1 pulse prepared in the single-photon state and 7 surrounding pulses in the vacuum state) were acquired, transferred to

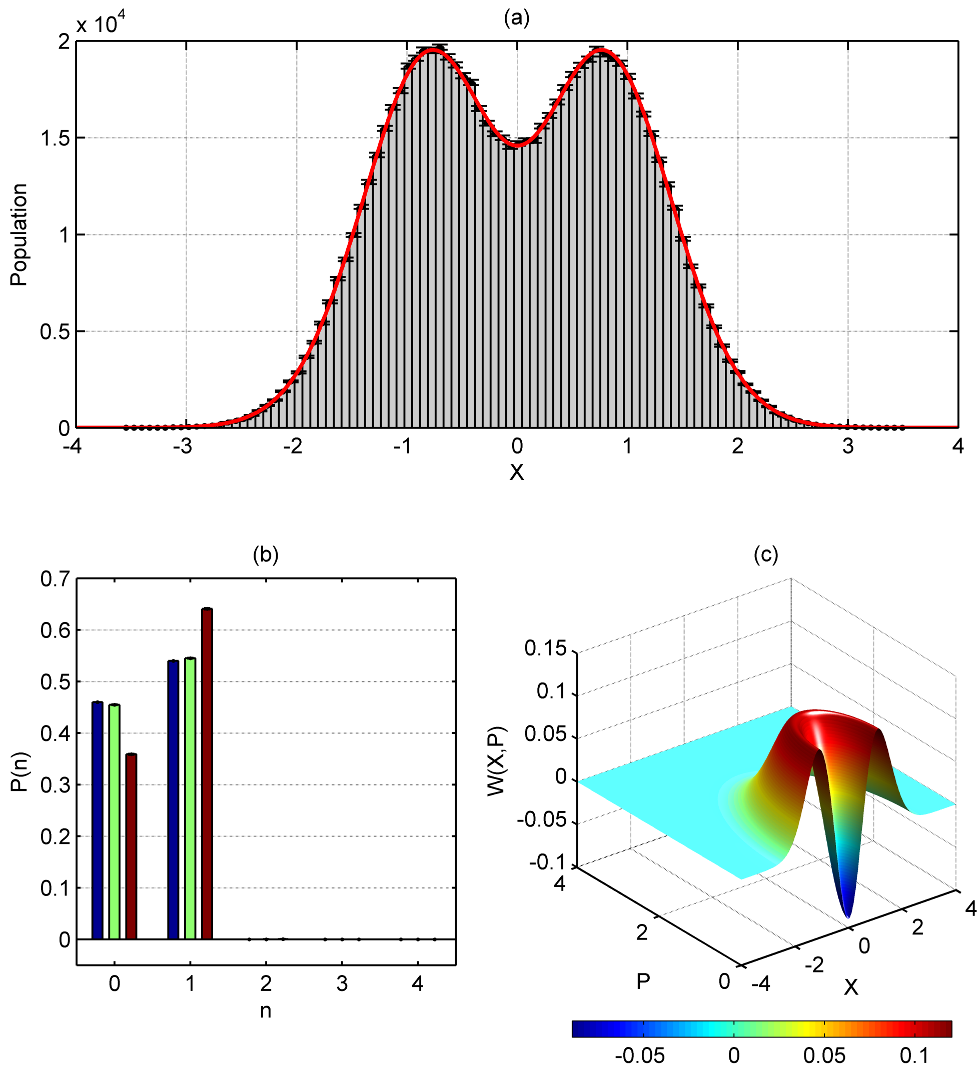

Figure 4.15: Reconstruction of heralded single-photon Fock state: (a) Histogram of acquired quadrature samples, sorted into 100 bins in the interval $X \in [-4 : 4]$, with fit of theoretical marginal distribution for pure single-photon state undergoing loss $1-\eta_1$, red line. (b) Photon number statistics $P(n)$: predicted (blue), reconstructed directly (green) and reconstructed with correction for η_{bhd} (red). (c) Wigner function $W(X, P)$ for reconstructed state, corrected for η_{bhd}.

MATLAB and processed. The procedure was completely automated, including calibration of the BHD.*

The characteristic non-Gaussian structure expected for the single-photon Fock state quadrature probability distribution is clearly pronounced, figure 4.15(a). The red line is a fit of the theoretical marginal distribution for a pure single-photon state undergoing an optical loss of $1-\eta_1$. The best-fit value $\eta_1 = 0.546$ is in excellent agreement with the predicted preparation efficiency $\eta_{\text{net}} = 0.54$, equation 4.53. The predicted photon number statistics $P(n)$ based on $\eta_{\text{net}} = 0.54$, figure 4.15(b) (blue bars), are in excellent agreement with the reconstructed statistics (green bars). The state reconstruction was also performed with correction for the BHD efficiency η_{bhd} (red bars).

As anticipated, the reconstructed single-photon state exhibits negligible higher order photon-number components. This is a result of the relatively small value of the squeezing parameter $\lambda = \tanh(\zeta)$ which is estimated to be $\lambda \approxeq 0.07$ based on the observed trigger count rate, correcting for the efficiency of the heralding APD. The second-order correlation $g^{(2)}(0)$ of the heralded single-photon state may be calculated from the reconstructed density matrix according to

$$g^{(2)}(0) = \frac{\langle \hat{a}^\dagger \hat{a}^\dagger \hat{a} \hat{a} \rangle}{\langle \hat{a}^\dagger \hat{a} \rangle^2} = 0.0023. \tag{4.58}$$

The ideal value for a single-photon state is $g^{(2)}(0) = 0$†. This quantitatively demonstrates the excellent quality of the heralded state, in terms of minimal higher-order photon-number components.

The corrected Wigner function $W(X,P)$ was calculated, figure 4.15(c), and clearly exhibits strong negativity at the origin of phase space, $W(0,0) = -0.090$. The fidelity F

*The acquisition rate for the single-photon state was limited by the data processing, not the raw heralding rate since this was of the order 1.8×10^5 s^{-1}.

†$g^{(2)}(0)$ is independent of loss.

defined as

$$F = \mathrm{Tr}\left(\sqrt{\sqrt{\hat{\rho}_{\mathrm{p}}}\hat{\rho}_{\mathrm{r}}\sqrt{\hat{\rho}_{\mathrm{p}}}}\right)^2, \tag{4.59}$$

where $\hat{\rho}_{\mathrm{p}}$ is the predicted density matrix and $\hat{\rho}_{\mathrm{r}}$ is the reconstructed density matrix (without correction for η_{bhd}) was calculated as $F_1 = 1.00$, thus confirming the excellent agreement between the reconstructed and predicted state heralded from the SPDC source for the one-click event.

Two- and three-photon states

For the two- and three-photon states, heralding rates of approximately 200 s^{-1} and 1 s^{-1} respectively were observed. For the two-photon state, 5×10^5 quadrature samples were acquired in approximately 2 hours, whilst for the three-photon state 3.8×10^4 samples were acquired in approximately 12 hours. It is interesting to note that 12 hours is roughly the same time required to perform the original OHT experiment of the single-photon Fock state by Lvovsky *et al.*, one decade previous to this work [159]. This demonstrates the improvement in both heralded photon sources and BHD bandwidth,* which enabled the three-photon state homodyne tomography of this work. The first two-photon OHT experiment of Ourjoumtsev *et al.* [143] employed a cavity-dumped Ti:Sapphire oscillator which enabled collection of 1.05×10^5 quadrature samples in 2 hours – despite the relatively low 800 KHz repetition rate of the laser system. However, the high pump pulse energy lead to significant higher-order photon-number components [143]. Alternatively, the two-photon OHT experiment of Zavatta *et al.* [206] employed a cavity to enhance the available SPDC pump power (82 MHz repetition rate), resulting in a two-photon state production

*The latter was a key limitation for the work of [159], where a pulse-picker was employed in the LO path to reduce the LO repetition rate due to the limited electronic bandwidth of the BHD employed [96, 205].

rate of 0.15 s^{-1} which enabled 7000 quadrature samples to be recorded in a 14 hour experimental run. In this work, the combination of an 80 MHz repetition rate source which does not require narrowband spectral filtering in the triggering mode [162] with high-bandwidth homodyne detection circumvents the necessity for an amplified laser system or enhancement cavity in order to perform OHT of not only the two-photon Fock state but also the three-photon Fock state.

Results of the two-photon state reconstruction are shown in figure 4.16. The red line is a fit of the theoretical marginal distribution for a pure two-photon state undergoing an optical loss of $1 - \eta_2$. The best-fit value $\eta_2 = 0.501$ is slightly lower than the estimated value $\eta_{\mathrm{net}} = 0.54$. This is likely due to degraded spatial overlap of the LO and heralded state during this experimental run.* Nevertheless, the fidelity between the predicted and reconstructed state (equation 4.59) is $F_2 = 0.99$. Similarly, results for the three-photon experiment are shown in figure 4.17. The fit to the measured statistics yields an efficiency estimate of $\eta_3 = 0.570$ whilst the fidelity between the predicted and measured state is $F_3 = 1.00$.

The error bars for the quadrature histograms and reconstructed photon number statistics are most evident for the three-photon state due to the smaller data set. The histogram error bars were calculated based on the uncertainty $\sqrt{N}$ for each bin containing N events. These errors were propagated through the maximum-likelihood state reconstruction algorithm [90] to estimate uncertainties for the reconstructed photon-number distributions. This was done by Monte-Carlo simulation whereby the reconstruction algorithm was run for 2×10^3 separate histograms according to the error of $\sqrt{N}$ for each bin. The mean estimate is the estimate provided by the original histogram whilst the dispersion is provided by analysing the standard deviation of each matrix element from the set of reconstructed

*Drifts in the heralding efficiency of 4-5% are typical.

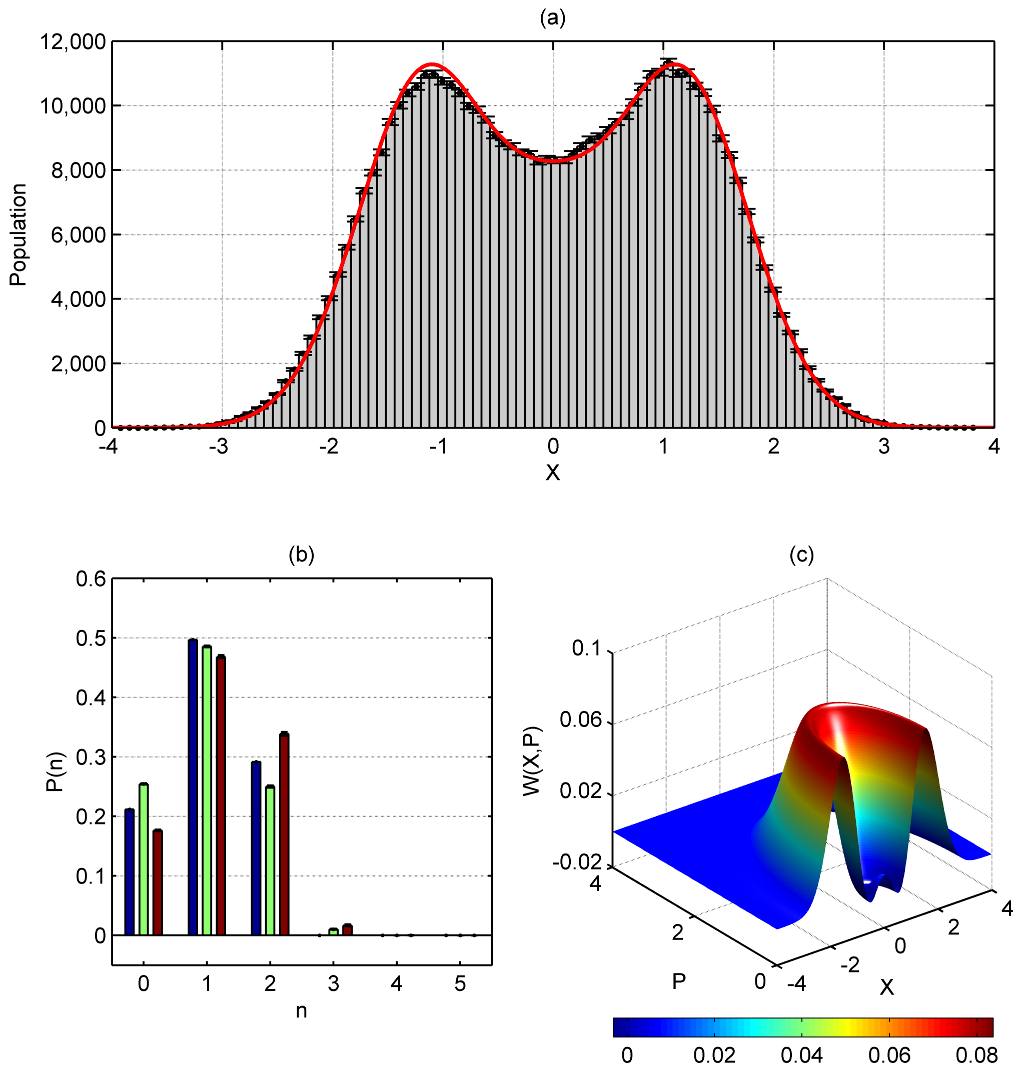

Figure 4.16: Reconstruction of heralded two-photon Fock state: (a) Histogram of acquired quadrature samples, sorted into 100 bins in the interval $X \in [-4 : 4]$, with fit of theoretical marginal distribution for pure two-photon state undergoing loss $1 - \eta_2$, red line. (b) Photon number statistics $P(n)$: predicted (blue), reconstructed directly (green) and reconstructed with correction for η_{bhd} (red). (c) Wigner function $W(X, P)$ for reconstructed state, corrected for η_{bhd}.

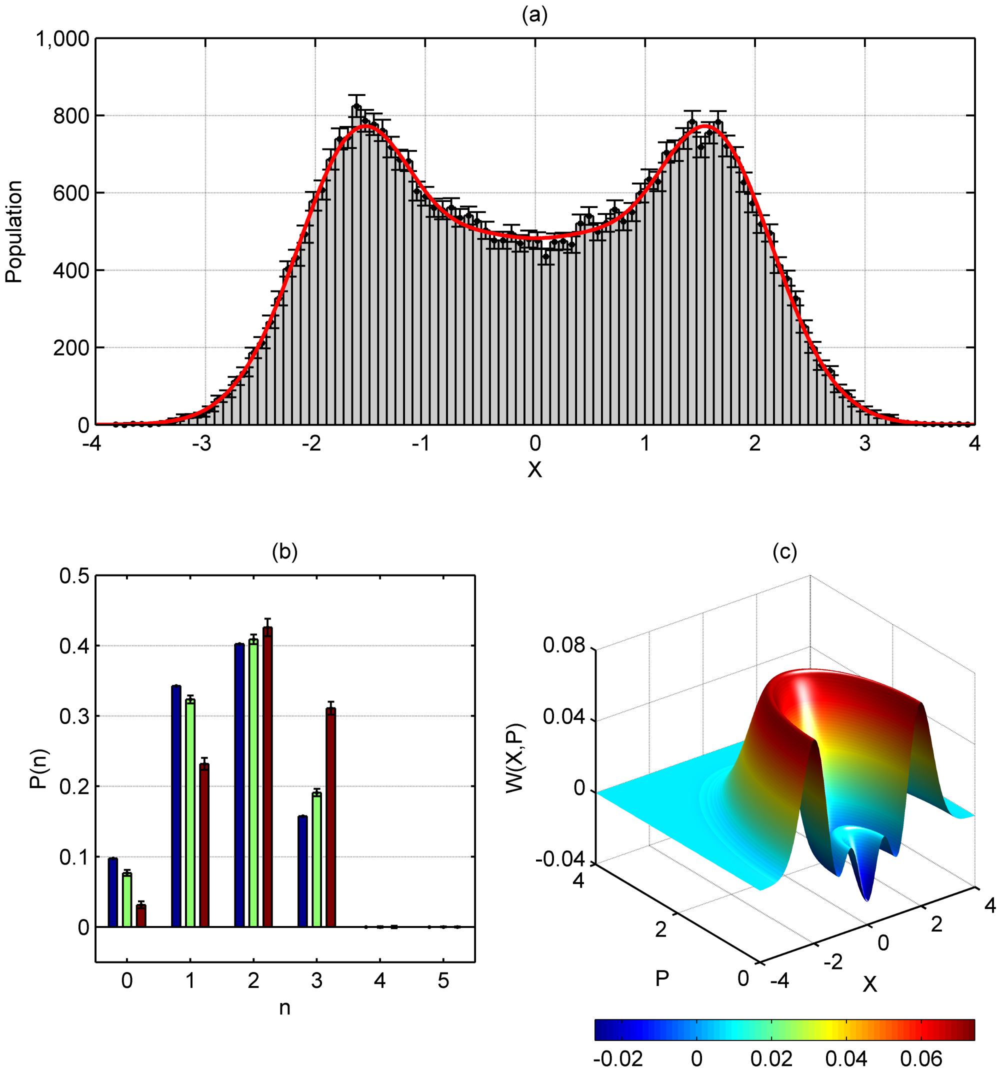

Figure 4.17: Reconstruction of heralded three-photon Fock state: (a) Histogram of acquired quadrature samples, sorted into 100 bins in the interval $X \in [-4 : 4]$, with fit of theoretical marginal distribution for pure three-photon state undergoing loss $1-\eta_3$, red line. (b) Photon number statistics $P(n)$: predicted (blue), reconstructed directly (green) and reconstructed with correction for $\eta_{\rm bhd}$ (red). (c) Wigner function $W(X,P)$ for reconstructed state, corrected for $\eta_{\rm bhd}$.

density matrices. This procedure enables estimation of only the statistical errors due to the finite data set. Systematic errors – arising for example from incorrect calibration of the BHD – are not accounted for.*

Data acquisition for the three-photon Fock state was complicated by the relatively low production rate of approximately 1 s^{-1}. For the one- and two-photon states, the oscilloscope was operated in the "fast frame" mode which enabled calibration of the BHD using adjacent vacuum state pulses, as described above. For the three-photon state, the trigger rate was insufficient to enable calibration of the BHD in this manner, due to the typical drift time scales encountered, as discussed in section 3.4. Therefore, on each trigger event a single large frame was recorded containing 16,000 pulses, i.e. one pulse prepared in the three-photon state and the remaining pulses in the vacuum state. In principle the vacuum state samples could then be extracted to calibrate the detector on each heralding event.† In order to do this, it was necessary to use an oscilloscope sampling rate such that there was an integer number of samples within a time $\tau_L = 1/R_L$, where R_L is the Ti:Sapphire oscillator repetition rate.‡ This was achieved by locking the oscilloscope timebase to the Ti:Sapphire oscillator. Since $R_L \approxeq 80$ MHz, a photodiode signal from the oscillator was down-converted by a factor of 10 using a frequency divider circuit, and fed to the external timebase input of the oscilloscope as a $f \approx 10$ MHz signal. Without locking the oscilloscope timebase to the Ti:Sapphire oscillator in this manner the post-processing of the homodyne voltage $V_{\mathrm{BHD}}(t)$ would have been significantly more complicated.§

*Systematic errors are discussed in chapter 6.

†Since ≈16,000 vacuum state samples were recorded on each heralding event.

‡If this were not the case the effective sampling point would move in time for each subsequent pulse, which leads to a sampling error.

§For example, the sampling point would have to be calcualted separately for small sections of the trace containing 16,000 pulses. This method would be more prone to noise due to the smaller sets of statistics involved.

	F_{pred}	η_{fit}	$\min[W(X,P)]$	Q_M	$\delta[\hat{\rho}]$
$\hat{\rho}_1$	1.00	0.55	-0.090	-0.64	0.64
$\hat{\rho}_2$	0.99	0.50	-0.003	-0.54	0.60
$\hat{\rho}_3$	1.00	0.57	-0.027	-0.67	1.03

Table 4.1: Summary of key properties of the generated Fock states analysed by means of optical homodyne tomography. F_{pred}: fidelity between predicted heralded state and reconstructed state; η_{fit}: raw detection efficiency from fit of theoretical quadrature probability distribution to measured histogram; $\min[W(X,P)]$: minimum value of the Wigner function; Q_M: Mandel Q parameter, equation 4.61; $\delta[\hat{\rho}]$ non-Gaussianity, equation 4.60. The last three parameters were calculated from the reconstructed states after correction for the BHD efficiency η_{bhd}.

4.3.6 Summary of properties of reconstructed states

A summary of the Fock state OHT results are presented in table 4.1. In addition to the parameters calculated in the previous section, such as the fidelity of the reconstructed state with the predicted state F_{pred} and the raw detection efficiency η_{fit} calculated from the theoretical fit to the measured histograms, several other quantities are presented.

One of the defining features of Fock states is the non-Gaussian nature of the Wigner function. The reconstructed Wigner functions presented in figures 4.15, 4.16 and 4.17 are clearly all non-Gaussian, with the number of oscillations proportional to the order of the Fock state [183]. A more quantitative analysis is made by calculating the non-Gaussianity [207–209] of the reconstructed states $\delta[\hat{\rho}]$ defined as [208]

$$\delta[\hat{\rho}] = S(\hat{\rho}||\hat{\tau}) = S(\hat{\tau}) - S(\hat{\rho}) \tag{4.60}$$

where $\hat{\rho}$ is the reconstructed Fock state density matrix, $\hat{\tau}$ is the Gaussian state which has the same covariance matrix and first-order moments vector as $\hat{\rho}$, $S(\hat{\rho}||\hat{\tau})$ is the quantum relative entropy [35] , and $S(\hat{\sigma})$ is the von Neumann entropy defined as $S(\hat{\sigma}) = -\text{Tr}(\hat{\sigma}\ln\hat{\sigma})$ [35]. $\delta[\hat{\rho}] = 0$ for Gaussian states such as coherent states and squeezed states, whereas $\delta[\hat{\rho}] > 0$ for non-Gaussian states. As shown in table 4.1, the reconstructed Fock states (corrected for the BHD efficiency η_{bhd}) are all non-Gaussian by the measure of equation 4.60.

Non-Gaussianity by itself does not imply non-classicality. For example, a mixture of two coherent states with differing amplitudes is non-Gaussian – it is not fully parametrized by a covariance matrix and first-order moments vector – but is also completely classical. Non-classicality is indicated by negativity of the Wigner function [210] or sub-Poissonian photon number statistics [168]. The minimum values of the Wigner functions $\min[W(X,P)]$ for the three reconstructed Fock states (corrected for η_{bhd}) are presented in table 4.1. Whilst all three states exhibit negative Wigner functions this is only a signature of non-classicality [211]. A more quantitative measure is provided by the Mandel Q parameter [212] defined as

$$Q_M(\hat{\rho}) = \frac{\langle(\Delta n)^2\rangle - \langle n\rangle}{\langle n\rangle} = \frac{\mathrm{Tr}(\hat{\rho}\hat{n}^2) - [\mathrm{Tr}(\hat{\rho}\hat{n})]^2}{\mathrm{Tr}(\hat{\rho}\hat{n})} - 1, \tag{4.61}$$

where $\hat{n}$ is the photon-number operator. The Mandel Q parameter is negative for states exhibiting sub-Poissonian photon number statistics [83]. The three reconstructed Fock states clearly exhibit negative Mandel Q values, table 4.1. Thus all three of the Fock states generated by SPDC and investigated by means of OHT are both non-classical and non-Gaussian.

4.4 Summary

Fock states are a primary resource in quantum technologies which can be generated through conditional measurements on a TMSV state generated by SPDC. The modal purity and structure of heralded Fock states is a key factor which dictates the visibility achievable in interference with auxiliary states – potentially limiting the efficacy of certain protocols. In this chapter, SPDC was employed to herald multi-photon Fock states occupying well-timed near-single-mode wave packets. The degree of mode matching between the heralded states and the LO used for homodyne detection was estimated through determining the Fock state modal purity and overlap with the LO. One-, two- and three-photon states were heralded and analysed by means of OHT – a measurement scheme which ensures that only a single mode is examined. The reconstructed Fock states in the mode analysed were found to be both non-Gaussian and non-classical. Furthermore, the overall detection efficiency of the Fock states was found to closely match the predicted value. Future work to improve the spatial mode overlap of the heralded Fock states with the LO and increase the brightness of the TMSV state should enable improved detection efficiency and the analysis of higher-order Fock states.

5 Photon-Level Quantum Operations

Optics is arguably the ideal platform for encoding, manipulating and transmitting quantum information – photons do not interact strongly with the environment enabling good coherence to be maintained even for long-distance communications [31]. However, this apparent advantage also poses a serious challenge, namely that photon-photon interactions – which are crucial for manipulations such as two-qubit logic gates – are extremely weak and would require extremely large optical non-linearities [213, 35]. In 2001 Knill, Laflamme and Milburn proposed the concept of linear optics quantum computation (LOQC) [34]. It was shown that large probabilistic non-linearities could be invoked with the aid of ancilla photons and projective measurements – thus enabling the implementation of two-qubit gates [34].

Outside the realm of quantum computation, similar probabilistic interactions can be used to arbitrarily manipulate the modal properties or photon-number statistics of light. The basic building block of most schemes is the post-selected beam splitter [214, 215]. Such schemes often employ an ancilla state to generate entanglement at a beam splitter [150], in addition to conditional measurements. This concept has given rise to a whole host of quantum optical state engineering protocols including photon subtraction [216, 217], photon addition [218, 219], cat-state generation [154, 220], quantum scissors [221], photon

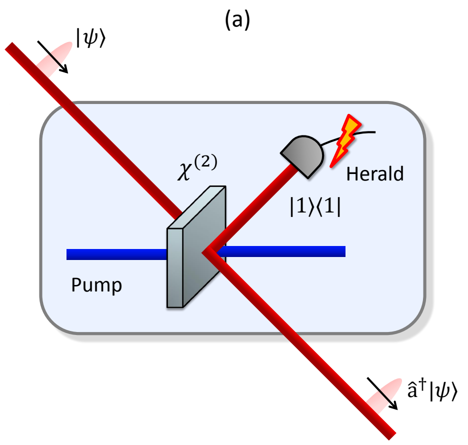

Figure 5.1: (a) Photon addition can be implemented by employing a down-converter to generate a two-mode photon-number correlated state. If state $|\psi\rangle$ is fed into one mode of the down-converter and a single-photon is detected in the conjugate output mode then a photon must have been added to the input state – effecting the operation $\hat{a}^\dagger|\psi\rangle$. (b) Approximate implementation of the photon subtraction operation. A single-photon detection event in one output port of an asymmetric beam splitter approximately effects the operation $\hat{a}|\psi\rangle$ [131].

catalysis [222, 153], noiseless amplification [223–225], entanglement distillation [226, 227] and Fock state filtration [157, 158]. A thorough review of photon-level manipulations on travelling modes of light can be found in reference [228].

A variation on the post-selected beam splitter is to use a photon-number correlated beam or single-mode squeezed state as the initial resource, enabling generation of arbitrary quantum states through conditional measurement [152, 144, 229, 230]. The latter scheme has become the method of choice to implement the photon addition operation [231, 23], figure 5.1(a). In this scheme, one mode of a down-converter is stimulated by input quantum state $|\psi\rangle$. The conjugate mode is monitored by a photon-number resolving detector. When a single photon is detected in this mode, owing to the photon-number correlations of the down-converted light a single photon must also have been added to the other mode – thus effecting the operation $\hat{a}^\dagger|\psi\rangle$ which constitutes photon addition. Figure 5.1(b) shows the opposite scheme of photon subtraction, in this case no down-converter is employed. Instead a beam splitter is used to generate entanglement which can be harnessed to effect

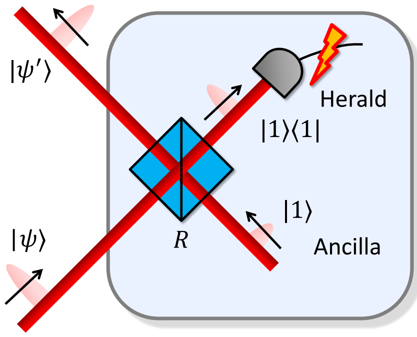

Figure 5.2: Schmatic of the ideal Fock state filtration quantum operation. Input (pure) quantum state $|\psi\rangle$ is combined with an ancilla single photon $|1\rangle$ at a beam splitter of reflectivity R. One output mode is registered by a photon-number resolving detector, which conditions the operation. Detection of a single photon heralds the success of Fock state filtration, whereby the output state $|\psi'\rangle$ is generated.

the removal of a photon from the input state conditional on detecting a photon in the reflected mode. Thus photon subtraction as depicted is an example of a post-selected beam splitter. In 2013 Kumar *et al* demonstrated quantum process tomography of the photon addition and annihilation operations [131], as depicted in figure 5.1.

Experimentally, photon-level manipulations of a single mode of light are impeded due to non-ideal ancilla states and the lack of availability of photon-number resolving detection. In this chapter the scheme known as Fock state filtration [157, 158] is investigated in the presence of experimental imperfections – culminating in the complete characterization of a realistic implementation via quantum process tomography.

5.1 Fock state filtration

Fock state filtration (FSF) was proposed by Sanaka *et al.* in 2006 [157] and is schematically identical to the single-photon catalysis demonstrated by Lvovsky *et al.* in 2002 [155]. The schematic of the ideal FSF quantum operation is shown in figue 5.2. An arbitrary pure input quantum state $|\psi\rangle$ is combined with an ancilla single photon $|1\rangle$ at a beam splitter of reflectivity R. One output mode of the beam splitter is registered by a photon-number resolving detector. Only events corresponding to detection of one photon in this output conditioning mode are accepted; whereby the output state $|\psi'\rangle$ is generated in the other mode. Thus detection of a single-photon in the conditioning mode heralds the success of the filter operation. The filtered state $|\psi'\rangle$ contains a 'hole' [232] in the photon-number distribution for particular choices of the beam-splitter reflectivity R [157].

The term catalysis is sometimes used to describe such an arrangement because internally to the operation, an ancilla single photon is both created and detected [155, 233, 153]. However, owing to quantum interference between the possible paths leading to a single-photon in the conditioning mode, the input state $|\psi\rangle$ is transformed in a non-trivial manner to a different state $|\psi'\rangle$. FSF and the more general catalysis variants [155, 153] have been shown to be applicable to the generation of non-classical states of light including photon-number states [234] and Schrödinger cat states [235, 153]. Furthermore, it has been proposed that information could be encoded and stored within 'holes' in the photon-number distribution [236]. FSF has also been demonstrated as a technique for generating entanglement [158] and may be useful as a non-Gaussian operation [209] when photon subtraction does not suffice.* Finally, optical states with one or more 'holes' in their photon-number distribution are necessarily non-classical [232]. According to the Glauber-Sudarshan P-representation of the quantum state $P(\alpha)$ [17] the photon-number distribution p_n is given by

$$p_n = \langle n|\hat{\rho}|n\rangle = \int_{-\infty}^{\infty} d^2\alpha P(\alpha)|\langle n|\alpha\rangle|^2. \tag{5.1}$$

In order for the P-function $P(\alpha)$ to be a true probability density it is required that $p_n \neq 0,\ \forall n$, since $|\langle n|\alpha\rangle| > 0$ for $|\alpha| > 0$. Therefore the P-function for a state $\hat{\rho}$ containing a 'hole' in the photon-number distribution cannot be a true probability density and thus

*Photon subtraction does not de-Gaussify a coherent state, for example.

the state is non-classical by definition [232].

5.1.1 Ideal operation

To derive the transformation induced by the conditional FSF operation on the input state $|\psi\rangle$, the action on input Fock states is considered. Since the operation is linear, if the response to input Fock states is known then so is the response to an arbitrary superposition given by

$$|\psi\rangle = \sum_{n=0}^{\infty} C_n |n\rangle, \tag{5.2}$$

where $\sum_n |C_n|^2 = 1$ and $|n\rangle$ denotes the n-photon Fock state. The probability amplitude to have n photons in the output mode and one photon in the heralding mode given there were n photons in the input mode and one photon in the ancilla mode is given by [215]

$$A_{n,1} = \langle n, 1|\hat{U}|n, 1\rangle, \tag{5.3}$$

where $\hat{U}$ is the unitary transformation describing the beam splitter. The beam splitter transforms modes represented by field operators $\hat{a}_1$ and $\hat{a}_2$ for the input and ancilla respectively according to [215]

$$\begin{aligned} \hat{a}_1 &\Rightarrow \sqrt{R}\hat{a}_1 + i\sqrt{1-R}\hat{a}_2, \\ \hat{a}_2 &\Rightarrow i\sqrt{1-R}\hat{a}_1 + \sqrt{R}\hat{a}_2. \end{aligned} \tag{5.4}$$

Thus the probability amplitude $A_{n,1}$ may be written using the transformed field operators as

$$A_{n,1} = \left\langle n,1 \middle| \left(\sqrt{R}\hat{a}_1^\dagger + i\sqrt{1-R}\hat{a}_2^\dagger\right)^n \left(i\sqrt{1-R}\hat{a}_1^\dagger + \sqrt{R}\hat{a}_2^\dagger\right) \middle| \text{vac} \right\rangle,$$
$$= \left\langle n,1 \middle| \frac{1}{n!}\sum_k \binom{n}{k} \left(\sqrt{R}\hat{a}_1^\dagger\right)^{n-k} \left(i\sqrt{1-R}\hat{a}_2^\dagger\right)^k \left(i\sqrt{1-R}\hat{a}_1^\dagger + \sqrt{R}\hat{a}_2^\dagger\right) \middle| \text{vac} \right\rangle, \quad (5.5)$$

where the identity $(x+y)^n = \sum_k x^{n-k}y^k$ is used. Owing to orthonormality of the Fock states, the expression of equation 5.5 has only two non-vanishing terms such that

$$A_{n,1} = \sqrt{R}^{n-1}\left(R - n[1-R]\right). \quad (5.6)$$

Having derived the probability amplitude as a function of the input Fock state order n, the superposition filter input state $|\psi\rangle$ thus transforms as

$$\boxed{|\psi\rangle = \sum_{n=0}^{\infty} C_n|n\rangle \Rightarrow \mathcal{N}\sum_{n=0}^{\infty} A_{n,1}C_n|n\rangle = \mathcal{N}\sum_{n=0}^{\infty}\sqrt{R}^{n-1}\left(R - n[1-R]\right)C_n|n\rangle = |\psi'\rangle,} \quad (5.7)$$

where $\mathcal{N}$ is a re-normalization factor associated with the probabilistic nature of the filter operation.

There are two important properties of the state transformation of equation 5.7. Firstly, for certain values of the beam splitter reflectivity R the probability amplitude $A_{n,1}$ is equal to zero. This occurs for values of R such that

$$R = \frac{n}{n+1}. \quad (5.8)$$

This property demonstrates that FSF can selectively remove particular Fock layers n from the input state by choosing the beam splitter reflectivity according to equation 5.8.

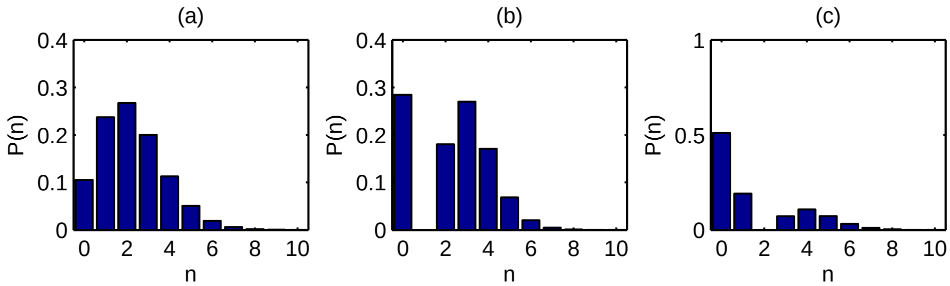

Figure 5.3: Action of the ideal FSF operation on a coherent state of amplitude $|\alpha| = 1.5$. (a): photon-number statistics of input coherent state. (b) and (c): photon-number statistics after FSF operation for $R = 1/2$ and $R = 2/3$ respectively.

Hence FSF can be thought of as a conditional n-photon absorber [157, 158], demonstrating the measurement induced non-linearity of this operation. Secondly, the output state $|\psi'\rangle$ cannot contain any population in Fock layers which were not populated in the original state.* Thus the FSF operation cannot re-populate Fock layers which have been filtered. This property enables preparation of Fock states from input coherent or thermal states by implementing a series of FSF operations with different beam splitter reflectivities – successively filtering out all but one dominant Fock layer [234]. The action of FSF on a coherent state of amplitude $|\alpha| = 1.5$ for $R = 1/2$ and $R = 2/3$ is shown in figure 5.3. The photon number distributions after filtration are observed to contain 'holes' [232, 236, 237] in the $n = 1$ and $n = 2$ Fock layers respectively.

Having derived the state transformation for the ideal FSF operation, it is also possible to derive an expression for the process tensor $\mathcal{E}$. Consider the filter input state is described by density matrix $\hat{\rho} = \sum_{m,n=0}^{\infty} \rho_{mn}|m\rangle\langle n|$ in the Fock basis, which evolves according to the linear completely-positive (CP) map described by process tensor $\mathcal{E}$, resulting in the filter output state $\hat{\rho}'$ given by

$$\hat{\rho}' = \mathcal{E}(\hat{\rho}) = \sum_{m,n=0}^{\infty} \rho_{mn}\mathcal{E}\left(|m\rangle\langle n|\right) = \sum_{j,k,m,n=0}^{\infty} \mathcal{E}_{jk}^{mn}\rho_{mn}|j\rangle\langle k| \tag{5.9}$$

*Due to the C_n term which is carried through the transformation.

where matrix elements of the rank-4 process tensor $\mathcal{E}$ are given by [60]

$$\mathcal{E}_{jk}^{mn} = \langle j|\mathcal{E}(|m\rangle\langle n|)|k\rangle. \tag{5.10}$$

In general, it is not obvious what the form of the process tensor is for a particular quantum operation. To derive the form of the process tensor describing an arbitrary quantum operation in the Fock basis, Rahimi-Keshari *et al.* showed that it is convenient to consider the action of the process on coherent states [60]. According to this approach, the elements of the process tensor are given by

$$\mathcal{E}_{jk}^{mn} = \frac{1}{\sqrt{m!n!}} \frac{\partial^m}{\partial\alpha^m} \frac{\partial^n}{\partial\alpha^{*n}} \left[\exp\left(|\alpha|^2\right)\langle j|\hat{\rho}'(\alpha)|k\rangle\right]\Big|_{\alpha=0}, \tag{5.11}$$

where $\hat{\rho}'(\alpha)$ is the output density matrix of the quantum operation obtained when the input state is a coherent state with complex amplitude α. Applying the transformation of equation 5.6 to a coherent state input $\hat{\rho} = |\alpha\rangle\langle\alpha| = \sum_{m,n} \exp\left(-|\alpha|^2\right)\frac{\alpha^m\alpha^{*n}}{\sqrt{m!n!}}|m\rangle\langle n|$ yields output state $\hat{\rho}'$ given by*

$$\hat{\rho}' = \sum_{m,n=0}^{\infty} \exp\left(-|\alpha|^2\right)\frac{\alpha^m\alpha^{*n}}{\sqrt{m!n!}}\sqrt{R}^{(m+n-2)}\left(R - m[1-R]\right)\left(R - n[1-R]\right)|m\rangle\langle n|. \tag{5.12}$$

With this expression for the filter output state given a coherent state input, equation 5.11 may now be applied to derive the process tensor $\mathcal{E}$, such that

$$\mathcal{E}_{jk}^{mn} = \sqrt{\frac{j!k!}{m!n!}}\delta_{mj}\delta_{nk}\sqrt{R}^{(j+k-2)}\left(R - j[1-R]\right)\left(R - k[1-R]\right). \tag{5.13}$$

It is instructive to consider the diagonal elements of the process tensor $\mathcal{E}_{kk}^{mm}$ – correspond-

*Note, the output state is not normalized as to derive the process tensor it is necessary to retain information about the success probability of the process.

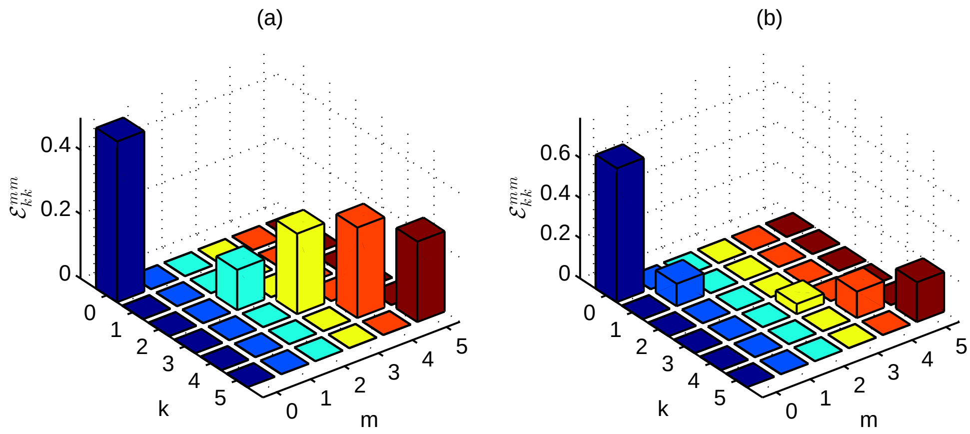

Figure 5.4: Diagonal elements $\mathcal{E}_{kk}^{mm}$ of the process tensor for ideal FSF for (a) $R = 1/2$ and (b) $R = 2/3$.

ing to the probability of obtaining k photons at the process output given m input photons [56, 61]. This is shown in figure 5.4 for the FSF operation with $R = 1/2$ and $R = 2/3$ corresponding to filtration of the $n = 1$ and $n = 2$ Fock layers respectively. This is evident from the form of $\mathcal{E}_{kk}^{mm}$ for the two cases – where $\mathcal{E}_{kk}^{11} = 0$ and $\mathcal{E}_{kk}^{22} = 0$ respectively. Notice also that the other unfiltered Fock layers are re-scaled by varying amounts, reflecting the differing success probabilities of FSF for different input Fock states. However, unlike linear loss, other input Fock states are perfectly preserved – provided the filter is successful, i.e. a heralding event is produced. This demonstrates the non-linear nature of FSF – it suppresses one particular Fock layer whilst 'transmitting' all others [157, 158].

5.1.2 Non-ideal operation

The treatment of section 5.1.1 assumes that ideal ancilla single-photon states and number-resolving detection are available – thus eliciting the ideal FSF operation, with perfect suppression of the filtered Fock layer. In practice such ideal operation is often infeasible with current technology. Motivated by this, a more realistic model of the FSF operation is developed in this section – taking into account three key factors impacting the performance

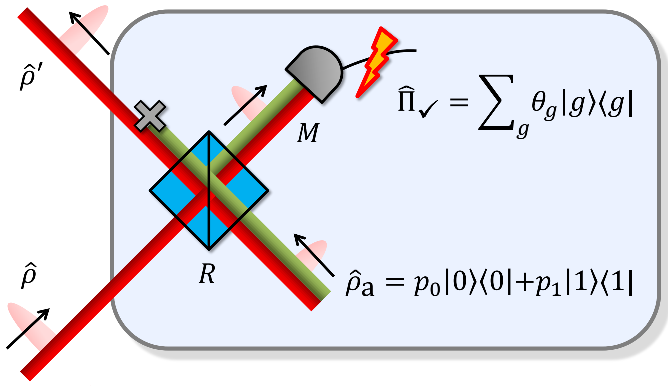

Figure 5.5: Schematic of the non-ideal FSF operation with three sources of imperfection taking into account a realistic heralding detector, non-ideal ancilla state and the multi-mode nature of the heralding detector.

of FSF. Although Lvovsky *et al.* attempted to model realistic operation of single-photon catalysis [155], their treatment was limited to just two Fock layers. Later work by Bartley *et al.* in 2012 [153], in which the scheme of reference [155] was extended to higher-order catalysis did not model imperfection of either the ancilla states or the conditioning detectors, i.e. perfect number-resolving detection was assumed.* Furthermore, no attempt has yet been made to derive the full process tensor describing a realistic catalysis or FSF operation – or indeed any post-selected beam splitter operation apart from photon subtraction. Development of such a realistic model is instructive since it allows diagnosis of sources of imperfection in a realistic device exploiting such quantum operations.

Figure 5.5 shows the FSF operation including sources of imperfection, in contrast to figure 5.2 for the ideal operation. Three sources of imperfection are considered: 1) projection onto one photon in the heralding mode is replaced by a more general POVM element describing the heralding event denoted $\hat{\Pi}_{\checkmark}$, assumed to be diagonal in the photon-number basis such that $\hat{\Pi}_{\checkmark} = \sum_g \theta_g |g\rangle\langle g|$; 2) impurity of the ancilla single-photon state in terms of admixture of the vacuum state, i.e. non-unity heralding efficiency, such that

*After the conclusion of the work presented here, Sperling *et al.* [238] published a theory paper in which the realistic performance of quantum protocols heralded by 'click' detectors was considered.

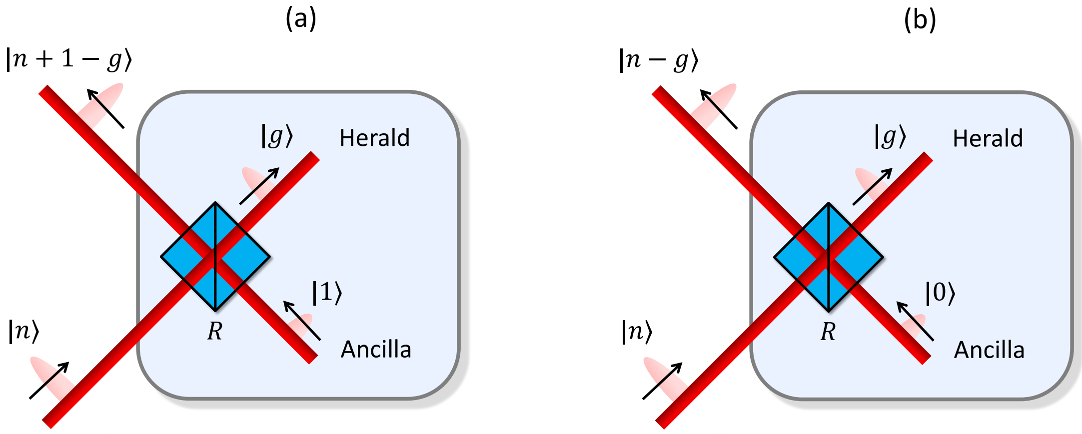

Figure 5.6: Scenario pertaining to (a) probability amplitude $A'_{n+1-g,g}$ and (b) $A''_{n-g,g}$.

the ancilla state density matrix $\hat{\rho}_a = p_0|0\rangle\langle 0| + p_1|1\rangle\langle 1|$; 3) the multi-mode nature of the heralding detector, quantified by parameter M. In what follows, the full process tensor incorporating these three sources of imperfection is derived.

Realistic heralding detector

Ideally the filter only operates when precisely one photon is present in the heralding mode of the beam splitter, which corresponds to the heralding detector success event being described by a POVM element of the form $\hat{\Pi}_{\checkmark} = |1\rangle\langle 1|$. To understand the effect of a general, diagonal POVM element of the form $\hat{\Pi}_{\checkmark} = \sum_g \theta_g |g\rangle\langle g|$ on the filter operation, matrix elements of the form $\langle n+1-g, g|\hat{U}|n, 1\rangle$ are considered. This gives the probability amplitude to have g photons in the heralding mode and therefore (by photon-number conservation) $n+1-g$ photons in the filter output mode, given n photons incident in the filter input mode in addition to the ancilla single photon, as depicted in figure 5.6(a). Following a similar procedure to that used to derive equation 5.5 leads to probability amplitudes given by

$$A'_{n+1-g,g} = \langle n+1-g, g|\hat{U}|n,1\rangle$$
$$= \sqrt{\frac{(n-g+1)!g!}{n!}}\sqrt{R}^{n-g}(i\sqrt{1-R})^{g-1}\left[\binom{n}{g-1}R - (1-R)\binom{n}{g}\right], \quad (5.14)$$

where the binomial coefficients are defined such that

$$\binom{n}{k} = \begin{cases} 0, & k<0, k>n \\ \frac{n!}{(n-k)!k!}, & \text{otherwise.} \end{cases}$$

For projection onto $g \geq 1$ photons in the heralding mode an arbitrary input superposition state will transform as*

$$|\psi\rangle = \sum_{n=0}^{\infty} C_n|n\rangle \Rightarrow \mathcal{N}\sum_{n=g-1}^{\infty} C_n A'_{n-g+1,g}|n+1-g\rangle = |\psi'\rangle. \quad (5.15)$$

For a POVM element of the form $\hat{\Pi}_{\checkmark} = \sum_g \theta_g|g\rangle\langle g|$, a pure input state is transformed to a mixed state. More generally, an input state $\hat{\rho}$ transforms as

$$\hat{\rho} = \sum_{m=0}^{\infty}\sum_{n=0}^{\infty} C_{mn}|m\rangle\langle n| \Rightarrow \sum_{g=1}^{\infty}\theta_g \sum_{m=g-1}^{\infty}\sum_{n=g-1}^{\infty}$$
$$C_{mn}A'_{m-g+1,g}A'^{*}_{n-g+1,g}|m+1-g\rangle\langle n+1-g| = \hat{\rho}', \quad (5.16)$$

which is nothing but a mixture of transformations of the form given by equation 5.15, weighted according to the coefficients θ_g describing the heralding POVM element in the Fock basis.

*The case where $g=0$ corresponds to a vacuum heralding event and is not considered here. This corresponds to ignoring dark counts in the heralding detector which is reasonable since the actual FSF operation is heralded only when both the heralding detector and a single-photon ancilla are heralded at the same time. This has the effect of almost eliminating effective dark counts.

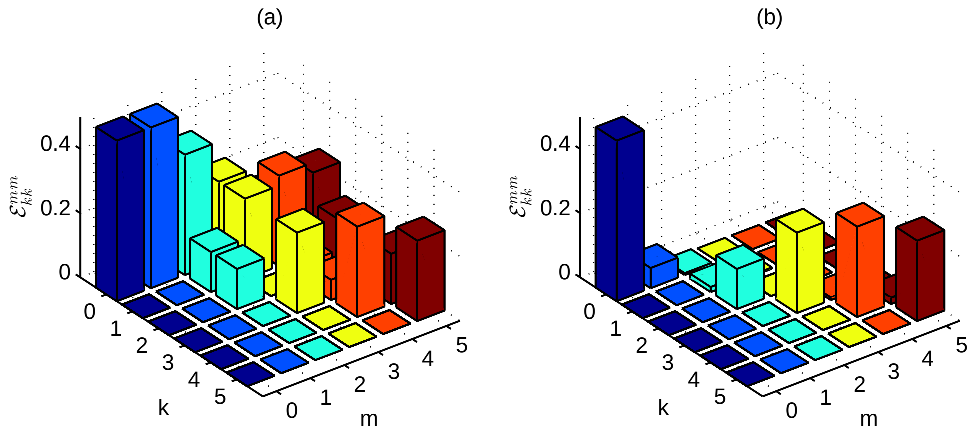

Figure 5.7: Diagonal elements $(\mathcal{E}_1)^{mm}_{kk}$ of the process tensor for FSF with (a) APD used as heralding detector, (b) 8-bin TMD used as heralding detector. Both detectors have unit quantum efficiency.

Having derived the output density matrix $\hat{\rho}'$ for a general diagonal heralding POVM element, the process tensor may be determined according to the procedure set out in section 5.1.1 [60]. The process tensor for FSF when considering a general heralding detector POVM, denoted $(\mathcal{E}_1)^{mn}_{jk}$, is given by

$$\begin{aligned}(\mathcal{E}_1)^{mn}_{jk} = \sqrt{\frac{j!k!}{m!n!}} \sum_{g=1}^{\infty} \theta_g g! \sqrt{R}^{j+k-2} \sqrt{1-R}^{2(g-1)} \\ \times \left[\binom{j+g-1}{g-1} R - (1-R) \binom{j+g+1}{g} \right] \\ \times \left[\binom{k+g-1}{g-1} R - (1-R) \binom{k+g-1}{g} \right] \\ \times \delta_{m,j+g-1} \delta_{n,k+g-1}. \qquad (5.17)\end{aligned}$$

The diagonal elements of the process tensor elements derived in equation 5.17 are plotted in figure 5.7 for two different heralding detectors for the case where $R = 1/2$, i.e. for filtration of the $n = 1$ Fock layer. In figure 5.7(a), the POVM of an avalanche photodiode (APD) with perfect quantum efficiency was assumed. This results in diagonal elements in stark contrast to the ideal FSF operation, shown in figure 5.4(a). Most strikingly, a redistribution of higher Fock layer components into lower Fock layers is evident, thus indicating that perfect filtering is not possible owing to the lack of photon-number resolution in the heralding detector. Furthermore, unlike ideal FSF, the operation now has a non-zero probability of success when a single-photon is input to the process. In this case, photon-bunching at the beam splitter results in the two-mode output state $1/\sqrt{2}(|02\rangle + |20\rangle)$. The APD cannot discriminate between one and two photons and thus the operation is heralded with a probability of 0.5, resulting in the vacuum state in the FSF output mode, thus $(\mathcal{E}_1)^{11}_{00} = 0.5$. In contrast, figure 5.7(b) shows the FSF process tensor diagonal elements for an 8-bin time-multiplexed detector (TMD) [81] with perfect quantum efficiency. By inspection the pseudo number-resolving capability of the TMD results in a tensor which more closely matches the ideal tensor of figure 5.4(a)*.

Ancilla state heralding efficiency

In chapter 4 the generation of multi-photon Fock states was explored experimentally. It was found that the ability to mode-match the heralded Fock states with an auxiliary mode such as the LO used for balanced homodyne detection could be quantified by an overall efficiency parameter. Thus in the realistic FSF operation, figure 5.5, the pure ancilla single photon is replaced by a mixed state such that

$$\hat{\rho}_{\mathrm{a}} = p_0|0\rangle\langle 0| + p_1|1\rangle\langle 1|, \tag{5.18}$$

where $p_1 = 1 - p_0 = \eta_{\mathrm{H}}$ describes the effective heralding efficiency of the ancilla single-photon state.† To model the effect of non-unit heralding efficiency, the situation of figure 5.6(b) is considered, which accounts for the heralding events which occur when the ancilla

*For non-ideal quantum efficiency this is far from the case.

†Higher-order terms are neglected.

state is in the vacuum state. As before, the probability amplitudes are derived for input Fock states and are given by

$$A''_{n-g,g} = \langle n-g, g|\hat{U}|n, 0\rangle = \sqrt{\binom{n}{g}}\sqrt{R}^{n-g}(i\sqrt{1-R})^{g}. \tag{5.19}$$

In exact analogy to equation 5.16, for a realistic heralding detector described by POVM element $\hat{\Pi}_{\checkmark} = \sum_g \theta_g |g\rangle\langle g|$ an arbitrary input state described by density matrix $\hat{\rho}$ will transform as

$$\hat{\rho} = \sum_{m=0}^{\infty}\sum_{n=0}^{\infty} C_{mn}|m\rangle\langle n| \Rightarrow \sum_{g=1}^{\infty}\theta_g \sum_{m=g}^{\infty}\sum_{n=g}^{\infty} C_{mn}A''_{m-g,g}A''^{*}_{n-g,g}|m-g\rangle\langle n-g| = \hat{\rho}', \tag{5.20}$$

where as before dark counts in the heralding detector are neglected. Finally, the process tensor describing the state transformation of equation 5.20 is obtained as before. Denoted $(\mathcal{E}_0)^{mn}_{jk}$, the tensor is given by

$$(\mathcal{E}_0)^{mn}_{jk} = \frac{1}{\sqrt{m!n!}}\sum_{g=1}^{\infty}\theta_g\sqrt{(j+g!)(k+g)!}\sqrt{R}^{j+k}\sqrt{1-R}^{2g}\sqrt{\binom{j+g}{g}\binom{k+g}{g}}$$
$$\times\, \delta_{m,j+g}\delta_{n,k+g}. \tag{5.21}$$

By linearity, the mixed ancilla state $\hat{\rho}_{\mathrm{a}}$ will lead directly to a mixture of the two process tensors derived in this section and the preceding section, i.e. a mixture of $\mathcal{E}_0$ and $\mathcal{E}_1$, weighted according to the heralding efficiency η_{H}. Thus the process tensor for realistic FSF is given by

$$\mathcal{E}_{\mathrm{FSF}} = \eta_{\mathrm{H}}\mathcal{E}_1 + (1-\eta_{\mathrm{H}})\mathcal{E}_0. \tag{5.22}$$

Multi-mode heralding detector

Photon-counting detectors such as APDs and TMDs are general spatially, temporally and polarization multi-mode. A well-defined spatial mode and polarization are typically selected by coupling the detector using a single-mode fiber and placing a polarizing element in front of the detector. However, since the response time of a typical photon-counting detector is often far greater than the optical pulse duration, such detectors are inherently temporally multi-mode [75]. As discussed in chapter 4, this multi-mode nature can have adverse effects when heralding Fock states by conditional measurements on the output of a down-converter. Indeed, the same is true for other scenarios where such detectors are employed to herald the success of a particular quantum operation.

Tualle-Brouri *et al.* studied the impact of using a multi-mode heralding detector in a scheme to prepare Schrödinger cat states by photon subtraction from squeezed states of light [239]. It was shown that for such a scheme, the problem could be reduced to two effective modes [239], thus aiding analysis of the multi-mode effects. In the realistic FSF scheme depicted in figure 5.5 a similar two-mode decomposition may be performed. For the purpose of this analysis, homodyne detection of the FSF output state $\hat{\rho}'$ is considered. Furthermore, it is assumed that the FSF input state $\hat{\rho}$ (e.g. a coherent state) can be well-matched to the LO, which defines the spatial-temporal mode for performing homodyne detection, see section 3.2.2. The impact of the multi-mode heralding detector arises due to the potentially multi-mode nature of the ancilla state $\hat{\rho}_{\mathrm{a}}$.

Assuming the FSF input state $\hat{\rho}$ is perfectly matched with the LO, the problem can be decomposed into two effective modes: 1) the mode defined by the LO and 2) the set of modes orthogonal to the LO [239]. Ideally, the ancilla state mode would perfectly match the LO and then the problem reduces to a single mode. In practice, a fraction of the ancilla mode may not be overlapped with the LO but may still lead to detection events in the heralding detector. In figure 5.5 this is represented pictorially by the green-shaded part of the ancilla state mode. A 'multi-mode' parameter M is defined such that

$$M = \frac{\eta_{\mathrm{H}}}{\eta'_{\mathrm{H}}}, \tag{5.23}$$

where η_{H} is the heralding efficiency of the ancilla single-photon state in the FSF output mode examined by homodyne detection and η'_{H} is the heralding efficiency registered by the multi-mode FSF heralding detector, such that $\eta'_{\mathrm{H}} \geq \eta_{\mathrm{H}}$.

For $M = 1$ the problem is single-mode and thus the process tensor of equation 5.22 applies. How should the process tensor be modified for $M < 1$? Events where the FSF heralding detector 'clicks' due to detection of part of the ancilla single-photon mode which is not overlapped with the input state or LO corresponds to there having been no interaction between the input state $\hat{\rho}$ and the ancilla. This can be modelled as a probabilistic attenuation process, where the intensity is attenuated by a factor of $1 - R$. The process tensor describing attenuation is given by [60]

$$(\mathcal{E}_{\mathrm{att}})^{mn}_{jk} = \sqrt{\frac{m!n!}{j!k!}} \frac{\sqrt{\eta}^{j+k}(1-\eta)^{m-j}}{(m-j)!} \delta_{m-j,n-k}, \tag{5.24}$$

where η is the fraction of the incoming intensity which is passed to the output mode of the beam splitter, i.e. $\eta = R$ (see figure 5.2).

Finally, the complete process tensor describing the realistic FSF operation as depicted in figure 5.5 is given by

$$\boxed{\mathcal{E}_{\mathrm{FSF}} = M\Big[\eta_{\mathrm{H}}\mathcal{E}_1 + (1-\eta_{\mathrm{H}})\mathcal{E}_0\Big] + (1-M)\eta_{\mathrm{det}} R \mathcal{E}_{\mathrm{att}},} \tag{5.25}$$

where R is the FSF beam splitter reflectivity and η_{det} is the quantum efficiency of the heralding detector – both of which must be included explicitly as multiplicative factors for the attenuation component in order that the success probability is correctly accounted for.*

5.2 Quantum progress tomography

Quantum process tomography (QPT) aims to reconstruct the completely-positive trace non-increasing map $\mathcal{E}$ by probing the process with a set of known input states and performing known measurement at the output [52, 35]. As with QST, the measurements performed must be tomographically complete and furthermore, the input probe states must span the input Hilbert space $\mathcal{H}$ on which the process acts [240]. Methods for QPT relying on direct inversion of experimental data will most likely lead to a reconstructed operator $\mathcal{E}$ which is not physical [49]. To this end, a maximum-likelihood approaches to QPT was developed [241, 71, 49], which has the advantage of ensuring the reconstructed process is physical, i.e. it should be a completely-positive (CP) trace non-increasing map [49].

5.2.1 Maximum-likelihood reconstruction

The Jamiołkowski-Choi isomorphism between linear CP maps $\mathcal{E}$ from operators on the Hilbert space $\mathcal{H}$ to operators on the Hilbert space $\mathcal{K}$ and positive semidefinite operators $\hat{E}$ on the Hilbert space $\mathcal{H} \otimes \mathcal{K}$ enables a simplification of the analysis of QPT [49]. Using this isomorphism the process output state $\hat{\rho}'$ may be expressed as

$$\hat{\rho}' = \mathrm{Tr}_{\mathcal{H}} \left[\hat{E} \hat{\rho}^T \otimes \hat{\mathcal{I}}_{\mathcal{K}} \right] , \tag{5.26}$$

*Note that both of these factors are included implicitly within $\mathcal{E}_{1,0}$.

where $\hat{\rho}$ is the input state and the explicit relation between $\mathcal{E}$ and $\hat{E}$ is given by

$$\hat{E} = \sum_{m,n,j,k} \mathcal{E}_{jk}^{mn} |m\rangle\langle n| \otimes |j\rangle\langle k|. \tag{5.27}$$

To perform QPT, assume the process is probed by M different probe states $\{\hat{\rho}_m\}$, $m = 1...M$ and measurements described by POVM elements $\hat{\Pi}_i$ are carried out on each corresponding output state $\mathcal{E}(\hat{\rho}_m)$. Experimentally, one records the relative frequency f_{mi} with which each measurement outcome $\hat{\Pi}_i$ is observed for each input probe state $\hat{\rho}_m$. The relative frequency is an estimate of the underlying probability such that

$$f_{mi} \approxeq p_{mi} = \mathrm{Tr}\left[\mathcal{E}(\hat{\rho}_m)\hat{\Pi}_i\right] = \mathrm{Tr}\left[\hat{E}\hat{\rho}_m^T \otimes \hat{\Pi}_i\right], \tag{5.28}$$

where the Jamiołkowski-Choi isomorphism of equation 5.26 has been invoked. The aim of QPT is to estimate the operator $\hat{E}$ from knowledge of the input states $\hat{\rho}_m$ and the relative frequencies f_{mi}, given a *known* set of measurements $\hat{\Pi}_i$. This can be achieved by maximum-likelihood estimation, where the estimated operator $\hat{E}$ should maximise the functional [242, 71, 49]

$$\begin{aligned} \mathcal{L}(\hat{E}) &= \sum_{m,i} f_{mi} \ln p_{mi} - \mathrm{Tr}\left[\hat{\Lambda}\hat{E}\right], \\ &= \sum_{m,i} f_{mi} \ln \mathrm{Tr}\left[\hat{E}\hat{\rho}_m^T \otimes \hat{\Pi}_i\right] - \mathrm{Tr}\left[\hat{\Lambda}\hat{E}\right], \end{aligned} \tag{5.29}$$

where $\hat{\Lambda} = \hat{\lambda} \otimes \hat{\mathcal{I}}_{\mathcal{K}}$ and λ is a matrix of Lagrange multipliers that account for the trace-preservation condition such that $\mathrm{Tr}_{\mathcal{K}}[\hat{E}] = \hat{\mathcal{I}}_{\mathcal{H}}$.* For the operator $\hat{E}$ which maximizes the functional of equation 5.29, the functional should be stationary for small changes $\delta\hat{E}$ at

*This condition follows from the fact that for the map to be trace-preserving $\mathrm{Tr}_{\mathcal{K}}[\hat{\rho}'] = \mathrm{Tr}_{\mathcal{H}}[\hat{\rho}]$, where $\hat{\rho}$ and $\hat{\rho}'$ are the process input and output states respectively. This must hold for all possible states, thus leading to the condition $\mathrm{Tr}_{\mathcal{K}}[\hat{E}] = \hat{\mathcal{I}}_{\mathcal{H}}$.

this point. Thus an extremal equation can be obtained by varying equation 5.29 with respect to $\hat{E}$ such that [49]

$$\delta\mathcal{L}(\hat{E}) = \mathcal{L}(\hat{E} + \delta\hat{E}) - \mathcal{L}(\hat{E}) = 0. \tag{5.30}$$

This leads to the expression

$$\mathrm{Tr}\left[\left(\sum_{m,i} \frac{f_{mi}}{p_{mi}} \hat{\rho}_m^T \otimes \hat{\Pi}_i - \hat{\Lambda}\right) \delta\hat{E}\right] = 0, \tag{5.31}$$

which must hold for all $\delta\hat{E}$ such that $\hat{E} = \hat{\Lambda}^{-1}\hat{K}\hat{E}$ [49], where operator $\hat{K}$ is given by

$$\hat{K} = \sum_{m,i} \frac{f_{mi}}{p_{mi}} \hat{\rho}_m^T \otimes \hat{\Pi}_i. \tag{5.32}$$

An iterative approach can be employed to find solution $\hat{E}$ maximizing the likelihood functional of equation 5.29 starting from an unbiased initial operator such as the identity process, such that $\hat{E}_{(0)} = \mathcal{I}_{\mathcal{H}\otimes\mathcal{K}}/\mathrm{dim}[\mathcal{K}]$. Owing to Hermicity a suitable operator for iterations is given by [49]

$$\boxed{\hat{E}_{(n+1)} = \hat{\Lambda}_{(n)}^{-1}\hat{K}_{(n)}\hat{E}_{(n)}\hat{K}_{(n)}\hat{\Lambda}_{(n)}^{-1}} \tag{5.33}$$

which constitutes the iterative maximum-likelihood algorithm for QPT, where $\hat{\Lambda}_{(n)} = \hat{\lambda}_{(n)} \otimes \hat{\mathcal{I}}_{\mathcal{K}}$ is determined by tracing equation 5.33 over output Hilbert space $\mathcal{K}$ and employing the trace-preservation condition $\mathrm{Tr}_{\mathcal{K}}[\hat{E}] = \hat{\mathcal{I}}_{\mathcal{H}}$, leading to [49]

$$\hat{\lambda}_{(n)} = \left(\mathrm{Tr}_{\mathcal{K}}[\hat{K}_{(n)}\hat{E}_{(n)}\hat{K}_{(n)}]\right)^{1/2}. \tag{5.34}$$

5.2.2 Probabilistic processes

In the preceding section it was assumed that the process being reconstructed was trace-preserving, that is to say deterministic, such that the constraint $\mathrm{Tr}_{\mathcal{K}}[\hat{E}] = \hat{\mathcal{I}}_{\mathcal{H}}$ was applied during the reconstruction procedure. However, most quantum operations are heralded by observing a particular measurement outcome during a preparation step [243, 244, 153, 131], and are thus inherently non-deterministic.

In the maximum-likelihood algorithm for QPT, reconstruction of probabilistic CP maps is achieved by artificially extending the output Hilbert space such that $\mathcal{K}_{\text{tot}} = \mathcal{K} \oplus \mathcal{K}_{\text{fail}}$, where the one-dimensional space $\mathcal{K}_{\text{fail}}$ is spanned by a fictitious state $|\emptyset\rangle$ associated with POVM element $\hat{\Pi}_{\emptyset}$ [49]. When the process is unsuccessful, the output state is assumed to be $|\emptyset\rangle$. During the experiment, the frequency of failure*, denoted $f_{m\emptyset}$, is recorded and employed within the modified likelihood functional such that

$$\mathcal{L}(\hat{\hat{E}}) = \sum_{m,i} f_{mi} \ln p_{mi} + \sum_{m} f_{m\emptyset} \ln p_{m\emptyset} - \mathrm{Tr}\left[\hat{\Lambda}\hat{E}\right]. \tag{5.35}$$

The essence of the reconstruction procedure is the same as that presented above where the CP map $\hat{\hat{E}}$ is trace-preserving. One can then extract the operator corresponding to the 'success' events by projecting $\hat{\hat{E}}$ onto the subspace $\mathcal{H} \otimes \mathcal{K}$ [49].

5.2.3 Coherent state QPT

In 2008 Lobino *et al.* introduced a technique for performing QPT by probing with coherent states and performing homodyne measurements of the process output states [56]. Initially relying on a regularized form of the P-function, the technique was later refined to entirely

*Note that in some circumstances it is not possible to know the frequency of failure. An example of this would be an experiment employing a continuous-wave pumped down-converter. In this case, a trial is not well defined *per se*. However, when working with pulsed sources a trial can be defined as sending a pump pulse into non-linear medium where down-conversion takes place.

avoid the quasi-probability representation [60]. Known as coherent-state quantum process tomography (csQPT), the technique offers the advantage that the coherent states used as probes are easily produced in the laboratory. To date, csQPT has been employed to characterize a quantum memory [245], photon subtraction and addition [131], and most recently the multi-mode process of a beam splitter [246].

The same maximum-likelihood procedure outlined in the preceding section has been applied to csQPT [61]. In this case, the measurement operators $\hat{\Pi}_i$ correspond to projectors onto quadrature eigenstates, see section 3.3, and the input states density matrices correspond to coherent states such that $\{\hat{\rho}_m\} = \{|\alpha_m\rangle\langle\alpha_m|\}$. Viewed in this sense, there is actually nothing remarkable about csQPT – it simply relies on that fact that the coherent states form a suitable set of input probes and balanced homodyne detection proves a robust and efficient method for performing a tomographically complete set of measurements on the procss output states.

5.3 Complete characterization of realistic Fock state filter

Fock state filtration was first demonstrated experimentally by Sanaka *et al.* in 2006 [157] and later by Resch *et al.* in 2007 [158]. Both experimental demonstrations were similar in that the non-linear absorption property of the filter was inferred from two- and four-fold coincidence measurements performed for incident one- and two-photon Fock states respectively as the filter input state $\hat{\rho}$. The beam splitter reflectivity R was varied and the Hong-Ou-Mandel visibility [16] recorded for the two input Fock states. Operation of the filter consistent with the theory presented in section 5.1.1 was inferred by noting that for an incident one-photon Fock state the best visibility occurred for $R = 1/2$ and for an incident two-photon Fock state for $R = 2/3$ [157, 158].

Although these experiments go some way towards demonstrating the filter operation, such coincidence measurements are inherently post-selected on preservation of photon-number, and are thus loss insensitive – thus masking the effect of non-unit heralding efficiency and to some extent enabling a degree of number-resolution in the APD heralding detector.* Furthermore, probing the filter with Fock states does not enable preservation of coherence between Fock layers to be verified. Resch *et al.* pointed out that [158]

> The Fock-state filter could be tested by creating a number-state superposition, applying the filter, and tomographically measuring the resulting state. In practice, each step of this naive approach is impractical: creating non-classical number-state superpositions is onerous and they are easily destroyed by loss; the Fock-state filter requires an ancilla photon on demand and a perfect-efficiency number-resolving detector; and tomography needs high-efficiency homodyne measurement.

However, the technique of csQPT – which emerged after publication of the work of reference [158] – does not require the use of non-classical number-state superpositions to probe a quantum process. Furthermore, although ideal filter operation which requires a perfect number-resolving detector and ancilla photon state may not be achievable, there is nevertheless merit in probing the non-ideal process. Thus with this argument in mind, to verify the realistic model of FSF developed in section 5.1.2, csQPT is performed with an experimental implementation of the FSF operation, enabling reconstruction of the process tensor $\mathcal{E}_{\mathrm{FSF}}$ from experimental data.

5.3.1 Experimental setup: FSF

The complete optical schematic of the setup used to perform csQPT of the FSF operation is shown in figure 5.8 and is split into four distinct stages: (a) preparation of the ancilla single photon $\hat{\rho}_{\mathrm{a}}$, (b) preparation of coherent states $\hat{\rho}_m = |\alpha_m\rangle\langle\alpha_m|$ used to probe the

*For example, if it is known that two photons have been sent into the beam splitter (i.e. a single-photon ancilla and a single-photon probe) then the measurement is post-selected on two-fold coincidence measurements in the two beam splitter output ports. This means the heralding detector of the FSF operation can only have detected a single photon (ignoring dark counts).

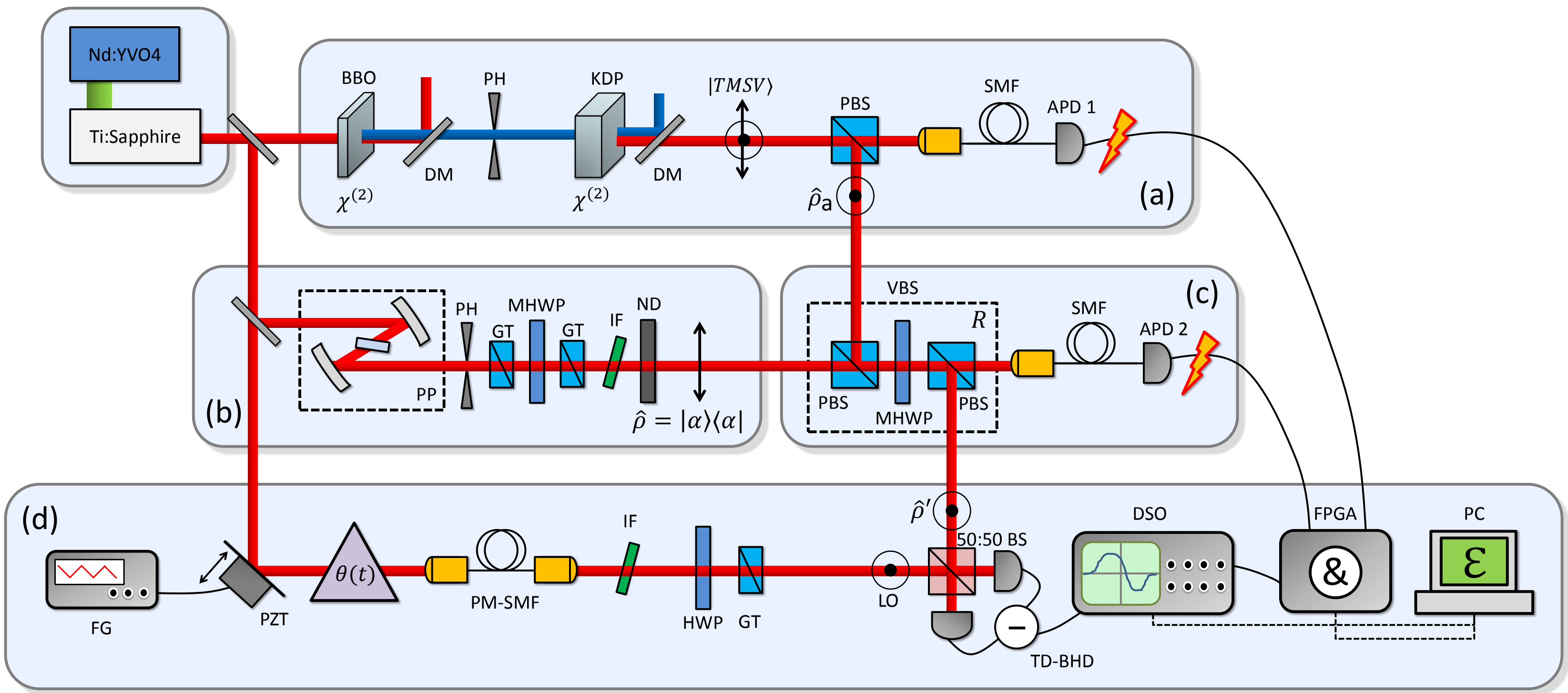

Figure 5.8: Experimental setup for performing csQPT of the Fock state filter. The output of a Ti:Sapphire oscillator is split into 3 spatial paths to serve as the pump for second-harmonic generation (SHG), the coherent state probes and the local oscillator (LO). (a) The SHG output pumps an 8 mm thick KDP crystal where Type-II degenerate spontaneous parametric down-conversion (SPDC) occurs. The output modes from the down-converter are separated at a polarizing beam splitter (PBS). One mode is coupled into a single-mode fiber (SMF) and detected with APD 1 to herald the single photon ancilla state $\hat{\rho}_a$. (b) The pulse train for the coherent state probes is reduced in repetition rate using a pulse picker (PP). Spatial and spectral filtering is achieved using a pinhole (PH) and interference filter (IF) respectively. The probe state amplitude control consists of a half-wave plate (HWP) situated between two Glan-Taylor polarizers (GT) followed by neutral density (ND) filters. (c) The coherent state $\hat{\rho} = |\alpha\rangle\langle\alpha|$ and heralded ancilla state $\hat{\rho}_a$ are combined at a variable beam splitter (VBS). One output mode of the VBS is coupled to a SMF and detected with APD 2 to herald the success of the FSF process. (d) The FSF output state $\hat{\rho}'$ is combined with the LO on a 50:50 beam splitter to perform balanced homodyne detection. A digital storage oscilloscope (DSO) triggered from the APDs records the time-domain balanced homodyne detector (TD-BHD) output. The success probability is recorded with an FPGA. The LO phase $\theta_{\mathrm{LO}}(t)$ is swept by a piezo-electric transducer (PZT), driven with a triangular wave from a function generator (FG).

FSF operation, (c) the FSF beam splitter and heralding measurement and (d) homodyne detection of the FSF output state $\hat{\rho}'$ to perform complete csQPT.

The ancilla single photon $\hat{\rho}_{\mathrm{a}}$ is prepared by spontaneous parametric down-conversion, as described in chapter 3, where APD 1 is used as the heralding detector for the ancilla state. The heralding efficiency η_{H} in the mode examined by homodyne detection is assessed at regular intervals during the QPT experiment by directing the ancilla state directly to the BHD by rotating the motorized half-wave plate (MWHP) in the FSF variable beam splitter (VBS). The VBS comprises a polarizing beam splitter (PBS) to combine the ancilla and probe states into a single spatial mode followed by the MHWP and a second PBS to enable any beam splitter ratio to be selected, figure 5.8(c). In addition, the heralding efficiency of the ancilla state as measured by the FSF heralding detector (APD 2) denoted η'_{H} is recorded using an FPGA. Measurement of η_{H} and η'_{H} allows the multi-mode parameter M to be determined, section 5.1.2.

During the experiment the heralding efficiency in the mode examined by homodyne detection was determined to be $\eta_{\mathrm{H}} = 0.45 \pm 0.04$, after correction for the BHD efficiency.* The full quantum state tomography results for the ancilla state are presented in figure 5.9. The heralding efficiency registered by APD 2 was determined to be $\eta'_{\mathrm{H}} = 0.62$, after correction for the APD efficiency $\eta_{\mathrm{apd}} = 0.45$. This gives a value of the multi-mode parameter $M = \eta_{\mathrm{H}}/\eta'_{\mathrm{H}} = 0.45/0.62 = 0.73$ which implies that approximately 1 out of 4 heralding events of the FSF operation correspond to the case where the LO and probe state mode does not 'overlap' with the ancilla state, section 5.1.2.

A fraction of the original 830 nm Ti:Sapphire oscillator output is split off to serve as both the local oscillator (LO) for performing balanced homodyne detection and to prepare

*Note that this heralding efficiency is slightly lower than the value quoted in chapter 4. This is partly due to the increased number of optical elements between the SPDC source and the BHD in the FSF setup. In addition, it was discovered that the KDP crystal in the SPDC source had become damaged by the time of the QPT experiment, potentially causing a further reduction in η_{H}.

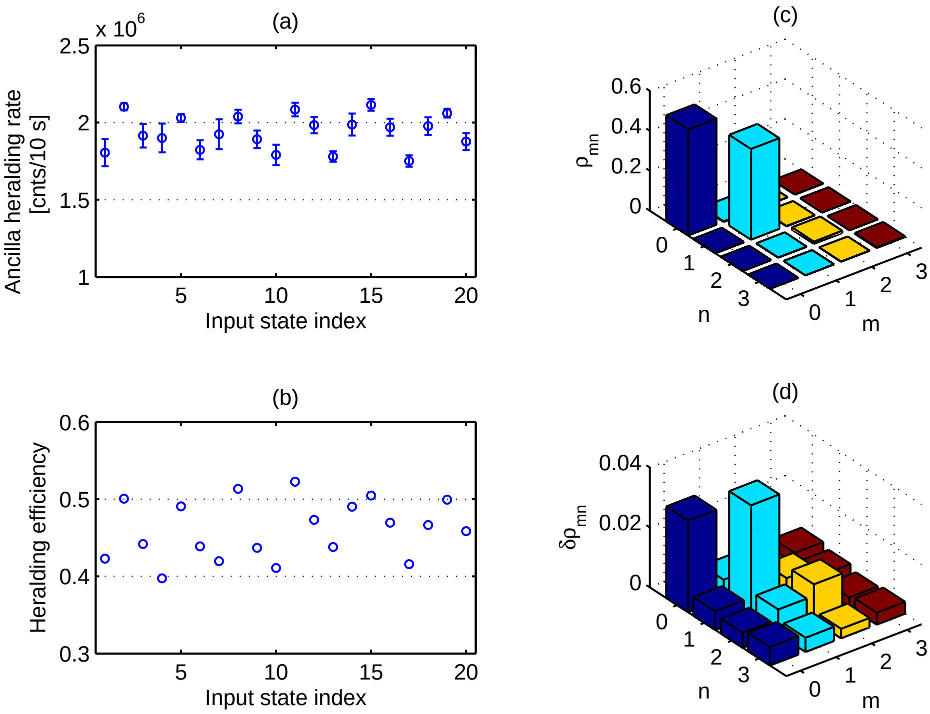

Figure 5.9: Characterization of ancilla single-photon Fock state $\hat{\rho}_{\mathrm{a}}$ by homodyne tomography. (a) Heralding rate registered by APD 1, recorded by the FPGA. Fluctuations are mainly due to instability of the 415 nm pump beam pointing. (b) Heralding efficiency η_{H} of the ancilla single photon in the spatial-temporal mode examined by the BHD. Fluctuations in the heralding efficiency are correlated with fluctuations in the heralding rate, thus indicating the fluctuations are due to the SPDC pump pointing instability. (c) Reconstructed density matrix and (d) associated errors obtained by performing QST of the ancilla state. Higher-order photon-number terms are negligible. The heralding efficiency of the ancilla single-photon state is determined to be $\eta_{\mathrm{H}} = 0.45 \pm 0.04$.

the coherent state probes to perform csQPT, figure 5.8. The probe state repetition rate is reduced by a factor of 20 using a pulse picker (APE Angewandte Physik & Elektronik GmbH pulseSelect kit) and subsequently spatially filtered with a pinhole and spectrally filtered with an interference filter (Semrock LL01-830-12.5) to match the mode of the local oscillator, figure 5.8(b). The probe state amplitude control consists of a motorized half-wave plate (MHWP) sandwiched between two Glan-Taylor polarizers followed by a set of neutral density filters to enable attenuation to the few-photon level. The repetition rate reduction of the probe states serves two purposes. Firstly, it prevents the FSF heralding detector (APD 2) from becoming saturated when relatively bright coherent states are used to probe the filter. Secondly, it enables access to a set of 'dark' pulses in the vacuum state with which to contemporaneously calibrate the BHD during data acquisition. This ensures the acquired quadrature data are free from systematic errors due to drifting of the BHD [121]. The input probe state amplitude $|\alpha|$ is accurately measured throughout the experiment by performing conventional maximum-likelihood quantum state tomography of the input states directly, by adjusting the MHWP within the FSF VBS to direct the probe state to the BHD.

The FSF process is heralded by detection with a single APD, figure 5.8(c). At first this may seem surprising given that the discussion in section 5.1.2 implied that using for example an 8-bin TMD would result in operation of the filter much closer to the ideal. In fact, when losses within the TMD are taken into account, even an 8-bin device does not yield performance significantly better than a single APD for filter input states at the few-photon level. To demonstrate this, the process tensor was calculated according to the realistic model developed in section 5.1.2 for two POVMs: one describing the 'click' event of an APD with 50% quantum efficiency (according to equation 3.2) and the other

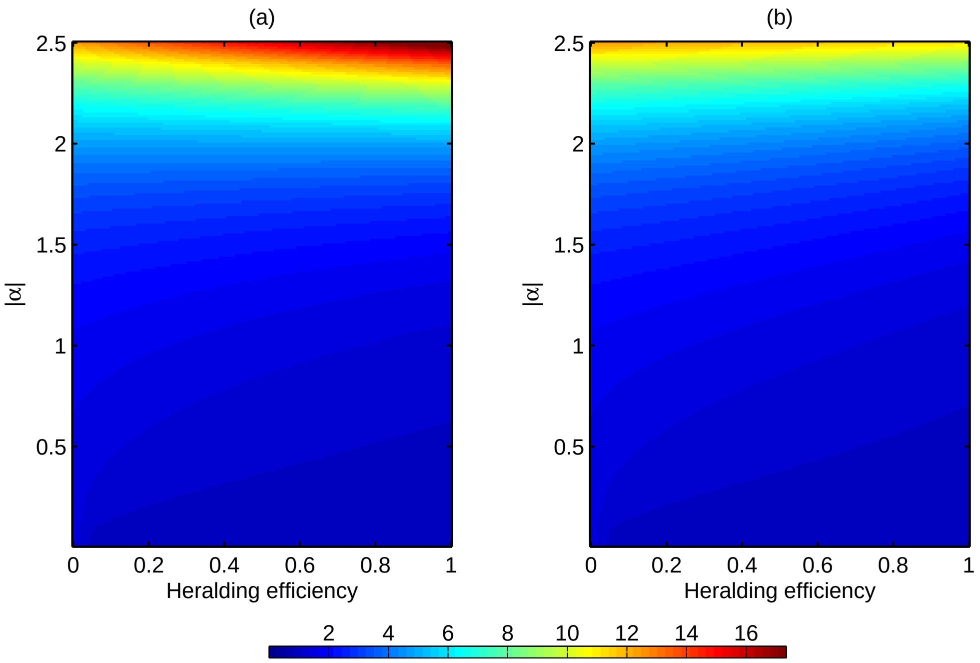

Figure 5.10: Parameter Δ quantifying the quality of the filter operation, equation 5.36, for the FSF operation heralded by (a) an APD with 50% quantum efficiency, (b) an 8-bin TMD also with 50% quantum efficiency, with varying input coherent state amplitude $|\alpha|$ and ancilla single-photon state heralding efficiency.

describing the 'one-click' event of a TMD,* also with 50% quantum efficiency. A figure of merit quantifying the filter operation in a single number was sought to compare the performance of the filter for the two heralding detectors. To this end, a parameter Δ is defined according to

$$\Delta = \frac{P'(n)}{P(n)} = \frac{\langle n|\hat{\rho}'|n\rangle}{\langle n|\hat{\rho}|n\rangle}, \tag{5.36}$$

where n is the Fock layer removed by the filter, i.e. $n = R/(1-R)$, and $\hat{\rho}$ ($\hat{\rho}'$) is the pre- (post-) filter state. For perfect filter operation $\Delta = 0$, whereas for non-ideal operation $\Delta > 0$. Δ was evaluated for a range of input coherent state amplitudes as a function of the ancilla state heralding efficiency for the two detector POVMs under consideration.† The results are shown in figure 5.10 and demonstrate that Δ is not significantly larger when heralding with a single APD compared with an 8-bin TMD for realistic a detector efficiency, for input states in the few-photon regime.‡ Moreover, heralding with an 8-bin TMD would require significantly more complex trigger logic.

5.3.2 Experimental test: attenuation

Before attempting full csQPT of FSF, in order to test the algorithm with experimental data the process tensors corresponding to different levels of optical attenuation were reconstructed. The optical setup is identical to that for FSF shown in figure 5.8 except that the down-converter is not used, i.e. the ancilla state $\hat{\rho}_{\mathrm{a}}$ is in the vacuum state and no conditioning measurement is performed at the output of the VBS, figure 5.8(c). The

*The theoretical POVM for a TMD can be found in [247] or [248].

†For this simulation it was assumed the heralding detector was single-mode, i.e. $M = 1$

‡Of course, far superior performance could be achieved by using a high-efficincy number-resolving detector such as a superconducting transition-edge sensor [79]. However, no such device was available for this work and in any case, the objective is to experimentally verify the model developed in section 5.1.2, rather than achieve ideal filter operation *per se*.

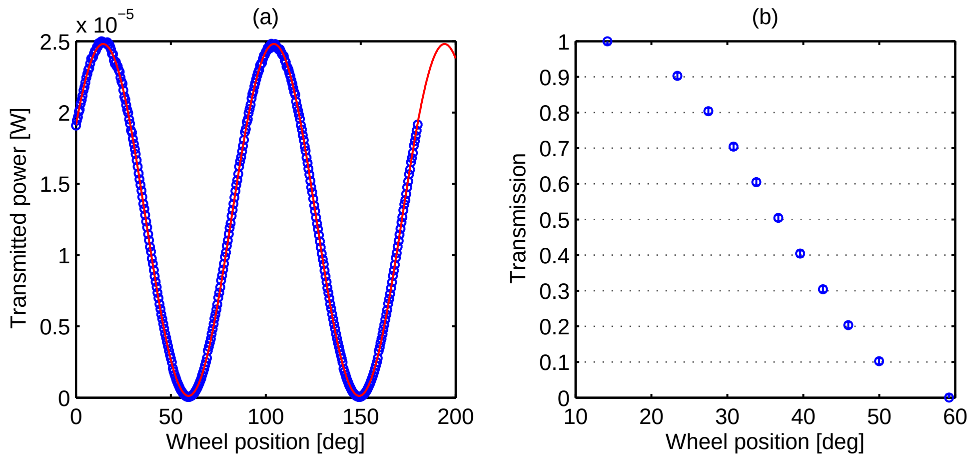

Figure 5.11: Bright light calibration of the VBS. (a) Power transmitted to VBS output mode as a function of MHWP angle with sinusodial fit (red line). (b) MHWP angle giving rise to particular transmissions as extracted from fit.

VBS thus acts as a variable attenuator which is first calibrated with a bright beam by measuring the fraction of the input intensity which is transmitted to the output mode where balanced homodyne detection is usually performed for csQPT. The output power in this case is simply measured with a power meter as the MHWP in the VBS is rotated, figure 5.11(a). By performing a sinusoidal fit to the measured data the MHWP angle for a given transmission can be calculated, figure 5.11(b). This constitutes the bright light calibration of the variable attenuator.

To perform csQPT, 11 coherent states to act as probe states are prepared in the same manner as described in section 5.3.1. The amplitudes $|\alpha|$ are distributed in approximately equal steps between 0.3 and 1.8. For each probe state, a total of 2.5×10^5 pulses are recorded by the BHD. The phase of the LO is swept using a piezo-mounted mirror driven with a triangle wave voltage from a function generator. The LO phase θ is extracted from time-ordered sequences of the state quadrature samples. The smoothed quadrature value as a function of time enables estimation of θ since $\langle \hat{X}_\theta(t) \rangle \propto A + B\cos(\theta)$, where constants A and B can be determined from the vacuum state calibration and $\langle ... \rangle$ denotes the time-domain smoothing operation which averages out the noise associated with quantum

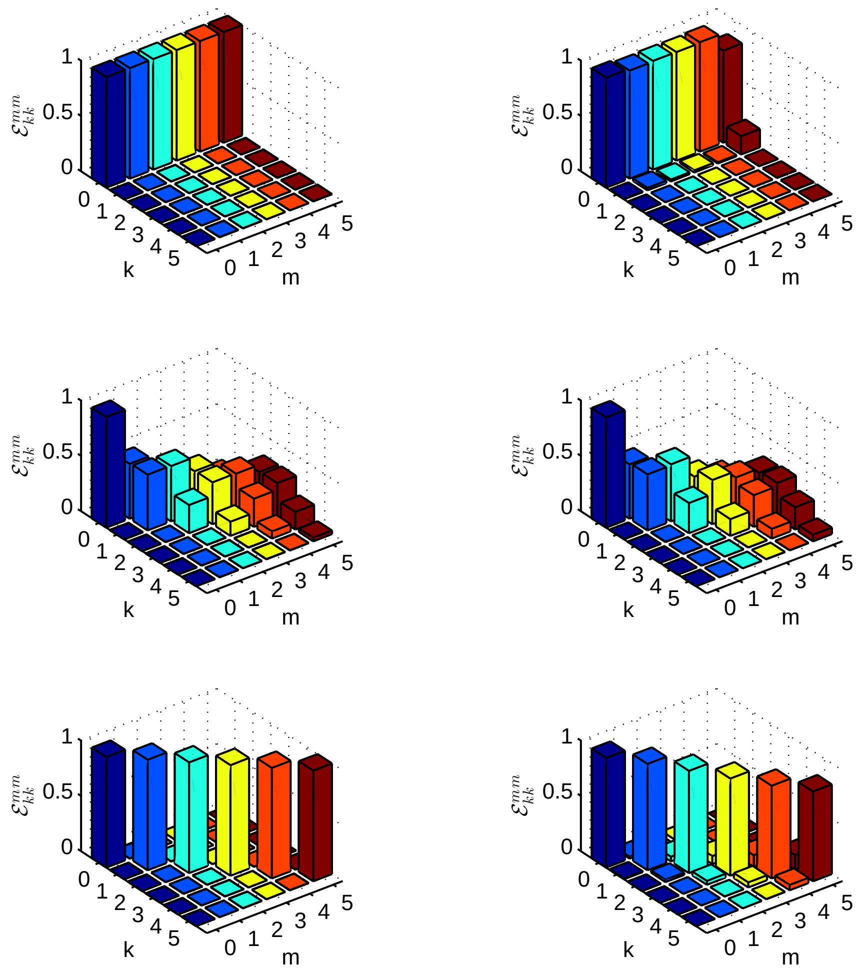

Figure 5.12: Diagonal elements $\mathcal{E}_{kk}^{mm}$ of the process tensors for attenuation by 100% (top), 50% (middle) and 0% (bottom). The left hand column shows the theoretical tensors according to equation 5.24 whilst the right hand column displays the experimentally reconstructed tensors.

fluctuations of the state field quadrature.

The inversion algorithm requires the set of input density matrices $\{\hat{\rho}_m\}$ and the measurement outcome frequency distributions for the process output states $\{\hat{\rho}'\} = \{\mathcal{E}(\hat{\rho}_m)\}$. The input state density matrices are obtained by performing maximum-likelihood QST on quadrature data acquired for the input probe states with the attenuator set to unit transmission. The frequency distributions for the process output states are formed by binning the acquired quadrature samples for the output states into 51 quadrature bins spanning the interval $[-5, 5]$ and 20 phase bins on the interval $[0, \pi]$. Each bin is associated with a POVM element* $\hat{\Pi}_i$, used in the iterative procedure of equation 5.33.

The process tensors for attenuation by 100%, 50% and 0% are reconstructed and compared with the prediction for the process tensor according to the bright light calibration, where the theoretical tensor describing the attenuation process is given by equation 5.24. A total of 100 iterations are performed for each reconstruction, according to the iterative reconstruction procedure of reference [61]. The iterative algorithm is implemented in MATLAB and each reconstruction takes approximately 5 minutes on an Intel Core i7 desktop computer with 28 GB RAM. The results are presented in figure 5.12 and indicate excellent agreement between the predicted and reconstructed process tensors, with small discrepancies in the $n = 5$ Fock layer most likely due to insufficient overlap with the input probe state density matrices [61].

5.3.3 Experimental reconstruction of FSF process

To perform csQPT of the FSF operation the full optical setup of figure 5.8 is employed. A total of 20 probe states are used to probe the filter, with amplitude $|\alpha|$ ranging from 0.1 to

*For a large number of bins these correspond approximately to the quadrature eigenstate projectors of equation 3.31. However, if larger bins are used, the approximation is no longer good and thus one must invoke projectors of the form $\hat{\Pi}_i \propto \int_{X_i-\delta X/2}^{X_i+\delta X/2} \int_{\theta_i-\delta\theta/2}^{\theta_i+\delta\theta/2} |X_{\theta,i}\rangle\langle X_{\theta,i}|$, where δX and $\delta\theta$ are the bin sizes for the quadrature and LO phase respectively.

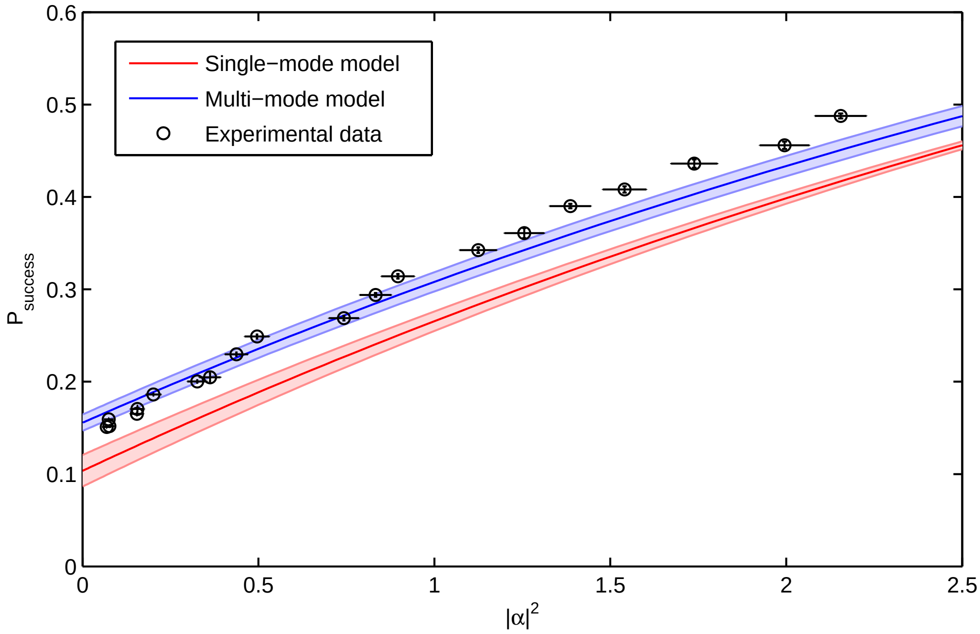

Figure 5.13: Success probability of the FSF operation as a function of the input coherent state intensity $|\alpha|^2$. Experimental values recorded by the FPGA (black circles), prediction of multi-mode model of FSF (blue) and single-mode model (red).

1.5. Data acquisition from the BHD is triggered by three events occurring in coincidence: 1) a control pulse indicating the pulse picker has generated a probe state $\hat{\rho} = |\alpha\rangle\langle\alpha|$, 2) an ancilla photon heralding event from APD 1 and 3) a FSF success heralding event from APD 2. The internal pattern trigger function of the oscilloscope is used to automatically select these events. The oscilloscope is operated in 'Fast Frame' mode such that for each input probe state, 40 sets of 8000 frames are recorded, i.e. a total of 3.2×10^5 quadrature samples for each process output state $\hat{\rho}' = \mathcal{E}(|\alpha\rangle\langle\alpha|)$. Each frame consists of one pulse containing a single sample of the output state and 9 pulses containing samples of the vacuum state to calibrate the BHD, see chapter 3.

Since FSF is a conditional process, heralded by the simultaneous generation of an ancilla single-photon state $\hat{\rho}_\mathrm{a}$ and the detection of a photon in the FSF heralding mode, it is necessary to record the success probability $P(|\alpha|^2)$ of the operation in order to perform csQPT, as discussed in section 5.2.2. The data captured by the BHD do not contain information about the success probability. The success probability is monitored using a coincidence counting circuit implemented in a field-programmable gate array (FPGA), figure 5.8(d). The output TTL pulses from APD 1 and APD 2 are split between the DSO for triggering data acquisition from the BHD and the FPGA to record the success probability. The measured success probability as a function of the probe state intensity $|\alpha|^2$ is shown in figure 5.13 in addition to the predicted success probability according the single-mode and multi-mode models of FSF derived in section 5.1.2, where the parameter values measured in section 5.3.1 are used. The input probe state intensities $|\alpha|^2$ were determined by performing QST of the input probe states and performing a least-squares fit to the photon-number statistics of a coherent state*. The experimentally measured success probability $P(|\alpha|^2)$ is consistent with the multi-mode model of FSF, using the parameter values determined in 5.3.1 – whilst the single-mode model predicts a consistently lower probability of success. The emergent discrepancy between the multi-mode model success probability and the experimental success probability for $|\alpha|^2 > 1.25$ is an indication that the probe state mode and LO mode are not perfectly overlapped – as was assumed in order to decompose the problem into two effective modes. However, in principle these modes can be made to match perfectly since they are derived from the same laser.

The raw quadrature samples for the FSF output states recorded by the BHD are binned with 30 phase bins in the interval $\theta \in [0, \pi]$ and 601 quadrature bins in the interval $X \in [-5, 5]$. The reconstruction is performed up to a maximum photon number $n = 6$. Thus the reconstructed process tensor is able to predict the evolution of an arbitrary input state $\hat{\rho} = \sum_{m,n=0}^{6} \rho_{mn} |m\rangle\langle n|$ on the truncated input Hilbert space $\mathcal{H}$. The maximum-likelihood

*The MHWP in the VBS, figure 5.8(c), is set to transmit the whole input probe state to the BHD, thus enabling QST of the input probe states.

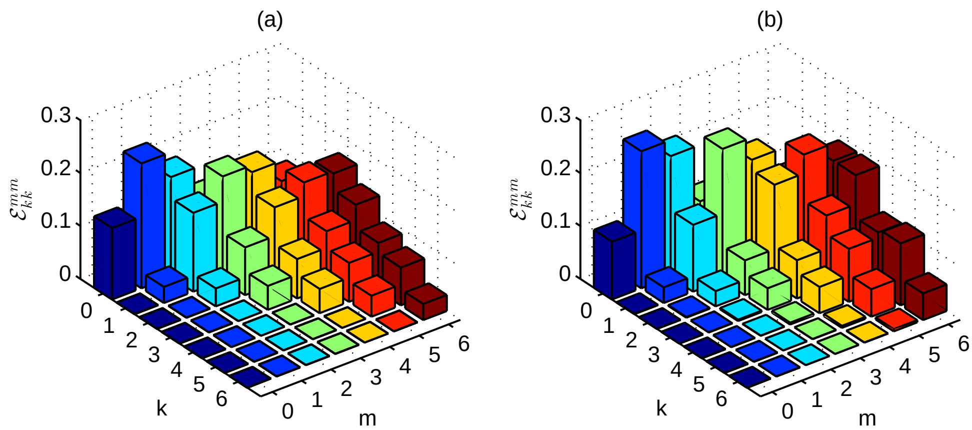

Figure 5.14: Diagonal elements $\mathcal{E}_{kk}^{mm}$ of the model (a) and reconstructed (b) process tensors for Fock state filtration. The model tensor was calculated according to equation 5.25 with parameter values as determined in section 5.3.1.

reconstruction algorithm took approximately 6.5 hours to perform 150 iterations.* Figure 5.14(a) shows diagonal elements $\mathcal{E}_{kk}^{mm}$ of the model process tensor (equation 5.25), where the model parameters are those determined in section 5.3.1, and (b) of the reconstructed process tensor.

On inspection the model and reconstructed diagonal elements are similar, both in terms of the structure within each input Fock layer and the sum of each input Fock layer, which represents the success probability for a particular input Fock state. A more quantitative analysis is afforded by calculating the fidelity between the reconstructed and model process tensors according to

$$F = \mathrm{Tr}\left(\sqrt{\sqrt{\hat{E}_{\text{recon}}}\hat{E}_{\text{model}}\sqrt{\hat{E}_{\text{recon}}}}\right)^2, \tag{5.37}$$

where the processes are represented as operators† on Hilbert space $\mathcal{H} \otimes \mathcal{K}$ according to

*The iterations are stopped when the change in the likelihood approaches the machine precision corresponding to negligable change of the process tensor elements. Furthermore, dilution of $\mu = 0.5$ was used [249] to curb oscillations in the likelihood at the start of the reconstruction. Thus the iteration operator (equation 5.32) becomes $\hat{K} \to \mu\hat{K} + (1-\mu)\hat{I}_{\mathcal{H}\otimes\mathcal{K}}$. Monotonic increase of the likelihood is guaranteed for $0 < \mu \ll 1$ [61].

†In order that the fidelity F be bounded such that $0 \leq F \leq 1$ it is necessary to normalize each operator

the Jamiołkowski-Choi isomorphism, section 5.2.1. The fidelity thus defined is a function of the whole process tensor, i.e. not just the diagonal elements displayed in figure 5.14.

The fidelity is a multi-dimensional function of the model parameters and would ideally be maximal for the parameter values experimentally determined in section 5.3.1. To this end, two cuts of the fidelity as a function of the model parameters were calculated. Figure 5.15(a) shows the fidelity as a function of the ancilla state heralding efficiency η_{H} and APD efficiency η_{apd} used in the model of equation 5.25, with the beam splitter reflectivity $R = 0.5$ and the multi-mode parameter $M = 0.73$, as determined in section 5.3.1. The fidelity peaks for the expected parameter values of $\eta_{\mathrm{H}} = 0.45 \pm 0.04$ and $\eta_{\mathrm{apd}} = 0.45$. Notice also that the fidelity is only weakly dependent on the APD efficiency assumed in the model. Figure 5.15(b) shows the fidelity as a function of the ancilla state heralding efficiency η_{H} and the beam splitter reflectivity R for fixed $M = 0.73$ and $\eta_{\mathrm{apd}} = 0.45$. In the experiment, the beam splitter reflectivity was set to $R = 0.5$ according to the calibration presented in figure 5.11, i.e. the filter was set to filter out the $n = 1$ component, equation 5.8. The fidelity peaks in the region of $R = 0.5$, adding further confirmation that the reconstructed process tensor is consistent with that predicted by the full model, equation 5.25.

A further test performed on the reconstructed tensor is to compare the fidelity between output quantum states predicted by the model and by the reconstructed tensor. To this end, 10^5 random input quantum states were generated for increasing values of maximum photon number n_{max} in the state. The random input states were evolved according to the reconstructed and model tensors to give two normalized output states for each random

$\hat{E}$. This still preserves the relative success probability for each input Fock layer and effectively amounts to changing the overall 'gain' of the process.

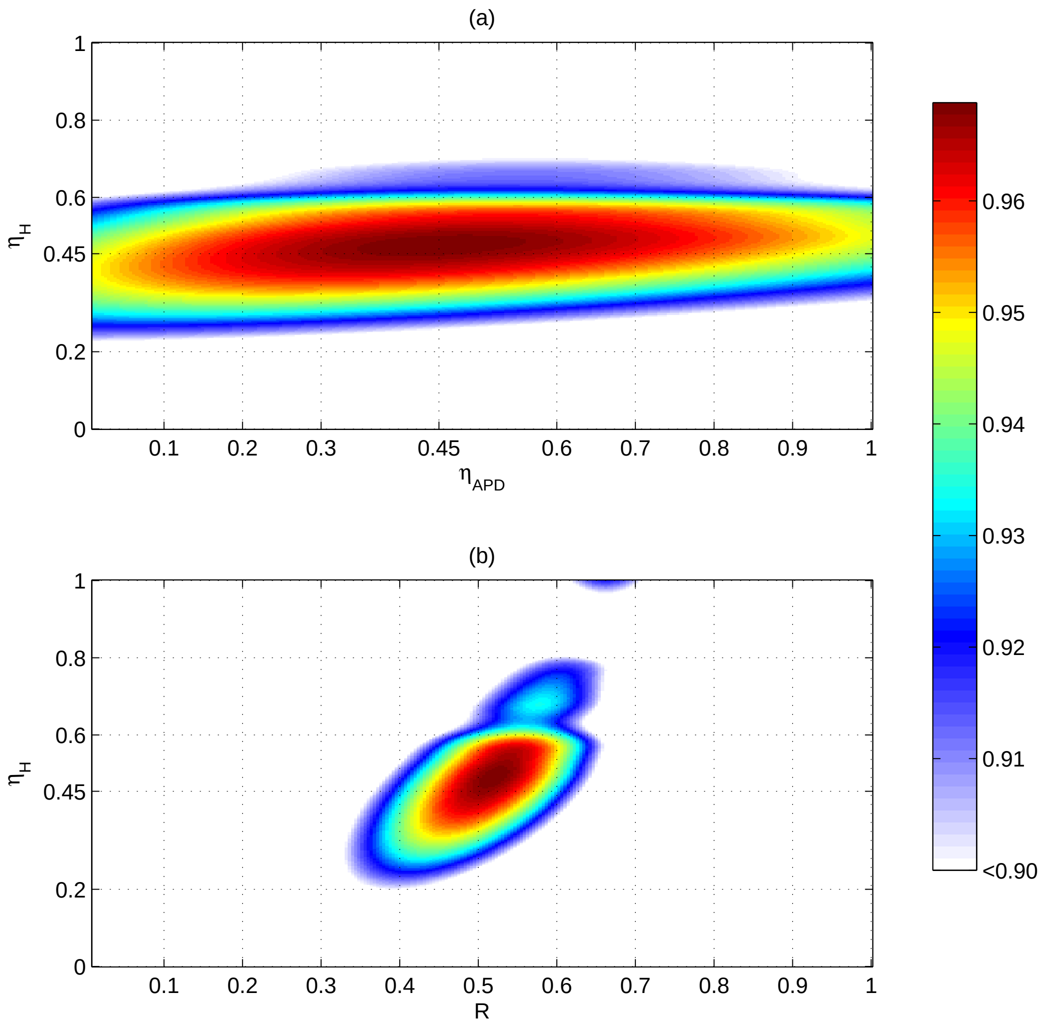

Figure 5.15: Fidelity between reconstructed tensor and model tensor of FSF as a function of model parameter values. (a) Fidelity as a function of the APD efficiency η_{APD} and heralding efficiency η_{H} for fixed $M = 0.73$, $R = 0.5$. (b) Fidelity as a function of the beam splitter reflectivity R and heralding efficiency η_{H} for fixed $M = 0.73$ and $\eta_{\mathrm{APD}} = 0.45$. The fidelity peaks in the region of the parameters values determined in section 5.3.1. Thus the model tensor provides the best match to the reconstructed tensor for the expected parameter values – further indicating validity of the model tensor, equation 5.25.

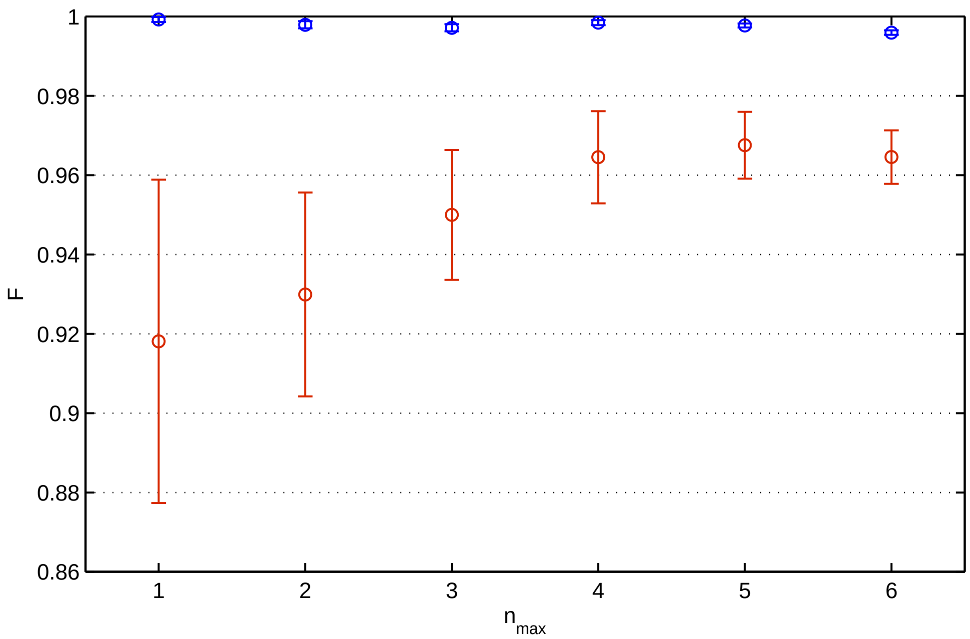

Figure 5.16: Fidelity between output states due to reconstructed tensor and model tensor as a function of maximum photon number $n_{\max}$ where the model assumed was the full realistic FSF model developed in section 5.1.2 (blue) and a simple 50% attenuation process (red).

input state, according to

$$\hat{\rho}'_{\text{recon}} = \frac{\mathcal{E}_{\text{recon}}(\hat{\rho})}{\text{Tr}\left[\mathcal{E}_{\text{recon}}(\hat{\rho})\right]}, \qquad \hat{\rho}'_{\text{model}} = \frac{\mathcal{E}_{\text{model}}(\hat{\rho})}{\text{Tr}\left[\mathcal{E}_{\text{model}}(\hat{\rho})\right]}. \tag{5.38}$$

The standard definition for fidelity between two quantum states was employed, equation 4.59. From the set of input states both the mean fidelity and standard deviation could be estimated as a function of n_{max}, blue data in figure 5.16. First, note that the fidelity between the output states is effectively unity when the model process tensor corresponds to the realistic FSF model developed in section 5.1.2, with the parameter values taken as those experimentally determined in section 5.3.1.

As a demonstration that the reconstructed tensor is distinct from the process of 50% attenuation, the same fidelity was calculated where the model tensor was taken to be attenuation by 50%, red data in figure 5.16. The results indicate that the full model describing realistic FSF developed in section 5.1.2 provides a far better description of the state evolution than a simple 50% attenuation process. The reason why this result is important can be understood by examining the schematic of FSF in figure 5.2. If the heralding measurement and ancilla state would have no effect on the filter input state then the effect of the operation would simply be to attenuate the input state by a factor $1 - R$. Thus by demonstrating that the reconstructed tensor corresponding to the experimental filter is distinct from such an attenuation process the presence of a non-trivial state transformation due to the FSF operation is identified.

The FSF beam splitter reflectivity $R = 0.5$ for this experiment, thus according to equation 5.8 the filter should be preferentially filtering out the $m = 1$ photon-number component of the input state $\hat{\rho}$. The *un-normalized* photon-number statistics at the filter output given that m photons were incident at the filter input are given by

$$\tilde{P}(k|m) = \mathcal{E}_{kk}^{mm}, \tag{5.39}$$

where as usual $\mathcal{E}_{kk}^{mm}$ are the diagonal elements of the process tensor and $\tilde{P}$ denotes the fact that the distribution is not normalized. Summing over k gives the success probability of the FSF operation given that m photons were incident. For the following analysis, the photon-number statistics at the filter output are of interest only when the operation is successful, i.e. a heralding event is observed. Thus the distribution $\tilde{P}(k|m)$ can be normalized according to

$$P(k|m) = \frac{\tilde{P}(k|m)}{\sum_k \tilde{P}(k|m)}, \tag{5.40}$$

where $P(k|m)$ is the *normalized* photon-number distribution at the filter output given that m photons were incident to the filter *and* a heralding event was observed.

From the reconstructed tensor, $P(1|1) = 0.101$, and $P(0|1) = 0.899$ – in other words, if a single-photon is sent into the filter and a heralding event is observed, approximately 9 times out of 10 the filter output state is the vacuum state – thus the filter exhibits approximately 90% loss for a single-photon state. If the filter were a passive optical element exhibiting linear loss then one would expect

$$P(m|m) = P(1|1)^m, \tag{5.41}$$

since for linear loss if a single-photon has a probability P of transmission then a two-photon state has a probability P^2 of being preserved and so forth for the higher-order Fock states. This linear loss behaviour is plotted in figure 5.17 (red circles), based on the

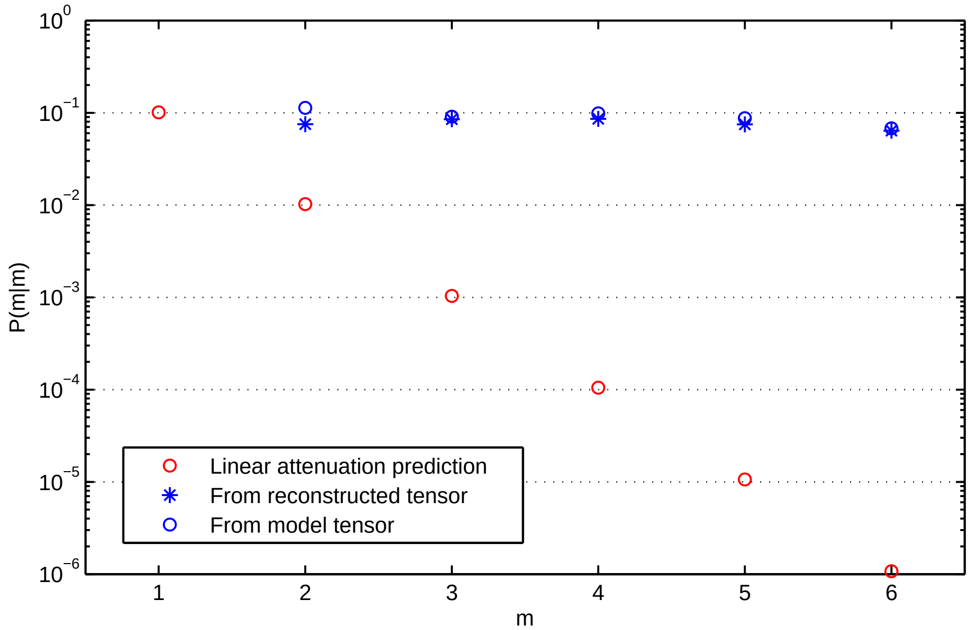

Figure 5.17: Probability to obtain m photons at the filter output given m photons were incident to the filter *and* a heralding event is observed, denoted $P(m|m)$. Red circles: based on a linear loss model, blue asterisks: extracted from reconstructed process tensor, blue circles: according to model process tensor. The filter exhibits a non-linear response since it effectively presents a greater loss to the $m = 1$ photon Fock state compared with higher-order Fock states.

value $P(1|1) = 0.101$ extracted from the reconstructed tensor, and applying equation 5.41 to predict the behaviour of the filter if it were considered as linear loss. This is compared against the *actual* values $P(m|m),\ m > 1$, extracted from the reconstructed process tensor – plotted as the blue asterisks in figure 5.17.

Remarkably, the reconstructed process tensor predicts an approximately flat probability of 'survival' $P(m|m)$ for the higher-order input Fock states, whereas the values based on a linear loss model decrease factorially. Thus the filter effectively exhibits significantly less loss for Fock states of order $m > 1$ than for the $m = 1$ Fock state – consistent with the beam splitter reflectivity $R = 1/2$, equation 5.8. This demonstrates that the filter is preferentially removing the $m = 1$ photon-number component from the input state [157, 158] – i.e. the filter exhibits a non-linear response to the input state. $P(m|m)$ was also calculated from the model process tensor of equation 5.25 using the parameter values obtained in section 5.3.1 – plotted as the blue circles in figure 5.17. The predicted values for $P(m|m)$ are in excellent agreement with those extracted from the reconstructed tensor and again are completely distinct from the behaviour of linear loss.

5.4 Summary

In this chapter photon-level quantum operations acting on a single electromagnetic field mode were considered, with specific attention paid to Fock state filtration [157] – a quantum operation which relies on measurement-induced non-linearity to remove specific photon-number components from an arbitrary quantum state. The process tensor describing the filter operation was derived for the ideal case where perfect ancilla states and photon-number resolving detection are assumed. A realistic model of the filter operation was developed incorporating experimental imperfections which was then put to the test by performing quantum process tomography of an experimental implementation of the Fock state filter.

Although the practical filter operation was found to be far from ideal, the full process tensor reconstruction goes beyond previous filter demonstrations based on Hong-Ou-Mandel interference [157, 158] – where no attempt at realistic modelling of the filter operation was attempted. The key experimental challenges were identified – with the main issue being the unambiguous determination of photon-number in the FSF heralding mode. With the emergence of high-efficiency photon-number resolving detectors [79, 250] and improved sources of photonic Fock states [251] it should be possible to achieve near-ideal Fock state filtration and hence also photon-catalysis [153] – enabling the generation of arbitrary quantum optical states in the continuous-variable domain. The results presented here indicate that coherent-state quantum process tomography [60, 61] should serve as a reliable diagnosis tool for such photon-level quantum operations.

6

Calibration of Quantum Detectors

One often relies on instruments being well calibrated in order to make judgements and decisions based on their readings. Consider for example the altimeter – an instrument which reports the height above sea level and is to be found on board every commercial airliner. Without accurate calibration for the atmospheric pressure at sea level, the altimeter reading could be wildly invalid, with obvious consequences for aviation safety. Accurate knowledge of the operation of a measurement apparatus is important for both fundamental experimental physics and technological applications. In the classical domain, instruments are often calibrated against known references or standards such that the raw output of the instrument, for example a continuous voltage, may be linked to some underlying physical quantity of interest such as temperature or pressure.

In quantum mechanics, measurements and thus measurement apparatuses are described mathematically by a POVM $\{\hat{\Pi}_i\}$, introduced in chapter 2. Accurate knowledge of the POVM enables the probability of each measurement outcome to be faithfully predicted for a known quantum state of the system under measurement. Importantly, methods for quantum state tomography (QST) and quantum process tomography (QPT) rely on accurate calibration of the measurement apparatus. Incorrect calibration will lead to systematic errors in determination of the quantum state or process [252]. With the emergence of quantum-enhanced technologies, it is becoming increasingly important to have well-calibrated detectors for the successful realization of real-world applications such as quantum key distribution, quantum random number generation and quantum-enhanced metrology [31]. Within the framework of the POVM description, calibration constitutes determining the POVM describing a measurement apparatus.

In the domain of quantum optics and thus photodetection at the few-photon level, the task of detector calibration was initially tackled by so-called 'absolute' calibration [253–255], which enables accurate calibration of the detector quantum efficiency by exploiting entangled photon sources. However, such methods do not constitute complete determination of the POVM and may rely on phenomenological assumptions about the workings of the detector. Complete POVM reconstruction was demonstrated experimentally for optical detectors in in 2008 [53], using a method which has come to be known as quantum detector tomography (QDT) – in line with QST/QPT.

In this chapter an overview of detector calibration by QDT is presented, followed by the description of a more recent technique known as *fitting of data patterns* (FDP) which enables reliable QST by incorporating calibration of the detector in the state reconstruction procedure [72, 256]. An experimental demonstration of the FDP method is presented and the method is contrasted with QDT. Finally, the original proposal of QST by the FDP method is extended to the tomography of quantum processes, thus enabling QPT with calibrated detectors.

6.1 Quantum detector tomography

As outlined above, one approach to detector calibration is to determine the complete POVM set $\{\hat{\Pi}_i\}$ describing the apparatus [257, 242, 258]. Knowledge of $\{\hat{\Pi}_i\}$ then allows the measurement outcome statistics for input state $\hat{\rho}$ to be predicted according to the

Born rule

$$p_i = \mathrm{Tr}(\hat{\Pi}_i \hat{\rho}). \tag{6.1}$$

Application of the determined POVM set $\{\hat{\Pi}_i\}$ in a quantum state or process reconstruction algorithm, such as the maximum-likelihood algorithm discussed in section 3.3, should guarantee that the estimate is not degraded by systematic errors which could potentially arise if a phenomenological model of the detector were assumed.* Such a complete characterization has become known as quantum detector tomography (QDT) and was first demonstrated experimentally by Lundeen *et al.* in 2008 [53] – where the POVM sets describing intensity detection by an avalanche photodiode (APD) and an 8-bin time-multiplexed detector (TMD) were reconstructed.

To perform QDT, a set of M known probe states denoted $\{\hat{\rho}_m\}$ are prepared and sent to the detector under scrutiny. The probability of registering outcome i for input state $\hat{\rho}_m$, denoted $p_{i|m} = \mathrm{Tr}(\hat{\Pi}_i \hat{\rho}_m)$, can only be determined precisely in the limit that an infinite number of trials are performed. Practically speaking one estimates the underlying probabilities $p_{i|m}$ from the observed frequency distributions $f_{i|m}$ according to

$$p_{i|m} = \mathrm{Tr}(\hat{\Pi}_i \hat{\rho}_m) = \sum_{j,k=1}^{d} \hat{\Pi}_{i,jk} \hat{\rho}_{m,kj} \approx \frac{f_{i|m}}{\sum_i f_{i|m}}, \tag{6.2}$$

where d is the dimension of the truncated Hilbert space. The estimates of $p_{i|m}$ obtained for a set of probe states $\{\hat{\rho}_m\}$ enable the POVM to be determined by linear inversion of equation 6.2 [242]. However, such a direct inversion does not guarantee that the reconstructed POVM elements are positive semi-definite Hermitian operators and correctly

*Although statistical errors due to the finite set of data will remian.

normalized such that

$$\hat{\Pi}_i \geq 0, \qquad \sum_{i=1}^{N} \hat{\Pi}_i = \hat{I}, \tag{6.3}$$

where N is the total number of measurement outcomes which can be registered with the detector.* A more robust approach is to define a cost function which can then be minimized subject to the constraints of equation 6.3. One possibility is to to define a likelihood functional in a similar vein to that used for state tomography [242], such that

$$\mathcal{L}\left(\{\hat{\Pi}_i\}\right) = \prod_{i=1}^{N}\prod_{m=1}^{M}\left[\mathrm{Tr}\left(\hat{\Pi}_i\hat{\rho}_m\right)\right]^{f_{i|m}}. \tag{6.4}$$

Maximization of equation 6.4 will find the POVM set most likely to give the observed outcome frequency distributions. Importantly, the maximization may be performed subject to the constraints of equation 6.3 such that a physically plausible estimate of $\{\hat{\Pi}_i\}$ is obtained [242].†

For QDT to be mathematically feasible it is required that the set of probe states $\{\hat{\rho}_m\}$ be tomographically complete [53, 259, 260]. That is to say, the chosen probe states must form a basis for the truncated Hilbert of dimension d in which the reconstruction is performed. In situations where it is desired to reconstruct the photon-number representation of the POVM, the Hilbert space must be truncated at some maximum photon number $K = d - 1$, typically chosen to be at least equal to the number of photons required to saturate the detector [261, 94]. Furthermore, experimental considerations dictate that the probe states should be easily and rapidly generated in the laboratory.

So-called ancilla-assisted approaches to QDT rely on non-classically correlated twin-

*Strictly speaking for application of the POVM set in a MLE state reconstruction it is sufficient that $\sum_i \hat{\Pi}_i = A\hat{I}$, where A is some constant.

†If the POVM satisfies the constraints of equation 6.4 and is a solution to equation 6.2 then the maximum-likelihood solution is nothing but the solution obtained by linear inversion [242].

beam states, e.g. those generated by SPDC, to prepare probe states through conditional measurements on one mode of the twin-beam made by a well-known detector or 'tomographer' [258]. Brida *et al.* demonstrated the ancilla-assisted approach in 2012, where the POVM of a simple two-APD multiplexed detector was reconstructed [262]. However, the approach is hampered by the limited brightness of available twin-beam states and the requirement for a 'tomographer' which must be well-calibrated in the quantum regime.

A simple choice of experimentally feasible probe states are the coherent states, $|\alpha\rangle$. A finite set of tomographically complete coherent states $\{|\alpha\rangle\langle\alpha|\}$ may be prepared by attenuating and phase-shifting the output of a laser [53, 259, 260]. With coherent state probes, the inferred measurement outcome probabilities are nothing but the rescaled Husimi Q-distributions [54, 168] such that

$$p_{i|m} = \langle\alpha_m|\hat{\Pi}_i|\alpha_m\rangle = \pi Q_i(\alpha_m), \quad \alpha_m \in \mathbb{C}. \tag{6.5}$$

Thus it is clear that in principle, since the Q-distribution carries complete information about $\hat{\Pi}_i$, the POVM elements may be obtained through probing the detector with coherent states.

The POVM elements may be expanded in the photon-number basis. In the case of direct detection, i.e. photon counting, the measurement statistics should be independent of the phase of the input state. This means the POVM elements are diagonal in the photon-number basis [53, 259, 260] such that

$$\hat{\Pi}_i = \sum_{k=0}^{K} \theta_k^{(i)} |k\rangle\langle k|, \tag{6.6}$$

where $|k\rangle$ denotes the k-photon Fock state, $\theta_k^{(i)}$ are the expansion coefficients for detector outcome i and K is the maximum photon-number. Linearity of equation 6.5 with respect to the probe states and POVM elements allows it to be expressed in matrix form as

$$P = F\Pi, \tag{6.7}$$

where F contains the diagonal matrix elements of the probe states (assumed to be known), Π contains the diagonal elements of the set of POVM operators and P is a matrix formed of the measured frequency distributions [53, 259, 260]. Convex optimization may then be performed to determine Π and hence the POVM set $\{\hat{\Pi}_i\}$ by minimizing the difference between the measured statistics and the predicted statistics according to

$$\boxed{\min\left\{||P - F\Pi||_2 + g(\Pi)\right\}, \qquad \text{s.t.} \;\; \hat{\Pi}_i \geq 0, \;\; \sum_{i=1}^{N} \hat{\Pi}_i = \hat{I},} \tag{6.8}$$

where $||...||_2$ denotes the matrix 2-norm. A penalty function $g(\Pi)$ has been introduced to prevent over-fitting [259]. Such regularization is a common technique in the field of inverse problems [263]. Care must be taken to ensure the choice of $g(\Pi)$ does not impose a model on the reconstruction, i.e. it should be detector independent [259]. The form of this optimization constitutes a semi-definte program which can be solved using standard toolboxes such as SDPT [264] for MATLAB.

To date, QDT has been successfully applied in a variety of experimental settings [53, 260, 265–268, 94, 269], predominantly to investigate photon-counting detectors with limited numbers of detection outcomes N. Zhang *et al.* proposed [261] and experimentally demonstrated [94] a modified technique known as recursive QDT in 2012, to address reconstruction of off-diagonal elements of the POVM. The technique operates as above, where each diagonal of the POVM is obtained through a separate convex optimization procedure according to equation 6.8. The experimenter can choose the number of off-diagonals to reconstruct, based on considerations such as decoherence due to loss and phase instability

[94]. The recursive technique enabled the first QDT of a weak-field homodyne detector [93]. POVM reconstruction was primarily carried out in order to confirm validity of a phenomenological model of the detector under investigation, the agreement typically being confirmed through a fidelity parameter [53, 265, 94, 266]. Thus the reconstructed POVMs were not directly applied in a state or process tomography algorithm.

QDT as defined in [53, 259, 261] requires that the set of probe states should be chosen such that the brightest state saturates the detector response. This ensures that the full detector behaviour is captured and sets a natural truncation in the photon-number basis at $d-1$, where $d-1=K$ is the number of photons required to saturate the detector [261]. Although this prescription is necessary if the experimenter wishes to reconstruct the complete POVM, in practice only a restricted subspace of dimension (d'), $d'<d$ may be of interest. One such scenario is application of the reconstructed POVM in a quantum state tomography algorithm [115, 90], where the experimenter has *a priori* knowledge that the state is confined to a restricted subspace, e.g. comprises a limited number of photons. Brida *et al.* modified the 'standard' prescription of QDT to enable partial POVM reconstruction without saturating the detector [266]. This was achieved by artificially grouping detector outcomes corresponding to increased numbers of excitations into one bin, such that in the set of N POVM elements $\{\hat{\Pi}_i\}$, the final element $\hat{\Pi}_N$ is given by [266]

$$\hat{\Pi}_N = \hat{I} - \sum_{i=1}^{N-1} \hat{\Pi}_i, \tag{6.9}$$

and the program of equation 6.8 is applied. Such an approach may allow the experimenter to limit the the region of input Hilbert space to a finite domain.

6.2 Fitting of data patterns

Aside from making comparisons between the reconstructed and theoretical POVM for a particular detector, one may ask if it is necessary to perform QDT to extract the POVM if the goal is ultimately to perform reliable QST by using a calibrated detector. In 2010, Řeháček *et al.* proposed a novel method for performing QST which combines calibration of the measurement apparatus with the state reconstruction procedure [72]. Known as the *fitting of data patterns* (FDP), the method entirely bypasses the POVM representation of the detector. This has a number of advantages *viz.*, FDP enables QST with a calibrated detector in one data analysis step – as opposed to two distinct steps required for the QDT+QST approach.* Secondly, the FDP method naturally lends itself to characterization of a measurement apparatus within a well-defined field-of-view set by the experimenter [72, 256]; an issue which is currently not resolved by the QDT approach. Finally, the FDP method makes use of a single, comparatively simple least-squares fit – without the requirement for regularization. This is not only computationally less intensive compared to the QDT+QST approach but also enables efficient propagation of errors. Some of the results reported here have been published [270].

6.2.1 Outline of FDP procedure

The FDP approach – much like QDT – begins by recording the detector response to a set of M known probe states $\{\hat{\rho}_m\}$, figure 6.1(a). Unlike standard QDT where the set of probe states should be tomographically complete in the subspace of dimension d, where $d - 1 = K$ photons saturate the detector [53, 259, 261], the FDP method requires only that the probe states span the region of Hilbert space of interest to the experimenter, i.e.

*Where the POVM set obtained through QDT fitting is employed in a separate algorithm, e.g. maximum-likelihood estimation, to determine the quantum state.

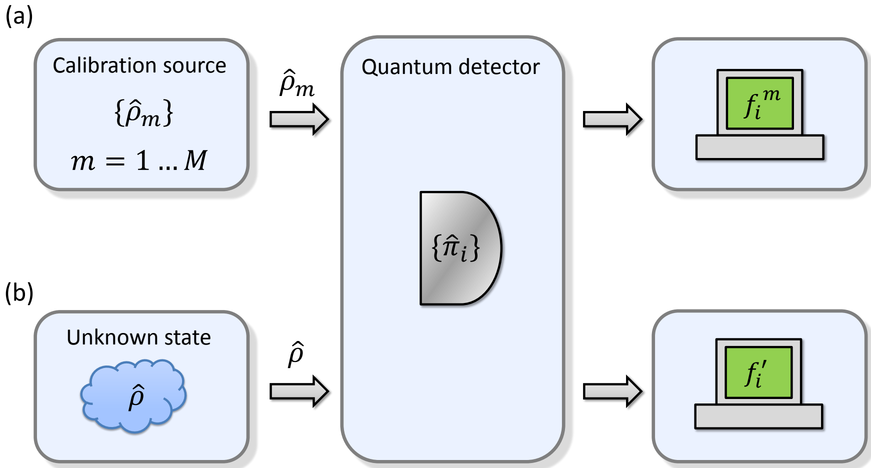

Figure 6.1: Outline of the FDP data acquisition procedure for detector calibration and QST. (a) Known probe states $\{\hat{\rho}_m\}$ are prepared and measured by the detector. Frequency distributions $\{f_i^m\}$ are built up, constituting the data pattern set. (b) An unknown quantum state $\hat{\rho}$ to be estimated is registered by the same detector, from which the measurement outcome frequency distribution f_i' formed.

the region where one wishes to have sensitivity to perform QST.

Multiple copies of each probe state $\hat{\rho}_m$ are prepared and registered by the detector, implicitly described by the POVM set $\{\hat{\Pi}_i\}$, figure 6.1(a). For each probe state $\hat{\rho}_m$ the normalized frequency distribution of measurement outcomes i, denoted f_i^m, is recorded. The set of frequency distributions $\{f_i^m\}$ is known as the data pattern set and constitutes the detector calibration within the field-of-view defined by the probe states. At this stage no attempt is made to process the data pattern set $\{f_i^m\}$ to extract the POVM. Unlike QDT followed by QST, with the FDP approach one cannot describe the detector calibration in isolation to the state tomography itself [72]. To estimate an unknown quantum state $\hat{\rho}$, multiple copies are prepared and registered by the detector under identical operating conditions as for measurement of the data pattern set, figure 6.1(b). The frequency distribution of measurement outcomes for the unknown state, denoted f_i', is determined from the acquired data in the same manner as for the data pattern set.

Let us suppose that the unknown state $\hat{\rho}$ can be adequately represented by a weighted sum of the probe states $\{\hat{\rho}_m\}$ such that the estimated state denoted $\hat{\rho}_{\text{fdp}}$ is given by

$$\hat{\rho}_{\text{fdp}} = \sum_{m=1}^{M} a_m \hat{\rho}_m, \tag{6.10}$$

where $\{a_m\}$ are real-valued expansion coefficients [72, 256]. The goal is to determine coefficients $\{a_m\}$ such that the estimated state $\hat{\rho}_{\text{fdp}}$ is representative of the underlying, unknown state $\hat{\rho}$. The optimal coefficients are found according to the convex optimization procedure [72]

$$\boxed{\min\ E\left(\{a_m\}\right) = \sum_{i=1}^{N} \left(f'_i - \sum_{m=1}^{M} a_m f_i^m \right)^2, \quad \text{s.t.} \sum_{m=1}^{M} a_m = 1, \ \sum_{m=1}^{M} a_m \hat{\rho}_m \geq 0,} \tag{6.11}$$

where $E\left(\{a_m\}\right)$ is the functional describing the distance between the unknown state frequency distribution and the weighted data patterns. The constraints guarantee that the estimated ensemble $\hat{\rho}_{\text{fdp}}$ corresponds to a physical density matrix. Note that one optimization procedure, equation 6.11, is used to perform QST – incorporating the detector calibration through the data pattern set $\{f_i^m\}$. Minimizing $E\left(\{a_m\}\right)$ reduces the difference between the *actual* underlying probability distribution for the unknown state $p'_i \approxeq f'_i$ and that calculated from the estimated state p_i^{fdp} according to the Born rule

$$p_i^{\text{fdp}} = \text{Tr}(\hat{\Pi}_i \hat{\rho}_{\text{fdp}}) = \sum_{m=1}^{M} a_m \text{Tr}(\hat{\Pi}_i \hat{\rho}_m) \approxeq \sum_{m=1}^{M} a_m f_i^m, \tag{6.12}$$

where probability distributions are approximated by their corresponding normalized frequency distributions.

6.2.2 Probe state requirements

As with QDT, the probe states $\{\hat{\rho}_m\}$ should be easily and precisely generated in the laboratory. The Glauber-Sudarshan P-representation dictates that an arbitrary state $\hat{\rho}$ may be expressed in the basis of coherent states such that

$$\hat{\rho} = \int d^2\alpha P(\alpha)|\alpha\rangle\langle\alpha|, \tag{6.13}$$

where $P(\alpha)$ is the P function of the state [17, 271]. Thus if coherent states were chosen as the probe states with the FDP method, the representation of equation 6.10 resembles a discrete P-representation [256]. The accuracy of the representation will depend on the number and phase-space distribution of the chosen set of coherent state probes. If it may be assumed *a priori* that the detector has no phase sensitivity then one might expect that coherent state probes of different phase but identical amplitude will elicit the same response. In this case, it is convenient to use phase-averaged coherent states (PHAVs) defined as

$$\hat{\rho}_m = \frac{1}{2\pi}\int_0^{2\pi} d\theta|\alpha_m\rangle\langle\alpha_m| = \exp\left(-|\alpha_m|^2\right)\sum_{n=0}^{\infty}\frac{|\alpha_m|^{2n}}{n!}|n\rangle\langle n|, \tag{6.14}$$

where $|\alpha_m|$ is the PHAV amplitude. Note that even if the detector does have phase sensitivity, e.g. a BHD, phase-averaged probe states may still be used. In this scenario, the field-of-view of the state tomography is limited to diagonal elements of the density matrix, in other words the photon-number statistics.* Thus the effective field-of-view of the FDP state tomography method is a function both of the intrinsic capabilities of the

*Similarly, one could probe a phase-insensitive detector with a full grid of coherent states. States of equal amplitude but different phase will elicit the same response, and thus these states will contribute equally in the representation of equation 6.10, thus averaging out the phase and obtaining an approximately diagonal density matrix.

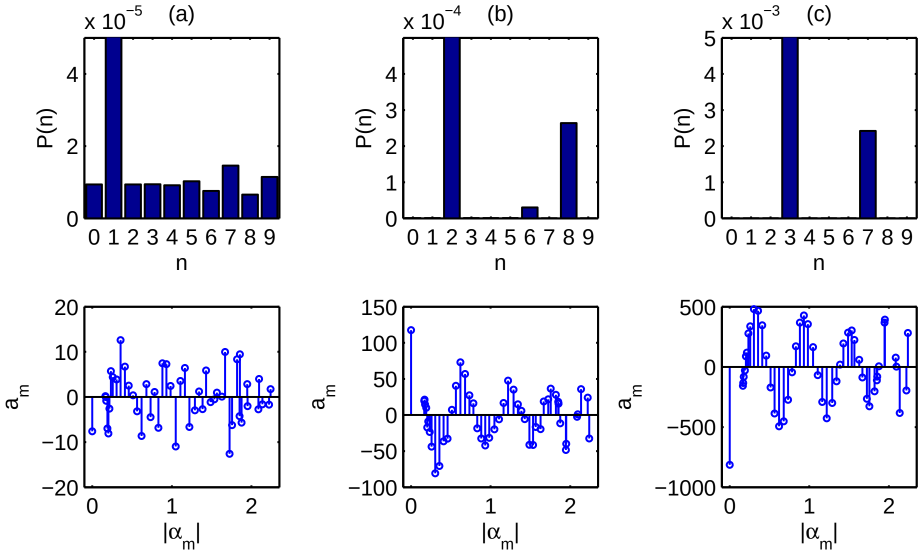

Figure 6.2: Representation of the one- (a), two- (b), and three-photon Fock state (c) in terms of a set of 49 PHAVs. Top: photon-number statistics for each state represented according to equation 6.10, note the y-axis has been scaled to show the small discrepancies from the ideal photon-number statistics. Bottom: optimal coefficients $\{a_m\}$ found according to equation 6.15.

detector and the choice of probe states.

As a demonstration of the representation of non-classical states in terms of a discrete set of PHAVs, the density matrices of the one-, two- and three-photon Fock state were represented in terms of a set of 49 PHAVs with amplitude $|\alpha|$ ranging from 0 to 2.3. To find the optimal set of coefficients $\{a_m\}$ in equation 6.10 for each Fock state, the distance between the target density matrix $\hat{\rho}$ and the estimated density matrix $\hat{\rho}_{\text{est}}$ was minimized

$$\min ||\hat{\rho} - \hat{\rho}_{\text{est}}||_2, \quad \text{s.t.} \sum_{m=1}^{M} a_m = 1, \;\; \hat{\rho}_{\text{est}} \geq 0. \tag{6.15}$$

The representations are presented in figure 6.2. For the m-photon Fock state one expects $P(m) = 1, \;\; P(m' \neq m) = 0$. The results demonstrate that with only 49 probe states the representations are extremely accurate for all three states. Residual probability is of the order 10^{-5} for the one-photon state, 10^{-4} for the two-photon state and 10^{-3} for the three-photon state. In all three cases the fidelity between the target and estimated state exceeds 0.999.

6.2.3 Simulation: optical homodyne tomography

To demonstrate the complete FDP procedure for QST with a calibrated detector, optical homodyne tomography (OHT) of a coherent state superposition was simulated. As discussed in section 3.3, OHT is usually performed either by inverse Radon transform of the acquired quadrature probability distributions or by maximum-likelihood estimation (MLE). The inverse Radon transform method assumes the BHD has a uniform response spanning the full detector output range whilst the MLE method typically assumes a POVM of the form given in equation 3.31. The FDP method on the other hand does not require any such assumption. The coherent state superposition is given by

$$|\psi\rangle = \frac{1}{\sqrt{2}}\left(|\alpha\rangle + |-\alpha\rangle\right), \tag{6.16}$$

where the amplitude $\alpha = \alpha_{\mathrm{R}} + i\alpha_{\mathrm{I}} = (1+i)/\sqrt{2}$ in the simulation. A total of 81 coherent states were used to probe the BHD, with amplitudes forming uniform grid, figure 6.3(a). The maximum coherent state amplitude used was $|\alpha| = 1$. For each state, 9 LO phase settings were simulated, uniformly distributed such that $\theta \in [0, \pi)$. For each LO phase, 10^6 measurements were simulated and the resulting samples were collected into 150 bins for each LO phase. In principle the data patterns should be a function of both X_θ (the quadrature bin centres) and θ (the LO phase). However, the underlying physical meaning of the outcomes is not important (and, in the case of a real experiment, not known) for the FDP approach. Thus the indices labelling the quadrature bins and LO phases can effectively be concatenated to give a generic index of measurement outcomes i. The only

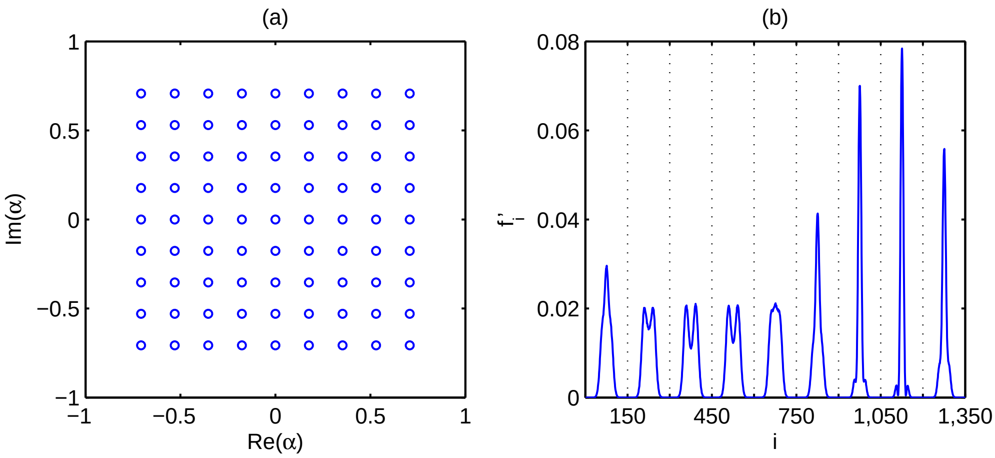

Figure 6.3: (a) Amplitudes of the 81 coherent state probes used in the simulation of OHT by the FDP method. The states are distributed uniformly in phase space. The maximum amplitude $|\alpha| = 1.0$. (b) Simulated measurement outcome frequency distribution f'_i for the coherent state superposition. The quadrature bins (150) and LO phases (9) are concatenated to give one index i. This there are a total of 1350 different measurement outcomes.

caveat for the FDP method to work is that this must be done in a consistent manner for all probe states and unknown states.

The simulated measurement outcome frequency distribution f'_i for the coherent state superposition is shown in figure 6.3(b). The data pattern set $\{f_i^m\}$ obtained for the coherent state probes is not shown. The functional of equation 6.11 was minimized in MATLAB using the Yalmip toolbox [272] to script the minimization programme and SDPT3 [264] to perform the optimization. The optimization procedure took approximately 2 seconds to perform. The target and reconstructed state Wigner functions and density matrices are shown in figure 6.4, and exhibit a fidelity of 0.89. This relatively low fidelity belies the fact that the Wigner functions and density matrices appear to have very similar structure. The chosen set of probe states was verified to be suitable for adequately representing the cat state, and therefore the conclusion is that the chosen LO phases and quadrature binning may not be optimal.*

*No attempt was made to optimize these parameters for the simulation.

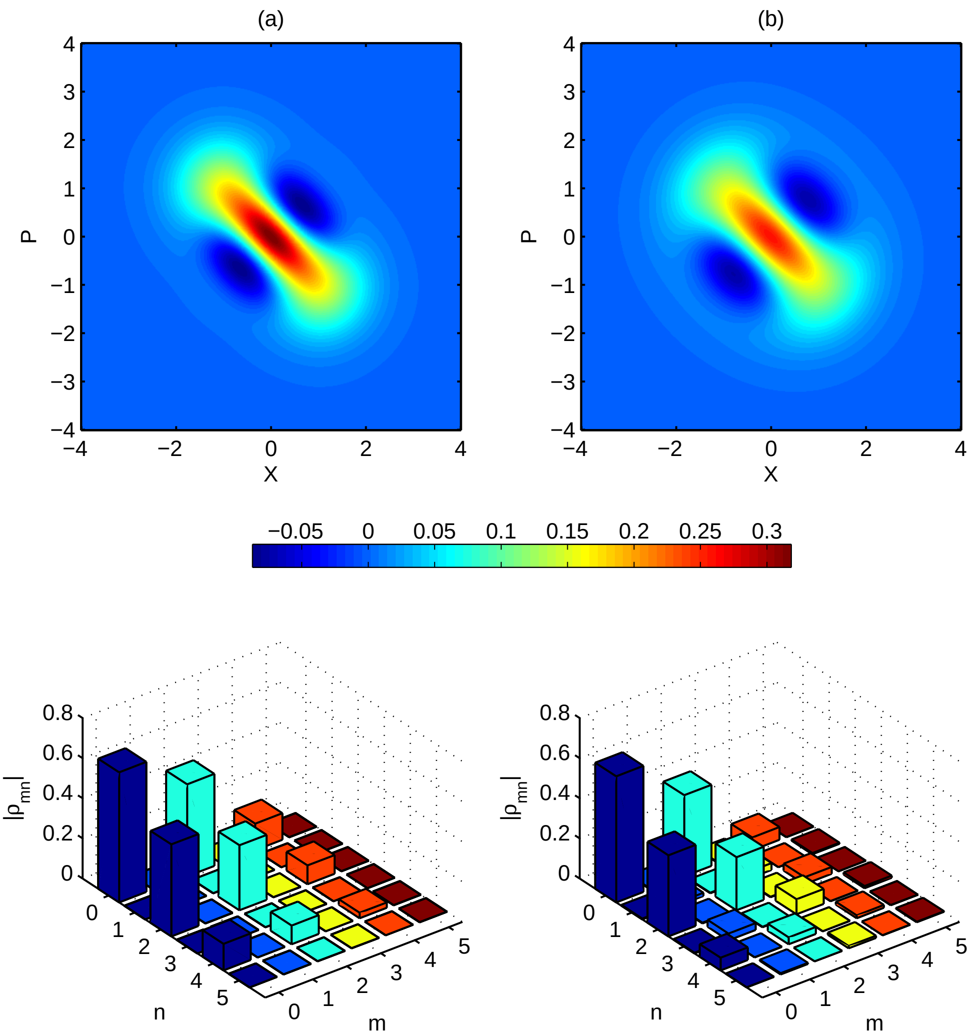

Figure 6.4: Simulation of FDP approach for state estimation of a coherent state superposition. (a) target and (b) reconstructed. Top: Wigner functions $W(X, P)$ and bottom: density matrix absolute values $|\rho_{mn}|$. The fidelity between the target and reconstructed state is 0.89.

At this point it is natural to discuss the question of how many quadrature bins and LO phases are required. Sych *et al.* recently showed that for a truncated Hilbert space of dimension d, there are a total of d^2 linearly independent POVM elements when d different LO phases are used [273]. This sets a limit on the maximum discretization of the quadrature outcomes, i.e. the minimum number of bins. However, what if one does not assume an underlying POVM? This question is relevant to the discussion of the FDP method where a POVM is neither assumed nor determined. In this case, since binning of the measurement outcomes is performed as a post-processing step one can try a range of bin sizes and observe that the structure of the underlying probability distribution is adequately sampled and that the bin size is sufficiently large that statistical noise does not dominate [132]. Outside of OHT, other measurement devices naturally produce a discretized output, e.g. APDs and TMDs, and therefore this ambiguity does not arise.

6.3 Experimental demonstration of the FDP method

To experimentally demonstrate the FDP technique for performing QST with a calibrated detector, the BHD developed in chapter 3 was investigated. Although BHDs are a vital resource for continuous-variable (CV) quantum optics applications [50, 47, 56], there had until now been no attempt to independently characterize a BHD by any method. Although the output voltage of a BHD is typically discretized, the number of possible outcomes is typically still of the order several hundred. Furthermore, unlike photon-counting detectors, it is less clear what the saturation point of a BHD is – since it depends on a number of factors such as the chosen amplifier gain and LO strength. These two factors make application of the standard QDT approach (outlined in section 6.1) more challenging.

A typical BHD designed for use in CV experiments is sensitive to both optical states near the vacuum and relatively bright states comprising several tens of photons. Although

BHDs are capable of exhibiting such a large dynamic range*, in specific applications the experimental conditions dictate the operating parameters, whether in terms of average photon number or the region of optical phase space in which target states lie. Therefore it is sufficient in such scenarios to calibrate the detector 'locally', i.e. in the region of interest. As outlined in section 6.2.2, the FDP approach naturally allows the experimenter to define a calibration field-of-view through the choice of probe states $\{\hat{\rho}_m\}$ – whereas such a clear imposition of calibration locality is yet to be properly defined with the QDT approach.

The target of this experimental demonstration is to perform QST of the non-classical Fock states discussed in chapter 4 by the FDP approach. Since it is assumed *a priori* that the quantum states under investigation are mixtures of Fock states†, it is natural to use PHAV probe states, as discussed in section 6.2.2. This limits the calibration field-of-view to the photon-number statistics of the unknown quantum states, which in the specific case of phase-invariant states constitutes complete QST.‡

6.3.1 Probe state preparation

The PHAVs are generated by attenuating and phase-averaging a pick-off of the Ti:Sapphire oscillator, figure 6.5(a). A piezoelectric transducer (PZT) driven by a triangle wave from a function generator (FG) averages the interferometer phase.§ The 80 MHz repetition rate of the Ti:Sapphire oscillator is first reduced using a pulse picker. The pulse picker was

*Dynamic range often comes at the expense of resolution due to digitizer limitations, as discussed in section 3.4.

†This is well-motivated since the states are obtained by heralding from a TMSV state with a phase-insensitive detector.

‡Note that preparation of a set of coherent states, such as in section 6.2.3, is an experimentally onerous task owing to the requirement of a phase-stabilizer system enabling preparation and measurement of each probe state.

§In theory driving a PZT with a triangle wave should cause phase-averaging since all positions of the mirror and thus phases of the interferometer are sampled equally. However, owing to both non-linearity of the PZT response and random drifts in the interferometer, the phase may not be truly averaged. To this end, the phase was monitored and sorted into 10 bins in the interval $[0, \pi]$. Samples were then rejected at random from bins containing more samples than the least-populated bin – effectively post-selecting a phase-averaged set of data. This procedure has limited impact in practice since the phase was found to be nearly uniformly sampled.

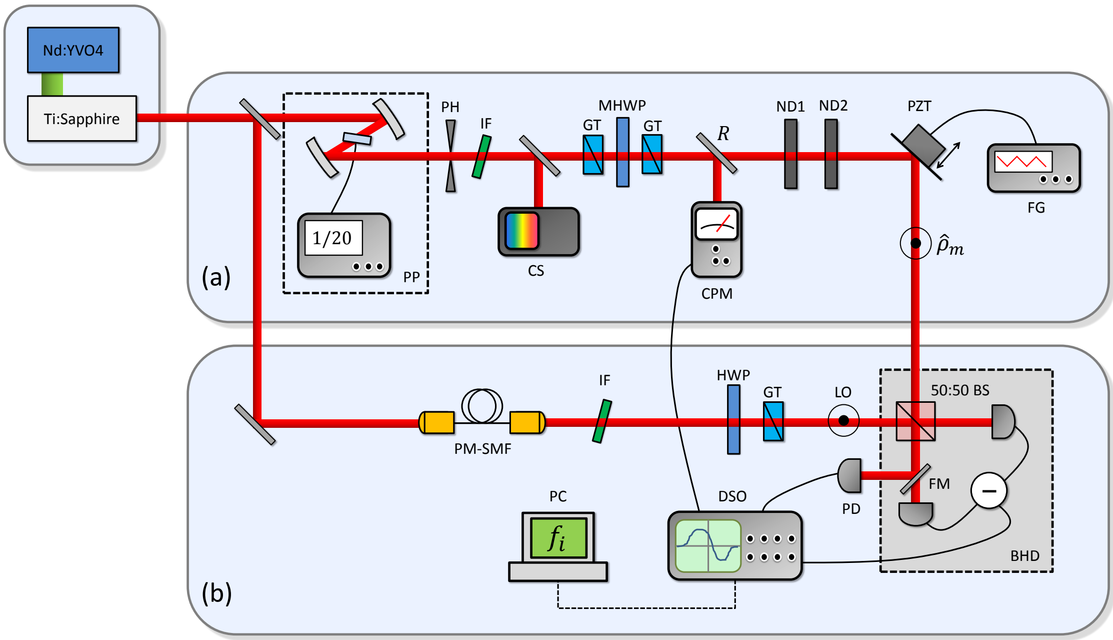

Figure 6.5: Schematic of the optical setup used to prepare PHAV probe states $\{\hat{\rho}_m\}$, subsequently measured by the BHD to obtain the data pattern set $\{f_i^m\}$. (a) Probe state preparation. (b) Balanced homodyne detection and data acquisition. Full details in main text.

primarily installed for use with a separate experiment (detailed in chapter 5). However, having a reduced probe state repetition rate whilst retaining the LO used for balanced homodyne detection at the full 80 MHz repetition rate has one key advantage. Namely, the LO pulses where the probe state is 'switched off' provide valuable vacuum state pulses which can be used to calibrate the BHD contemporaneously with acquisition of the probe state 'on' pulses. The pulse picker is a kit manufactured by APE GmbH.

The output of the pulse picker is spatially filtered with a pinhole (PH) and spectrally filtered with an interference filter (IF) (Semrock LL01-830-12.5) to match the spectrum of the LO – the resulting spectrum is monitored using a compact spectrometer (CS) (Thorlabs CCS175). Having prepared the desired spatial-temporal mode, an amplitude control comprising a motorized half-waveplate (MHWP) and Glan Taylor (GT) polarizer enables fine control of the probe state amplitude $|\alpha_m|$. Following the amplitude control, a

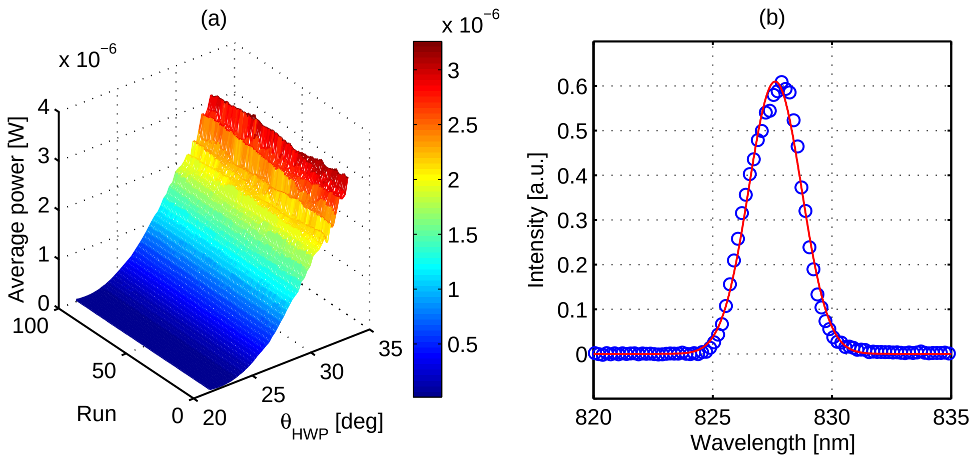

Figure 6.6: (a) Average optical power recorded by the power meter as a function of the MWHP angle θ_{HWP}. For each waveplate setting a total of 100 experimental runs were performed. (b) Spectrum of the probe state pulses recorded by the spectrometer, FWHM=2.6 nm.

fixed-ratio non-polarizing beam splitter, reflectivity R, enables a fraction of the light to be directed to a calibrated power meter (CPM) to monitor the absolute optical power after the amplitude control. The CPM used for the experiment was the Coherent FieldMax-II-TO and is computer controlled to enable full automation of the probe state preparation. The transmitted portion of the light is attenuated by many orders of magnitude using two calibrated neutral density (ND) filters, to reduce the PHAV amplitude to the few-photon level. In theory, the effective PHAV amplitude $|\alpha_m|$ registered by the BHD is given by

$$|\alpha_m| = \sqrt{P_{\text{meas},m}\left(\frac{T}{R}\right)10^{-\text{OD}_1-\text{OD}_2}\mathcal{V}^2\frac{\lambda_0}{hcN_p}}, \tag{6.17}$$

where $P_{\text{meas},m}$ is the average optical power registered by the CPM for probe state $\hat{\rho}_m$, $T(R)$ is the transmissivity (reflectivity) of the beam splitter used to direct light to the CPM, $\text{OD}_{1(2)}$ is the optical density of ND filter 1(2), $\lambda_0 = 827.6$ nm is the central wavelength as monitored by the spectrometer (figure 6.6(b)), $N_p = 3.997$ MHz is the probe state repetition rate after the pulse picker and $\mathcal{V}$ is the interference visibility between the probe

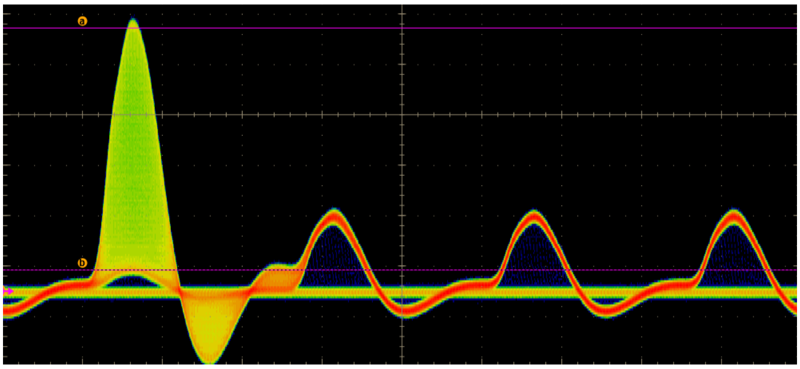

Figure 6.7: Traces acquired from a fast photodiode used to monitor the interference visibility between the LO and probe state modes. The persistence mode of the oscilloscope overlays many traces, as the interferometric phase is modulated by the PZT. The pulse picker is on only for the first pulse.

state mode and the LO mode.*

For the FDP method to work reliably the probe states $\{\hat{\rho}_m\}$ must be well-determined. Assuming the Ti:Sapphire oscillator produces a coherent state [53, 260, 94], this requires that the amplitude of each PHAV $|\alpha_m|$, specified by equation 6.17, be determined with high accuracy. The largest source of uncertainty is the optical power $P_{\text{meas},m}$ – limited by the 5% accuracy of the CPM calibration. Care was taken to ensure that stray light was not registered by the CPM and that the CPM read zero when the input beam was blocked. Figure 6.6(a) shows the average power registered by the CPM for 48 different settings of the MHWP angle in the amplitude control. For each setting of the MHWP, 100 experimental runs were performed for the FDP experiment. For each run $P_{\text{meas},m}$ was recorded, and exhibited small variations due to fluctuations of the Ti:Sapphire oscillator output power. This was taken into account by defining each probe state $\hat{\rho}_m$ as a statistical mixture of PHAVs, with an amplitude distribution determined from the fluctuations observed in $P_{\text{meas},m}$ [53, 259].

The interference visibility $\mathcal{V}$ between the LO and probe state modes is determined by removing the ND filters from the probe state path, figure 6.5(a), and directing one output

*The visibility allows the mode overlap to be determined according to equation 3.27.

of the 50:50 beam splitter used for balanced homodyne detection to a fast photodiode (PD) using a flip mirror (FM), figure 6.5(b). The signal registered by the PD is observed to fluctuate due to modulation of the interferometric phase by the PZT. Voltage traces from the PD were captured using the Tektronix MSO5104 operating in persistence mode, figure 6.7. The first pulse of the four pulses shown in figure 6.7 corresponds to the temporal mode where the pulse picker is switched on, and thus interference is observed.* The interference visibility $\mathcal{V}$ can be adequately extracted using the cursors feature of the oscilloscope and was determined to be $\mathcal{V} = 0.85$.† The group delay introduced by the ND filters would normally require that a delay be introduced in the LO path when replacing the ND filters after recording the interference visibility.‡ This could introduce an error, meaning that the effective interference visibility between the probe and LO modes is different from that determined without the ND filters in place.§ To circumvent the requirement to reset a delay, the LO and probe beam paths are aligned parallel and separated by approximately 5 cm. Step ND filters (Thorlabs NDL-25S-2 and NDL-25S-4) are used – with the LO mode aligned on the region of lowest optical density and the probe state mode aligned on the region of highest optical density. The filters exhibit minimal thickness variation¶ and thus both modes obtain the same group delay and hence no relative group delay is introduced.

Having determined all the parameters in equation 6.17, the average optical power recorded by the CPM as a function of the MHWP angle θ_{HWP}, figure 6.6(a), can be converted to probe state amplitude $|\alpha_m|$, shown as the red points in figure 6.8, which are labelled as “independent” since the values were determined independently using equation

*For the subsequent three pulses the pulse picker is off and thus no interference is observed.

†It was found to be easier to extract the visibility using the persistence traces than by offline analysis of a set of waveforms.

‡The pulse duration is of the order 300 fs, whereas the group delay introduced by a 3 mm thick ND filter is of the order 15 ps.

§The ND filters have to be removed to determine $\mathcal{V}$ because the PD is not sufficiently sensitive to register the attenuated mode.

¶Wedge specified to be < 3 arc minutes.

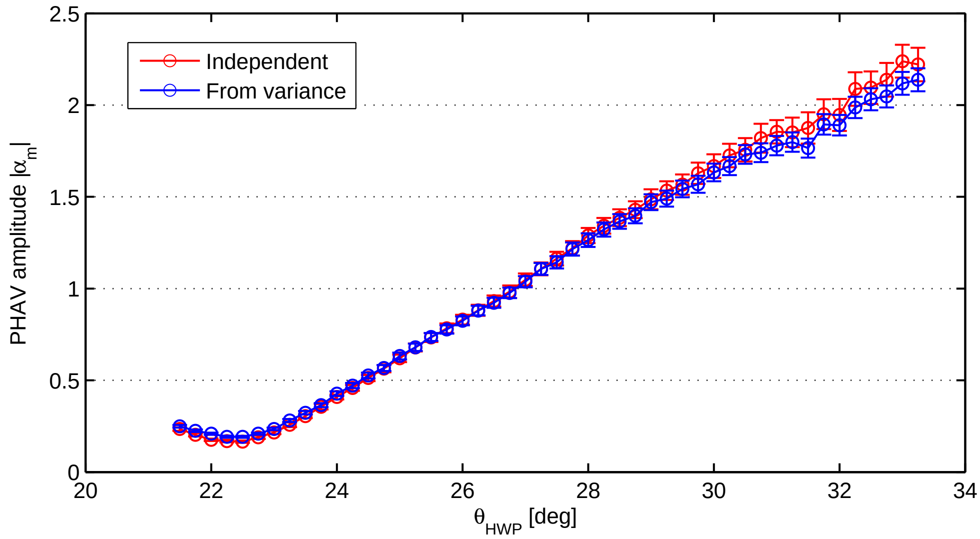

Figure 6.8: Amplitudes of PHAV probe states determined from independent calibration according to equation 6.17 (red) and from the variance of quadrature samples acquired by the BHD (blue).

6.17 and the various parameter values.* For the range of θ_{HWP} used, the probe state amplitude ranges from 0.17 to 2.24. Error bars are calculated taking into account the laser output power fluctuations and the uncertainty of 5% in the power meter calibration. Since the minimum amplitude is not zero† the vacuum state is additionally included in the probe set by blocking the probe mode. This gives a total of $M = 49$ probe states used in the experiment.

*The blue data in figure 6.8 are not used to determine the probe states $\{\hat{\rho}_m\}$ but serve as a cross-check that the amplitude calibration according to equation 6.17 is reasonable. These data were obtained by calculating the variance of quadrature samples recorded by the BHD for each MHWP setting. For an ideal PHAV of amplitude $|\alpha|$ the quadrature variance $\text{Var}[X_\theta]$ is given by

$$\text{Var}[X_\theta] = \langle X_\theta^2 \rangle - \langle X_\theta \rangle^2 = \exp(-|\alpha|^2) \sum_{n=0}^{\infty} \frac{|\alpha|^{2n}}{n!} \frac{(2n+1)}{2}. \tag{6.18}$$

Thus from the experimentally determined variance, the amplitude of the probe state can be determined according to equation 6.18 (the BHD efficiency $\eta_{\text{bhd}} = 0.86$ must be factored out). The correspondence between the two sets of data shown in figure 6.8 is an early indication that the BHD behaves in a near-ideal manner in the field-of-view explored by the probe states, i.e. it measures the field quadrature $\hat{X}_\theta = \hat{X}\cos\theta + \hat{P}\sin\theta$.

†Most likely due to imperfect polarization extinction in the amplitude control.

6.3.2 Determination of data pattern set

For each probe state $\hat{\rho}_m$ a total of 10^6 frames were recorded in 100 separate runs.* The oscilloscope was operated in 'fast frame' mode and triggered from the pulse picker. Each frame contained one pulse corresponding to the probe state and three pulses corresponding to the vacuum state, see figure 6.7. Drifts in the detector balance and gain are compensated by rescaling the measured voltage V according to $V' = AV - B$. The rescaling parameters A and B are determined from the voltage samples corresponding to the vacuum state $\{V_0\}$ which should satisfy

$$\langle V_0' \rangle = C_1, \qquad \langle V_0'^2 \rangle - \langle V_0' \rangle^2 = C_2, \tag{6.19}$$

where C_1 and C_2 are constants.† The rescaled voltage samples for three probe states are shown in figure 6.9. Note that rescaling the voltages in this manner constitutes an entirely operational procedure, i.e. block the input signal and register a set of detector outcomes with which to perform the scaling of equation 6.19. The rescaling is necessary since the FDP method relies on the assumption that the unknown detector response is invariant with respect to time.

The frequency distribution of measurement outcomes i for probe state $\hat{\rho}_m$, denoted f_i^m, is formed by binning the rescaled voltage samples for the probe state pulse $\{V'\}$. A total of 151 bins of uniform width are used, where the bin width is chosen such that no samples fall outside the bins for any probe state in the set $\{\hat{\rho}_m\}$. It was ensured that the underlying probability distribution was adequately sampled whilst minimizing statistical errors [132]. It should be stressed that no physical interpretation of the nature of the measurement outcomes i is made [72, 256], see section 6.2.3. The complete data pattern

*The oscilloscope memory is insufficient to acquire all 10^6 frames at once.

†This leads to the relations $A = \sqrt{(C_2/\mathrm{Var}[V_0])}$ and $B = A\langle V_0 \rangle - C_1$.

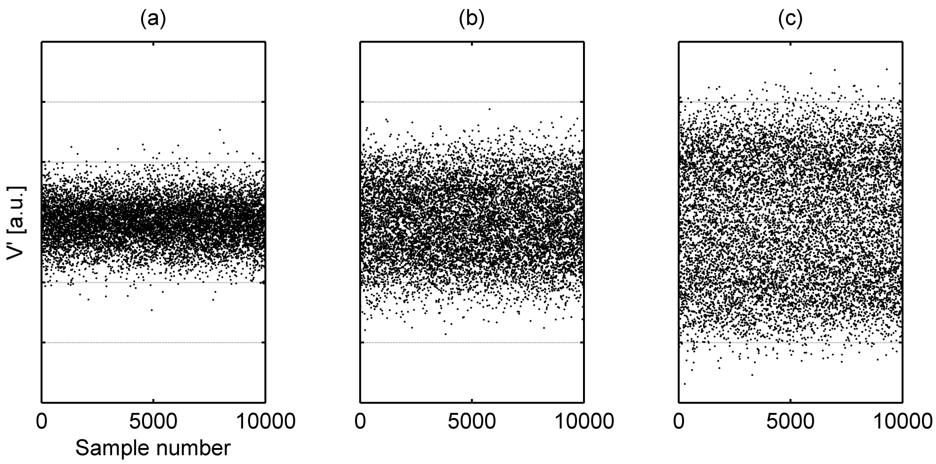

Figure 6.9: Rescaled voltage samples $\{V'\}$ obtained from the BHD for three different probe states: (a) vacuum state, (b) $|\alpha| = 1.11$, (c) $|\alpha| = 2.24$. Note, only 10^4 out of the total of 10^6 sample are shown. The vertical scale is in units of rescaled voltage and is the same for all three plots.

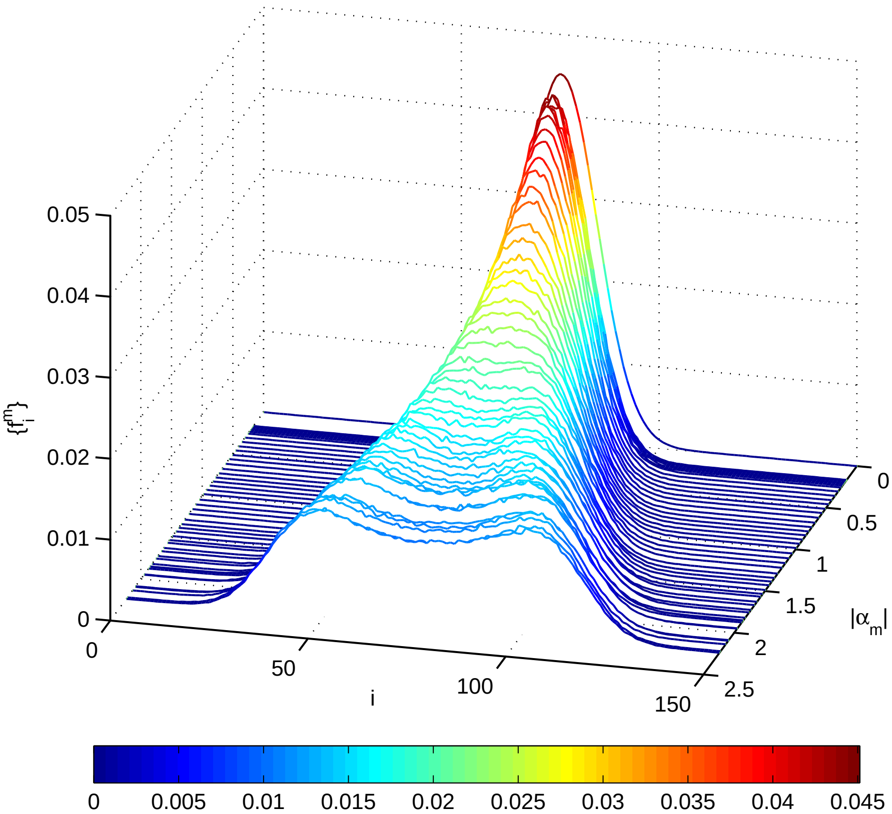

Figure 6.10: Data pattern set $\{f_i^m\}$. The 48 PHAV probe states have amplitude $|\alpha_m|$ ranging from 0.17 to 2.24, determined independently according to equation 6.17. Additionally, the vacuum state was added to the set to give a total of 49 probe states.

set $\{f_i^m\}$ for the 49 probe states is shown in figure 6.10. The choice of binning means that the detector effectively has 151 possible outcomes. This is an order of magnitude greater than any QDT experiment performed to date [53, 260, 265, 267, 266, 94, 269]

6.3.3 Tomography of non-classical quantum states

The raw samples acquired from the BHD for the heralded one-, two- and three-photon Fock states are binned in an identical manner to the probe state samples in order to obtain a measurement outcome frequency distribution f_i' for each state. Since the BHD setup remained invariant, the Fock state data are the same data detailed in chapter 4 and thus acquisition of the samples is not discussed here.*

For each of the three Fock states the functional of equation 6.11 is minimized to obtain the optimal set of coefficients $\{a_m\}$ for each state, left hand column of figure 6.11. The optimization procedure was performed in MATLAB using YALMIP [272] to code the programme of equation 6.11 and SDPT3 [264] as the solver. Typically 10 iterations were required for each optimization, which took approximately 1.5 seconds on an Intel Core i7 desktop computer. The right-hand column of figure 6.11 shows the measured state frequency distribution (red curve), the frequency distribution of the estimated state $\sum_m a_m f_i^m$ (blue curve) and the residuals defined as $f_i' - \sum_m a_m f_i^m$ (green curve) for each of the three Fock states. The residuals give a measure of the deviation between the measured and estimated frequency distributions and are largest for three-photon Fock state due to the greater statistical noise owing to the smaller number of samples making the state frequency distribution f_i'.

Having found the optimal coefficients $\{a_m\}$ for each Fock state, the density matrix of each state $\hat{\rho}_{\text{fdp}}$ may be estimated according to equation 6.10, where the probe state den-

*Experimental factors such as the LO spectrum, beam waist and power were identical for all experiments.

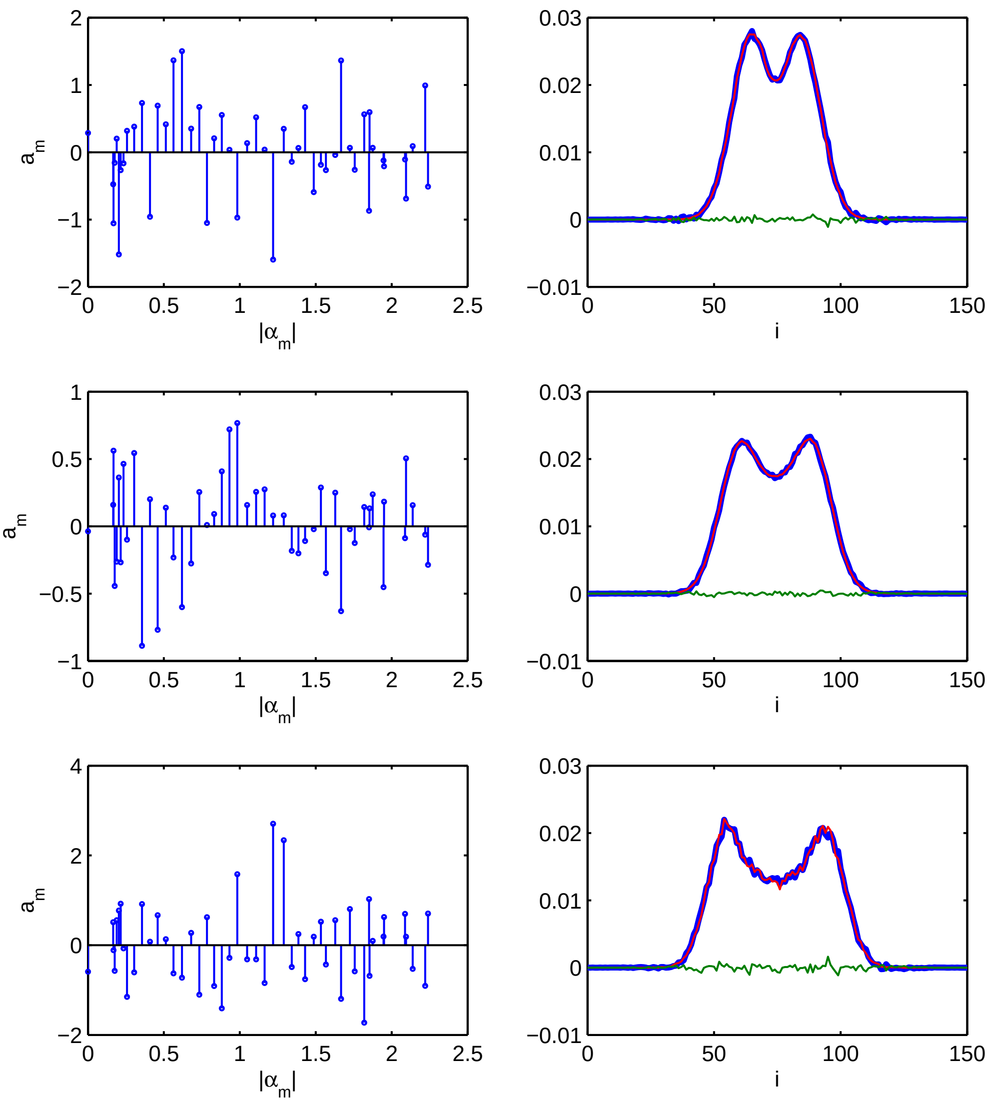

Figure 6.11: Left: optimal coefficients $\{a_m\}$ obtained by minimizing the FDP functional, equation 6.11, for the one-, two- and three-photon Fock states (top to bottom). Right: measured state frequency distribution (red curve), the frequency distribution of the estimated state $\sum_m a_m f_i^m$ (blue curve) and the residuals defined as $f_i' - \sum_m a_m f_i^m$ (green curve) for each of the three Fock states.

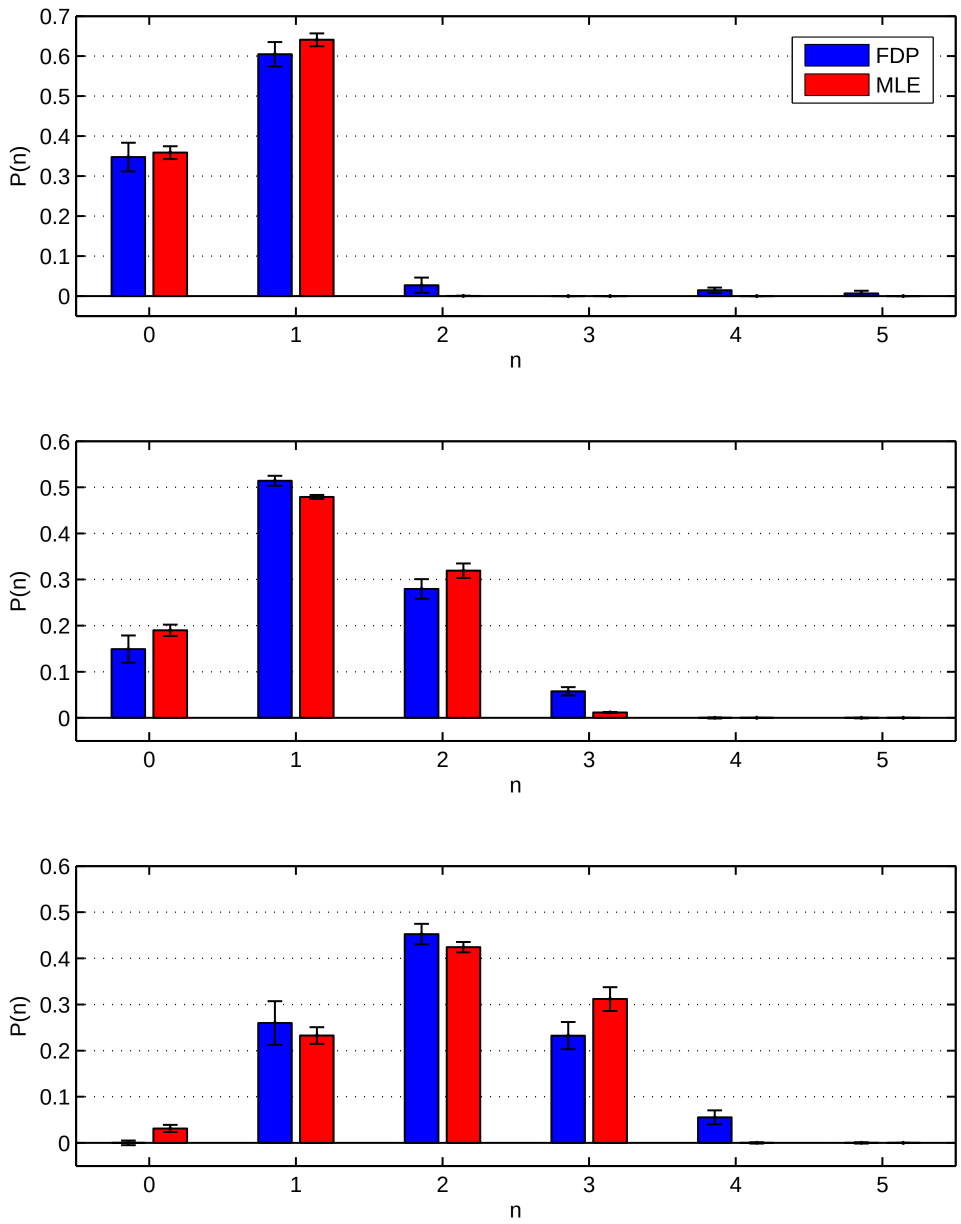

Figure 6.12: Photon number staistics obtained by the FDP method (blue bars) and maximum-likelihood estimation (red bars) for the one-, two- and three-photon Fock states (top to bottom). Error bars indicate the 1 standard deviation confidence interval.

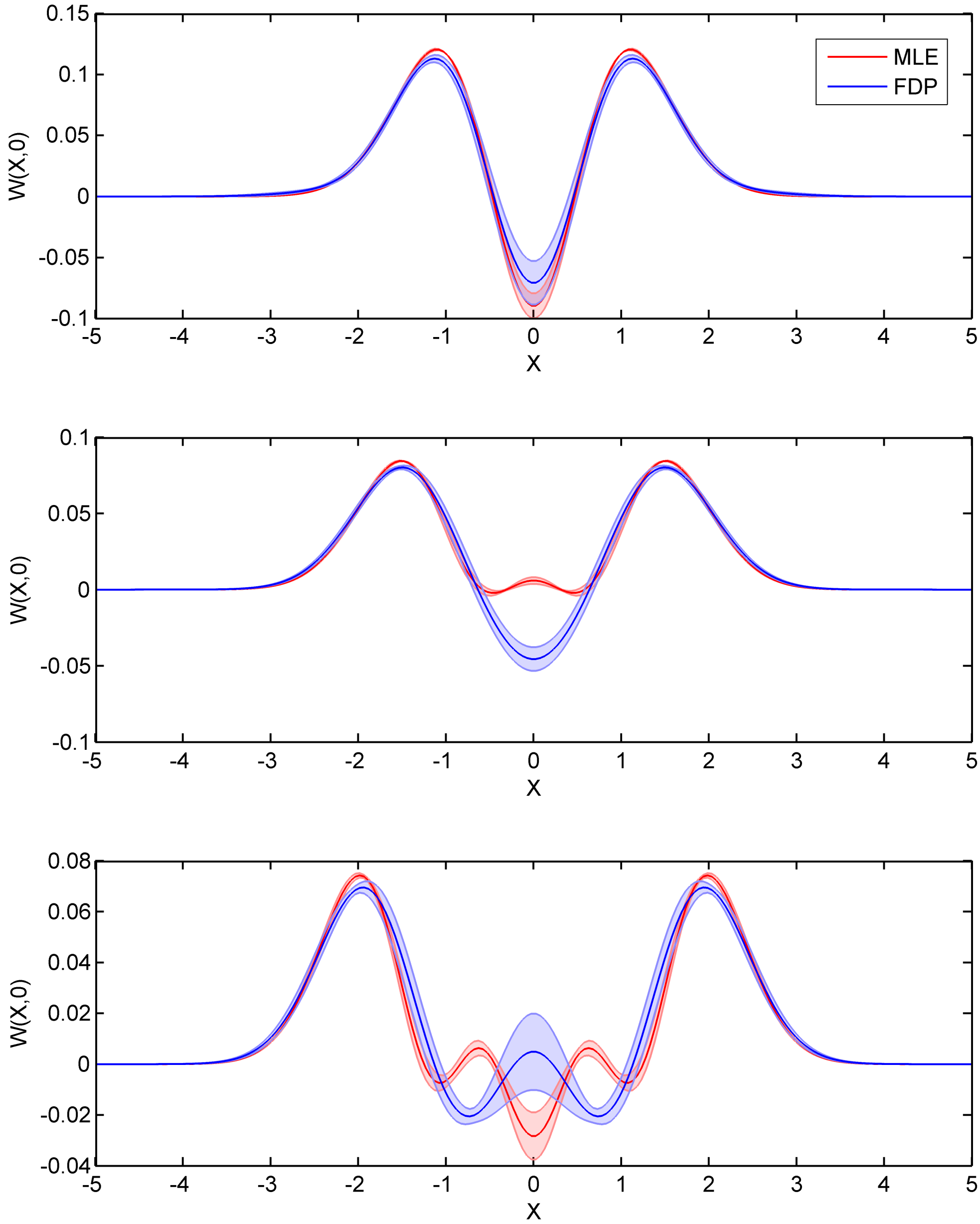

Figure 6.13: Cross section of Wigner functions in the $P = 0$ plane for $\hat{\rho}_{\rm fdp}$ (blue) and $\hat{\rho}_{\rm ml}$ (red) for the one-, two- and three-photon states (top to bottom). Uncertainties in the Wigner functions corresponding to 1 standard deviation are indicated by the shaded bands.

sity matrices were determined in section 6.3.1. The diagonal elements of the reconstructed density matrices, corresponding to the photon number statistics $P(n) = \langle n|\hat{\rho}_{\text{fdp}}|n\rangle$, are presented in figure 6.12 (blue bars). In order to have a reference against which to compare the results of the FDP state tomography method the results of the maximum-likelihood estimation (MLE) technique from chapter 4 are also presented (red bars), where the standard POVM of equation 3.31 is assumed. Since the FDP method incorporates complete calibration of the BHD, it also automatically corrects for the BHD efficiency $\eta_{\text{bhd}} = 0.86$. Therefore the MLE results have been corrected for $\eta_{\text{bhd}} = 0.86$ in order to enable direct comparison. The Wigner functions corresponding to the states reconstructed by the FDP and MLE techniques are shown in figure 6.13.

A quantitative analysis of the agreement between the results of the two state estimation techniques is made by calculating the fidelity F between the ensemble estimated by the FDP technique $\hat{\rho}_{\text{fdp}}$ and that obtained from MLE $\hat{\rho}_{\text{ml}}$ defined as

$$F = \text{Tr}\left(\sqrt{\sqrt{\hat{\rho}_{\text{fdp}}}\hat{\rho}_{\text{ml}}\sqrt{\hat{\rho}_{\text{fdp}}}}\right)^2. \tag{6.20}$$

Fidelities of $F_1 = 0.97 \pm 0.02$, $F_2 = 0.98 \pm 0.01$ and $F_3 = 0.91 \pm 0.02$ were obtained for the one-, two- and three-photon Fock states respectively. The uncertainties arise due to uncertainties in the estimate of each state. For the FDP method, statistical errors arise due to the finite number of measurement events used to generate the data pattern set $\{f_i^m\}$ and the frequency distribution for each of the Fock states f_i'. Each frequency distribution (histogram) was assumed to have an error of $\sqrt{N_i}$ for each bin i containing N_i events. The probe state amplitudes also carry an uncertainty, largely due to the power meter calibration, as discussed in section 6.3.1. Monte-Carlo simulation was performed with a total of 1000 trials to obtain a set of estimates of $\hat{\rho}_{\text{fdp}}$ from which the standard deviation

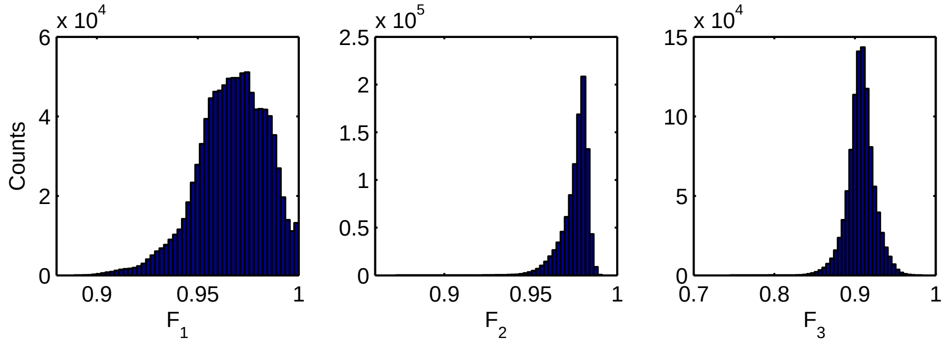

Figure 6.14: Distribution of fidelities between maximum-likelihood reconstruction and FDP reconstruction for the one-, two- and three-photon Fock states (left to right), obtained from Monte-Carlo simulation.

of each density matrix element could be evaluated. For the MLE technique, the statistical errors due to a finite number of samples were taken into account in a similar manner. The distributions of state fidelities for each of the three estimated states are shown in figure 6.14.

The most obvious discrepancy between the ensembles estimated by the two methods is the tendency of the FDP method to introduce over-inflated higher-order photon-number components. This feature of the FDP technique was also observed in simulations and is believed to originate from the discrete representation of equation 6.10. Since such a discrete representation with coherent states or PHAVs is often incomplete [256], there will be non-vanishing higher-order components in the estimated state, as shown in figure 6.2. The additional sources of experimental error, as discussed above, lead to an inflation of these small terms such that they can become appreciable and impact the fidelity between the FDP and MLE states. In fact, if the Hilbert space is truncated at n photons for the estimate of the n-photon Fock state the fidelity is nearly unity for all three estimates. This indicates that the non-unity fidelity largely stems from the higher-order photon-number components introduced in the FDP technique.* Having identified this as the primary

*In spite of the potential over-inflation of high-order photon-number components, the FDP method does not appear to suffer from the well-known problem of zero eigenvalues which is an issue with MLE [274]. As a case in point, the iterative MLE algorithm [90] was used to invert the data for the one-photon Fock source of infidelity the conclusion can be drawn that the POVM describing balanced homodyne detection assumed in the MLE is accurate within the field-of-view experimentally examined by the PHAV probes.

6.4 Comparison between QDT+QST and FDP

In order to make a qualitative comparison between the FDP method on the one hand and POVM reconstruction by QDT on the other, it is first important to reiterate that the FDP method is not in the first instance a quantum detector calibration method. The FDP method is primarily concerned with the reliable determination of an object, i.e. the quantum state $\hat{\rho}$. This objective is achieved through the formulation of an entirely novel tomography method which relies on the representation of the unknown object $\hat{\rho}$ as a combination of known reference objects [72, 256], *viz.* the probe states.

The FDP method uses an operational characterization of the quantum detector response, encapsulated in the data pattern set $\{f_i^m\}$, to perform reliable QST by minimizing only one functional, equation 6.11. The detector calibration consists only of the directly obtained measurement outcome distributions and thus does not require further numerical analysis. The alternative approach of performing QDT+QST (using a conventional QST algorithm such as maximum-likelihood estimation [90]) entails two separate numerical optimization procedures, each performed subject to separate constraints and, in the case of QDT, often regularization [53, 259, 261]. This two-step approach to QST with a calibrated detector is not only more resource intensive, owing to the two separate numerical optimizations, but also more likely to suffer from artefacts introduced from one or both of

state for increasing iteration number. The size of the two-photon component $P(n=2) = \langle 2|\hat{\rho}_{\mathrm{ml}}|2\rangle$ was monitored as the number of iterations increased. Although expected to be small, due to the nature of the TMSV state the two-photon component should be non-zero. Based on the estimated squeezing parameter of $\lambda = \tanh(\zeta) = 0.07$ (section 4.3.5) the two-photon component should be of the order $P(2) \approx 10^{-3}$. Increasing the iteration number in MLE is observed to drive the two-photon component to zero – whereas the FDP estimated state has $P(2) = 0.03 \pm 0.02$.

the separate optimization procedures [274]. Error propagation is thus more efficient using the FDP approach. Finally, the FDP method lends itself to mapping the response of the detector in an isolated, local region of the input Hilbert space. Thus for example if *a priori* knowledge suggests that the input states are constrained in amplitude, the response of the detector up to the saturation point need not be investigated.

6.5 FDP process tomography

In this section, the original proposal of FDP for performing reliable QST [72] is extended to the estimation of a quantum process. Quantum process tomography (QPT) was discussed in chapter 5, with specific attention paid to the maximum-likelihood method [49, 242, 71]. This method relies on knowledge of the POVM set $\{\hat{\Pi}_i\}$ describing the measurement apparatus, as well as knowledge of the input probe states $\{\hat{\rho}_m\}$, see section 5.2.1. Just as with QST, a separate QDT step could be employed to first determine the POVM set prior to performing maximum-likelihood QPT. However, motivated by the FDP approach to QST a method is sought to enable direct estimation of an unknown quantum process which fully incorporates calibration of the measurement apparatus.

6.5.1 Description of procedure

A schematic of the FDP approach to QPT is presented in figure 6.15. A set of M known probe states $\{\hat{\rho}_m\}$ is required which should span the region of interest of the input Hilbert space $\mathcal{H}$ of the process. The process is represented as a trace non-increasing CP map $\mathcal{E}$. Many copies of each probe state $\hat{\rho}_m$ are prepared and evolve according to the process $\mathcal{E}$ resulting in output state $\hat{\rho}'_m = \mathcal{E}(\hat{\rho}_m)$, figure 6.15(a). The output state is registered by a detector, implicitly described by a POVM set $\{\hat{\Pi}_i\}$, which is assumed to be unknown. Repeating the procedure for each copy of input probe state $\hat{\rho}_m$ enables the frequency of

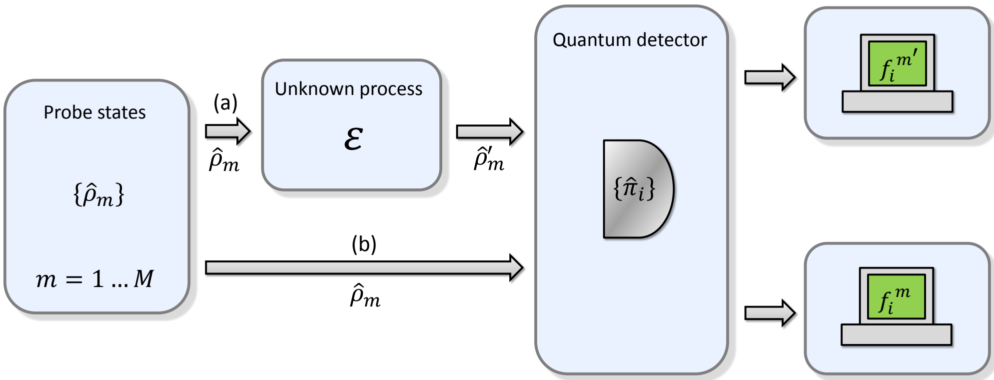

Figure 6.15: Schematic of FDP approach to QPT. (a) Known input probe states $\hat{\rho}_m$ transform to output states $\hat{\rho}'_m = \mathcal{E}(\hat{\rho}_m)$ due to the unknown process $\mathcal{E}$. The output states are registered by a detector with an unknown POVM leading to measurement outcome frequency distributions f'^m_i. (b) Same as in (a) except the known input states are registered directly by the detector, bypassing the process, leading to measurement outcome distributions f_i^m.

measurement outcomes for the process output state $\hat{\rho}'_m$ denoted f'^m_i to be determined, where

$$f'^m_i \cong \mathrm{Tr}\left[\hat{\rho}'_m \hat{\Pi}_i\right]. \tag{6.21}$$

It is assumed that the unknown process $\mathcal{E}$ can effectively be switched off, such that the input probe states $\{\hat{\rho}_m\}$ may additionally be registered directly by the detector, without undergoing any transformation, figure 6.15(b). This enables the frequency distribution of measurement outcomes for the *known* input states, denoted f_i^m to be determined, where

$$f_i^m \cong \mathrm{Tr}\left[\hat{\rho}_m \hat{\Pi}_i\right]. \tag{6.22}$$

The goal of the procedure is to estimate the process $\mathcal{E}$ from only the measured frequency distributions and knowledge of the input probe states. The set of measurement outcome frequency distributions for the input states with no process in place, denoted $\{f_i^m\}$, constitutes the data pattern set since it incorporates the detector response to the *known* probe states which have not undergone transformation by the process.

By employing the Jamiolkowski-Choi isomorphism introduced in section 5.2.1, the measurement outcome frequency distributions for the process output states may be expressed as

$$\begin{aligned} f'^{m}_{i} &\cong \mathrm{Tr}_{\mathcal{K}}\left[\hat{\rho}'_m \hat{\Pi}_i\right] \\ &\cong \mathrm{Tr}_{\mathcal{K}}\mathrm{Tr}_{\mathcal{H}}\left[\hat{E}(\hat{\rho}_m^T \otimes \hat{I})(\hat{I} \otimes \hat{\Pi}_i)\right], \end{aligned} \tag{6.23}$$

where the process is represented as the positive operator $\hat{E}$ on the Hilbert space $\mathcal{H}\otimes\mathcal{K}$, with the exact relation between $\hat{E}$ and $\mathcal{E}$ given by equation 5.27, and T denotes transposition in the photon-number basis [49]. The key step is to realize that provided the set of probe states $\{\hat{\rho}_m\}$ are sufficient to form a basis for both the input and output Hilbert space of the process, operator $\hat{E}$ may be expanded as

$$\boxed{\hat{E} = \sum_{x,y} a_{xy} \hat{\rho}_x^T \otimes \hat{\rho}_y,} \tag{6.24}$$

where $\hat{\rho}_{x,y} \in \{\hat{\rho}_m\}$ and the expansion coefficients a_{xy} are to be determined by the FDP procedure. Substituting this expression for $\hat{E}$ into equation 6.23 gives

$$\begin{aligned} f'^{m}_{i} &\cong \mathrm{Tr}_{\mathcal{K}}\mathrm{Tr}_{\mathcal{H}}\left[\sum_{x,y} a_{xy}\left(\hat{\rho}_x^T \hat{\rho}_m^T \otimes \hat{\rho}_y \hat{\Pi}_i\right)\right], \\ &\cong \sum_{x,y} a_{xy} \mathrm{Tr}\left[\hat{\rho}_x^T \hat{\rho}_m^T\right] f_i^y, \end{aligned} \tag{6.25}$$

where f_i^y is nothing but the frequency distribution of measurement outcomes for the input probe state $y \in m$, defined in equation 6.22 and measured as part of the FDP procedure, figure 6.15.

By inspection of the right-hand side of equation 6.25, the input state frequency distributions f_i^y are measured experimentally and the probe state density matrices are known. Thus equation 6.25 makes a prediction of the process output state frequency distributions through the unknown expansion coefficients a_{xy}, in exact analogy to the FDP approach to QST, section 6.2.1. The coefficients may be determined by minimizing the functional

$$\mathcal{G}(\{a_{xy}\}) = \sum_m \sum_i \left({f'}_i^m - \sum_{x,y} a_{xy} \mathrm{Tr}[\hat{\rho}_x^T \hat{\rho}_m^T] f_i^y \right)^2 , \tag{6.26}$$

where summation is carried out over the probe states $\{\hat{\rho}_m\}$ and the measurement outcomes i. The functional is similar in form to that used for FDP quantum state tomography, equation 6.11. However, notice that there are effectively two additional summations compared with equation 6.11, both running over the probe state index $m = 1...M$. This is already an indicator of the increased computational complexity of the FDP approach to QPT. This stems from the requirement to characterize the process operator $\hat{E}$ which resides in the combined Hilbert space $\mathcal{H} \otimes \mathcal{K}$ as opposed to a density operator on Hilbert space $\mathcal{H}$. Note that nothing is assumed about the underlying detector POVM $\{\hat{\Pi}_i\}$, and thus calibration of the detector enters implicitly through the data pattern set $\{f_i^m\}$, in exact analogy to FDP state tomography.

6.5.2 Trace-preserving processes

For trace preserving quantum processes, e.g. attenuation, the operator $\hat{E}$ must satisfy the constraints [49]

$$\hat{E} \geq 0, \qquad \mathrm{Tr}_{\mathcal{K}} \left[\hat{E} \right] = \hat{I}_{\mathcal{H}}. \tag{6.27}$$

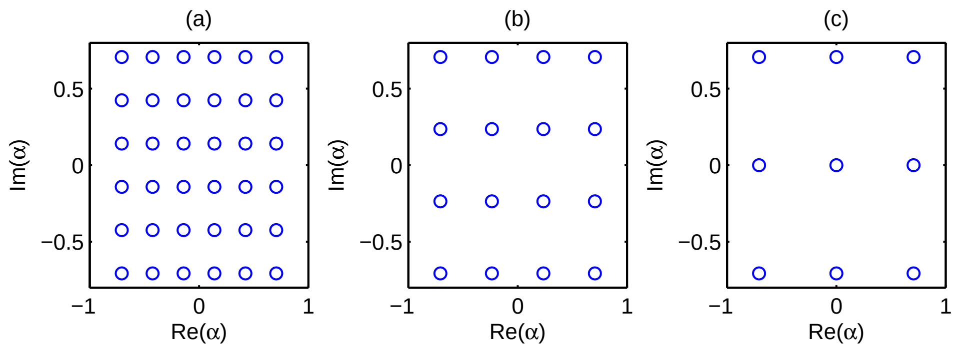

Figure 6.16: Coherent state probe amplitudes used in the simulation of FDP QPT of 50% attenuation process.

These constraints can be incorporated during the minimization of the functional of equation 6.26 when using standard toolboxes such as YALMIP [272] or `fmincon` in MATLAB to form the semi-definite program

$$\boxed{\min \mathcal{G}(\{a_{xy}\}), \qquad \text{s.t.} \quad \hat{E} \geq 0 \quad \mathrm{Tr}_{\mathcal{K}}\left[\hat{E}\right] = \hat{I}_{\mathcal{H}},} \tag{6.28}$$

which constitutes the reconstruction procedure for trace-preserving quantum processes.

As a test of the FDP method for QPT, a simulation was performed to reconstruct the process tensor corresponding to attenuation. Coherent states were used as the probe states $\{\hat{\rho}_m\}$ with amplitudes as shown in figure 6.16, i.e. three different cases were simulated: (a) 36 coherent state probes, (b) 16 coherent state probes and (c) 9 coherent state probes. The maximum amplitude in each set was $|\alpha| = 1$.

For QPT it is now imperative to use a full grid of probes rather than using phase-averaged states or coherent states of differing amplitude but fixed phase. This is because the operator $\hat{E}$ describing the process lives in the combined input/output Hilbert space $\mathcal{H} \otimes K$ and necessarily has non-zero off-diagonal elements. Logically this is because the process must be able to predict the evolution of any input space on Hilbert space $\mathcal{H}$. Thus for the representation of $\hat{E}$ according to equation 6.24 to be possible, the probe states must form a basis for $\mathcal{H}$ and $\mathcal{K}$ and therefore also $\mathcal{H} \otimes \mathcal{K}$.

In the simulation, balanced homodyne measurements of the process input and output states were performed with a total of 10^6 measurements for each of 6 LO phases θ equally spaced such that $\theta \in [0, \pi)$. The theoretical process tensor for attenuation by 50%, equation 5.24, was applied to the input probe state density matrices to generate the output states. The simulated balanced homodyne samples were sorted into 100 bins for each LO phase, to give the measurement outcome frequency distributions of the process input and output states, f_i^m and f'^m_i respectively, shown in figure 6.17 for the case where 36 probe states were used. The output frequency distributions comprise Gaussian distributions, as is the case for the input frequency distributions, but show less spread across the quadrature bins owing to the effect of attenuation on the coherent states – namely to displace the states towards the origin of phase space.

For each set of probe states the program of equation 6.28 was run in MATLAB using `fmincon` as the solver. For the purpose of this simulation, in order to produce frequency distributions corresponding to what would be measured in the laboratory, i.e. Gaussian distributions of quadrature outcomes, the dimension of the Hilbert space d used to generate the frequency distributions was set at $d = 10$ – thus ensuring near-perfect representation of the coherent state density matrices. However, the set of probe states is not sufficient to reconstruct the process tensor for the whole Hilbert space of dimension $d = 10$. Therefore during the reconstruction procedure, equation 6.28, the constraints of equation 6.27 were only enforced within a truncated Hilbert space of dimension $d' < d$, where $d' = 3$. Outside of this sub-space the process tensor is unconstrained and therefore the reconstruction in this region is not reliable.

For the case of 36 probe states, corresponding to a total of $36^2 = 1296$ parameters in the optimization problem, approximately 10 hours were required to find the optimal

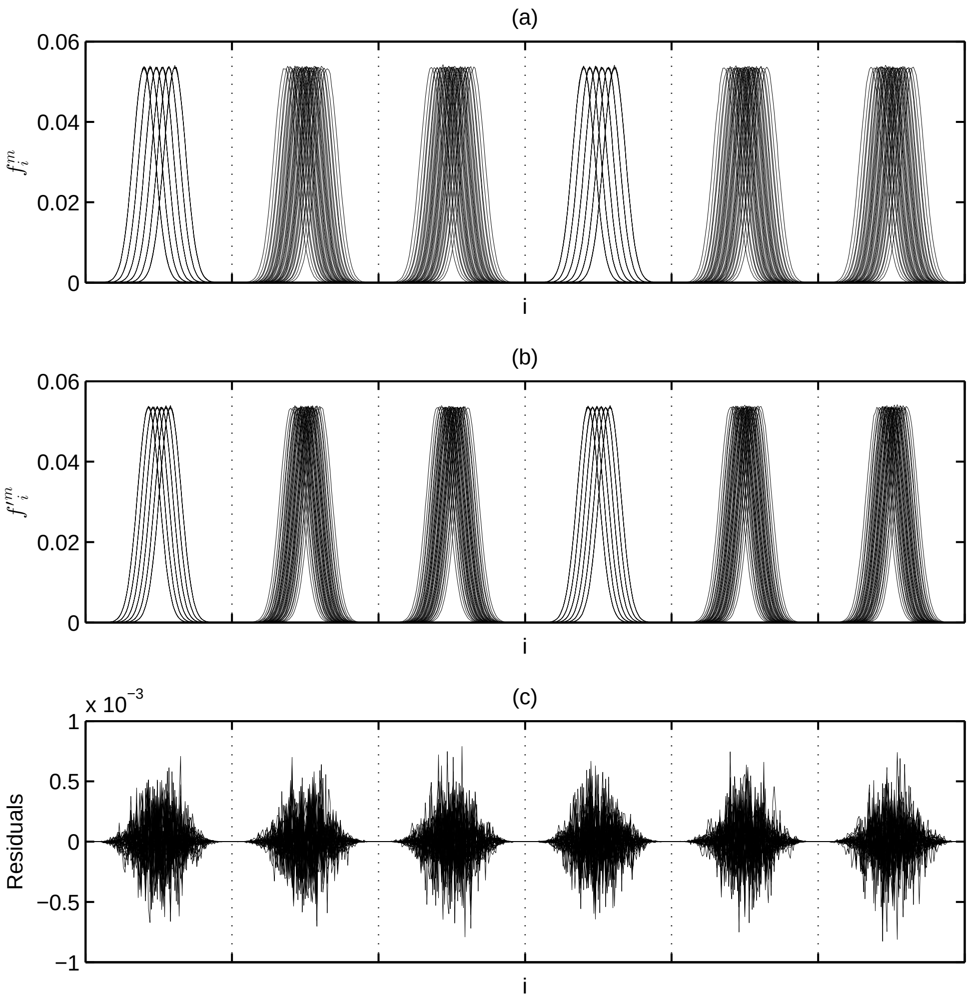

Figure 6.17: Measurement outcome frequency distributions of the input and output states f_i^m (a) and f'^m_i (b) respectively. (c) Difference between the actual and estimated output frequency distributions, corresponding to the term inside the bracket of equation 6.26

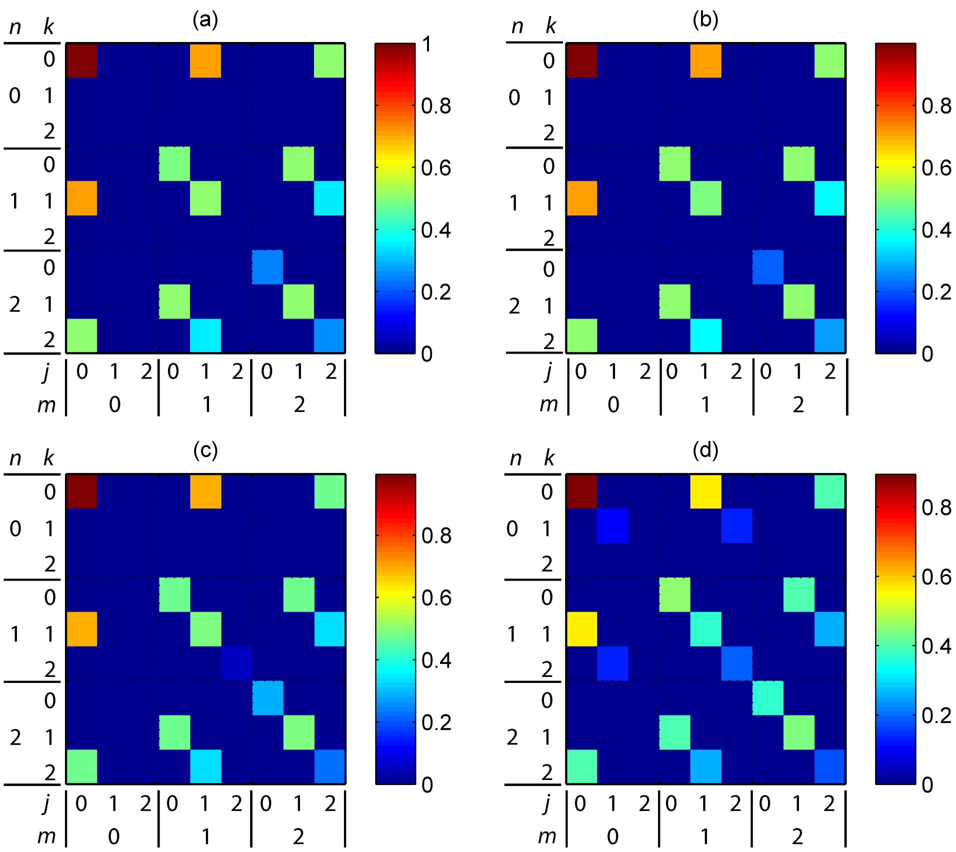

Figure 6.18: Process tensors for 50% attenuation in the Jamiolkowski-Choi representation. (a) theoretical, (b) reconstructed from 36 probes, (c) reconstructed from 16 probes, (d) reconstructed from 9 probes.

solution. The difference between the actual and estimated output frequency distributions – corresponding to the term inside the bracket of equation 6.26 – is plotted in figure 6.17(c). The reconstructed process tensors in the Jamiolkowski-Choi representation are shown in figure 6.18. For an input state to the process described by density matrix $\hat{\rho}$ with matrix elements $\rho_{mn} = \langle m|\hat{\rho}|n\rangle$, the tensor as represented in figure 6.18 depicts how each matrix element transforms due to the process. Thus, for example in figure 6.18(a), the component $\rho_{11}|1\rangle\langle 1|$ of the input state will transform as

$$\rho_{11}|1\rangle\langle 1| \rightarrow \frac{\rho_{11}}{2}\left(|0\rangle\langle 0|| + |1\rangle\langle 1|\right), \tag{6.29}$$

such that if the input state to the process were a pure single photon state the output would be the mixed state $\hat{\rho}' = \frac{1}{2}(|0\rangle\langle 0|| + |1\rangle\langle 1|)$. The fidelity between the reconstructed and theoretical tensor, defined in equation 5.37, is 0.993 for the case of 36 probe states, 0.982 for the case of 16 probe states and 0.880 for the case of 9 probe states.

In principle, for a sub-space $\mathcal{H}'$ of dimension d' only $M = (d')^2$ linearly independent probe states are required to characterize the process within this sub-space, since the dimension of linear operators on the sub-space $\dim(\mathcal{L}(\mathcal{H}')) = (d')^2$. For the case considered here of $d' = 3$ this implies only 9 linearly independent probe states are necessary. However, the simulated reconstruction for the case where 9 coherent state probes are used is relatively poor with respect to the target operator, figure 6.18(d). Indeed even with 16 probe states the reconstruction is not perfect. The results indicate that the reconstructed tensor asymptotically approaches the target as the number of coherent states increases, with 36 probe states proving sufficient for a near-ideal reconstruction exhibiting a fidelity of 0.993 with the target, figure 6.18(b). The issue has been identified as being due to the use of coherent states as probes. If instead a linearly independent set of Fock states and

Fock state superposition states spanning the sub-space $\mathcal{H}'$ is used, a perfect reconstruction is obtained for only 9 linearly independent probes – the theoretical minimum required for a general process.* An exact criterion for the number of coherent state probes required for a near-perfect reconstruction is hard to establish and requires further research [61].

One could conjecture that the reason for the difficulty with coherent states stems from the fact that the Gaussian probability distributions obtained from homodyne measurement are dependent on information about the state lying outside of the sub-space $\mathcal{H}'$. This means that the functional of equation 6.11 cannot be zero, even in the case of an infinite number of measurements, i.e. no statistical noise.† To some extent this can be alleviated by simply using more probes, allowing the functional to approach zero and hence obtaining a better reconstruction. Finally, note that for reconstruction of DV processes this issue does not arise. One example would be application of the FDP-QPT method for characterizing a CNOT gate where the qubits are encoded in the polarization of single photons [35].

6.5.3 Probabilistic processes

Recall that for probabilistic quantum processes $\mathcal{E}$ the trace of the output state gives the probability of success p_m such that

$$p_m = \mathrm{Tr}\left[\hat{\rho}'_m\right] = \mathrm{Tr}\left[\mathcal{E}(\hat{\rho}_m)\right] \leq 1. \tag{6.30}$$

Intuitively the additional information about the success probability for each probe state $\hat{\rho}_m$ must be incorporated in the reconstruction procedure in order to reconstruct the process tensor pertaining to the probabilistic CP map. In section 5.2.1 it was outlined how this is

*N.B. if the process is phase-invariant then the number of probes M required for a sub-space of dimension d' is only $M = 2(d' - 1)$ [60].

†For Fock state and Fock state superposition states the frequency distributions are related to the Hermite polynomials which form a basis [273]. For coherent states one obtains a set of Gaussian distributions which do not form a basis.

achieved in the maximum-likelihood reconstruction – by artificially extending the output Hilbert space $\mathcal{K}$ such that the process could be treated as trace-preserving on the enlarged space.

For the FDP approach to QPT a conceptually different method is proposed. The measurement outcome frequency distributions for the process output states, denoted f'^m_i, are only formed from events when the process succeeded. If both the input and output state frequency distributions are normalized* then information about the success probability is lost. However, the success probability p_m can be recorded as part of the experiment and re-introduced into the functional such that

$$\mathcal{G}'(\{a_{xy}\}) = \sum_m \sum_i \left(p_m f'^m_i - \sum_{x,y} a_{xy} \mathrm{Tr}[\hat{\rho}_x^T \hat{\rho}_m^T] f_i^y \right)^2 , \tag{6.31}$$

which for the case of a trace-preserving process corresponds to the original functional (equation 6.26) since $p_m = 1,\ \forall\, m$. The reconstruction proceeds as before but without the constraint $\mathrm{Tr}_{\mathcal{K}} \left[\hat{E} \right] = \hat{I}_{\mathcal{H}}$ such that the optimization program is

$$\boxed{\min \mathcal{G}'(\{a_{xy}\}), \qquad \text{s.t.} \quad \hat{E} \geq 0.} \tag{6.32}$$

This procedure was tested in a simulation to reconstruct the process tensor corresponding to photon addition, i.e. $\hat{\rho}' = \mathcal{E}(\hat{\rho}) = \hat{a}^\dagger \hat{\rho} \hat{a}$. The process was reconstructed in a Hilbert sub-space $\mathcal{H}'$ of dimension $d' = 6$ and thus 36 random, linearly-independent probe states forming a tomographically complete set on $\mathcal{L}(\mathcal{H}')$ were generated. Each state was measured by a BHD both with and without the process in place, according to the FDP QPT procedure of figure 6.15. In the simulation, 10^6 samples were recorded for each state for each of 6 uniformly distributed LO phases in the interval $\theta \in [0, \pi)$. Reconstruction

*Either explicitly or implicitly due to the fact that an equal number of measurements were made on both the input and output states such that $\sum_i f'^m_i = \sum_i f^m_i = \text{const},\ \forall\, m$.

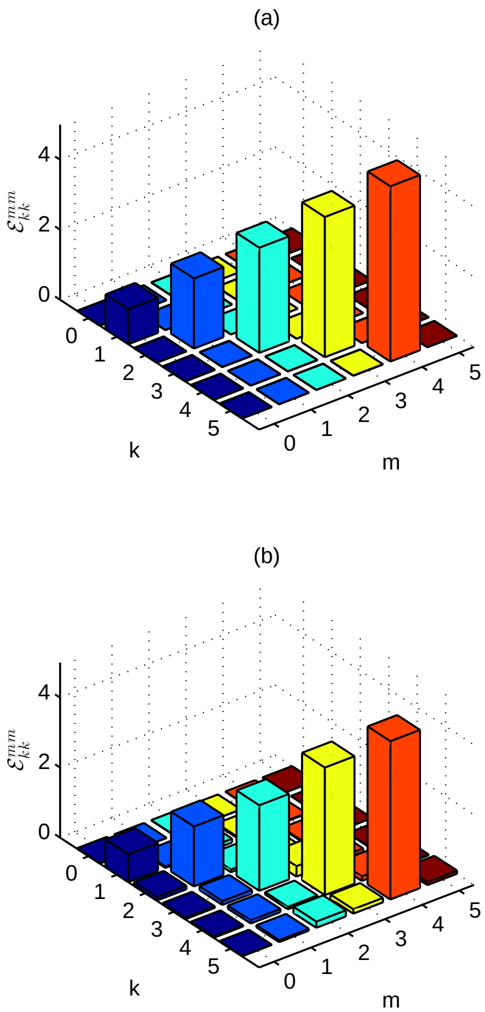

Figure 6.19: Theoretical (a) and reconstructed (b) diagonal elements of the process tensor corresponding to photon addition. The reconstruction was performed with the FDP method where a set of random, tomographically complete input states were used.

was performed according to the program of equation 6.32. Using `fmincon` the reconstruction procedure took approximately 40 seconds per iteration and a total of 1500 iterations were performed. The target and reconstructed process tensors are shown in figure 6.19 and exhibit a fidelity of 0.88 according to the definition of equation 5.37. Since the probe states used in the simulation were random states they are unlikely to be optimal. However, the reconstruction results indicate that probabilistic processes can be reconstructed in this manner with the FDP approach.

6.6 Summary

In this chapter the importance of detector calibration in the quantum domain was motivated and the favoured technique of quantum detector tomography reviewed. For CV detectors this technique can be challenging owing to the apparent necessity to saturate the detector and perform regularization during the reconstruction procedure. If only a certain input Hilbert space is of interest to the experiment then the fitting of data patterns (FDP) [72] technique provides a natural method for performing quantum state tomography in a manner which incorporates calibration of the detector. The competitively new technique was demonstrated experimentally for the first time by probing the balanced homodyne detector developed in chapter 3 with a set of phase-averaged coherent states. This local map of the detector response was then used within the FDP algorithm to estimate non-classical Fock states without any assumptions of the detector positive operator-valued measure. Finally, motivated by the success of the technique in a CV setting, the FDP method was extended to the estimation of quantum processes – where the same benefits apply. Simulations were performed to confirm the validity of the technique for estimating both trace-preserving and probabilistic quantum processes.

7 Conclusion

In this thesis the manipulation and measurement of the quantum state of a single, travelling optical field mode has been discussed. Quantum tomography is a field which started in 1989 and has become an extensive field of research in itself. In this work some of the more recent developments in quantum tomography were harnessed to probe the generation of non-classical multi-photon Fock states and to verify a newly-developed model incorporating the effect of experimental imperfections to predict the behaviour of realistic photon-level manipulations. It is hoped that this demonstration that it is possible to probe such abstract manipulations with sufficient resolution and accuracy to verify a mathematical model of the process will spur on efforts in both tomography and quantum state engineering – towards arbitrary manipulations of the quantum state of light. These experiments were only made possible by the development of a balanced homodyne detector with sufficient bandwidth and noise characteristics to faithfully measure field quadratures at the shot-noise limit. Thus in the endeavour to probe genuine quantum phenomena, along the way it was necessary to take a step aside and indulge in electrical engineering and prototyping of photodetection apparatuses. Few groups in the world are presently capable of such measurements and it is hoped that this work will go some way towards opening up discussion of the challenges and techniques such that further development and experimentation can flourish. Next, attention was turned to furthering the broad field of tomography in two respects. The first experimental demonstration of a conceptually unique tomography scheme was presented. The *fitting of data patterns* (FDP) approach was harnessed to implicitly calibrate the balanced homodyne detector within a local field-of-view and for the first time, non-classical Fock states were reconstructed with no *a priori* assumptions about the workings of the detector. This scheme should prove to be valuable in scenarios where a full characterization via quantum detector tomography is infeasible. Finally it was shown how the spirit of the FDP approach could be applied to the estimation of quantum processes – where prior detector calibration is not required. This technique could prove to be powerful for unearthing the nature of the complex operations occurring inside the quantum information processors of tomorrow and will hopefully serve as a valued part of the quantum tomography toolbox for future decades.

7.1 Future directions

With the availability of enhanced tools – both experimental and theoretical – the door is opened ever wider for exploration of the quantum world. Here a few potential routes for further research and development are outlined.

7.1.1 FPGA-based signal processing and heralding logic

One of the practical challenges when working with balanced homodyne detection is that the output signal generated is an analogue voltage which must be digitized with sufficient resolution to faithfully resolve the underlying quadrature probability distribution. In hybrid schemes bridging the DV and CV domains [47, 202, 48] one is often interested in performing homodyne measurements conditional on one or more heralding events. This necessarily implies a mixture of both analogue and digital signals within one system. For small-scale proof-of-principle experiments the challenges tend to be dealt with in an *ad hoc* manner – employing for example a digital oscilloscope to acquire the output voltage from the balanced homodyne detector (BHD) which is either triggered in real-time from a series of heralding detector TTL logic pulses or analysed off-line – where interesting events are time-stamped relative to a common clock.

For more complex systems this approach is evidently not scalable. Oscilloscopes are primarily a diagnosis tool and are not designed for a dedicated application. Furthermore, triggering arrangements can become cumbersome when multiple heralding detectors must be monitored. To this end, the ultimate goal would be to perform both the signal processing of the BHD voltage *and* the triggering logic within a single field-programmable gate array (FPGA) circuit. An analogue-to-digital converter would serve as the front end for the homodyne inputs with the processing to perform calibration of the BHD and extraction of quadrature samples performed on the FPGA. Furthermore, triggering logic is already calculated within existing FPGA designs. Such a scheme would be inherently scalable, more cost-effective and would enable schemes such as homodyne heralding [200, 199, 275] 'on-the-fly' for the first time.

7.1.2 Improved squeezed and Fock state sources

The amount of squeezing which can be generated through single-pass parametric down-conversion in bulk media is currently a limiting factor in generating higher-order Fock states through heralding [276] or generating CV entanglement as a resource for cluster-state quantum computing [277]. Furthermore, as explored in chapter 4, mode-matching of the down-converted light with a local oscillator (LO) can be challenging since for bulk sources there is no waveguide structure to define a spatial mode and in the pulsed domain an enhancement cavity – which would allow matching of the LO by using an identical cavity as a mode cleaner [28] – seems a challenging prospect. Experiments employing continuous-wave pumped optical parametric oscillators are able to make use of such cavities and have demonstrated exceptional interference visibility between a heralded Fock state and the LO [190]. However, pulsed sources are desirable owing to the well-defined timing structure which enables multiple sources to be concatenated.

One solution may be to generate squeezing through spontaneous four-wave mixing (SFWM) in either birefringent fiber [142] or waveguides [251] – both of which provide a well-defined spatial mode which can be overlapped with the LO. The road-block to employing such sources with homodyne techniques stems from the nature of the SFWM process. The photon pairs are emitted at different wavelengths, separate from that of the pump. This has the unfortunate consequence that the master laser cannot be used as the LO, since it is at a different wavelength to the heralded states. One solution could be to employ a separate OPO to generate the LO at the correct wavelength. However, this is likely to be technically challenging and unstable.

Perhaps wave-guided parametric down-conversion could provide the best of both worlds. Karpinski *et al.* [278] demonstrated the generation of spatially single-mode parametric down conversion in a $KTiOPO_4$ waveguide.* Two near-identical waveguides could be employed with one used to perform down-conversion and the other used to spatially filter the LO to match the spatial mode of the down-converted light – similar in principle to the mode-cleaners used with OPO sources. This could provide a route to improving the interference visibility between the LO and heralded Fock states or squeezed states in the pulsed domain.

*i.e. the spatial-domain analog of the spectrally single-mode down-conversion employed in this thesis based on the work of Mosley [162].

7.1.3 On-chip homodyne detection

Undoubtedly the best solution to overcoming the mode-matching issues discussed above would be to integrate the balanced homodyne detector within a photonic chip [279]. Arguably photonic quantum information processors are certainly moving in the direction of integrated photonics with on-chip photon-number-resolving detection already having been realized [280]. An on-chip platform would naturally solve the mode-matching issues discussed before, and would also offer enhanced phase stability – crucial for realizing quantum-enhanced phase estimation based on coherent states [281] and homodyne heralding protocols [200].

Integration of a balanced homodyne detector within a planar structure has even been proposed as a method to probe the Casimir force between two plates at large separation [282].

7.1.4 Full characterization of BHD

The first complete detector tomography of a phase-sensitive detector was recently demonstrated by Zhang *et al.* [94] for a weak homodyne detector – a scheme combining particle and wave sensitivity by using a coherent local oscillator but replacing conventional photodiodes by multiplexed click detectors. Detector tomography of a conventional homodyne detector with phase sensitivity is yet to be demonstrated and would provide an interesting comparison with the work of [94]. Yet this is likely to be challenging since the ideal quadrature eigenstate projectors normally assumed as the positive operator-valued measure (POVM) elements for homodyne detection do not have a finite representation in either phase-space or in the photon-number basis. It is likely that the recently introduced recursive detector tomography scheme will have to be adapted to enable this [261]. The assumed POVM elements corresponding to homodyne detection are not smooth in the photon-number basis – unlike those of most photon-number resolving detectors. Thus the usual regularization employed to ensure stability of the QDT algorithm [259] might not be permissible. In parallel to this endeavour it would be instructive to experimentally acquire a data pattern set for use in the FDP approach using a full grid of coherent state probes. This would require a phase stabilizer system and might be better suited to implementation within a photonic chip.

7.1.5 QPT of down-conversion

Coherent-state quantum process tomography (csQPT) [56, 60, 61], introduced in chapter 5, is proving to be an invaluable technique for characterizing quantum operations on one [245, 245, 131] or two [246] optical field modes. Yet there remain fundamental processes yet to be probed by this technique. This work took the complexity of single-mode operations characterized to date a step further by examining a post-selected beam splitter assisted by a non-classical ancilla state. An exciting prospect would be to probe single- and two-mode squeezing by csQPT – thus verifying the squeezing Hamiltonian. Other potential processes yet to be fully characterized are noiseless amplification and the quadrature operator. The latter has been proposed as a method of generating the orthogonal state to any input pure state [283].

A

Source alignment procedure using DFG

The following alignment procedure was established to perform initial alignment of the parametric down-conversion (PDC) source using difference frequency generation (DFG) (all component references relate to figure 4.6):

1. Align seed and pump beams such that they are collinear. This is typically achieved by monitoring the two beams on CCD cameras placed in the near- and far-field. In order to allow the pump beam passage through the down-converter the dichroic mirror (DM3) and Schott glass filter (RGF), shown in figure 4.6, are removed to perform this operation.

2. Adjust polarization of seed beam with QWP1 and HWP1 to ensure minimal leakage into signal mode (reflection from PBS2). The optical power in the reflected mode is monitored with a power meter.

3. Adjust delay 1 to optimize temporal overlap of seed and pump pulses in KDP crystal. The e-ray emission is monitored in the reflected mode from PBS2 using a power meter. As delay 1 is scanned the pump and seed pulses will overlap in the KDP crystal and DFG will result, thus an increase in power in the e-ray mode will be observed, figure 4.7(b).

4. Recouple LO into SMF2, which serves as a reference of the LO spatial mode.*

5. Couple stimulated e-ray into SMF2, thus aligning the LO and e-ray spatial modes. Coupling efficiency is measured with a power meter (PM2).

6. Couple seed beam (o-ray) into SMF1, using a power meter (PM1) to optimize coupling efficiency. SMF1 collects the trigger mode of the TMSV state when the PDC source is operated in the spontaneous regime.

7. Adjust tilt of KDP crystal to set optic axis angle $\mathbf{c}(\theta)$ with respect to input pump beam wave vector. This adjusts the phase matching to obtain DFG emission at the desired wavelengths.

8. Overlap LO and seeded e-ray spectra using interference filter (IF) in LO mode. Spectra monitored using CS.

9. Adjust delay 2 in e-ray mode to obtain interference between LO and seeded e-ray. Interference fringes observed either on CS as spectral fringes or by monitoring a fast photodiode (PD) with oscilloscope.

*Provided the coupling efficiency of the LO into the fiber is high. A coupling efficieny in excess of 90% is typically achieved.

B
Oscilloscope configuration

For the experiments reported in this thesis, data collection based on heralding events was performed in real-time using the internal pattern state trigger functionality of the Tektronix MSO5104 oscilloscope. The oscilloscope has 4 analogue channels and 16 digital channels. Ordinarily the digital channels would be used to monitor the APDs since the APD output is a TTL pulse. However, in the experiments reported there were sufficient analogue channels available for monitoring the APDs and recording the voltage from the balanced homodyne detector (BHD). This had the advantage of being able to see the timing of the APD TTL pulses precisely. An example of the pattern state trigger setup is shown in figure B.1. The BHD is on channel 1 whilst two APDs and the pulse picker control pulse* are on channels 1-3. The trigger logic is set such that the oscilloscope will trigger only when channels 1, 2 and 3 are high simultaneously. The similar "state" trigger mode also enables specification of the minimum time the selected channels' TTL pulses should overlap, thus reducing dark counts and double-pulse events. This was found to be useful for the Fock state filtration experiment reported in chapter 5.

*Also a TTL pulse

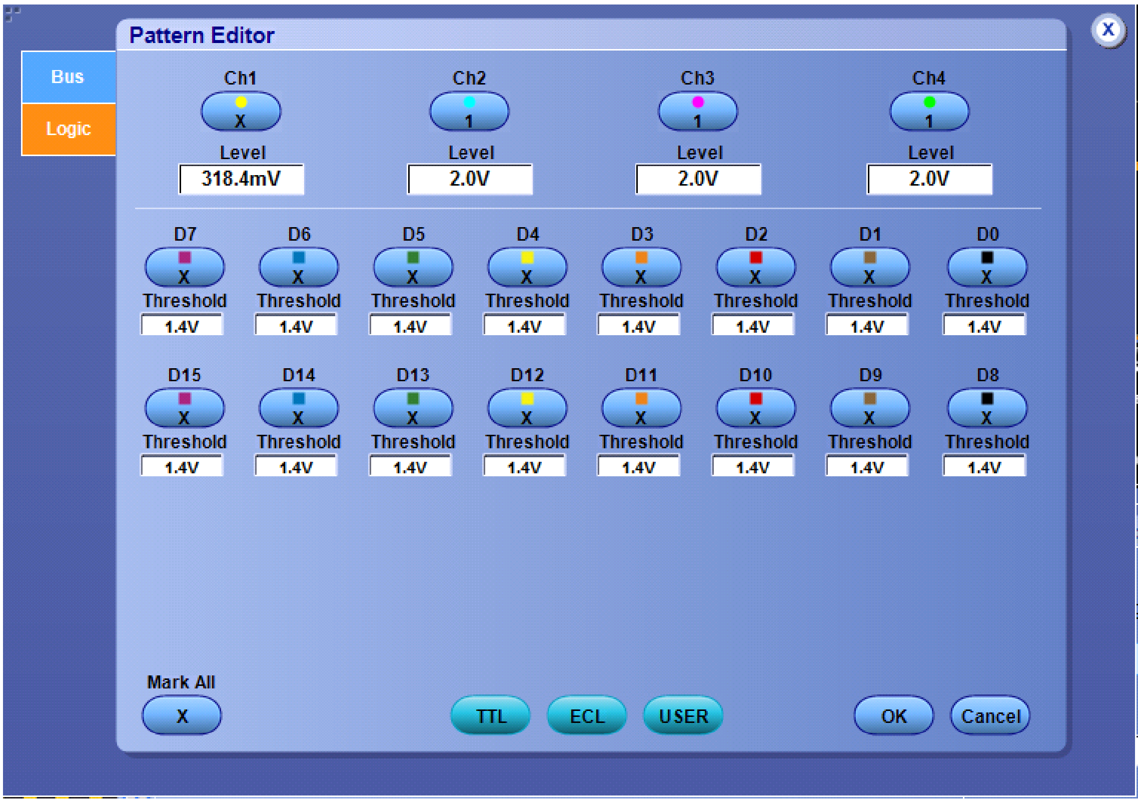

Figure B.1: Pattern trigger setup on the Tektronix MSO5104 oscilloscope. The oscilloscope will trigger when channels 1, 2 and 3 are logic high simultaneously.

C

BHD Printed Circuit Board Layout

The printed circuit board (PCB) design for the BHD developed as part of this thesis, detailed in chapter 3, is presented in this appendix, figure C.1. The PCB layout was designed with the Cadsoft EAGLE program and the PCBs were manufactured by APCircuits in Alberta, Canada. The PCB measures 6.5 cm by 4.5 cm and thus the BHD is quite compact. The primary design considerations were to place the two S3883 photodiodes as close together as practical with the track between the diodes and the first operational amplifier also kept to the minimum possible length. The PCB has a top and bottom ground plane which greatly aids in reducing cross-talk between adjacent tracks. Most of the components are placed on the top of the board. The bottom of the PCB comprises a ground plane and the feedback components for the two operational amplifiers. The latter were placed on the reverse side of the PCB to ease track congestion on the top. A BNC connector is mounted on the bottom of the PCB to enable easy connection of the BHD to a digitizer with a 50 Ω co-axial patch cable.

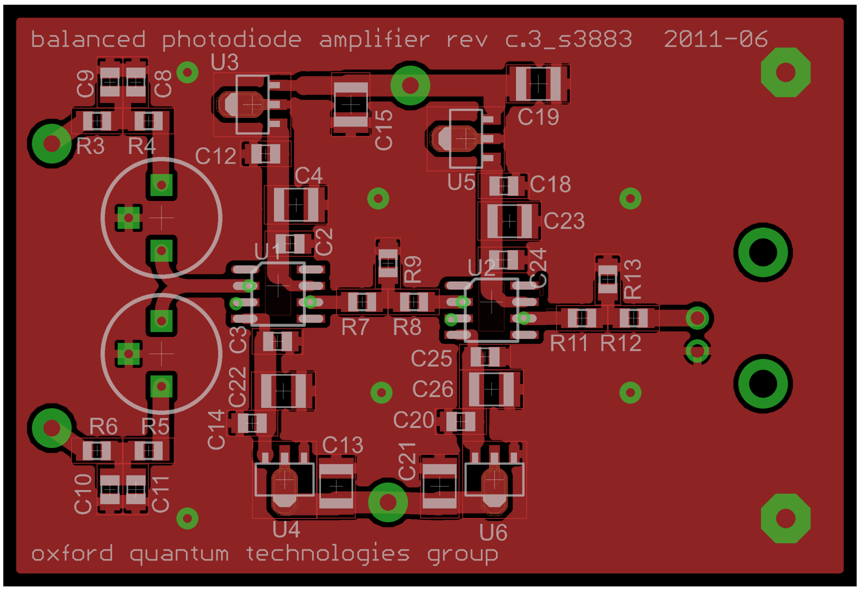

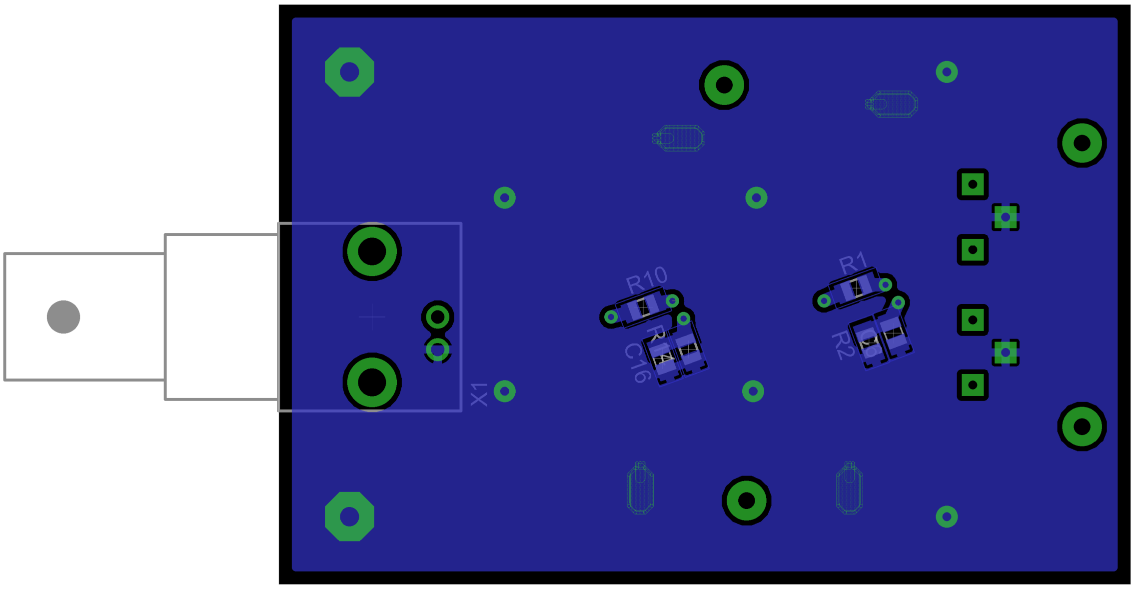

Figure C.1: Printed circuit board for the balanced homodyne detector. Top: top-side of PCB, bottom: reverse side.

D

Laboratory setup

The author's doctoral studies commenced in the autumn of 2010 in the new laboratories of Dr Brian J. Smith – situated within the Denys Wilkinson Building, Oxford. From the Oxford University physics department website:

> *The building was built in the 1960s on the north-east corner of Keble and Banbury Roads to house the new Department of Nuclear Physics. It was originally named the Nuclear Physics Laboratory. Since then the various physics areas have been unified into a single Department of Physics with 6 sub-Departments. The sub-Departments of Astrophysics and Particle Physics are now the main occupants of the building. In 2001 the building was renamed the Denys Wilkinson Building, in honour of Sir Denys Wilkinson who was instrumental in its creation.*

The latest major addition to the Denys Wilkinson building are the 8 new laser laboratories situated within its basement – a former target hall from the nuclear physics era.* The author's experimental work was conducted in one of the new laboratories. At the commencement of the author's D.Phil. the laboratory stood as an empty room. Experiments began in spring 2011 after taking delivery of a Ti:Sapphire oscillator and optical table, figure D.1. The laboratory as it stood near the conclusion of the author's experimental work is depicted in figure D.2.

*With 1 m thick walls to prove the point.

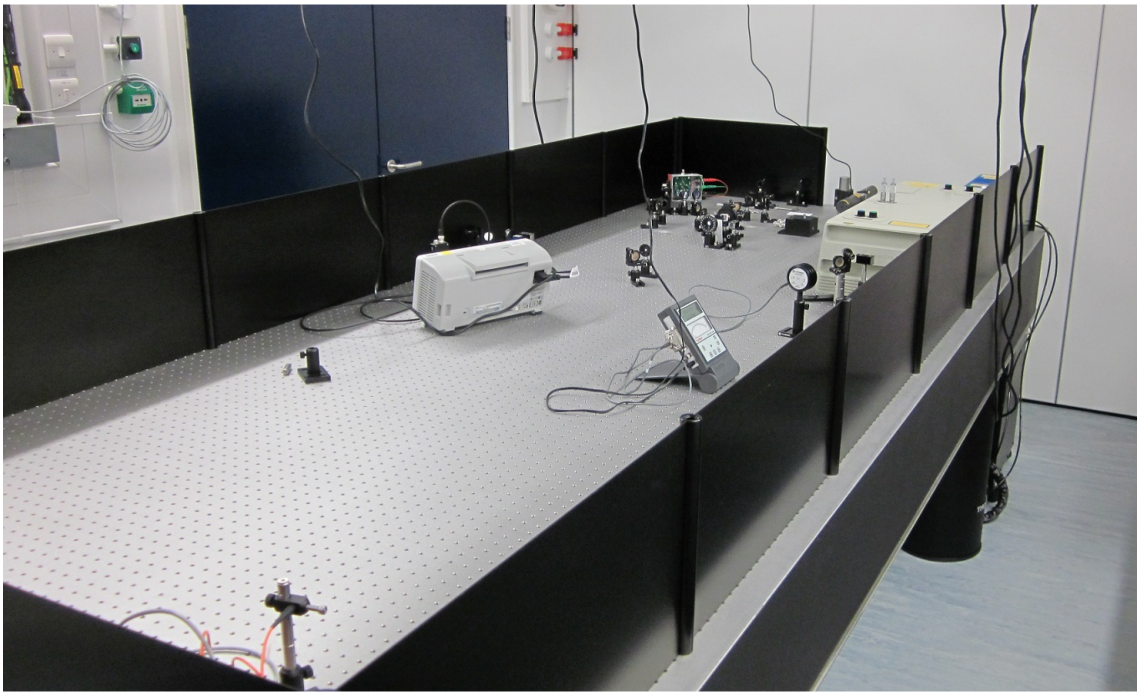

Figure D.1: Laboratory in spring 2011

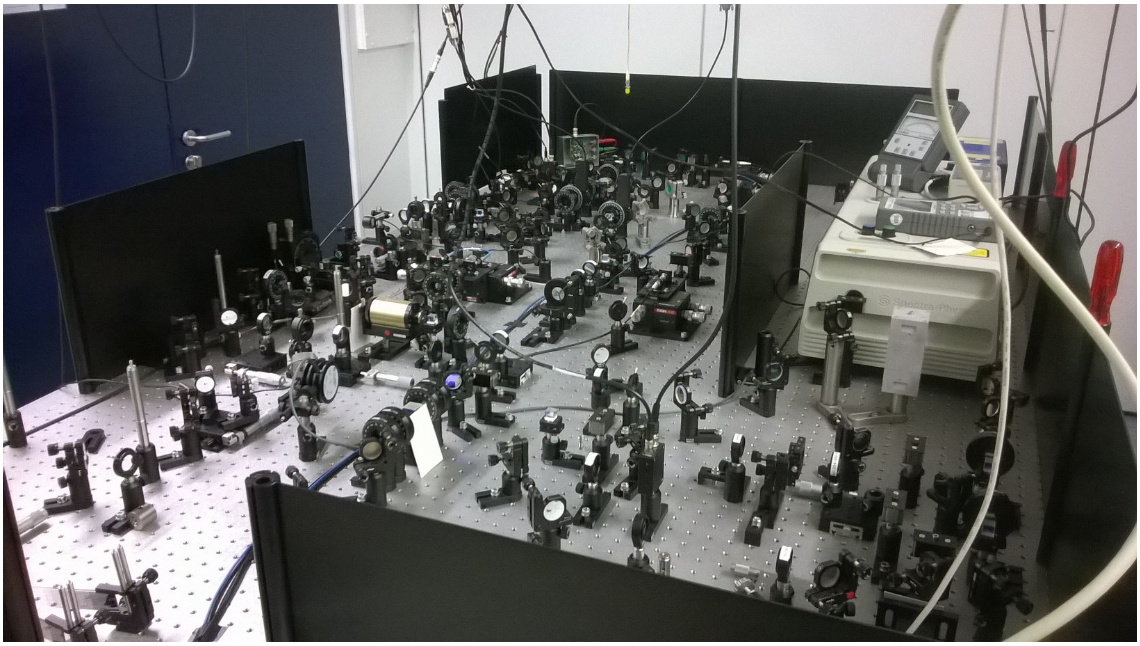

Figure D.2: Laboratory in summer 2014.

Bibliography

[1] J. Enoch. History of mirrors dating back 8000 years. *Optometry & Vision Science*, 83(10): 775–781, 2006.

[2] A. H. Layard. *Discoveries among the ruins of Nineveh and Babylon.* New York, Harper & brothers, 1853.

[3] O. Darrigol. *A history of optics from Greek antiquity to the nineteenth century.* Oxford University Press, 2012.

[4] A. Rupert Hall and Isaac Newton. *All was light : an introduction to Newton's Opticks.* Clarendon Press, 1993.

[5] E. J. Atzema. Lenses and waves. christiaan huygens and the mathematical science of optics in the seventeenth century. *Historia Mathematica*, 33(3):367–369, 2006.

[6] E. Hecht. *Optics.* Addison Wesley, 4th edition, 2002.

[7] J. C. Maxwell. *A treatise on electricity and magnetism.* Clarendon Press ; Oxford University Press, unabridged 3rd edition, 1998.

[8] M. Planck. *The theory of heat radiation.* Dover Publications, 1959.

[9] A. Einstein. Über einen die Erzeugung und Verwandlung des Lichtes betreffenden heuristischen Gesichtspunkt. *Annalen der Physik*, 322(6):132–148, 1905.

[10] G. Taylor. Interference fringes with feeble light. *Proceedings of the Cambridge Philosophical Society*, 15:114–115, 1909.

[11] G. Lewis. The conservation of photons. *Nature*, 118(2981):874–875, 1926.

[12] P. A. M. Dirac. The quantum theory of the emission and absorption of radiation. *Proceedings of the Royal Society of London. Series A*, 114(767):243–265, 1927.

[13] M. Fox. *Quantum optics: an introduction.* Oxford master series in physics Atomic, optical, and laser physics. Oxford University Press, 2006.

[14] R. Loudon. *The quantum theory of light.* Clarendon Press, 3rd edition, 2000.

[15] L. Mandel and E. Wolf. *Optical coherence and quantum optics*. Cambridge University Press, 1995.

[16] C. K. Hong, Z. Y. Ou, and L. Mandel. Measurement of subpicosecond time intervals between two photons by interference. *Physical Review Letters*, 59(18):2044–2046, 1987.

[17] R. J. Glauber. Coherent and incoherent states of radiation field. *Physical Review*, 131(6): 2766, 1963.

[18] H. J. Kimble, M. Dagenais, and L. Mandel. Photon antibunching in resonance fluorescence. *Physical Review Letters*, 39(11):691–695, 1977.

[19] A. Aspect, P. Grangier, and G. Roger. Experimental tests of realistic local theories via Bell's theorem. *Physical Review Letters*, 47(7):460–463, 1981.

[20] J. Bell. On the Einstein Podolsky Rosen paradox. *Physics*, 1(3):195–200, 1964.

[21] H. A. Bachor and T. C. Ralph. *A guide to experiments in quantum optics*. Wiley-VCH, 2nd, rev. and enl. edition, 2004.

[22] A. Steinberg, P. Kwiat, and R. Chiao. *Quantum Optical Tests of the Foundations of Physics*, book section 80, pages 1185–1213. Springer New York, 2006.

[23] V. Parigi, A. Zavatta, M. Kim, and M. Bellini. Probing quantum commutation rules by addition and subtraction of single photons to/from a light field. *Science*, 317(5846):1890–1893, 2007.

[24] B. Giorgio, G. Marco, and P. Fabrizio. Recent experimental progresses in testing quantum mechanics. *Journal of Physics: Conference Series*, 306(1):012011, 2011.

[25] N. Bruno, A. Martin, P. Sekatski, N. Sangouard, R. T. Thew, and N. Gisin. Displacement of entanglement back and forth between the micro and macro domains. *Nature Physics*, 9 (9):545–548, 2013.

[26] A. I. Lvovsky, R. Ghobadi, A. Chandra, A. S. Prasad, and C. Simon. Observation of micro-macro entanglement of light. *Nature Physics*, 9(9):541–544, 2013.

[27] R. E. Slusher, L. W. Hollberg, B. Yurke, J. C. Mertz, and J. F. Valley. Observation of squeezed states generated by 4-wave mixing in an optical cavity. *Physical Review Letters*, 55 (22):2409–2412, 1985.

[28] The LIGO Scientific Collaboration. Enhanced sensitivity of the LIGO gravitational wave detector by using squeezed states of light. *Nature Photonics*, 7(8):613–619, 2013.

[29] I. Pikovski, M. R. Vanner, M. Aspelmeyer, M. S. Kim, and C. Brukner. Probing Planck-scale physics with quantum optics. *Nature Physics*, 8(5):393–397, 2012.

[30] J. P. Dowling and G. J. Milburn. Quantum technology: the second quantum revolution. *Philosophical Transactions of the Royal Society of London Series a-Mathematical Physical and Engineering Sciences*, 361(1809):1655–1674, 2003.

[31] J. L. O'Brien, A. Furusawa, and J. Vuckovic. Photonic quantum technologies. *Nature Photonics*, 3(12):687–695, 2009.

[32] R. P. Feynman. Simulating physics with computers. *International Journal of Theoretical Physics*, 21(6-7):467–488, 1982.

[33] D. Deutsch. Quantum-theory, the Church-Turing principle and the universal quantum computer. *Proceedings of the Royal Society of London Series a-Mathematical Physical and Engineering Sciences*, 400(1818):97–117, 1985.

[34] E. Knill, R. Laflamme, and G. J. Milburn. A scheme for efficient quantum computation with linear optics. *Nature*, 409(6816):46–52, 2001.

[35] M. A. Nielsen and I. L. Chuang. *Quantum computation and quantum information*. Cambridge University Press, new edition, 2010.

[36] R. Raussendorf and H. J. Briegel. A one-way quantum computer. *Physical Review Letters*, 86(22):5188–5191, 2001.

[37] T. C. Ralph and P. K. Lam. A bright future for quantum communications. *Nature Photonics*, 3(12):671–673, 2009.

[38] C. H. Bennett and G. Brassard. Quantum cryptography: Public key distribution and coin tossing. *Proceedings of the IEEE International Conference on Computers, Systems and Signal Processing*, pages 175–179, 1984.

[39] K. Banaszek, R. Demkowicz-Dobrzanski, and I. A. Walmsley. Quantum states made to measure. *Nature Photonics*, 3(12):673–676, 2009.

[40] M. A. Taylor, J. Janousek, V. Daria, J. Knittel, B. Hage, H. A. Bachor, and W. P. Bowen. Biological measurement beyond the quantum limit. *Nature Photonics*, 7(3):229–233, 2013.

[41] C. Gabriel, C. Wittmann, D. Sych, R. F. Dong, W. Mauerer, U. L. Andersen, C. Marquardt, and G. Leuchs. A generator for unique quantum random numbers based on vacuum states. *Nature Photonics*, 4(10):711–715, 2010.

[42] W. Heisenberg. Über den anschaulichen Inhalt der quantentheoretischen Kinematik und Mechanik. *Zeitschrift für Physik*, 43(3-4):172–198, 1927.

[43] C. Elliott, A. Colvin, D. Pearson, O. Pikalo, J. Schlafer, and H. Yeh. Current status of the DARPA quantum network. *Quantum Information and Computation III*, 5815:138–149, 2005.

[44] M. Sasaki, M. Fujiwara, H. Ishizuka, W. Klaus, K. Wakui, M. Takeoka, S. Miki, T. Yamashita, Z. Wang, A. Tanaka, K. Yoshino, Y. Nambu, S. Takahashi, A. Tajima, A. Tomita, T. Domeki, T. Hasegawa, Y. Sakai, H. Kobayashi, T. Asai, K. Shimizu, T. Tokura, T. Tsurumaru, M. Matsui, T. Honjo, K. Tamaki, H. Takesue, Y. Tokura, J. F. Dynes, A. R. Dixon, A. W. Sharpe, Z. L. Yuan, A. J. Shields, S. Uchikoga, M. Legre, S. Robyr, P. Trinkler, L. Monat, J. B. Page, G. Ribordy, A. Poppe, A. Allacher, O. Maurhart, T. Langer, M. Peev, and A. Zeilinger. Field test of quantum key distribution in the Tokyo QKD network. *Optics Express*, 19(11):10387–10409, 2011.

[45] S. L. Braunstein and P. van Loock. Quantum information with continuous variables. *Reviews of Modern Physics*, 77(2):513–577, 2005.

[46] U. L. Andersen, G. Leuchs, and C. Silberhorn. Continuous-variable quantum information processing. *Laser & Photonics Reviews*, 4(3):337–354, 2010.

[47] P. van Loock. Optical hybrid approaches to quantum information. *Laser & Photonics Reviews*, 5(2):167–200, 2011.

[48] S. Takeda and A. Furusawa. Optical hybrid quantum information processing. *ArXiv e-prints*, April 2014.

[49] M. Paris and J. Řeháček. *Quantum state estimation.* Lecture notes in physics. Springer, 2004.

[50] A. I. Lvovsky and M. G. Raymer. Continuous-variable optical quantum-state tomography. *Reviews of Modern Physics*, 81(1):299–332, 2009.

[51] M. G. Raymer. Measuring the quantum mechanical wave function. *Contemporary Physics*, 38(5):343–355, 1997.

[52] I. L. Chuang and M. A. Nielsen. Prescription for experimental determination of the dynamics of a quantum black box. *Journal of Modern Optics*, 44(11-12):2455–2467, 1997.

[53] J. S. Lundeen, A. Feito, H. Coldenstrodt-Ronge, K. L. Pregnell, Ch Silberhorn, T. C. Ralph, J. Eisert, M. B. Plenio, and I. A. Walmsley. Tomography of quantum detectors. *Nature Physics*, 5(1):27–30, 2008.

[54] U. Leonhardt. *Measuring the quantum state of light.* Cambridge studies in modern optics. Cambridge University Press, 1997.

[55] D. T. Smithey, M. Beck, M. G. Raymer, and A. Faridani. Measurement of the Wigner distribution and the density-matrix of a light mode using optical homodyne tomography - application to squeezed states and the vacuum. *Physical Review Letters*, 70(9):1244–1247, 1993.

[56] M. Lobino, D. Korystov, C. Kupchak, E. Figueroa, B. C. Sanders, and A. I. Lvovsky. Complete characterization of quantum-optical processes. *Science*, 322(5901):563–6, 2008.

[57] S. Lloyd and S. L. Braunstein. Quantum computation over continuous variables. *Physical Review Letters*, 82(8):1784–1787, 1999.

[58] M. L. Gu, C. Weedbrook, N. C. Menicucci, T. C. Ralph, and P. van Loock. Quantum computing with continuous-variable clusters. *Physical Review A*, 79(6):062318, 2009.

[59] K. Kraus, A. Böhm, J. D. Dollard, and W. H. Wootters. *States, effects, and operations : fundamental notions of quantum theory : lectures in mathematical physics at the University of Texas at Austin.* Lecture notes in physics. Springer-Verlag, 1983.

[60] S. Rahimi-Keshari, A. Scherer, A. Mann, A. T. Rezakhani, A. I. Lvovsky, and B. C. Sanders. Quantum process tomography with coherent states. *New Journal of Physics*, 13:013006, 2011.

[61] A. Anis and A. I. Lvovsky. Maximum-likelihood coherent-state quantum process tomography. *New Journal of Physics*, 14:105021, 2012.

[62] C. C. Gerry and P. Knight. *Introductory quantum optics.* Cambridge University Press, 2004.

[63] J. Bertrand and P. Bertrand. A tomographic approach to Wigner function. *Foundations of Physics*, 17(4):397–405, 1987.

[64] E. Wigner. On the quantum correction for thermodynamic equilibrium. *Physical Review*, 40 (5):749–759, 1932.

[65] M. Hillery, R. F. O'Connell, M. O. Scully, and E. P. Wigner. Distribution functions in physics: Fundamentals. *Physics Reports*, 106(3):121–167, 1984.

[66] K. Vogel and H. Risken. Determination of quasiprobability distributions in terms of probability-distributions for the rotated quadrature phase. *Physical Review A*, 40(5):2847–2849, 1989.

[67] J. Radon. On the determination of functions from their integral values along certain manifolds. *Medical Imaging, IEEE Transactions on*, 5(4):170–176, 1986.

[68] A. C. Kak and M. Slaney. *Principles of computerized tomographic imaging.* Society for Industrial and Applied Mathematics, 2001.

[69] D. Leibfried, D. M. Meekhof, B. E. King, C. Monroe, W. M. Itano, and D. J. Wineland. Experimental determination of the motional quantum state of a trapped atom. *Phys. Rev. Lett.*, 77:4281–4285, 1996.

[70] T. J. Dunn, I. A. Walmsley, and S. Mukamel. Experimental determination of the quantum-mechanical state of a molecular vibrational mode using fluorescence tomography. *Phys. Rev. Lett.*, 74:884–887, 1995.

[71] M. Jezek, J. Fiurášek, and Z. Hradil. Quantum inference of states and processes. *Physical Review A*, 68(1):012305, 2003.

[72] J. Řeháček, D. Mogilevtsev, and Z. Hradil. Operational tomography: fitting of data patterns. *Physical Review Letters*, 105(1):010402, 2010.

[73] D. Mogilevtsev, J. Rehacek, and Z. Hradil. Self-calibration for self-consistent tomography. *New Journal of Physics*, 14:095001, 2012.

[74] G. Jerald. *Photodiode amplifiers : op-amp solutions.* McGraw Hill, 1995.

[75] C. Silberhorn. Detecting quantum light. *Contemporary Physics*, 48(3):143–156, 2007.

[76] K. G. Mckay. Avalanche breakdown in silicon. *Physical Review*, 94(4):877–884, 1954.

[77] H. Dautet, P. Deschamps, B. Dion, A. D. Macgregor, D. Macsween, R. J. Mcintyre, C. Trottier, and P. P. Webb. Photon-counting techniques with silicon avalanche photodiodes. *Applied Optics*, 32(21):3894–3900, 1993.

[78] P. P. Webb and R. J. Mcintyre. Single photon detection with avalanche photodiodes. *Bulletin of the American Physical Society*, 15(6):813, 1970.

[79] R. H. Hadfield. Single-photon detectors for optical quantum information applications. *Nature Photonics*, 3(12):696–705, 2009.

[80] K. Banaszek and I. A. Walmsley. Photon counting with a loop detector. *Optics Letters*, 28 (1):52–54, 2003.

[81] D. Achilles, C. Silberhorn, C. Śliwa, K. Banaszek, and I. A. Walmsley. Fiber-assisted detection with photon number resolution. *Optics Letters*, 28(23):2387–2389, 2003.

[82] M. J. Fitch, B. C. Jacobs, T. B. Pittman, and J. D. Franson. Photon-number resolution using time-multiplexed single-photon detectors. *Physical Review A*, 68(4):043814, 2003.

[83] T. J. Bartley, G. Donati, X. M. Jin, A. Datta, M. Barbieri, and I. A. Walmsley. Direct observation of sub-binomial light. *Physical Review Letters*, 110(17):173602, 2013.

[84] H. P. Yuen and V. W. S. Chan. Noise in homodyne and heterodyne-detection. *Optics Letters*, 8(3):177–179, 1983.

[85] C. R. Müller, M. A. Usuga, C. Wittmann, M. Takeoka, C. Marquardt, U. L. Andersen, and G. Leuchs. Quadrature phase shift keying coherent state discrimination via a hybrid receiver. *New Journal of Physics*, 14:083009, 2012.

[86] C. Wittmann, M. Takeoka, K. N. Cassemiro, M. Sasaki, G. Leuchs, and U. L. Andersen. Demonstration of near-optimal discrimination of optical coherent states. *Physical Review Letters*, 101(21):210501, 2008.

[87] F. Grosshans, G. Van Assche, J. Wenger, R. Brouri, N. J. Cerf, and P. Grangier. Quantum key distribution using gaussian-modulated coherent states. *Nature*, 421(6920):238–241, 2003.

[88] B. Heim, D. Elser, T. Bartley, M. Sabuncu, C. Wittmann, D. Sych, C. Marquardt, and G. Leuchs. Atmospheric channel characteristics for quantum communication with continuous polarization variables. *Applied Physics B-Lasers and Optics*, 98(4):635–640, 2010.

[89] P. Jouguet, S. Kunz-Jacques, A. Leverrier, P. Grangier, and E. Diamanti. Experimental demonstration of long-distance continuous-variable quantum key distribution. *Nature Photonics*, 7(5):378–381, 2013.

[90] A. I. Lvovsky. Iterative maximum-likelihood reconstruction in quantum homodyne tomography. *Journal of Optics B-Quantum and Semiclassical Optics*, 6(6):S556–S559, 2004.

[91] S. Pirandola. Quantum reading of a classical digital memory. *Physical Review Letters*, 106 (9):090504, 2011.

[92] C. Dorrer, D. C. Kilper, H. R. Stuart, G. Raybon, and M. G. Raymer. Linear optical sampling. *IEEE Photonics Technology Letters*, 15(12):1746–1748, 2003.

[93] G. Puentes, J. S. Lundeen, M. P. A. Branderhorst, H. B. Coldenstrodt-Ronge, B. J. Smith, and I. A. Walmsley. Bridging particle and wave sensitivity in a configurable detector of positive operator-valued measures. *Physical Review Letters*, 102(8):080404, 2009.

[94] L. J. Zhang, H. B. Coldenstrodt-Ronge, A. Datta, G. Puentes, J. S. Lundeen, X. M. Jin, B. J. Smith, M. B. Plenio, and I. A. Walmsley. Mapping coherence in measurement via full quantum tomography of a hybrid optical detector. *Nature Photonics*, 6(6):364–368, 2012.

[95] K. Laiho, M. Avenhaus, K. N. Cassemiro, and C. Silberhorn. Direct probing of the Wigner function by time-multiplexed detection of photon statistics. *New Journal of Physics*, 11: 043012, 2009.

[96] H. Hansen, T. Aichele, C. Hettich, P. Lodahl, A. I. Lvovsky, J. Mlynek, and S. Schiller. Ultrasensitive pulsed, balanced homodyne detector: application to time-domain quantum measurements. *Optics Letters*, 26(21):1714–6, 2001.

[97] A. Zavatta, M. Bellini, P. L. Ramazza, F. Marin, and F. T. Arecchi. Time-domain analysis of quantum states of light: noise characterization and homodyne tomography. *Journal of the Optical Society of America B-Optical Physics*, 19(5):1189–1194, 2002.

[98] A. Zavatta, S. Viciani, and M. Bellini. Non-classical field characterization by high-frequency, time-domain quantum homodyne tomography. *Laser Physics Letters*, 3(1):3–16, 2006.

[99] R. Okubo, M. Hirano, Y. Zhang, and T. Hirano. Pulse-resolved measurement of quadrature phase amplitudes of squeezed pulse trains at a repetition rate of 76 Mhz. *Optics Letters*, 33 (13):1458–1460, 2008.

[100] O. Haderka, V. Michalek, V. Urbasek, and M. Jezek. Fast time-domain balanced homodyne detection of light. *Applied optics*, 48(15):2884–9, 2009.

[101] Y. M. Chi, B. Qi, W. Zhu, L. Qian, H. K. Lo, S. H. Youn, A. I. Lvovsky, and L. A. Tian. A balanced homodyne detector for high-rate Gaussian-modulated coherent-state quantum key distribution. *New Journal of Physics*, 13:013003, 2011.

[102] X. Y. Wang, Z. L. Bai, P. Y. Du, Y. M. Li, and K. C. Peng. Ultrastable fiber-based time-domain balanced homodyne detector for quantum communication. *Chinese Physics Letters*, 29(12):124202, 2012.

[103] R. Kumar, E. Barrios, A. MacRae, E. Cairns, E. H. Huntington, and A. I. Lvovsky. Versatile wideband balanced detector for quantum optical homodyne tomography. *Optics Communications*, 285(24):5259–5267, 2012.

[104] G. L. Abbas, V. W. S. Chan, and T. K. Yee. Local-oscillator excess-noise suppression for homodyne and heterodyne-detection. *Optics Letters*, 8(8):419–421, 1983.

[105] G. Breitenbach, S. Schiller, and J. Mlynek. Measurement of the quantum states of squeezed light. *Nature*, 387(6632):471–475, 1997.

[106] U. M. Titulaer and R. J. Glauber. Density operators for coherent fields. *Physical Review*, 145(4):1041, 1966.

[107] B. J. Smith and M. G. Raymer. Photon wave functions, wave-packet quantization of light, and coherence theory. *New Journal of Physics*, 9:414, 2007.

[108] M. G. Raymer, J. Cooper, H. J. Carmichael, M. Beck, and D. T. Smithey. Ultrafast measurement of optical-field statistics by DC-balanced homodyne detection. *Journal of the Optical Society of America B-Optical Physics*, 12(10):1801–1812, 1995.

[109] U. Leonhardt. Quantum and classical tomography with equidistant reference angles. *Journal of Modern Optics*, 44(11-12):2271–2280, 1997.

[110] F. Grosshans and P. Grangier. Effective quantum efficiency in the pulsed homodyne detection of a n-photon state. *European Physical Journal D*, 14(1):119–125, 2001.

[111] T. Aichele, A. I. Lvovsky, and S. Schiller. Optical mode characterization of single photons prepared by means of conditional measurements on a biphoton state. *European Physical Journal D*, 18(2):237–245, 2002.

[112] M. Born, E. Wolf, and A. B. Bhatia. *Principles of optics : electromagnetic theory of propagation, interference and diffraction of light.* Cambridge University Press, 7th (expanded) edition, 2002.

[113] U. Leonhardt, M. Munroe, T. Kiss, T. Richter, and M. G. Raymer. Sampling of photon statistics and density matrix using homodyne detection. *Optics Communications*, 127(1-3): 144–160, 1996.

[114] U. Leonhardt, H. Paul, and G. M. Dariano. Tomographic reconstruction of the density-matrix via pattern functions. *Physical Review A*, 52(6):4899–4907, 1995.

[115] Z. Hradil. Quantum-state estimation. *Physical Review A*, 55(3):R1561–R1564, 1997.

[116] K. Banaszek. Maximum-likelihood estimation of photon-number distribution from homodyne statistics. *Physical Review A*, 57(6):5013–5015, 1998.

[117] K. Banaszek. Maximum-likelihood algorithm for quantum tomography. *Acta Physica Slovaca*, 49(4):633–638, 1999.

[118] K. Banaszek. Quantum homodyne tomography with a priori constraints. *Physical Review A*, 59(6):4797–4800, 1999.

[119] J. Řeháček, Z. Hradil, and M. Jezek. Iterative algorithm for reconstruction of entangled states. *Physical Review A*, 63(4):040303, 2001.

[120] M. Cooper, C. Söller, and B. J. Smith. High-stability time-domain balanced homodyne detector for ultrafast optical pulse applications. *2012 Conference on Lasers and Electro-Optics (CLEO)*, 2012.

[121] M. Cooper, C. Söller, and B. J. Smith. High-stability time-domain balanced homodyne detector for ultrafast optical pulse applications. *Journal of Modern Optics*, 60(8):611–616, 2013.

[122] P. C. D. Hobbs. *Building electro-optical systems: making it all work*. Wiley, 2000.

[123] G. H. Rieke. *Detection of light : from the ultraviolet to the submillimeter*. Cambridge University Press, 2nd edition, 2003.

[124] J. Appel, D. Hoffman, E. Figueroa, and A. I. Lvovsky. Electronic noise in optical homodyne tomography. *Physical Review A*, 75(3):035802, 2007.

[125] R. M. Shelby, M. D. Levenson, and P. W. Bayer. Guided acoustic-wave brillouin scattering. *Phys. Rev. B*, 31:5244–5252, 1985.

[126] D. Elser, U. L. Andersen, A. Korn, O. Glöckl, S. Lorenz, Ch. Marquardt, and G. Leuchs. Reduction of guided acoustic wave brillouin scattering in photonic crystal fibers. *Phys. Rev. Lett.*, 97:133901, 2006.

[127] Z. Zhang, X.-Q. Dinh, and P. L. Voss. The quantum noise of guided wave acoustic brillouin scattering with applications to continuous-variable quantum key distribution. *Journal of Modern Optics*, 58(12):988–993, 2011.

[128] M. S. Stefszky, C. M. Mow-Lowry, S. S. Y. Chua, D. A. Shaddock, B. C. Buchler, H. Vahlbruch, A. Khalaidovski, R. Schnabel, P. K. Lam, and D. E. McClelland. Balanced homodyne detection of optical quantum states at audio-band frequencies and below. *Classical and Quantum Gravity*, 29:145015, 2012.

[129] D. W. Allan. Statistics of atomic frequency standards. *Proceedings of the Institute of Electrical and Electronics Engineers*, 54(2):221–230, 1966.

[130] F. Czerwinski, A. C. Richardson, and L. B. Oddershede. Quantifying noise in optical tweezers by Allan variance. *Optics Express*, 17(15):13255–13269, 2009.

[131] R. Kumar, E. Barrios, C. Kupchak, and A. I. Lvovsky. Experimental characterization of bosonic creation and annihilation operators. *Physical Review Letters*, 110(13):130403, 2013.

[132] M. Bellini, A. S. Coelho, S. N. Filippov, V. I. Man'ko, and A. Zavatta. Towards higher precision and operational use of optical homodyne tomograms. *Physical Review A*, 85(5): 052129, 2012.

[133] J. Wenger, A. Ourjoumtsev, R. Tualle-Brouri, and P. Grangier. Time-resolved homodyne characterization of individual quadrature-entangled pulses. *The European Physical Journal D*, 32(3):391–396, 2004.

[134] J. Wenger, R. Tualle-Brouri, and P. Grangier. Pulsed homodyne measurements of femtosecond squeezed pulses generated by single-pass parametric deamplification. *Optics Letters*, 29 (11):1267–9, 2004.

[135] A. Kuhn, M. Hennrich, and G. Rempe. Deterministic single-photon source for distributed quantum networking. *Physical Review Letters*, 89(6):067901, 2002.

[136] M. Mucke, J. Bochmann, C. Hahn, A. Neuzner, C. Nolleke, A. Reiserer, G. Rempe, and S. Ritter. Generation of single photons from an atom-cavity system. *Physical Review A*, 87 (6):063805, 2013.

[137] C. Kurtsiefer, S. Mayer, P. Zarda, and H. Weinfurter. Stable solid-state source of single photons. *Physical Review Letters*, 85(2):290–293, 2000.

[138] C. Santori, M. Pelton, G. Solomon, Y. Dale, and E. Yamamoto. Triggered single photons from a quantum dot. *Physical Review Letters*, 86(8):1502–1505, 2001.

[139] P. K. Pathak and S. Hughes. Coherently triggered single photons from a quantum-dot cavity system. *Physical Review B*, 82(4):045308, 2010.

[140] C. K. Hong and L. Mandel. Experimental realization of a localized one-photon state. *Physical Review Letters*, 56(1):58–60, 1986.

[141] M. Halder, J. Fulconis, B. Cemlyn, A. Clark, C. Xiong, W. J. Wadsworth, and J. G. Rarity. Nonclassical 2-photon interference with separate intrinsically narrowband fibre sources. *Optics Express*, 17(6):4670–4676, 2009.

[142] C. Soller, O. Cohen, B. J. Smith, I. A. Walmsley, and C. Silberhorn. High-performance single-photon generation with commercial-grade optical fiber. *Physical Review A*, 83(3): 031806, 2011.

[143] A. Ourjoumtsev, R. Tualle-Brouri, and P. Grangier. Quantum homodyne tomography of a two-photon Fock state. *Physical Review Letters*, 96(21):213601, 2006.

[144] M. Yukawa, K. Miyata, T. Mizuta, H. Yonezawa, P. Marek, R. Filip, and A. Furusawa. Generating superposition of up-to three photons for continuous variable quantum information processing. *Optics Express*, 21(5):5529–35, 2013.

[145] S. Scheel. Single-photon sources-an introduction. *Journal of Modern Optics*, 56(2-3):141–160, 2009.

[146] A. L. Migdall, I. P. Degiovanni, J. Y. Cheung, S. V. Polyakov, and J. Y. Fan. Single-photon technologies. *Journal of Modern Optics*, 58(3-4):169–173, 2011.

[147] N. Sangouard and H. Zbinden. What are single photons good for? *Journal of Modern Optics*, 59(17):1458–1464, 2012.

[148] V. Giovannetti, S. Lloyd, and L. Maccone. Quantum-enhanced measurements: Beating the standard quantum limit. *Science*, 306(5700):1330–1336, 2004.

[149] H. J. Briegel, W. Dur, J. I. Cirac, and P. Zoller. Quantum repeaters: The role of imperfect local operations in quantum communication. *Physical Review Letters*, 81(26):5932–5935, 1998.

[150] M. S. Kim, W. Son, V. Buzek, and P. L. Knight. Entanglement by a beam splitter: Nonclassicality as a prerequisite for entanglement. *Physical Review A*, 65(3):032323, 2002.

[151] K. J. Resch, J. S. Lundeen, and A. M. Steinberg. Quantum state preparation and conditional coherence. *Physical Review Letters*, 88(11):113601, 2002.

[152] E. Bimbard, N. Jain, A. MacRae, and A. I. Lvovsky. Quantum-optical state engineering up to the two-photon level. *Nature Photonics*, 4(4):243–247, 2010.

[153] T. J. Bartley, G. Donati, J. B. Spring, X. M. Jin, M. Barbieri, A. Datta, B. J. Smith, and I. A. Walmsley. Multiphoton state engineering by heralded interference between single photons and coherent states. *Physical Review A*, 86(4):043820, 2012.

[154] A. Ourjoumtsev, H. Jeong, R. Tualle-Brouri, and P. Grangier. Generation of optical Schrödinger cats from photon number states. *Nature*, 448(7155):784–786, 2007.

[155] A. I. Lvovsky and J. Mlynek. Quantum-optical catalysis: generating nonclassical states of light by means of linear optics. *Physical Review Letters*, 88(25 Pt 1):250401, 2002.

[156] S. A. Babichev, B. Brezger, and A. I. Lvovsky. Remote preparation of a single-mode photonic qubit by measuring field quadrature noise. *Physical Review Letters*, 92(4):047903, 2004.

[157] K. Sanaka, K. J. Resch, and A. Zeilinger. Filtering out photonic Fock states. *Physical Review Letters*, 96(8):083601, 2006.

[158] K. J. Resch, J. L. O'Brien, T. J. Weinhold, K. Sanaka, B. P. Lanyon, N. K. Langford, and A. G. White. Entanglement generation by Fock-state filtration. *Physical Review Letters*, 98 (20):203602, 2007.

[159] A. I. Lvovsky, H. Hansen, T. Aichele, O. Benson, J. Mlynek, and S. Schiller. Quantum state reconstruction of the single-photon fock state. *Physical Review Letters*, 87(5):050402, 2001.

[160] M. Cooper, L. J. Wright, C. Söller, and B. J. Smith. Experimental generation of multi-photon Fock states. *Optics Express*, 21(5):5309–17, 2013.

[161] N. Jain, S. R. Huisman, E. Bimbard, and A. I. Lvovsky. A bridge between the single-photon and squeezed-vacuum states. *Optics Express*, 18(17):18254–18259, 2010.

[162] P. J. Mosley, J. S. Lundeen, B. J. Smith, P. Wasylczyk, A. B. U'Ren, C. Silberhorn, and I. A. Walmsley. Heralded generation of ultrafast single photons in pure quantum states. *Physical Review Letters*, 100(13):133601, 2008.

[163] A. Christ, K. Laiho, A. Eckstein, K. N. Cassemiro, and C. Silberhorn. Probing multimode squeezing with correlation functions. *New Journal of Physics*, 13:033027, 2011.

[164] A. Christ and C. Silberhorn. Limits on the deterministic creation of pure single-photon states using parametric down-conversion. *Physical Review A*, 85(2):023829, 2012.

[165] W. H. Louisell, A. E. Siegman, and A. Yariv. Quantum fluctuations and noise in parametric processes. *Physical Review*, 124(6):1646, 1961.

[166] C. K. Hong and L. Mandel. Theory of parametric frequency down conversion of light. *Physical Review A*, 31(4):2409–2418, 1985.

[167] M. H. Rubin, D. N. Klyshko, Y. H. Shih, and A. V. Sergienko. Theory of 2-photon entanglement in type-ii optical parametric down-conversion. *Physical Review A*, 50(6):5122–5133, 1994.

[168] S. M. Barnett and P. M. Radmore. *Methods in theoretical quantum optics*. Oxford series in optical and imaging sciences. Clarendon Press, 1997.

[169] A. B. U'ren, C. Silberhorn, K. Banaszek, I. A. Walmsley, R. Erdmann, W. P. Grice, and M. G. Raymer. Generation of pure-state single-photon wavepackets by conditional preparation based on spontaneous parametiric downconversion. *Laser Physics*, 15(1):146–161, 2005.

[170] C. K. Law, I. A. Walmsley, and J. H. Eberly. Continuous frequency entanglement: Effective finite Hilbert space and entropy control. *Physical Review Letters*, 84(23):5304–5307, 2000.

[171] P. P. Rohde, W. Mauerer, and C. Silberhorn. Spectral structure and decompositions of optical states, and their applications. *New Journal of Physics*, 9:91, 2007.

[172] L. J. Zhang, C. Soller, O. Cohen, B. J. Smith, and I. A. Walmsley. Heralded generation of single photons in pure quantum states. *Journal of Modern Optics*, 59(17):1525–1537, 2012.

[173] S. M. Barnett. *Quantum information*. Oxford master series in physics Atomic, optical, and laser physics. Oxford University Press, 2009.

[174] W. Wasilewski, A. I. Lvovsky, K. Banaszek, and C. Radzewicz. Pulsed squeezed light: Simultaneous squeezing of multiple modes. *Physical Review A*, 73(6):063819, 2006.

[175] A. I. Lvovsky, W. Wasilewski, and K. Banaszek. Decomposing a pulsed optical parametric amplifier into independent squeezers. *Journal of Modern Optics*, 54(5):721–733, 2007.

[176] J. H. Eberly. Schmidt analysis of pure-state entanglement. *Laser Physics*, 16(6):921–926, 2006.

[177] P. J. Mosley, J. S. Lundeen, B. J. Smith, and I. A. Walmsley. Conditional preparation of single photons using parametric downconversion: a recipe for purity. *New Journal of Physics*, 10:093011, 2008.

[178] R. W. Boyd. *Nonlinear optics*. Academic Press, 3rd edition, 2008.

[179] P. Mandel. *Nonlinear optics : an analytical approach*. Wiley-VCH, 2010.

[180] A. I. Lvovsky and T. Aichele. On the advanced wave model of parametric down-conversion. *Decoherence, Entanglement and Information Protection in Complex Quantum Systems*, 189: 41–48, 2005.

[181] D. N. Klyshko. Combined electron-paramagnetic-res and 2-slit experiments - interference of advanced waves. *Physics Letters A*, 132(6-7):299–304, 1988.

[182] C. H. Kim, R. D. Li, and P. Kumar. Deamplification response of a traveling-wave phase-sensitive optical parametric-amplifier. *Optics Letters*, 19(2):132–134, 1994.

[183] B. Yurke and D. Stoler. Measurement of amplitude probability-distributions for photon-number-operator eigenstates. *Physical Review A*, 36(4):1955–1958, 1987.

[184] A. Zavatta, S. Viciani, and M. Bellini. Tomographic reconstruction of the single-photon Fock state by high-frequency homodyne detection. *Physical Review A*, 70(5):053821, 2004.

[185] N. Jain, S. H. Youn, and A. I. Lvovsky. Quantum tomography of the single-photon state generated by down conversion in a periodically poled KTP crystal. *Quantum Communication, Measurement and Computing (Qcmc)*, 1110:201–204, 2009.

[186] S. R. Huisman, N. Jain, S. A. Babichev, F. Vewinger, A. N. Zhang, S. H. Youn, and A. I. Lvovsky. Instant single-photon Fock state tomography. *Optics Letters*, 34(18):2739–41, 2009.

[187] A. E. B. Nielsen and K. Molmer. Single-photon-state generation from a continuous-wave nondegenerate optical parametric oscillator. *Physical Review A*, 75(2):023806, 2007.

[188] A. E. B. Nielsen and K. Molmer. Photon number states generated from a continuous-wave light source. *Physical Review A*, 75(4):043801, 2007.

[189] A. MacRae, T. Brannan, R. Achal, and A. I. Lvovsky. Tomography of a high-purity narrow-band photon from a transient atomic collective excitation. *Physical Review Letters*, 109(3): 033601, 2012.

[190] O. Morin, V. D'Auria, C. Fabre, and J. Laurat. High-fidelity single-photon source based on a type II optical parametric oscillator. *Optics Letters*, 37(17):3738–3740, 2012.

[191] O. Morin, C. Fabre, and J. Laurat. Experimentally accessing the optimal temporal mode of traveling quantum light states. *Physical Review Letters*, 111(21):213602, 2013.

[192] J. Yoshikawa, K. Makino, S. Kurata, P. van Loock, and A. Furusawa. Creation, storage, and on-demand release of optical quantum states with a negative Wigner function. *Physical Review X*, 3(4):041028, 2013.

[193] E. Bimbard, R. Boddeda, N. Vitrant, A. Grankin, V. Parigi, J. Stanojevic, A. Ourjoumtsev, and P. Grangier. Homodyne tomography of a single photon retrieved on demand from a cavity-enhanced cold atom memory. *Physical Review Letters*, 112(3):033601, 2014.

[194] P. Fritschel, M. Evans, and V. Frolov. Balanced homodyne readout for quantum limited gravitational wave detectors. *Optics Express*, 22(4):4224–4234, 2014.

[195] P. Kok, W. J. Munro, K. Nemoto, T. C. Ralph, J. P. Dowling, and G. J. Milburn. Linear optical quantum computing with photonic qubits. *Reviews of Modern Physics*, 79(1):135–174, 2007.

[196] Y. X. Gong, X. B. Zou, T. C. Ralph, S. N. Zhu, and G. C. Guo. Linear optical quantum computation with imperfect entangled photon-pair sources and inefficient non-photon-number-resolving detectors. *Physical Review A*, 81(5):052303, 2010.

[197] M. Varnava, D. E. Browne, and T. Rudolph. How good must single photon sources and detectors be for efficient linear optical quantum computation? *Physical Review Letters*, 100 (6):060502, 2008.

[198] K. N. Cassemiro, K. Laiho, and C. Silberhorn. Accessing the purity of a single photon by the width of the Hong-Ou-Mandel interference. *New Journal of Physics*, 12:113502, 2010.

[199] A. M. Lance, H. Jeong, B. G. Nicolai, T. Symul, T. C. Ralph, and P. K. Lam. Quantum-state engineering with continuous-variable postselection. *Physical Review A*, 73(4):041801, 2006.

[200] A. Laghaout, J. S. Neergaard-Nielsen, I. Rigas, C. Kragh, A. Tipsmark, and U. L. Andersen. Amplification of realistic schrödinger-cat-state-like states by homodyne heralding. *Physical Review A*, 87(4):043826, 2013.

[201] N. Lee, H. Benichi, Y. Takeno, S. Takeda, J. Webb, E. Huntington, and A. Furusawa. Teleportation of nonclassical wave packets of light. *Science*, 332(6027):330–3, 2011.

[202] S. Takeda, T. Mizuta, M. Fuwa, P. van Loock, and A. Furusawa. Deterministic quantum teleportation of photonic quantum bits by a hybrid technique. *Nature*, 500(7462):315–318, 2013.

[203] Y. H. Kim and W. P. Grice. Measurement of the spectral properties of the two-photon state generated via type II spontaneous parametric downconversion. *Optics Letters*, 30(8): 908–910, 2005.

[204] A. I. Lvovsky and J. H. Shapiro. Nonclassical character of statistical mixtures of the single-photon and vacuum optical states. *Physical Review A*, 65(3):033830, 2002.

[205] H. Hansen. *Generation and Characterization of New Quantum States of the Light Field*. Thesis, Universität Konstanz, 2000.

[206] A. Zavatta, V. Parigi, and M. Bellini. Toward quantum frequency combs: Boosting the generation of highly nonclassical light states by cavity-enhanced parametric down-conversion at high repetition rates. *Physical Review A*, 78(3):033809, 2008.

[207] M. G. Genoni, M. G. A. Paris, and K. Banaszek. Measure of the non-Gaussian character of a quantum state. *Physical Review A*, 76(4):042327, 2007.

[208] M. G. Genoni, M. G. A. Paris, and K. Banaszek. Quantifying the non-Gaussian character of a quantum state by quantum relative entropy. *Physical Review A*, 78(6):060303, 2008.

[209] M. G. Genoni and M. G. A. Paris. Quantifying non-Gaussianity for quantum information. *Physical Review A*, 82(5):052341, 2010.

[210] A. Kenfack and K. Zyczkowski. Negativity of the Wigner function as an indicator of non-classicality. *Journal of Optics B-Quantum and Semiclassical Optics*, 6(10):396–404, 2004.

[211] A. Pathak and J. Banerji. Wigner distribution, nonclassicality and decoherence of generalized and reciprocal binomial states. *Physics Letters A*, 378(3):117–123, 2014.

[212] L. Mandel. Sub-Poissonian photon statistics in resonance fluorescence. *Optics Letters*, 4(7): 205–207, 1979.

[213] G. M. D'Ariano, L. Maccone, M. G. A. Paris, and M. F. Sacchi. Optical Fock-state synthesizer. *Physical Review A*, 61(5):053817, 2000.

[214] M. Dakna, L. Knöll, and D. G. Welsch. Quantum state engineering using conditional measurement on a beam splitter. *European Physical Journal D*, 3(3):295–307, 1998.

[215] H. F. Hofmann and Shigeki Takeuchi. Realization of quantum operations on photonic qubits by linear optics and post-selection. *arXiv preprint quant-ph/0204045*, 2002.

[216] N. Namekata, Y. Takahashi, G. Fujii, D. Fukuda, S. Kurimura, and S. Inoue. Non-Gaussian operation based on photon subtraction using a photon-number-resolving detector at a telecommunications wavelength. *Nature Photonics*, 4(9):655–660, 2010.

[217] J. S. Neergaard-nielsen, M. Takeuchi, K. Wakui, K. Hayasaka, M. Takeoka, and M. Sasaki. Photon subtraction from traveling fields - recent experimental demonstrations. *Progress in Informatics*, 8:5–18, 2011.

[218] M. Dakna, J. Clausen, L. Knöll, and D. G. Welsch. Generation of arbitrary quantum states of traveling fields. *Physical Review A*, 59(2):1658–1661, 1999.

[219] D. T. Pegg, L. S. Phillips, and S. M. Barnett. Optical state truncation by projection synthesis. *Physical Review Letters*, 81(8):1604–1606, 1998.

[220] A. Ourjoumtsev, R. Tualle-Brouri, J. Laurat, and P. Grangier. Generating optical Schrödinger kittens for quantum information processing. *Science*, 312(5770):83–86, 2006.

[221] S. K. Ozdemir, A. Miranowicz, M. Koashi, and N. Imoto. Quantum-scissors device for optical state truncation: A proposal for practical realization. *Physical Review A*, 64(6):063818, 2001.

[222] A. I. Lvovsky and S. A. Babichev. Synthesis and tomographic characterization of the displaced Fock state of light. *Physical Review A*, 66(1):011801, 2002.

[223] M. Barbieri, F. Ferreyrol, R. Blandino, R. Tualle-Brouri, and P. Grangier. Nondeterministic noiseless amplification of optical signals: a review of recent experiments. *Laser Physics Letters*, 8(6):411–417, 2011.

[224] A. Zavatta, J. Fiurášek, and M. Bellini. A high-fidelity noiseless amplifier for quantum light states. *Nature Photonics*, 5(1):52–56, 2011.

[225] F. Ferreyrol, R. Blandino, M. Barbieri, R. Tualle-Brouri, and P. Grangier. Experimental realization of a nondeterministic optical noiseless amplifier. *Physical Review A*, 83(6):063801, 2011.

[226] H. Takahashi, J. S. Neergaard-Nielsen, M. Takeuchi, M. Takeoka, K. Hayasaka, A. Furusawa, and M. Sasaki. Entanglement distillation from Gaussian input states. *Nature Photonics*, 4 (3):178–181, 2010.

[227] Y. Kurochkin, A. S. Prasad, and A. I. Lvovsky. Distillation of the two-mode squeezed state. *Physical Review Letters*, 112(7):070402, 2014.

[228] M. S. Kim. Recent developments in photon-level operations on travelling light fields. *Journal of Physics B-Atomic Molecular and Optical Physics*, 41(13):133001, 2008.

[229] J. Fiurášek. Engineering quantum operations on traveling light beams by multiple photon addition and subtraction. *Physical Review A*, 80(5):053822, 2009.

[230] S. Y. Lee and H. Nha. Quantum state engineering by a coherent superposition of photon subtraction and addition. *Physical Review A*, 82(5):053812, 2010.

[231] A. Zavatta, S. Viciani, and M. Bellini. Single-photon excitation of a coherent state: Catching the elementary step of stimulated light emission. *Physical Review A*, 72(2):023820, 2005.

[232] B. Baseia, M. H. Y. Moussa, and V. S. Bagnato. Hole burning in Fock space. *Physics Letters A*, 240(6):277–281, 1998.

[233] T. J. Bartley, G. Donati, X. M. Jin, J. B. Spring, M. Barbieri, B. J. Smith, A. Datta, L. J. Zhang, and I. A. Walmsley. Turning classical states quantum with linear optics and photon counting. *2012 Conference on Lasers and Electro-Optics (Cleo)*, 2012.

[234] K. Sanaka. Linear optical extraction of photon-number Fock states from coherent states. *Physical Review A*, 71(2):021801, 2005.

[235] M. Dakna, T. Anhut, T. Opatrný, L. Knöll, and D. G. Welsch. Generating Schrödinger-cat-like states by means of conditional measurements on a beam splitter. *Physical Review A*, 55 (4):3184–3194, 1997.

[236] J. M. C. Malbouisson and B. Baseia. Controlled hole burning in the photon-number distribution of field states in a cavity. *Physics Letters A*, 290(5-6):234–238, 2001.

[237] B. M. Escher, A. T. Avelar, T. M. da Rocha, and B. Baseia. Controlled hole burning in the fock space via conditional measurements on beam splitters. *Physical Review A*, 70(2): 025801, 2004.

[238] J. Sperling, W. Vogel, and G. S. Agarwal. Quantum state engineering by click counting. *Physical Review A*, 89(4):043829, 2014.

[239] R. Tualle-Brouri, A. Ourjoumtsev, A. Dantan, P. Grangier, M. Wubs, and A. S. Sorensen. Multimode model for projective photon-counting measurements. *Physical Review A*, 80(1): 013806, 2009.

[240] J. F. Poyatos, J. I. Cirac, and P. Zoller. Complete characterization of a quantum process: The two-bit quantum gate. *Physical Review Letters*, 78(2):390–393, 1997.

[241] J. Fiurášek and Z. Hradil. Maximum-likelihood estimation of quantum processes. *Physical Review A*, 63(2):020101, 2001.

[242] J. Fiurášek. Maximum-likelihood estimation of quantum measurement. *Physical Review A*, 64(2):024102, 2001.

[243] I. Bongioanni, L. Sansoni, F. Sciarrino, G. Vallone, and P. Mataloni. Experimental quantum process tomography of non-trace-preserving maps. *Physical Review A*, 82(4):042307, 2010.

[244] F. Ferreyrol, N. Spagnolo, R. Blandino, M. Barbieri, and R. Tualle-Brouri. Heralded processes on continuous-variable spaces as quantum maps. *Physical Review A*, 86(6):062327, 2012.

[245] M. Lobino, C. Kupchak, E. Figueroa, and A. I. Lvovsky. Memory for light as a quantum process. *Physical Review Letters*, 102(20):203601, 2009.

[246] I. A. Fedorov, A. K. Fedorov, Y. V. Kurochkin, and A. I. Lvovsky. Complete characterization of a multimode quantum black box. *ArXiv e-prints*, 1403:432, 2014.

[247] D. Achilles. *Generation and Characterisation of Multiphoton Nonclassical States of Light*. Thesis, University of Oxford, 2006.

[248] H. Coldenstrodt-Ronge. *Experimental technqiues for continuous variable photonic quantum information*. Thesis, University of Oxford, 2011.

[249] J. Rehacek, Z. Hradil, E. Knill, and A. I. Lvovsky. Diluted maximum-likelihood algorithm for quantum tomography. *Physical Review A*, 75:042108, 2007.

[250] B. Calkins, P. L. Mennea, A. E. Lita, B. J. Metcalf, W. S. Kolthammer, A. Lamas-Linares, J. B. Spring, P. C. Humphreys, R. P. Mirin, J. C. Gates, P. G. R. Smith, I. A. Walmsley, T. Gerrits, and S. W. Nam. High quantum-efficiency photon-number-resolving detector for photon icon-chip information processing. *Optics Express*, 21(19):22657–22670, 2013.

[251] J. B. Spring, P. S. Salter, B. J. Metcalf, P. C. Humphreys, M. Moore, N. Thomas-Peter, M. Barbieri, X. M. Jin, N. K. Langford, W. S. Kolthammer, M. J. Booth, and I. A. Walmsley. On-chip low loss heralded source of pure single photons. *Optics Express*, 21(11):13522–13532, 2013.

[252] T. Moroder, M. Kleinmann, P. Schindler, T. Monz, O. Guhne, and R. Blatt. Certifying systematic errors in quantum experiments. *Physical Review Letters*, 110(18):180401, 2013.

[253] D. N. Klyshko. On the use of a 2-photon light for absolute calibration of photoelectric detectors. *Kvantovaya Elektronika*, 7(9):1932–1940, 1980.

[254] G. Brida, M. Genovese, and M. Gramegna. Twin-photon techniques for photo-detector calibration. *Laser Physics Letters*, 3(3):115–123, 2006.

[255] A. P. Worsley, H. B. Coldenstrodt-Ronge, J. S. Lundeen, P. J. Mosley, B. J. Smith, G. Puentes, N. Thomas-Peter, and I. A. Walmsley. Absolute efficiency estimation of photon-number-resolving detectors using twin beams. *Optics Express*, 17(6):4397–4411, 2009.

[256] D. Mogilevtsev, A. Ignatenko, A. Maloshtan, B. Stoklasa, J. Rehacek, and Z. Hradil. Data pattern tomography: reconstruction with an unknown apparatus. *New Journal of Physics*, 15:025038, 2013.

[257] A. Luis and L. L. Sanchez-Soto. Complete characterization of arbitrary quantum measurement processes. *Physical Review Letters*, 83(18):3573–3576, 1999.

[258] G. M. D'Ariano, L. Maccone, and P. Lo Presti. Quantum calibration of measurement instrumentation. *Physical Review Letters*, 93(25):250407, 2004.

[259] A. Feito, J. S. Lundeen, H. Coldenstrodt-Ronge, J. Eisert, M. B. Plenio, and I. A. Walmsley. Measuring measurement: theory and practice. *New Journal of Physics*, 11:093038, 2009.

[260] H. B. Coldenstrodt-Ronge, J. S. Lundeen, K. L. Pregnell, A. Feito, B. J. Smith, W. Mauerer, C. Silberhorn, J. Eisert, M. B. Plenio, and I. A. Walmsley. A proposed testbed for detector tomography. *Journal of Modern Optics*, 56(2-3):432–441, 2009.

[261] L. J. Zhang, A. Datta, H. B. Coldenstrodt-Ronge, X. M. Jin, J. Eisert, M. B. Plenio, and I. A. Walmsley. Recursive quantum detector tomography. *New Journal of Physics*, 14:115005, 2012.

[262] G. Brida, L. Ciavarella, I. P. Degiovanni, M. Genovese, A. Migdall, M. G. Mingolla, M. G. A. Paris, F. Piacentini, and S. V. Polyakov. Ancilla-assisted calibration of a measuring apparatus. *Physical Review Letters*, 108(25):253601, 2012.

[263] B. Hofmann. Ill-posedness and regularization of inverse problems - a review of mathematical methods. *Inverse Problem*, pages 45–66, 1995.

[264] K. C. Toh, M. J. Todd, and R. H. Tutuncu. SDPT3 - a MATLAB software package for semidefinite programming, version 1.3. *Optimization Methods & Software*, 11-2(1-4):545–581, 1999.

[265] M. K. Akhlaghi, A. H. Majedi, and J. S. Lundeen. Nonlinearity in single photon detection: modeling and quantum tomography. *Optics Express*, 19(22):21305–21312, 2011.

[266] G. Brida, L. Ciavarella, I. P. Degiovanni, M. Genovese, L. Lolli, M. G. Mingolla, F. Piacentini, M. Rajteri, E. Taralli, and M. G. A. Paris. Quantum characterization of superconducting photon counters. *New Journal of Physics*, 14:085001, 2012.

[267] J. J. Renema, G. Frucci, Z. Zhou, F. Mattioli, A. Gaggero, R. Leoni, M. J. A. de Dood, A. Fiore, and M. P. van Exter. Modified detector tomography technique applied to a superconducting multiphoton nanodetector. *Optics Express*, 20(3):2806–2813, 2012.

[268] J. J. Renema, G. Frucci, M. J. A. de Dood, R. Gill, A. Fiore, and M. P. van Exter. Tomography and state reconstruction with superconducting single-photon detectors. *Physical Review A*, 86(6):062113, 2012.

[269] C. M. Natarajan, L. J. Zhang, H. Coldenstrodt-Ronge, G. Donati, S. N. Dorenbos, V. Zwiller, I. A. Walmsley, and R. H. Hadfield. Quantum detector tomography of a time-multiplexed superconducting nanowire single-photon detector at telecom wavelengths. *Optics Express*, 21(1):893–902, 2013.

[270] M. Cooper, M. Karpinski, and B. J. Smith. Quantum state estimation with unknown measurements. *ArXiv e-prints*, 1306:6431, 2013.

[271] E. C. G. Sudarshan. Equivalence of semiclassical and quantum mechanical descriptions of statistical light beams. *Physical Review Letters*, 10(7):277, 1963.

[272] J. Lofberg. YALMIP : a toolbox for modeling and optimization in MATLAB. *Computer Aided Control Systems Design, 2004 IEEE International Symposium on*, pages 284–289, 2004.

[273] D. Sych, J. Rehacek, Z. Hradil, G. Leuchs, and L. L. Sanchez-Soto. Informational completeness of continuous-variable measurements. *Physical Review A*, 86(5):052123, 2012.

[274] R. Blume-Kohout. Optimal, reliable estimation of quantum states. *New Journal of Physics*, 12:043034, 2010.

[275] J Etesse, R Blandino, B Kanseri, and R Tualle-Brouri. Generation of cat and comb states by homodyne heralding towards a loophole-free Bell test. *CLEO: 2013 Postdeadline*, page QTh5B.3, 2013.

[276] S. A. Castelletto and R. E. Scholten. Heralded single photon sources: a route towards quantum communication technology and photon standards. *European Physical Journal-Applied Physics*, 41(3):181–194, 2008.

[277] S. Yokoyama, R. Ukai, S. C. Armstrong, C. Sornphiphatphong, T. Kaji, S. Suzuki, J. Yoshikawa, H. Yonezawa, N. C. Menicucci, and A. Furusawa. Ultra-large-scale continuous-variable cluster states multiplexed in the time domain. *Nature Photonics*, advance online publication, 2013.

[278] M. Karpinski, C. Radzewicz, and K. Banaszek. Experimental characterization of three-wave mixing in a multimode nonlinear KTiOPO4 waveguide. *Applied Physics Letters*, 94:181105, 2009.

[279] A. Politi, J. C. F. Matthews, M. G. Thompson, and J. L. O'Brien. Integrated quantum photonics. *Ieee Journal of Selected Topics in Quantum Electronics*, 15(6):1673–1684, 2009.

[280] B. Calkins, P. L. Mennea, A. E. Lita, B. J. Metcalf, W. S. Kolthammer, A. Lamas-Linares, J. B. Spring, P. C. Humphreys, R. P. Mirin, J. C. Gates, P. G. R. Smith, I. A. Walmsley, T. Gerrits, and S. W. Nam. High quantum-efficiency photon-number-resolving detector for photon icon-chip information processing. *Optics Express*, 21(19):22657–22670, 2013.

[281] E. Distante, M. Ježek, and U. L. Andersen. Deterministic superresolution with coherent states at the shot noise limit. *Physical Review Letters*, 111(3):033603, 2013.

[282] P Antonini, G Bimonte, G Bressi, G Carugno, G Galeazzi, G Messineo, and G Ruoso. An experimental apparatus for measuring the casimir effect at large distances. *Journal of Physics: Conference Series*, 161(1):012006, 2009.

[283] M. R. Vanner, M. Aspelmeyer, and M. S. Kim. Quantum state orthogonalization and a toolset for quantum optomechanical phonon control. *Physical Review Letters*, 110(1):010504, 2013.